

Statistical properties of successive ocean wave parameters

Dr. ing. thesis

Hanne Therese Wist

Trondheim, December 2003



DEPARTMENT OF MARINE TECHNOLOGY
FACULTY OF ENGINEERING SCIENCE AND TECHNOLOGY
NORWEGIAN UNIVERSITY OF SCIENCE AND TECHNOLOGY

ISBN 82 771 5669 7

Abstract

For random waves the free surface elevation can be described by a number of individual wave parameters. The main object of this work has been to study the statistical properties of individual parameters in successive waves; the wave crest height, the wave height and the wave period.

In severe sea states the wave crest heights exhibit a nonlinear behavior, which must be reflected in the models. An existing marginal distribution that uses second order Stokes-type nonlinearity is transformed to a two-dimensional distribution by use of the two-dimensional Rayleigh distribution. This model only includes sum frequency effects. A two-dimensional distribution is also established by transforming a second order model including both sum and difference frequency effects. Both models are based on the narrow-band assumption, and the effect of finite water depth is included. A parametric wave crest height distribution proposed by Forristall (2000) has been extended to two dimensions by transformation of the two-dimensional Weibull distribution.

Two successive wave heights are modeled by a Gaussian copula, which is referred to as the Nataf model. Results with two initial distributions for the transformation are presented, the Næss (1985) model and a two-parameter Weibull distribution, where the latter is in best agreement with data. The results are compared with existing models. The Nataf model has also been used for modeling three successive wave heights. Results show that the Nataf transformation of three successive wave heights can be approximated by a first order autoregressive model. This means that the distribution of the wave height given the previous wave height is independent of the wave heights prior to the previous wave height. The simulation of successive wave heights can be done directly without simulating the time series of the complete surface elevation.

Successive wave periods are modeled with the Nataf transformation by using a two-parameter Weibull distribution and a generalized Gamma distribution as the initial distributions, where the latter is in best agreement with data. Results for the marginal and two-dimensional distributions are compared with existing models. In practical applications, it is often of interest to consider successive wave periods with corresponding wave heights exceeding a certain threshold. Results show that the distribution for successive wave periods when the corresponding wave heights exceed the root-mean-square value of the wave heights, can be approximated by a multivariate

Gaussian distribution. When comparing the results with data, a long time series is needed in order to obtain enough data cases. Results for three successive wave periods are also presented.

The models are compared with field data from the Draupner field and the Japan Sea, and with laboratory data from experiments at HR Wallingford. In addition, data from numerical simulations based on second order wave theory, including both sum and frequency effects, are included.

Acknowledgements

This work has been carried out under the supervision of Professor Dag Myrhaug at the Department of Marine Technology, Norwegian University of Science and Technology. His guidance is highly appreciated.

I appreciate the contribution from co-advisor Professor Håvard Rue at the Department of Mathematical Sciences. He has made it easy to keep in touch with the Group of Statistics at the Department of Mathematical Sciences.

This work has been financially supported by the Research Council of Norway. The wave data from Draupner were prepared and made available by Dr. Sverre Haver, Statoil. The wave data from the Japan Sea were prepared and made available by the National Maritime Research Institute, Mitaka, Tokyo. The laboratory data from HR Wallingford were collected during experimental studies carried out with financial support from the European Union under the TMR programme.

I would like to thank Dr. Carl Trygve Stansberg at Marintek for valuable discussions. Per Andreas Brodtkorb is acknowledged for help with computer programming.

I would also like to thank my fellow students and friends in Trondheim for making these years social enjoyable. I especially want to mention Marit Ronæss and Eirik Byklum, Gro and Rolf Baarholm, Hanne Hella and Jørn Jensen, Renate and Kjetil Skaugset.

My love and deepest gratitude go to Olav Rognebakke. His continuous support and encouragement have made this possible.

Contents

Abstract	i
Acknowledgements	iii
Contents	v
Nomenclature	ix
1 Introduction	1
1.1 Background and motivation	1
1.2 Previous work	3
1.3 Outline of the thesis	6
1.4 Major findings	7
2 Theory of stochastic processes and time series analysis, including analysis of the Draupner field data	9
2.1 Wave parameters	9
2.2 Time series analysis and definition of stochastic processes	11
2.2.1 Estimated parameters from the time series	11
2.2.2 Stationary stochastic process	12
2.2.3 Ergodic stochastic process	12
2.2.4 Narrow-banded stochastic process	13
2.3 Kernel density estimator	13
2.3.1 The kernel method in p dimensions	15
2.4 Description of Draupner field data	16
3 Joint distributions of successive wave crest heights and successive wave trough depths	21
3.1 Linear theory	21
3.2 Second order Stokes theory	22
3.2.1 Limitations of the second order Stokes theory	25
3.3 Probability distributions using second order Stokes-type nonlinearity	27

3.3.1	Marginal distribution of wave crest heights and wave trough depths . . .	27
3.3.2	Joint distributions of successive wave crest heights and successive wave trough depths	32
3.4	Forristall distribution	35
3.5	Second order wave theory	38
3.6	Extended second order model including sum and difference frequency effects . .	40
3.7	Example of using the extended second order model in prediction of green water load and volume	47
4	Joint probability distributions for successive wave heights	51
4.1	Longuet-Higgins model and Næss model	51
4.2	Gaussian distribution for successive wave heights using Nataf transformation . .	54
4.2.1	Copulas	54
4.2.2	Nataf model for successive wave heights	56
4.3	Successive wave heights modeled as a first order autoregressive (AR(1)) model .	65
4.3.1	Likelihood ratio test	69
4.3.2	Summary of AR(1) model	70
5	Joint probability distributions for successive wave periods	73
5.1	Marginal distributions for wave periods	73
5.2	Joint distribution of successive wave periods	77
5.2.1	Gaussian distribution for successive wave periods using Nataf transformation	78
5.3	Distribution of successive wave periods for large wave heights	87
6	Results and discussion	93
6.1	Data description	93
6.1.1	Draupner field	93
6.1.2	Japan Sea	95
6.1.3	Laboratory data from HR Wallingford	100
6.2	Results for wave crest heights and wave trough depths	105
6.2.1	Results for Draupner field data	105
6.2.2	Results for Japan Sea field data	110
6.2.3	Results for laboratory data	113
6.3	Results for wave heights	120
6.3.1	Wave height results for Draupner field data	120
6.3.2	Wave height results for Japan Sea field data	123
6.3.3	Wave height results for laboratory data	127
6.4	Results for wave periods	135
6.4.1	Wave period results for Draupner field data	135
6.4.2	Wave period results for Japan Sea field data	140
6.4.3	Wave period results for laboratory data	148
7	Conclusions and future perspectives	155
7.1	Summary and conclusions	155
7.2	Recommendation for further work	158

References	159
A Properties of the Rayleigh distribution	167
A.1 The marginal Rayleigh distribution	167
A.2 A two-dimensional Rayleigh distribution	167
B Perturbation technique in second order Stokes theory	171
C Limitations of wave amplitude in second order Stokes model and extended second order model	179
C.1 Second order Stokes model	179
C.2 Extended second order model	180
D Correlation coefficients	183
D.1 Correlation coefficients in the second order Stokes model	183
D.2 Correlation coefficient in the Forristall model	185
D.3 Correlation coefficients in the extended second order model	185
E Properties of the two-parameter Weibull distribution	187
E.1 The marginal Weibull distribution	187
E.2 A two-dimensional Weibull distribution	188
F Properties of the Gaussian distribution	189
F.1 The multivariate Gaussian distribution	189
F.2 Error-function	189
G Properties of the generalized Gamma distribution	191
G.1 Maximum likelihood estimators for the generalized Gamma distribution	192
H Additional results from data	193
H.1 Conditional expectation for wave crest heights and wave trough depths	193
H.2 Conditional expectation for wave heights	197
H.3 Results for wave periods	199
H.3.1 Results for Japan Sea field data	199
H.3.2 Results for laboratory data	200

Nomenclature

General rules

- Some letters are used to represent several things. However, the present meaning should be clear from the context.
- Matrices and vectors are represented by bold face characters

Roman letters

A	dimensionless surface elevation
A	stochastic variable of dimensionless linear wave amplitude
A_d	area of separated fore deck
a	dimensionless linear wave amplitude
a_{rms}	rms-value of linear wave amplitude
B	breadth of the ship
$B_1, \tilde{B}_1, B_2, \tilde{B}_2$	constants in second order Stokes perturbation technique
b	bow height at the stem
C	copula
C_B	Bernoulli constant
C_L	normalizing factor in Longuet-Higgins (1983) model
$C_{T,1}$	normalizing factor in Tayfun (1990) model
$C_{T,2}, C_{T,3}$	normalizing factor in Tayfun (1993) model
c	shape coefficient in generalized Gamma distribution
$c_{g,m}$	wave group velocity
c_p	volume of unit p -dimensional sphere
$\text{Cov}[]$	covariance

d	water depth
$E[\]$	expected value
$E(\kappa)$	complete elliptic integral of second kind
$E_{m,n}, E_{m,n}^+, E_{m,n}^-$	quadratic transfer function
$\text{erf}[\]$	error function
$\text{erf}^{-1}[\]$	inverse error function
$F(a, b; c; x)$	hypergeometric function
F_X	cumulative distribution function
F_X^{-1}	inverse of F_X
$F_X^{(-1)}$	quasi-inverse of F_X
f_X	probability density function
$\hat{f}_X(x)$	kernel density estimator
f^+, f^-	terms in the nonlinear crest height and trough depth models
g	acceleration of gravity
H_S	significant wave height
H_{m0}	significant wave height estimated from wave spectrum
$H_{1/3}$	significant wave height estimated from mean value of 1/3 highest waves
H_0	hypothesis
h	dimensionless wave height
\bar{h}	normalizing factor of wave height
\tilde{h}	given value of wave height
h_{rms}	rms-value of wave height
h_s	smoothing parameter
I	incomplete Gamma function
I_0	modified Bessel function of zeroth order
i	complex unit
J	determinant of the Jacobian
K_d	kernel function
$K(\kappa)$	complete elliptic integral of first kind
k	wave number
k_p	wave number corresponding to peak period
\bar{k}	mean wave number corresponding to T_{m02}
\bar{k}_1	wave number corresponding to T_{m01}
L	likelihood function
L_{max}	maximum value of green water load
L_{pp}	ship length
m_n	n th spectral moment
N	number of observations
$N_{\xi, -\xi}$	expected number of occurrences of the level crossings of ξ and $-\xi$
P	dimensionless pressure

$P(\cdot)$	probability
p	pressure
p	dimensions
Q	dimensionless Bernoulli constant
R	quantity in the extended second order model
$R(\tau)$	autocorrelation function
R_ϕ	ratio of velocity potential terms
r	characteristic wave steepness
r_+	characteristic wave steepness
$S(\omega)$	wave spectrum
S_1	wave steepness in Forristall (2000) model
s	average wave steepness
T	dimensionless time variable
T_{m02}	mean zero-crossing wave period estimated from wave spectrum
T_{m24}	mean period between maxima
T_{m01}	mean wave period
T_p	peak period
T_z	mean zero-crossing wave period estimated directly from time series
T_C	parameter in Cavanié (1976) distribution
t	time variable
t	dimensionless wave period
\tilde{t}	given value of wave period
\bar{U}_r	Ursell number
U_r	Ursell number in Forristall (2000) model
U_z	uniformly distributed variable
V_{\max}	maximum value of green water volume
$\text{Var}[\cdot]$	variance
\mathbf{v}	velocity
w_c	dimensionless wave crest height
w_t	dimensionless wave trough depth
X	stochastic variable
\mathbf{X}	vector of stochastic variables
X	dimensionless horizontal space variable
$X(t)$	stochastic process
x	variable
x	horizontal space variable
\dot{x}	velocity at level crossings
$\mathbf{x} = (x_1, \dots, x_n)$	realization of stochastic process
Y	stochastic variable
y_1, \dots, y_n	data points

Z	dimensionless vertical space variable
z	vertical space variable

Greek letters

α	Weibull parameter
α_1, α_2	parameters in Cavanié (1976) distribution
α_0	coefficient in green water load
β	Weibull parameter
β_0	coefficient in green water volume
Γ	gamma function
γ	location coefficient in generalized Gamma distribution
γ_J	peakedness parameter in JONSWAP spectrum
ϵ_2	spectral bandwidth parameter
ϵ_4	spectral bandwidth parameter
$\epsilon(t)$	zero mean Gaussian white noise process
ζ^2	rms-value of τ^2
η	surface elevation
η_a	linear wave amplitude
η_c	crest height
η_h	wave height
η_t	trough depth
$\bar{\eta}$	mean value of surface elevation
$\hat{\eta}_2$	fluctuating part of surface elevation
η_{\max}	relative water height
κ	parameter related to the correlation coefficient
Λ	likelihood ratio statistic
λ	shape coefficient in generalized Gamma distribution
λ_w	wave length
μ	expected value
μ_h	mean wave height
μ_r	r th central moment
$\mu_{t h}$	mean value in Tayfun (1993) model
$\mu_{t \bar{h}}$	expected value in distribution of wave periods for large wave heights
ν	scale coefficient in generalized Gamma distribution
ξ	phase
π_1, \dots, π_r	weights in AR model
ρ	density of water
ρ	correlation coefficient
ρ_3	skewness
ρ_4	kurtosis

ρ_N	parameter in Næss (1985) model
ρ_j	autocorrelation function
Σ	covariance matrix
$\Sigma_{t \bar{h}}$	covariance matrix in distribution of wave periods for large wave heights
σ^2	variance of surface elevation
$\sigma_{t h}$	standard deviation in Tayfun (1993) model
$\sigma_{t \bar{h}}$	standard deviation in distribution of wave periods for large wave heights
τ	wave period
$\bar{\tau}$	normalizing factor of wave period
Φ	standard Gaussian distribution
Φ	dimensionless velocity potential
ϕ	velocity potential
ϕ_{jj}	partial autocorrelation function
χ_p^2	chi-square distribution with p degrees of freedom
$\chi_{\alpha,p-1}^2$	α -quantile in χ_p^2 distribution
Ψ	Gaussian distributed variable resulted from Nataf transformation
ψ	phase function
$\dot{\psi}$	time derivative of the envelope phase
Ω	dimensionless wave frequency
ω	wave frequency
ω	angular wave frequency
$\bar{\omega}$	mean wave frequency
ω_p	peak frequency

Subscripts

a	wave amplitude
c	wave crest height
F	wave crest height in Forristall (2000) model
h	wave height
N	Næss (1985) model
rms	root-mean-square value
t	wave trough depth
τ	wave period
+	second order Stokes model

Other symbols

\mathcal{O}	order
\mathbb{R}	real numbers
\mathbb{R}^p	p -dimensional space of real numbers

CHAPTER 1

Introduction

1.1 Background and motivation

In design and analysis of ships and offshore structures a good description of the surface elevation is important. The surface elevation can be described by a number of parameters for individual waves, e.g., the wave height, the wave period, the wave length and the wave steepness. The surface elevation is far from deterministic, and it is important to find good statistical models that give accurate parameter predictions and corresponding uncertainty estimates. It is therefore of interest to find both marginal probability distributions as well as joint probability distributions for combined parameters or a single parameter in successive waves.

In most mild to moderate sea states, the surface elevation can be described by a linear model, and the statistics is determined from well-known distributions, e.g., the wave height is well described by the Rayleigh distribution. However, in severe sea states, which are of interest for design purposes, the nonlinear effects become significant, and more accurate models are required. A description of some cases, where the nonlinearity in the surface elevation is important, like wet-deck slamming and green water load, is given below.

Estimation of the probability of a wave height exceeding a critical level has long been recognized as important statistics in design and safety evaluation of coastal and offshore structures and vessels, e.g., when selecting the deck elevation for a fixed offshore platform. In this case it is the wave crest heights that are of interest, not the total wave height. Risk of water impact on decks of platforms has led to a large study of hydrodynamic loads and the structural response due to wave impact, see e.g., Kaplan (1992, 1995).



Figure 1.1: Model test of a semi-submersible in extreme waves. (From experiments at Marintek, Trondheim, Norway).

Weight and stability considerations will limit the deck height of floaters, such as semi-submersibles. A large air gap is therefore expensive, and in new design, extreme waves are allowed to hit the deck structure. Thus, it is important to estimate the frequency of wave impacts. Figure 1.1 shows a model test of a semi-submersible in extreme waves. One should note that the picture shows a rare event in a 100-year storm. Several methods of estimating the air gap are discussed in Sweetman and Winterstein (2003), where in particular the nonlinear behavior of the surface elevation is taken into account. The results are also compared with data from model tests.

In rough sea conditions the relative motion between the ship and wave can exceed the free-board of a ship, causing a compact mass of water on deck. This is referred to as green water. The

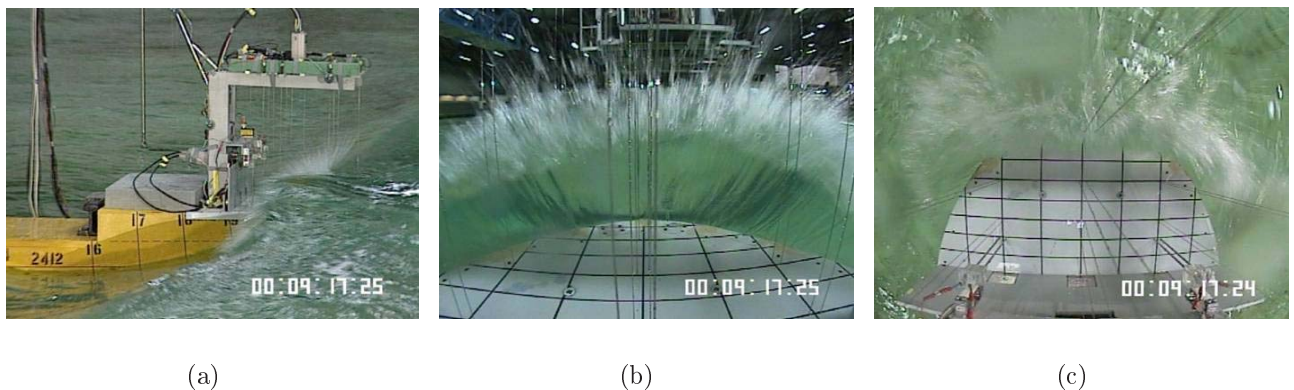


Figure 1.2: Model test of a turret moored FPSO in irregular waves. (a) From the side - bow (b) Forward from the deck house (c) From above - bow. (From Stansberg and Karlsen, 2001).

water impact can result in high pressure on the deck and on structures located at the deck, like the deck house. Green water loading can also contribute to the global loads of the ship. Probability distributions have been established in order to predict green water loads. Ogawa (2003) discussed a prediction method for green water load that is based on the distribution of relative water height. Green water incidents can be a risk factor for the stability of the ship, and water-on-deck casualties are a concern. Figure 1.2 shows a turret moored FPSO in irregular waves. The picture shows one of the most extreme and steep random wave events in both (a) side, (b) forward and (c) downward views.

Closely related to the joint distributions is the interest of knowing the conditional distribution, e.g., to know the probability of a wave crest exceeding a specified height given that the previous wave crest exceeded the same height. Several two-dimensional distributions exist for modeling two successive wave heights. These are based on transformations of well known joint distributions, e.g., the two-dimensional Weibull distribution. It is also of interest to look at a joint distribution for more than two successive wave heights, but no such distributions have been presented. The correlation between three successive wave heights, however, has been explored by several authors, see e.g. Arhan and Ezraty (1978). Extending the existing two-dimensional distributions to three-dimensional distributions or higher, is not possible, since a three-dimensional Weibull distribution is not known. Another approach must therefore be used.

The study of wave periods is relevant in analysis of ships and structures that can be excited to move near resonance. It is of interest to estimate the probability of two or more successive waves having periods close to the resonant period of the ship or structure.

For critical wave periods it is also of interest to know the corresponding wave height. Several joint distributions of wave height and wave period have been presented. These distributions can also be used to analyze the wave steepness. Closely related to this is the study of conditional distribution, e.g., to know the probability density function of two or more successive wave periods given that the corresponding wave heights exceeded a given value. This is of interest e.g. when studying parametric roll motion of ships. Ships in head sea can under given conditions experience parametric roll motion when the wave encounter period is approximately half the natural period of roll motion and the wave heights is exceeding a critical level, see France et al. (2003).

1.2 Previous work

Statistics of wave parameters has been a large field of interest for the past 50 years motivated by the stochastic nature of the surface elevation. Longuet-Higgins (1952) first introduced the Rayleigh distribution for prediction of the wave amplitude in a narrow-banded random sea. Cartwright and Longuet-Higgins (1956) modified the Rayleigh distribution to account for a more broad-banded random sea by including the spectral bandwidth parameter.

The analysis of wave groups have been made using two different approaches. Longuet-Higgins (1957), Nolte and Hsu (1972) and Ewing (1973) used the envelope function of the surface el-

evaluation to derive the group properties. A second approach, Kimura (1980), treated the time series of wave height as a Markov chain, where the transition probabilities for the wave height train were given by the two-dimensional Rayleigh distribution. Similarly, the sequence of wave periods was modeled with a Markov chain, where the transition probabilities were given by the two-dimensional Weibull distribution. The second approach was also discussed by Sobey (1996) for wave heights only. An overview of wave group statistics where both models are included is given in Longuet-Higgins (1984).

Ochi (1998) has a thorough description of joint distribution functions for linear waves, and there is also a description of developing distributions for non-Gaussian waves. Massel (1996) has a discussion of the statistical properties of ocean waves.

A realistic surface elevation is both irregular and skewed. Longuet-Higgins (1963) showed that the skewness is always positive at infinite water depth. It appears that laboratory waves generally have higher skewness and kurtosis than ocean waves, see e.g., Jha and Winterstein (2000).

A common assumption for the statistical distributions is that the sea state is narrow-banded. However, this will not be the case in a realistic sea state. Bitner (1980) considered waves in shallow water. The results showed that the assumption of Gaussian waves, and thus the narrow-band assumption, is not valid, and that nonlinear effects are significant. Different approaches of modeling nonlinear random waves are also summarized in Machado (2003).

In many engineering applications, it is the statistical properties of the wave crest height that are of most interest. A number of marginal distributions for the wave crest height are available, both theoretical models and empirical models. In severe sea states nonlinear effects must be taken into account. Tayfun (1980), Arhan and Plaisted (1981) and Tung and Huang (1985) have modified the Rayleigh distribution for wave crests and included second order Stokes nonlinear effects for deep water waves. Kriebel and Dawson (1991) clearly identified the nonlinearity in wave crest statistics from a laboratory wave record. Their model included second order Stokes nonlinearities, where a series expansion correct to second order was used. The method was extended to finite water depth in Kriebel and Dawson (1993). While these second order Stokes models only include the sum frequency effect, Prevosto et al. (2000) presented a probability distribution that also included the difference frequency effect. Forristall (1998) also identified the nonlinearity in wave crest statistics, and Forristall (2000) suggested a parametric crest height distribution based on second order simulations. Nerzic and Prevosto (1997, 1998) used a Gumbel distribution, where the parameters are found using a third order Stokes expansion of the surface elevation, to model the maximum wave height or the maximum wave crest height. A summary of some of the wave crest models can be found in Prevosto and Forristall (2002).

Another type of distribution is the Gram-Charlier series distribution. Longuet-Higgins (1963) used the cumulant generating function to obtain the probability density function for the surface elevation for non-Gaussian waves. This is the same concept as the Edgeworth expansion (see e.g. Barndorff-Nielsen and Cox, 1989). The expansion requires calculation of the cumulants up to sixth order. Al-Humoud et al. (2002) and Tayfun (1994) showed theoretical results based on a truncated form of the Gram-Charlier distribution. The theoretical distributions were compared with nonlinear wave data from a hurricane. A different approach is given by Srokosz (1998),

where the Pearson system of distributions (Pearson (1895), Johnson and Kotz (1970)) were used to derive the distributions for the surface elevation of weakly nonlinear waves. None of these types of distributions are considered in this work.

In order to verify the theoretical distributions, comparisons with field data, laboratory data and simulations are important. A vast selection of field data measurements are available. Among these are storm data measured at various locations in the Gulf of Mexico and in the North Sea in connection with installations of oil platforms. Analysis of 116 hours of hurricane generated waves (about 55000 individual waves) from the Gulf of Mexico were done by Forristall (1978), and a two-parameter Weibull distribution was fitted to the wave height data. The same data were analyzed by Haring et al. (1976). Vinje (1989) used wave data from the Statfjord field in the Northern part of the North Sea, including about 2.5 million individual waves, to compare with theoretical wave height distributions. Myrhaug and Slaattelid (1999) analyzed wave data from the Frigg field in the Central North Sea, including more than 3.3 million individual waves, and fitted a parametric model of the joint distribution of the successive wave periods. The same data were also analyzed by Nerzic and Prevosto (1998), where the data were compared to models of the maximum wave height or the maximum wave crest height.

Sharma and Dean (1981) presented a simulation method for second order directional seas that was based on the second order theory by Longuet-Higgins (1963) valid for infinite water depths. The second order theory was extended to arbitrary water depths. The model includes both sum frequency and difference frequency effects. Results from the simulation method are also described in Dean and Sharma (1981). Similar methods have been presented by Marthinsen and Winterstein (1992) and Stansberg (1993, 1998). These methods include both irregularity and skewness.

In addition to the distributions for the wave crest heights, several distributions have been proposed for the total wave height in order to improve the model of Longuet-Higgins (1952). Longuet-Higgins (1980) and Næss (1985), among others, have modified the model to give a better fit to measured wave data. A summary of some of the wave height models can be found in Vinje (1989).

The study of marginal probability distributions for wave periods have been addressed by Bretschneider (1959). He assumed that the wave length was proportional to the square of the wave period, and combined this with a transformation of the Rayleigh distribution. Longuet-Higgins (1975, 1983) presented two models for the marginal probability distributions for wave periods, where both models were obtained theoretically from the joint probability density function of the envelope amplitude and the time derivative of the envelope phase. The Longuet-Higgins (1975) model was symmetric about the mean wave period, while the Longuet-Higgins (1983) model was asymmetric. Cavanié et al. (1976) presented a joint probability density function for wave heights and wave periods that accounted for the asymmetry in the wave periods. Tayfun (1993) presented a joint distribution of wave heights and wave periods that was conditioned on the wave height being above a threshold, given by the mean wave height. The resulting distribution was Gaussian with modified mean value and standard deviation.

Most theoretical models are based on the narrow-band approximation, but Lindgren and Rychlik

(1982) presented a joint distribution of wave heights and wave periods that also are valid for broad-banded sea states. However, the expressions involved are not in a closed form, thus numerical integration is required. Rychlik et al. (1997) also presented distributions for ocean wave parameters using a transformed Gaussian model.

The study of distributions for wave heights and wave periods in sea states with two-peaked spectra have been addressed by Rodríguez and Guedes Soares using a four-parameter wave spectrum model, which is a combination of two JONSWAP spectra (Guedes Soares, 1984). A series of papers have been presented on wave heights (Rodríguez et al., 2002), wave periods (Rodríguez and Guedes Soares, 2000) and wave heights and wave periods (Rodríguez and Guedes Soares, 1999).

Fewer models have been presented for joint distribution of two successive wave periods. Kimura (1980) presented a two-dimensional Weibull distribution and compared the theoretical model with data from numerical simulations. Myrhaug and Rue (1993) presented a two-dimensional distribution based on the Bretschneider (1959) model. A revised model was given in Myrhaug and Rue (1998). Myrhaug and Slaattelid (1999) presented a parametric model of the joint distribution of two successive wave periods. The model was obtained as a best fit to measured wave data from the Frigg field in the Central North Sea. The data included more than 3 million individual waves. One application of these models is the study of near-resonant rolling of ships in beam seas, which was shown in Myrhaug et al. (2000).

1.3 Outline of the thesis

This thesis is divided into seven chapters, which can be grouped into three main parts.

Chapter 2 describes briefly the important concepts regarding stochastic processes and time series analysis. Definitions of some of the main wave parameters and a description of concepts that are extensively used throughout the thesis, e.g., the kernel density estimate, are given here. All examples that are given in the theoretical chapters use the data from the Draupner field in the Central North Sea, which is thoroughly described in Chapter 2.4.

The theoretical models for successive wave crests, wave troughs, wave heights and wave periods are described in Chapters 3 to 5. Both the existing models, the use of other models for problems in this field and extension of the existing models are discussed. The models are also compared with field data from the Draupner field.

Chapter 6 presents the results from different data sets, including successive wave crests, wave troughs, wave heights and wave periods. Both field data, laboratory data and data from numerical simulations are discussed. The results are compared with the theoretical models.

Finally, the main conclusions and some suggestions for further work are given in Chapter 7.

1.4 Major findings

When modeling the wave crest heights and wave trough depths, nonlinear effects should be included in the models to obtain reasonable accuracy. It is important to include the difference frequency effect in addition to the sum frequency effect, especially in finite water depths. A wave crest height and wave trough depth model based on the second order theory in Marthinsen and Winterstein (1992) for a narrow-banded random sea state includes both sum frequency and difference frequency effects. The effect of finite water depth is also included. The model agrees well with data.

The Nataf model, which transforms the distribution of the parameters of interest to a Gaussian distribution, is a powerful tool for modeling more than two successive waves. The main challenge is to select the initial distribution. Results show that the Weibull distribution gives the best agreement with data for the wave heights, while the generalized Gamma distribution gives the best agreement with data for the wave periods. The Nataf model can in theory be used when modeling more than three successive waves, but then the dependency structure should be further examined in order to validate that the correlation between the waves is correctly taken care of during the transformation.

Results show that the Nataf transformation, both of successive wave heights and successive wave periods, can be approximated by a first order autoregressive (AR(1)) model, which has the following properties. First, the time series has the Markov property, i.e., the distribution of the wave height or period is independent of the wave heights or periods prior to the previous wave height or period. Thus, only a two-dimensional distribution is needed to calculate the statistics. Second, the simulation of successive wave heights can be done directly by simulating a series of transformed wave heights and then find the wave heights by inverting the transformation. This is a simple and fast method for simulating wave heights if the time series of the complete surface elevation is not requested. The simulation of successive wave periods is more difficult, due to the difficulty of inverting the transformation when using the generalized Gamma distribution, which must be done numerically.

When considering successive wave periods conditioned on the corresponding wave heights exceeding a given level, e.g., the significant wave height or the rms-value of the wave height, the wave periods can be modeled by a multivariate Gaussian distribution. Thus, no transformation is necessary, and the model can in theory be used for modeling more than three successive wave periods for large waves.

The main contributions of this thesis are the transformation of existing wave crest height and wave trough depth models to two dimensions and the use of Nataf transformation to model individual wave heights and wave periods. It is shown that the process of successive wave heights and wave periods by use of Nataf transformation can be approximated by an AR(1) model. An extensive analysis of field data, laboratory data and data from numerical simulations has been made. Comparison between the data and the models is presented.

CHAPTER 2

Theory of stochastic processes and time series analysis, including analysis of the Draupner field data

This chapter gives a short introduction to important concepts regarding stochastic processes and time series analysis. Important aspects regarding density estimates, which are used in order to explore the properties of a given data set, are discussed. Definitions of important wave parameters are also given. Finally, the Draupner field data that will be used for comparison with theoretical models in Chapters 3 to 5 are described.

2.1 Wave parameters

The surface elevation in a random sea state can be described by several sea state parameters, e.g., the significant wave height, the mean wave period, the mean wave length and the mean wave steepness. These parameters can be calculated from a measured time series either directly from zero-crossing analysis or by spectral analysis. The latter is most frequently used.

The one-sided wave spectrum of a stochastic process is given by $S(\omega)$, where ω is the angular wave frequency. The n th spectral moment, m_n , is given by

$$m_n = \int_0^\infty \omega^n S(\omega) \, d\omega; \quad n = 0, 1, 2, \dots \quad (2.1)$$

In spectral analysis the wave parameters are related to the wave spectrum through the spectral moments, when assuming that the spectral moments are finite.

The mean zero-crossing wave period can be defined from the wave spectrum by either

$$T_{m01} = 2\pi \frac{m_0}{m_1}, \quad (2.2)$$

which is called the mean wave period, or

$$T_{m02} = 2\pi \sqrt{\frac{m_0}{m_2}}, \quad (2.3)$$

which is called the mean zero-crossing wave period. It can also be calculated from a zero-crossing analysis of the time series, and is then denoted as T_z .

The mean period between maxima, T_{m24} , is defined by

$$T_{m24} = 2\pi \sqrt{\frac{m_2}{m_4}}. \quad (2.4)$$

The significant wave height, H_S , is defined from the wave spectrum by

$$H_{m0} = 4\sqrt{m_0}. \quad (2.5)$$

When it is calculated from a zero-crossing analysis, it is given by the mean value of the 1/3 highest waves, $H_{1/3}$.

The average wave steepness, s , is defined as

$$s = \frac{H_{m0} k_p}{2\pi}, \quad (2.6)$$

where k_p is the wave number that corresponds to the peak period T_p .

2.2 Time series analysis and definition of stochastic processes

Newland (1993) and Wei (1990) give a good background for time series analysis. Fourier analysis and estimation of the spectrum are well described there. Newland also gives a short introduction in probability theory. A common assumption made in time series analysis, is that the time series is ergodic, and thereby stationary. Often the time series is also assumed to be narrow-banded. These concepts are defined in the following.

2.2.1 Estimated parameters from the time series

The free surface elevation at a fixed point can be considered as a stochastic process, $X(t)$, with expected value μ and variance σ^2 . Although the time variable, t , is continuous, the measurements are often discrete. Let $\mathbf{x} = (x_1, \dots, x_n)$ be a time series of discrete measurements of the free surface elevation at a fixed point. This is a realization of the stochastic process $X(t)$.

The two most important parameters measured from the time series is the mean value,

$$\mu = \bar{\mathbf{x}} = \frac{1}{n} \sum_{i=1}^n x_i, \quad (2.7)$$

and the variance

$$\sigma^2 = \frac{1}{n-1} \sum_{i=1}^n (x_i - \bar{\mathbf{x}})^2. \quad (2.8)$$

The variance of the free surface elevation is also equal to the zeroth spectral moment m_0 .

Two additional quantities of interest are the skewness

$$\rho_3 = \frac{\mu_3}{(\mu_2)^{3/2}}, \quad (2.9)$$

and the kurtosis

$$\rho_4 = \frac{\mu_4}{\mu_2^2}, \quad (2.10)$$

where μ_r is the r th central moment of the variable X , i.e.,

$$\mu_r = E[(X - E[X])^r]; \quad r = 1, 2, \dots \quad (2.11)$$

The skewness measures the lack of symmetry in the probability density function, while the kurtosis measures the peakedness or flatness. For a Gaussian distribution $\rho_3 = 0$ and $\rho_4 = 3$. Figure 2.1 illustrates the difference between a symmetric distribution and skewed distributions. Figure 2.1 (a) shows a standard Gaussian distribution that is symmetrical about zero. The distribution in (b) has a longer tail on the right and is said to be skewed to the right, while the distribution in (c) has a longer tail on the left and is said to be skewed to the left. The

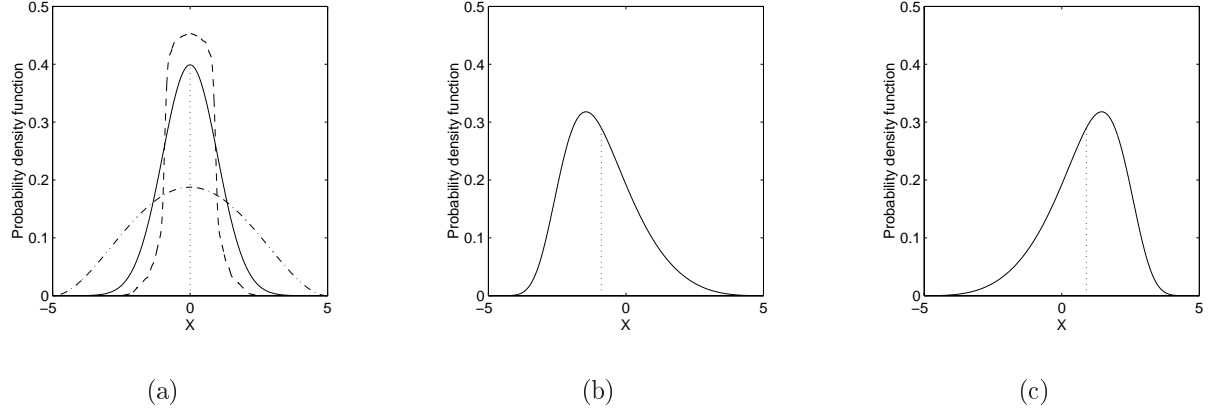


Figure 2.1: (a) Symmetric distributions ($\rho_3 = 0$), — standard Gaussian probability density function ($\rho_4 = 3$), -- more peaked about its mean ($\rho_4 > 3$), ··· less peaked about its mean ($\rho_4 < 3$). (b) Distribution skewed to the right ($\rho_3 > 0$). (c) Distribution skewed to the left ($\rho_3 < 0$). The dotted lines indicate the mean value.

skewness coefficient will be zero, positive or negative, depending on whether the distribution is symmetrical, skewed to the right or skewed to the left, respectively. Figure 2.1 (a) also illustrates the difference in the kurtosis of three distributions. One is more peaked about its mean than the Gaussian distribution ($\rho_4 > 3$), and one is less peaked about its mean than the Gaussian distribution ($\rho_4 < 3$).

2.2.2 Stationary stochastic process

A stochastic process is n th order stationary if the joint cumulative distribution function has the property

$$F_{X_1, \dots, X_n}(x_1, \dots, x_n) = F_{X_{1+j}, \dots, X_{n+j}}(x_{1+j}, \dots, x_{n+j}), \quad (2.12)$$

for any integer j . If Eq. (2.12) is true for any n , the process is strictly stationary. A stochastic process is weakly stationary if it is second order stationary, and if its first two moments exists and are finite.

A Gaussian stochastic process is uniquely described by its first two moments. This means that strictly and weakly stationarity are equivalent for a Gaussian process.

2.2.3 Ergodic stochastic process

A stochastic process is ergodic if the ensemble average, i.e., the mean value at a given time instant of several realizations of the process, is equal to the time average, i.e., the mean value in the entire time interval of one realization of the process. This also means that an ergodic

stochastic process must be stationary. If a stochastic process is ergodic, then only one infinitely long realization of the process is necessary to describe the process.

2.2.4 Narrow-banded stochastic process

A stochastic process is narrow-banded if most of the energy in the spectrum is concentrated around one frequency.

Two quantities that indicate if a stochastic process is narrow-banded are the spectral bandwidth parameters ϵ_2 and ϵ_4 given by (assuming that the spectral moments exist and are finite)

$$\epsilon_2 = \sqrt{\frac{m_0 m_2}{m_1^2} - 1} \quad (2.13)$$

$$\epsilon_4 = \sqrt{1 - \frac{m_2^2}{m_0 m_4}}. \quad (2.14)$$

The bandwidth parameters are $0 \leq \epsilon_2, \epsilon_4 \leq 1$, and the closer ϵ_2 and ϵ_4 are to 0, the more narrow-banded the process is, and the closer ϵ_2 and ϵ_4 are to 1, the more broad-banded the process is. A realistic sea state will never be completely narrow-banded.

The spectral parameters m_2 and m_4 depend on the behavior of the spectrum at high frequencies. Thus, the spectral bandwidth parameters will vary according to the cut-off frequency choice when calculating the spectral parameters (see Rye (1977) and Rye and Svec (1976)). Due to this instability, the use of especially the bandwidth parameter ϵ_4 in the distributions should be avoided. The effect on different wave statistics for varying bandwidth parameter ϵ_4 is also discussed in Goda (1970).

2.3 Kernel density estimator

Density estimates are used in order to investigate the properties of a given data set. Several methods are available to obtain the density estimates. The oldest and most widely used density estimator is the histogram. This simple method gives valuable information about the data set. However, the choice of the number of bins and the origin of the bins have strong influence of the resulting histograms and can be crucial in some cases. Also the discontinuity of the histograms can cause difficulty, e.g., if derivatives of the estimates are required. A more thorough discussion of density estimators is found in Silverman (1986).

A more robust density estimator is the kernel density estimator, which is defined by

$$\hat{f}_X(x) = \frac{1}{n h_s} \sum_{j=1}^n K_d \left(\frac{x - y_j}{h_s} \right), \quad (2.15)$$

where n is the number of data points, $y_1 \dots y_n$ is the data set, and h_s is the smoothing parameter or window width. The kernel function K_d satisfies the condition

$$\int_{-\infty}^{\infty} K_d(x) dx = 1. \quad (2.16)$$

Usually K_d will be a symmetric probability density function, e.g., the Gaussian density. To illustrate the method, consider the kernel estimator as a sum of 'bumps' placed at the observations. The shape of the bumps are given by the kernel function while the width is given by

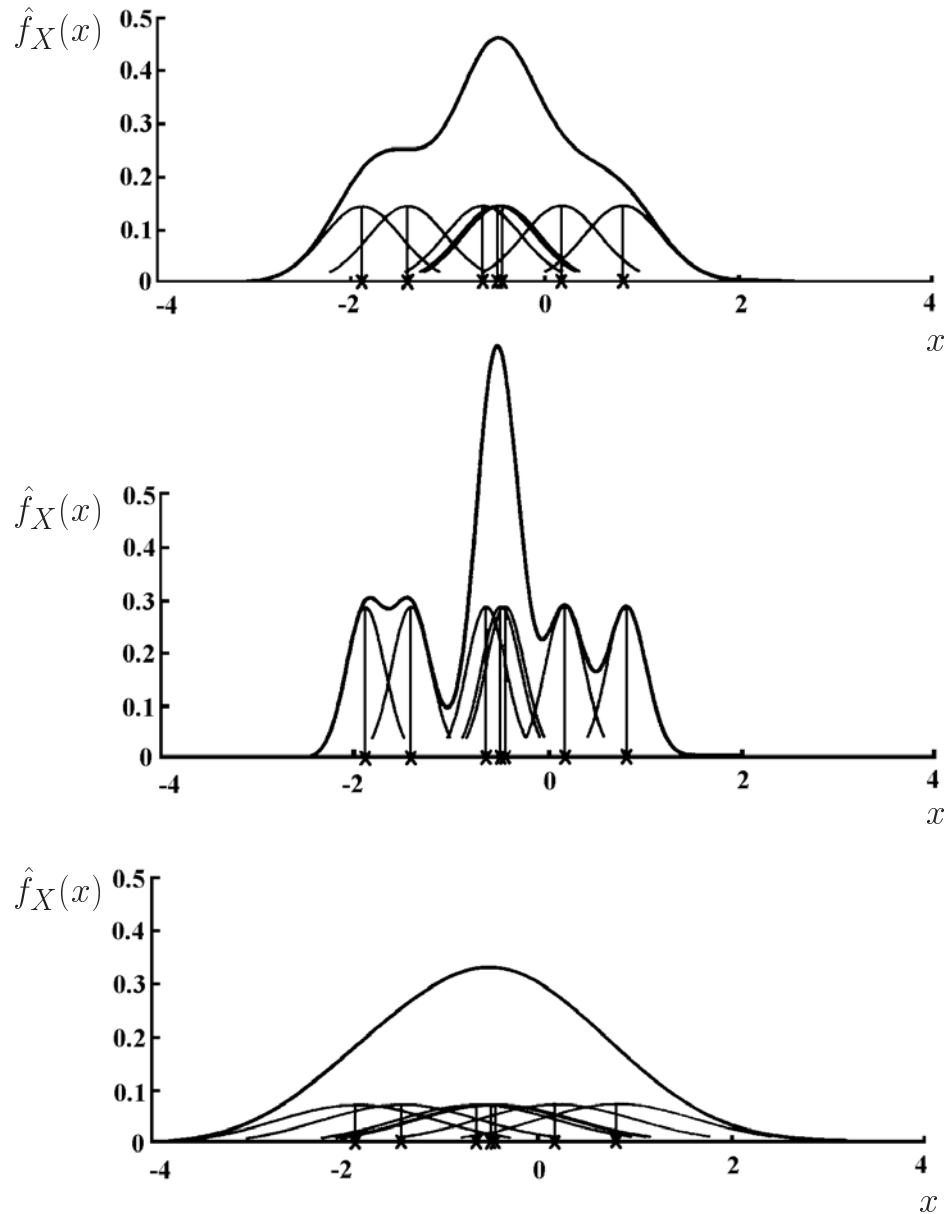


Figure 2.2: Kernel density estimate showing individual kernels and varying smoothing parameter. Top: $h_s = 0.4$; Middle: $h_s = 0.2$; Bottom: $h_s = 0.8$. (From Silverman, 1986).

the smoothing parameter. Figure 2.2 illustrates the principle of a kernel density estimate. The crosses mark the observations, and both the individual kernels and the resulting kernel density estimate are indicated. One should note that the small sample space are only used for the sake of clarity. The different figures show the effect of varying smoothing parameters. If h_s is too small, then each observation will be marked with a spike, and if h_s is too large, then all the details are obscured. The smoothing parameter can be selected by trying out several values and then selecting it 'by eye'. However, various methods are available, and are well discussed in Silverman (1986). The purpose of the density estimate will also influence the choice of the smoothing parameter.

Several kernel functions are available. The kernel function used in this thesis is the Epanechnikov kernel (Epanechnikov, 1969) given by

$$K_d(x) = \begin{cases} \frac{3}{4\sqrt{5}} (1 - \frac{1}{5}x^2) & -\sqrt{5} \leq x \leq \sqrt{5} \\ 0 & \text{otherwise.} \end{cases} \quad (2.17)$$

There are several measures of the discrepancy of the kernel density estimator from the true density. One possible measure that is often used is to minimize the approximate mean integrated square error, i.e., to minimize the approximate expression of

$$\mathbb{E} \left[\int \left\{ \hat{f}(x) - f(x) \right\}^2 dx \right]. \quad (2.18)$$

This is obtained by using the Epanechnikov kernel.

2.3.1 The kernel method in p dimensions

The multivariate kernel density estimator is defined by

$$\hat{f}_{\mathbf{x}}(\mathbf{x}) = \frac{1}{nh_s^p} \sum_{i=1}^n K_d \left(\frac{\mathbf{x} - \mathbf{y}_i}{h_s} \right), \quad (2.19)$$

where n is the number of data points, and $\mathbf{y}_1 \dots \mathbf{y}_n$ is a multivariate data set in p dimensions. The kernel function K_d defined for a p -dimensional \mathbf{x} satisfies

$$\int_{\mathbb{R}^p} K_d(\mathbf{x}) d\mathbf{x} = 1. \quad (2.20)$$

The multivariate Epanechnikov kernel is given by

$$K_d(\mathbf{x}) = \begin{cases} \frac{1}{2c_p} (p+2) (1 - \mathbf{x}^T \mathbf{x}) & \mathbf{x}^T \mathbf{x} < 1 \\ 0 & \text{otherwise,} \end{cases} \quad (2.21)$$

where c_p is the volume of the unit p -dimensional sphere, i.e., $c_1 = 2$, $c_2 = \pi$, etc.

2.4 Description of Draupner field data

In order to validate theoretical models, comparison with field data is important. The theoretical models that are discussed in Chapters 3 to 5 will be compared with data from the Draupner field. Results from other data sets, both field data, laboratory data and data from numerical simulations will be presented in Chapter 6. A description of the Draupner field data is given below.

Time series were measured at the Draupner platform in the Central North Sea in the period from 31st of December 1994 to 20th of January 1995. Figure 2.3 shows the location of the platform. In the same time period wind measurements were taken at the Sleipner field, which is located approximately 70 km Northwest of the Draupner platform. It is assumed that the wind conditions at the two locations are similar. The measured wind directions show that half of the data represent wind from the North, and the other half represent wind from the South. No information regarding the directional spreading of the waves is available for the data. Sunde (1995) gives a description of the meteorological conditions for January 1, 1995. A discussion of the data can also be found in Brodtkorb et al. (2000).

The data are measured by a down-looking laser sensor mounted on the Draupner jacket platform, and the waves are not expected to be seriously influenced by the structure of the platform. However, the finite water depth of 70 m does affect some waves, but overall the effect is considered to be insignificant. Thus the data can be considered to be taken as representing deep water waves. Measurements are done during 20 minutes in 3 hours intervals, with a sampling frequency of 2.1333 Hz.

Analysis of each of the 48 individual time series are made, and the descriptive statistics are

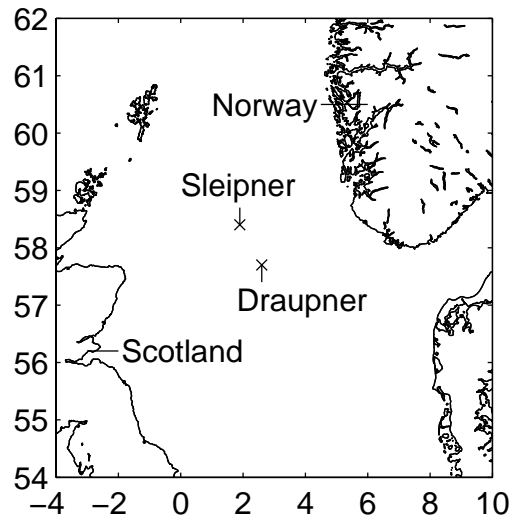


Figure 2.3: Map of the Central North Sea with the Draupner platform at 57.7°N , 2.6°E , and the Sleipner platform at 58.4°N , 1.9°E .

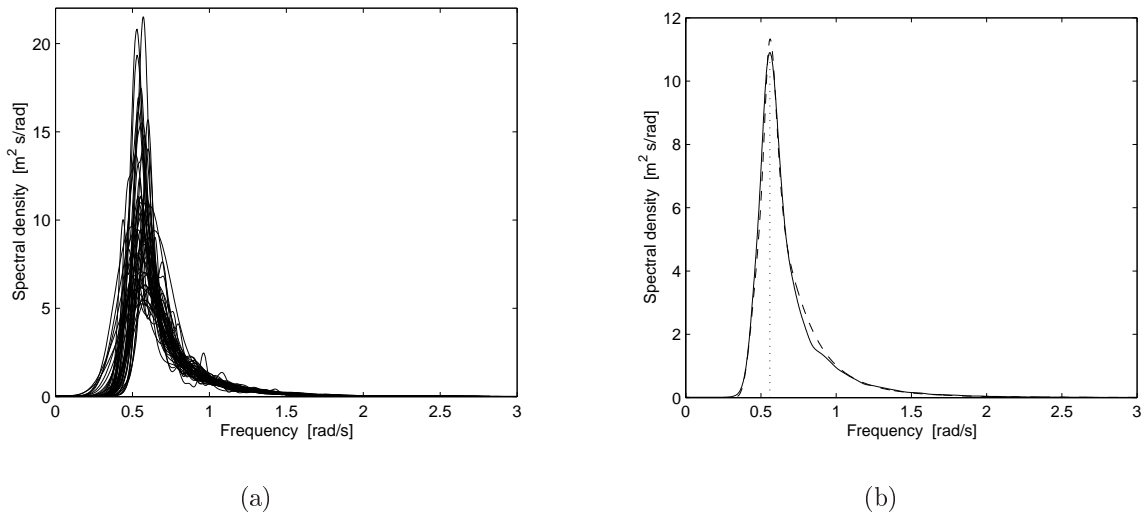


Figure 2.4: (a) Spectral densities of the 48 individual time series. (b) The spectral density of field data (solid); JONSWAP spectrum with $\gamma_J = 1.9$ (broken); Peak frequency of field data $\omega_p = 0.56$ rad/s (dotted).

Table 2.1: Descriptive statistics of the Draupner field data, from the individual records of 20 minutes.

		Mean	Min/Max	St.dev
H_{m0}	[m]	6.73	6.01/7.99	0.61
T_{m02}	[s]	8.29	7.82/9.05	0.32
T_{m01}	[s]	9.05	8.46/10.02	0.38
T_{m24}	[s]	4.35	3.11/4.88	0.34
T_p	[s]	11.27	9.80/13.24	0.75
\bar{k}	[rad/m]	0.0589	0.0492/0.0659	0.0044
\bar{k}_1	[rad/m]	0.0495	0.0404/0.0563	0.0041
a_{rms}	[m]	2.38	2.13/2.82	0.22
σ	[m]	1.68	1.50/2.00	0.15
ρ_3	[-]	0.147	0.021/0.302	0.062
ρ_4	[-]	2.96	2.55/3.69	0.22
ϵ_2	[-]	0.436	0.373/0.504	0.029
ϵ_4	[-]	0.850	0.816/0.931	0.023
s	[-]	0.035	0.024/0.048	0.005

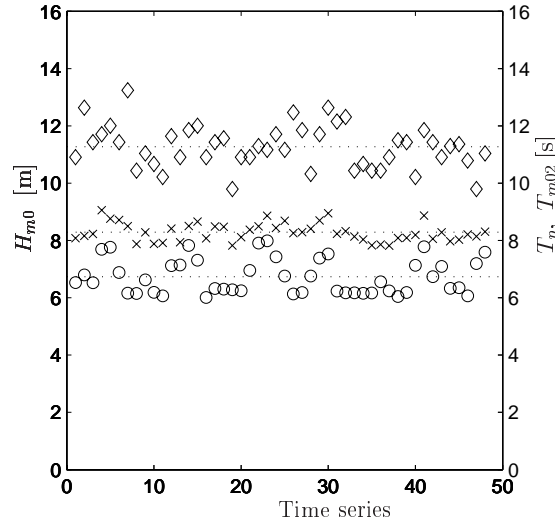


Figure 2.5: The parameters H_{m0} , T_p and T_{m02} for the individual time series. \circ H_{m0} ; \diamond T_p ; \times T_{m02} . The dotted lines indicate the mean values.

given in Table 2.1. The parameters \bar{k} , \bar{k}_1 and a_{rms} are the mean wave number corresponding to T_{m02} , the mean wave number corresponding to T_{m01} , and the rms (root-mean-square) value of the linear amplitude, respectively. These terms will be properly defined in Chapter 3.

The spectral densities are plotted in Fig. 2.4 (a) and show that all spectra have single peaks. Together with the descriptive statistics, it suggests that the data can be grouped into one single time series. With an increased record length, the fitted distribution will be more reliable, given that the sea state is more or less stationary during the entire time series. Figure 2.5 shows the parameters H_{m0} , T_p and T_{m02} for the individual time series. The parameter locations around the mean values show no significant increasing or decreasing trend. Together with the spectral densities in Fig. 2.4 (a) this indicates that the sea state is approximately stationary when considering all 48 time series as one time series.

The total record length is 15 hours and 53 minutes, including about 6300 individual zero-crossing waves. In the zero-crossing analysis, waves of amplitude less than 1/10 of the standard deviation above or below the zero line were neglected. Figure 2.4 (b) shows the spectral density for this time series, where the dotted line indicates the peak frequency. The spectrum for the field data corresponds to a JONSWAP spectrum with peakedness parameter $\gamma_J \approx 1.9$, and the JONSWAP spectrum is shown in the same figure, with a broken line. The descriptive statistics of the total time series are given in Table 2.2, and the values are very close to the mean values given in Table 2.1. Note that the skewness is positive and that the kurtosis is close to 3. Since the surface elevation is not completely Gaussian, nonlinear effects are expected. Figure 2.6 shows the histogram of the surface elevation compared to a Gaussian distribution with zero mean and variance equal to $(1.69 \text{ m})^2$.

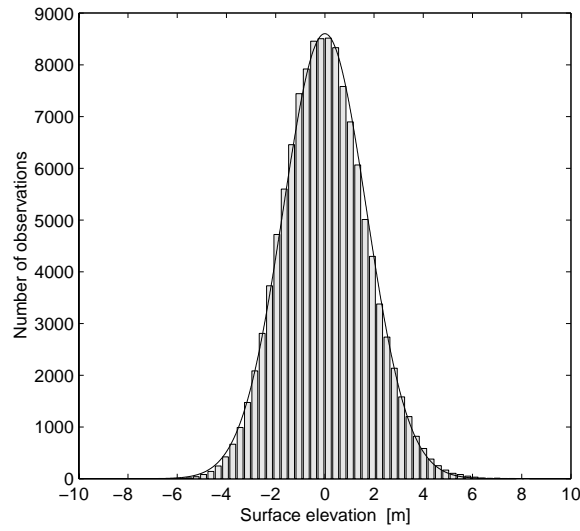


Figure 2.6: Histogram of the surface elevation. The line indicates a Gaussian distribution with zero mean and variance equal to $(1.69 \text{ m})^2$.

Table 2.2: Descriptive statistics of the Draupner field data, from the total time series.

H_{m0}	[m]	6.76
T_{m02}	[s]	8.37
T_{m01}	[s]	9.09
T_{m24}	[s]	4.44
T_p	[s]	11.23
\bar{k}	[rad/m]	0.0576
\bar{k}_1	[rad/m]	0.0488
a_{rms}	[m]	2.39
σ	[m]	1.69
ρ_3	[-]	0.151
ρ_4	[-]	3.05
ϵ_2	[-]	0.425
ϵ_4	[-]	0.847
s	[-]	0.035

CHAPTER 3

Joint distributions of successive wave crest heights and successive wave trough depths

3.1 Linear theory

A random sea with small wave amplitudes and a narrow-banded wave spectrum follows the Gaussian distribution. The surface elevation can be represented either by an infinite sum of sine-waves with variable amplitude and random phase or with a single sinusoidal wave with slowly varying amplitude and phase and with frequency equal to the mean wave frequency of the sea, see Rice (1945) and Longuet-Higgins (1952). The latter formulation gives the following expression for the surface elevation

$$\eta = \eta_a(t) \cos(\bar{\omega}t - \bar{k}x + \xi(t)), \quad (3.1)$$

where $\eta_a(t)$ is the slowly varying linear amplitude and $\xi(t)$ is the slowly varying phase. Furthermore, $\bar{\omega}$ is the mean wave frequency, and \bar{k} is the mean wave number given by the dispersion relationship for linear waves

$$\bar{\omega}^2 = g\bar{k} \tanh \bar{k}d, \quad (3.2)$$

where g is the acceleration of gravity, and d is the water depth. With these assumptions, the amplitude is distributed according to the Rayleigh distribution (Rayleigh (1880), Longuet-Higgins (1952)), i.e., the probability density function of the dimensionless linear amplitude A is given by

$$f_A(a) = 2a \exp \{-a^2\}; \quad a = \frac{\eta_a}{a_{\text{rms}}} \geq 0, \quad (3.3)$$

where $a_{\text{rms}} = (2m_0)^{(1/2)}$ is the rms (root-mean-square) value of η_a . A realistic sea state will not be completely narrow-banded. In this case \bar{k} will be taken as the mean wave number corresponding to T_{m02} .

There are numbers of possible forms of a two-dimensional distribution for the successive dimensionless linear wave amplitudes A_1 and A_2 , whose marginal distribution is Rayleigh. The most commonly used is (Longuet-Higgins, 1986)

$$f_{A_1, A_2}(a_1, a_2) = \frac{4a_1 a_2}{1 - \kappa_a^2} \exp \left\{ -\frac{a_1^2 + a_2^2}{1 - \kappa_a^2} \right\} I_0 \left[\frac{2\kappa_a a_1 a_2}{1 - \kappa_a^2} \right]; \quad a_1 = \frac{\eta_{a,1}}{a_{\text{rms}}}, \quad a_2 = \frac{\eta_{a,2}}{a_{\text{rms}}}, \quad (3.4)$$

where I_0 denotes the modified Bessel function of zeroth order given by

$$I_0(z) = \frac{1}{\pi} \int_0^\pi e^{z \cos \theta} d\theta. \quad (3.5)$$

Equation 3.4 has been referred to as the two-dimensional Rayleigh distribution, see Kimura (1980). Furthermore, the parameter κ_a is related to the correlation coefficient, ρ_a , between A_1 and A_2 by

$$\rho_a \equiv \rho_{A_1, A_2} = \frac{E(\kappa_a) - \frac{1}{2}(1 - \kappa_a^2)K(\kappa_a) - \frac{\pi}{4}}{1 - \frac{\pi}{4}}, \quad (3.6)$$

where $K(\kappa_a)$ and $E(\kappa_a)$ are complete elliptic integrals of the first and second kinds, respectively. Properties of the two-dimensional Rayleigh distribution and calculation of the correlation coefficient are given in Appendix A.

3.2 Second order Stokes theory

Linear theory is applicable in many situations. However, in severe sea states, which are of interest for design purposes, the Rayleigh distribution underestimates the crest heights, and higher order effects must be taken into account.

A description of the extension of linear theory to second order Stokes (1847) theory by using a perturbation approach based on the small quantity $\bar{k}\eta_a$ is given in e.g. Dean and Dalrymple (1984). A short summary of this technique is given here, and a more thorough description is given in Appendix B.

The governing equation for the velocity potential ϕ is the Laplace equation

$$\nabla^2 \phi = 0. \quad (3.7)$$

One should note that here the notation of Dean and Dalrymple is used, i.e., the velocity is given by $\mathbf{v} = -\nabla\phi$. The expansion parameter is $\bar{k}\eta_a \ll 1$. All quantities in the governing differential equation and boundary conditions are then decomposed into a power series in $\bar{k}\eta_a$. The resulting

first order solution is the linear theory

$$\phi_1 = -\frac{\eta_a g}{\bar{\omega}} \frac{\cosh \bar{k}(d+z)}{\cosh \bar{k}d} \sin(\bar{\omega}t - \bar{k}x) \quad (3.8)$$

$$\eta_1 = \eta_a \cos(\bar{\omega}t - \bar{k}x) \quad (3.9)$$

$$\bar{\omega}^2 = g\bar{k} \tanh \bar{k}d. \quad (3.10)$$

The second order perturbation solution is

$$\phi_2 = -\frac{3}{8} \frac{\eta_a \bar{\omega}}{\bar{k}} \frac{\cosh 2\bar{k}(d+z)}{\sinh^4 \bar{k}d} \sin 2(\bar{\omega}t - \bar{k}x) \quad (3.11)$$

$$\eta_2 = C_{B2} - \frac{\eta_a}{2 \sinh 2\bar{k}d} + \frac{\eta_a \cosh \bar{k}d(2 + \cosh 2\bar{k}d)}{2 \sinh^3 \bar{k}d} \cos 2(\bar{\omega}t - \bar{k}x), \quad (3.12)$$

where C_{B2} is the Bernoulli constant. The dispersion relationship remains the same as for first order, i.e., given by Eq. (3.10).

There are two options to specify the Bernoulli constant. First, C_{B2} can be put equal to zero, and the surface elevation can be separated in two parts

$$\eta_2 = \bar{\eta} + \hat{\eta}_2, \quad (3.13)$$

where $\bar{\eta}$ is the mean value of the surface elevation, and $\hat{\eta}_2$ is the fluctuating part, which is zero when taking the time average. The mean value $\bar{\eta}$ corresponds to the set-down effect and is zero in deep water. The resulting expressions for $\bar{\eta}$ and $\hat{\eta}_2$ are

$$\bar{\eta} = -\frac{\eta_a}{2 \sinh 2\bar{k}d} \quad (3.14)$$

$$\hat{\eta}_2 = \frac{1}{2} \eta_a \frac{\cosh \bar{k}d(2 + \cosh 2\bar{k}d)}{\sinh^3 \bar{k}d} \cos 2(\bar{\omega}t - \bar{k}x). \quad (3.15)$$

Second, d can be specified as the mean water level depth, giving the Bernoulli constant

$$C_{B2} = \frac{\eta_a}{2 \sinh 2\bar{k}d}. \quad (3.16)$$

Then the mean surface elevation is zero, while $\hat{\eta}_2$ is the same as before.

The difference between the two options for C_{B2} is illustrated in Figs. 3.1 and 3.2.

In the following the second approach is used. Then the velocity potential to second order is

$$\begin{aligned} \phi &= \phi_1 + \bar{k}\eta_a\phi_2 \\ &= -\frac{\eta_a g}{\bar{\omega}} \frac{\cosh \bar{k}(d+z)}{\cosh \bar{k}d} \sin(\bar{\omega}t - \bar{k}x) - \frac{3}{8} \eta_a^2 \bar{\omega} \frac{\cosh 2\bar{k}(d+z)}{\sinh^4 \bar{k}d} \sin 2(\bar{\omega}t - \bar{k}x), \end{aligned} \quad (3.17)$$

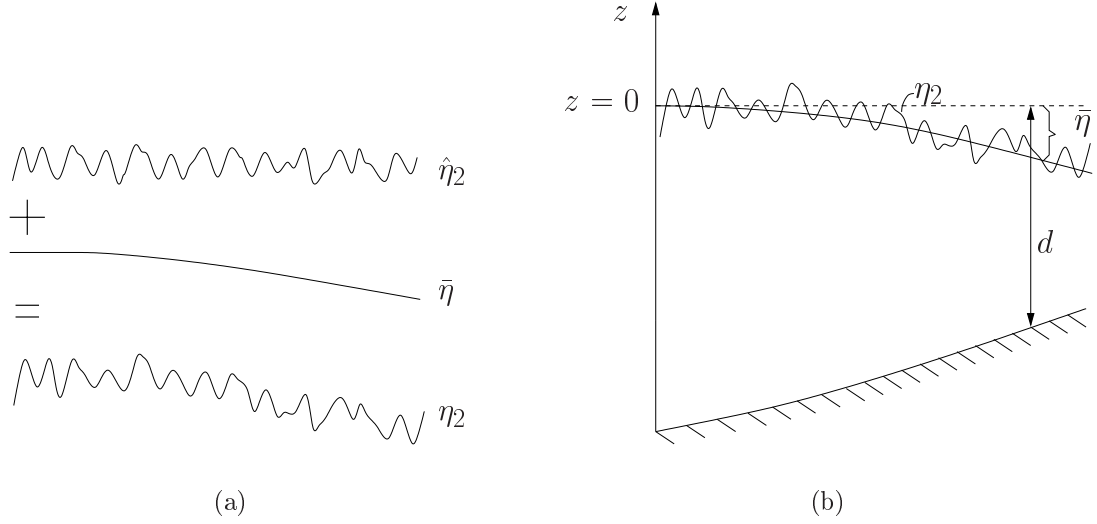


Figure 3.1: The Bernoulli constant C_{B2} is equal to zero, which means that $\bar{\eta}_2 = \bar{\eta}$. (a) The different components of the second order component of the surface elevation. (b) The relationship between the second order component of the surface elevation, mean water level and the sea bottom.

and the surface elevation is

$$\begin{aligned} \eta &= \eta_1 + \bar{k}\eta_a\eta_2 \\ &= \eta_a \cos(\bar{\omega}t - \bar{k}x) + \frac{1}{2}\bar{k}\eta_a^2 \frac{\cosh \bar{k}d(2 + \cosh 2\bar{k}d)}{2 \sinh^3 \bar{k}d} \cos 2(\bar{\omega}t - \bar{k}x). \end{aligned} \quad (3.18)$$

One should note that the second order Stokes theory only includes sum frequency effects, as opposed to full second order wave theory that will be discussed in Chapter 3.5. The difference

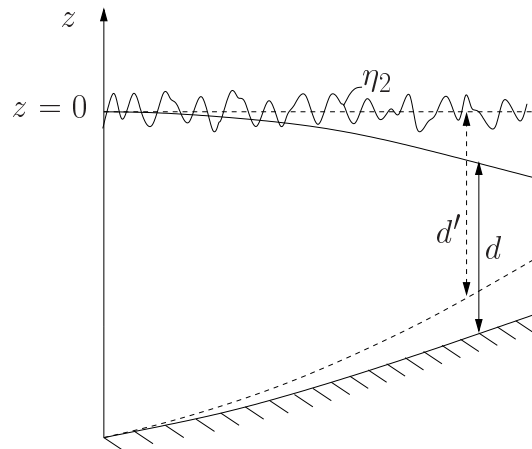


Figure 3.2: The Bernoulli constant C_{B2} is defined as in Eq. (3.16), which means that $\bar{\eta}_2 = 0$. Note that $d = d'$.

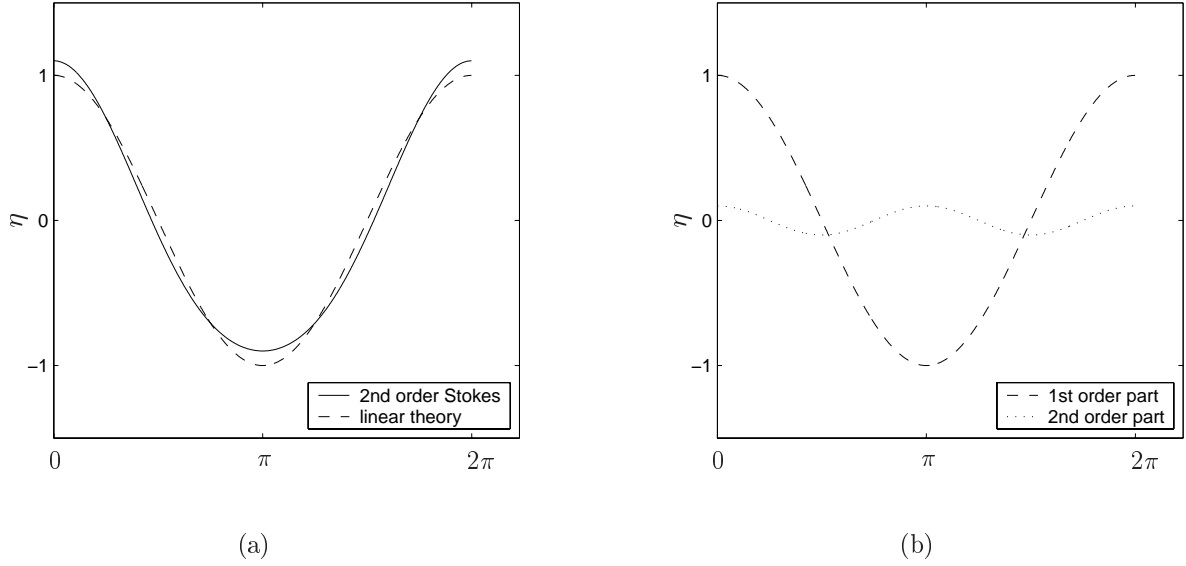


Figure 3.3: (a) Wave surface profile; — second order Stokes wave, -- linear wave. (b) First order (--) and second order (···) component of the second order Stokes wave.

between a second order Stokes wave profile and linear theory wave profile is shown in Fig. 3.3. The second order Stokes wave has higher crests and shallower troughs than the linear wave profile. However, the total wave height is the same, and it is equal to $2\eta_a$. The crest period, i.e., the period between a zero-upcrossing and a zero-downcrossing, is shorter for the second order Stokes wave than for the linear wave, while the trough period, i.e., the period between a zero-downcrossing and a zero-upcrossing, is longer.

3.2.1 Limitations of the second order Stokes theory

The second order Stokes theory is valid if two criteria are fulfilled. First, the convergence criterion on the power series ϕ , which means that the ratio of the second order term to the first order term must be much smaller than one, leads to

$$R_\phi = \frac{\bar{k}\eta_a\phi_2}{\phi_1} = \frac{3}{8} \frac{\bar{k}\eta_a \cosh 2\bar{k}d}{\cosh \bar{k}d \sinh^3 \bar{k}d} \ll 1. \quad (3.19)$$

Second, the physical properties of the wave profile require that there is no bump in the trough. This is indicated by a negative second derivative of the wave trough, which leads to the criterion

$$\bar{k}\eta_a < \frac{\sinh^3 \bar{k}d}{\cosh \bar{k}d (2 + \cosh 2\bar{k}d)}. \quad (3.20)$$

In addition to the second order Stokes criteria, the breaking criterion for the wave steepness must be fulfilled.

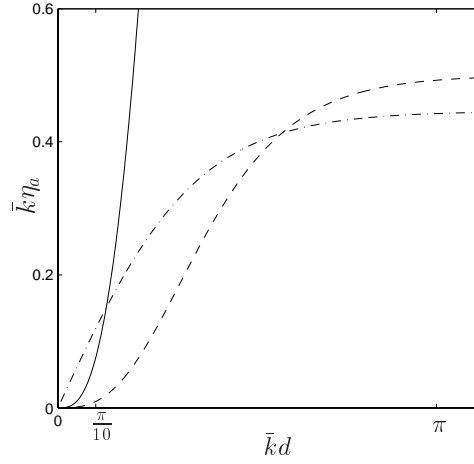


Figure 3.4: Different criteria for $\bar{k}\eta_a$ as a function of $\bar{k}d$; — convergence criterion, -- criterion for no bump in the trough, - · - wave steepness criterion.

In deep water, defined as $\bar{k}d > \pi$, the convergence criterion reduces to

$$R_\phi = 3e^{-2\bar{k}d}\bar{k}\eta_a, \quad (3.21)$$

while the criterion for no bump in the trough reduces to

$$\bar{k}\eta_a < \frac{1}{2}. \quad (3.22)$$

However, the breaking criterion for the wave steepness in deep water is

$$\bar{k}\eta_a < \frac{\pi}{7}, \quad (3.23)$$

which will be the most restrictive criterion. In this case $R_\phi \approx 0.0025$, and the convergence criterion is satisfied. So the criteria for Stokes waves in deep water are always satisfied.

In shallow water, defined as $\bar{k}d < \pi/10$, the convergence criterion reduces to

$$R_\phi = \frac{3}{8} \frac{\bar{k}\eta_a}{(\bar{k}d)^3}, \quad (3.24)$$

while the criterion for no bump in the trough reduces to

$$\bar{k}\eta_a < \frac{(\bar{k}d)^3}{3}. \quad (3.25)$$

The latter is the most restrictive. In terms of the Ursell number, \bar{U}_r , this criterion can be written as

$$\bar{U}_r = \frac{8\pi^2 \bar{k}\eta_a}{(\bar{k}d)^3} < \frac{8\pi^2}{3}. \quad (3.26)$$

The breaking criterion in arbitrary water depth is given by the Miche criterion (see e.g. Soulsby (1997))

$$\bar{k}\eta_a < \pi \cdot 0.142 \tanh \left(5.5 \frac{\bar{k}d}{2\pi} \right), \quad (3.27)$$

and is satisfied when the criterion for no bump in the trough is satisfied. Figure 3.4 illustrates the different criteria of $\bar{k}\eta_a$ as a function of $\bar{k}d$. One should note that $\bar{k}\eta_a$ must be much smaller than the values indicated for the convergence criterion. However, this is only a problem when $\bar{k}d \rightarrow 0$. Also, one should note that these restrictions on $\bar{k}\eta_a$ apply for all wave amplitudes, i.e., the criteria must be fulfilled for the maximum wave amplitude. If it is of interest to know the restrictions on a_{rms} , the values must be divided by $\sqrt{\ln N}$, where N is the number of zero-crossing waves in the current sea state.

3.3 Probability distributions using second order Stokes-type nonlinearity

3.3.1 Marginal distribution of wave crest heights and wave trough depths

Tayfun (1980), Tung and Huang (1985) and Kriebel and Dawson (1991) examined the effect of second order Stokes-type nonlinearity on the wave crest statistics in deep water. Kriebel and Dawson (1993) extended their (1991) model to finite water depth. The idea of using second order Stokes-type nonlinearity is adopted here, and is combined with a transformation of the two-dimensional Rayleigh distribution to obtain the joint distribution for successive wave crest heights. One should note that this approach includes the sum frequency effects only. A second order model that includes both sum frequency and difference frequency effects is described in Chapter 3.6. Although the wave crest height is the quantity of primary interest for engineering purposes, the results for the wave trough depth are included to illustrate the nonlinearity of the waves. This model is also described in Wist et al. (2002a), where the theoretical model is compared with data from the Draupner field, and in Wist et al. (2002b), where the theoretical model is compared with laboratory data.

The free surface elevation is considered at a fixed point in a stationary narrow-banded random sea state consistent with second order Stokes waves in finite water depth, i.e.,

$$\eta(t) = \eta_a(t) \cos[\bar{\omega}t + \xi(t)] + \frac{1}{2} \bar{k}\eta_a^2(t) f^+(\bar{k}d) \cos 2[\bar{\omega}t + \xi(t)], \quad (3.28)$$

where

$$f^+(\bar{k}d) = \frac{\cosh \bar{k}d (2 + \cosh 2\bar{k}d)}{2 \sinh^3 \bar{k}d} \quad (3.29)$$

contains the effect of finite water depth. The dispersion relationship is given by

$$\bar{\omega}^2 = g\bar{k} \tanh \bar{k}d. \quad (3.30)$$

For deep water waves $f^+(\bar{k}d) = 1$, and the dispersion relationship reduces to $\bar{\omega}^2 = g\bar{k}$.

At the wave crest ($\bar{\omega}t + \xi(t) = 0$) the nonlinear crest height, η_c , is determined from Eq. (3.28) in terms of the linear amplitude as

$$\eta_c = \eta_a + \frac{1}{2}\bar{k}\eta_a^2 f^+(\bar{k}d). \quad (3.31)$$

By introducing the characteristic steepness of the random waves, r_+ , defined by

$$r_+ = \bar{k}a_{\text{rms}} f^+(\bar{k}d), \quad (3.32)$$

the nonlinear non-dimensional crest height, $w_c = \eta_c/a_{\text{rms}}$, can be expressed in terms of the dimensionless linear amplitude as

$$w_c = a + \frac{1}{2}r_+ a^2. \quad (3.33)$$

This is an ordinary quadratic equation, and the solution of a can be found as

$$a = \frac{-1 \pm \sqrt{1 + 2r_+ w_c}}{r_+}. \quad (3.34)$$

The physical meaning of a , that is, the amplitude is always positive, means that only the positive square-root is a solution. While Tayfun (1980) and Tung and Huang (1985) used the exact solution in Eq. (3.34), Kriebel and Dawson (1993) used a series expansion of the positive square-root to second order, i.e.,

$$a \approx w_c - \frac{1}{2}r_+ w_c^2. \quad (3.35)$$

The probability density function of W_c is found from transformation of variables. The transformation of variables in one dimension, when the transformation is one-to-one, is given by

$$f_{W_c}(w_c) = f_A(a(w_c)) \left| \frac{da}{dw_c} \right|, \quad (3.36)$$

which gives

$$f_{W_c}(w_c) = \frac{2(\sqrt{1 + 2r_+ w_c} - 1)}{r_+ \sqrt{1 + 2r_+ w_c}} \exp \left\{ -\frac{(\sqrt{1 + 2r_+ w_c} - 1)^2}{r_+^2} \right\}; \quad w_c \geq 0. \quad (3.37)$$

The probability of exceedance is then given by

$$P(W_c > w_c) = 1 - F_{W_c}(w_c) = \exp \left\{ -\frac{(\sqrt{1 + 2r_+ w_c} - 1)^2}{r_+^2} \right\}. \quad (3.38)$$

Equation (3.37) reduces to the Rayleigh distribution in Eq. (3.3) for small wave steepness, i.e., $r_+ \approx 0$. In deep water $r_+ = \bar{k}a_{\text{rms}} = (\bar{\omega}^2/g)a_{\text{rms}}$. A series expansion of Eq. (3.37) to second order gives the approximate probability density function

$$f_{W_c}(w_c) \approx 2w_c \left(1 - \frac{3}{2}r_+ w_c + \frac{1}{2}r_+^2 w_c^2 \right) \exp \left\{ -w_c^2 \left(1 - \frac{1}{2}r_+ w_c \right)^2 \right\}, \quad (3.39)$$

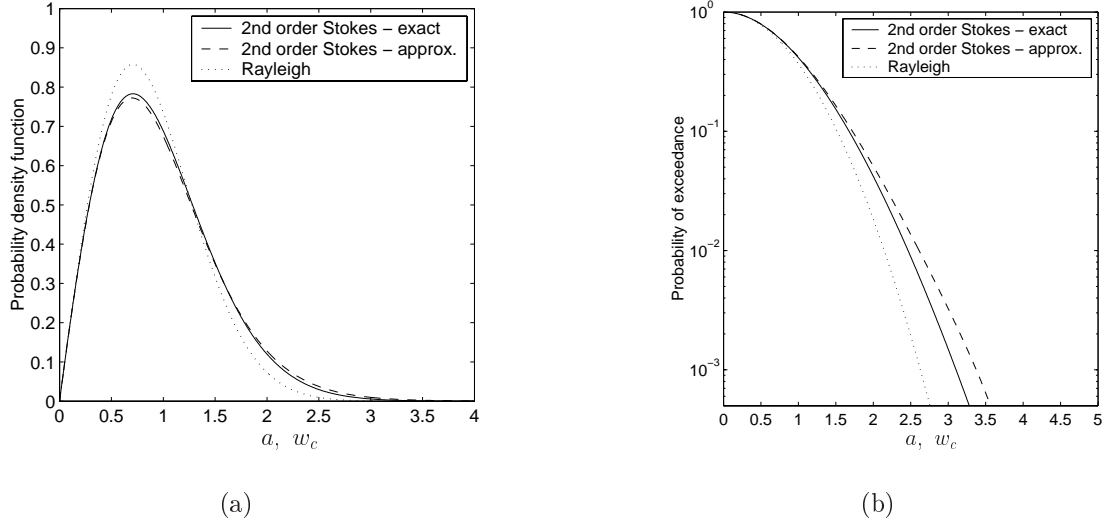


Figure 3.5: The difference between using the exact solution of a and the approximate solution in the transformation of the wave crest height. (a) Probability density function. (b) Probability of exceedance. ($r_+ = 0.138$, from Draupner data)

which is the same probability density function as in Kriebel and Dawson (1993). One should note that the approximative probability density function becomes negative for $w_c > \frac{1}{r_+}$. However, this will not cause any problems in practice, because the properties of the second order Stokes waves lead to the criterion $a < \frac{1}{2r_+}$, see Appendix C.1 for further details. This means that $w_c < \frac{5}{8r_+} < \frac{1}{r_+}$. A discussion of the approximative model is also given in Wist et al. (2001), where comparison with field measurements from the Draupner field is made.

Figure 3.5 shows the difference between using the exact solution of a , Eq. (3.34), and the approximate solution, Eq. (3.35), in the transformation, with the parameter r_+ calculated from the Draupner field data (see Table 3.1, page 33). The Rayleigh distribution is included for comparison. Even though the difference between the exact and approximative solution is seemingly small in the probability density function (a), it is clearly shown for high values of w_c in the probability of exceedance (b).

Similarly, at the wave trough ($\bar{\omega}t + \xi(t) = \pi$) the nonlinear trough depth, η_t , is determined from Eq. (3.28) in terms of the linear amplitude as

$$\eta_t = \eta_a - \frac{1}{2} \bar{k} \eta_a^2 f^+(\bar{k}d). \quad (3.40)$$

The nonlinear non-dimensional trough depth, $w_t = \eta_t/a_{\text{rms}}$, is given as

$$w_t = a - \frac{1}{2} r_+ a^2, \quad (3.41)$$

and the solution for a is

$$a = \frac{1 \pm \sqrt{1 - 2r_+ w_t}}{r_+}. \quad (3.42)$$

Considering the properties of the second order Stokes waves discussed in Chapter 3.2.1, the following restrictions are obtained for a . In deep water the wave steepness criteria in Eq. (3.23) is the most restrictive. This means that $\bar{k}\eta_a < \frac{\pi}{7}$ and $a < \frac{\pi}{7r_+} < \frac{1}{2r_+}$, see Appendix C.1 for further details. In shallow water the criterion for no bump in the trough in Eq. (3.25) is the most restrictive, i.e., $\bar{k}\eta_a < \frac{(\bar{k}d)^3}{3}$, which leads to $a < \frac{1}{2r_+}$. The result is that $a < \frac{1}{r_+}$, and thus only the negative square-root is a solution in Eq. (3.42), and the transformation is one-to-one. It is also easy to see that if the positive square-root is used, then a decreases when w_t increases, which is physically not correct. By transformation of variables the probability density function of W_t is given as

$$f_{W_t}(w_t) = \frac{2(1 - \sqrt{1 - 2r_+w_t})}{r_+\sqrt{1 - 2r_+w_t}} \exp \left\{ -\frac{(1 - \sqrt{1 - 2r_+w_t})^2}{r_+^2} \right\}; \quad w_t \geq 0. \quad (3.43)$$

Due to the properties of the second order Stokes waves, $w_t < \frac{3}{8r_+}$, there will not be any problem with negative values in the square-root.

Using the approximative solution of a , i.e.,

$$a \approx w_t + \frac{1}{2}r_+w_t^2, \quad (3.44)$$

the approximative probability density function for W_t is

$$f_{W_t}(w_t) \approx 2w_t \left(1 + \frac{3}{2}r_+w_t + \frac{1}{2}r_+^2w_t^2 \right) \exp \left\{ -w_t^2 \left(1 + \frac{1}{2}r_+w_t \right)^2 \right\}. \quad (3.45)$$

Figure 3.6 shows the difference between using the exact solution of a , Eq. (3.42), and the approximate solution, Eq. (3.44), in the transformation.

The differences between the second order Stokes crest height and trough depth distribution given in Eqs. (3.37) and (3.43) and the Rayleigh distribution in Eq. (3.3) are shown in Fig. 3.7 (a) in terms of the probability density function, and (b) in terms of the probability of exceedance. It is clear that the second order Stokes model deviates from the Rayleigh distribution both at the peak and tail of the distribution. The nonlinearity leads to a higher peak for the troughs and a smaller peak for the crests than the Rayleigh distribution, and vice versa for the tail of the distribution. Data from the Draupner field are included for comparison. The data fall between the second order Stokes model and the Rayleigh distribution. Thus, the data show a nonlinear behavior, but not as strong as the second order Stokes model. Note that the second order Stokes model only includes the sum frequency effects, and not the difference frequency effects.

Dawson (2001) proposed a modification of the Rayleigh distribution using fifth order Stokes theory in deep water. A description of fifth order Stokes theory can be found in Skjelbreia and Hendrickson (1960), which applies for arbitrary water depth. The approach for obtaining the probability distribution for the dimensionless crest height (and trough depth) was the same as in Kriebel and Dawson (1991). Since the relationship between the nonlinear crest height and the linear amplitude is a fifth order equation, no exact solution can be found, and an

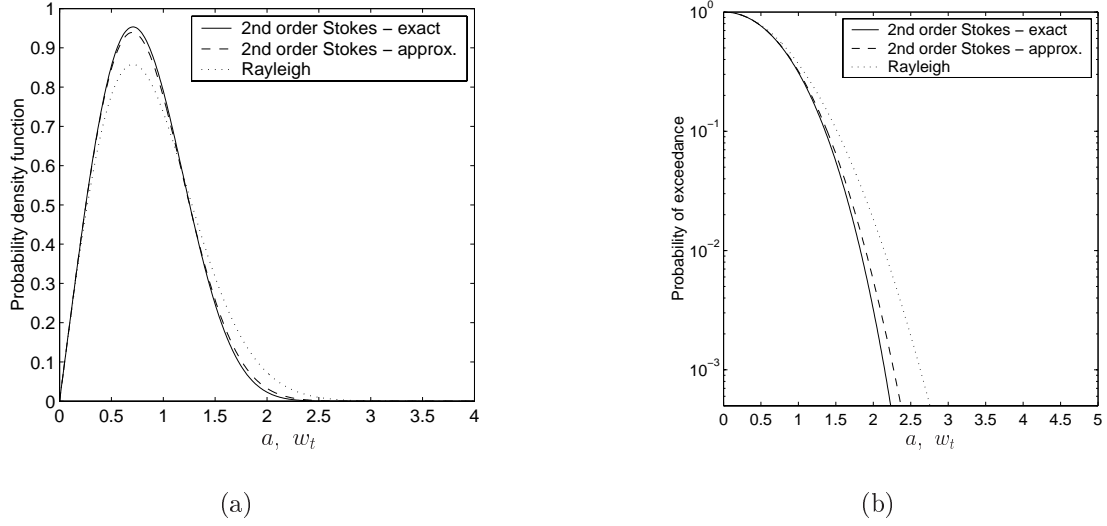


Figure 3.6: The difference between using the exact solution of a and the approximate solution in the transformation of the wave trough depth. (a) Probability density function. (b) Probability of exceedance. ($r_+ = 0.138$, from Draupner data)

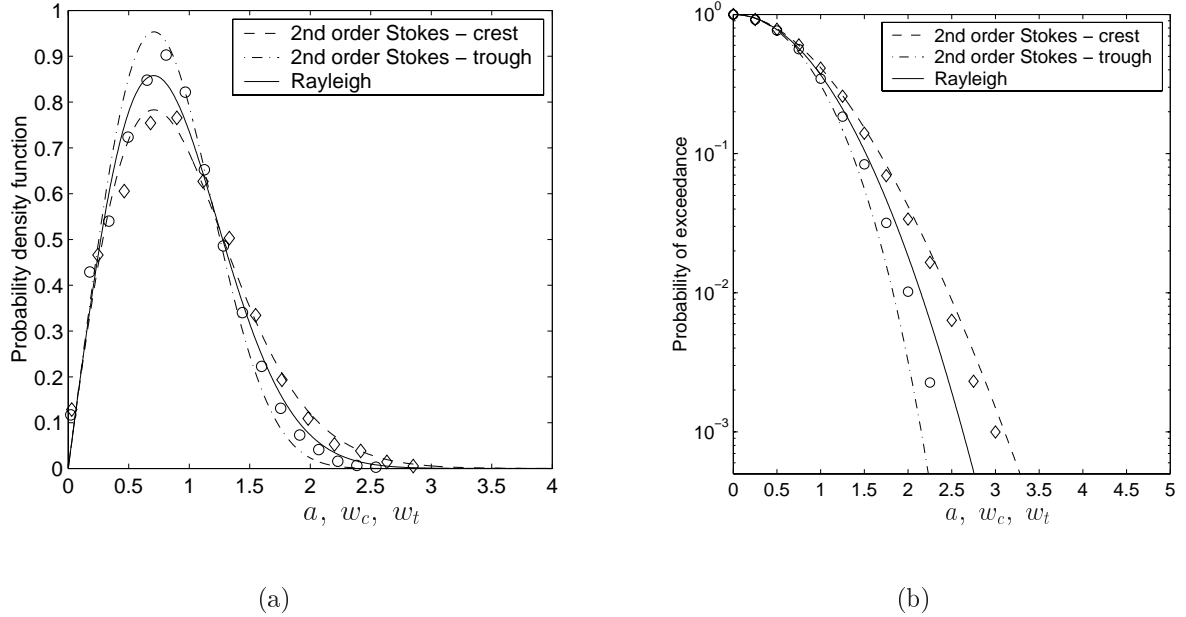


Figure 3.7: (a) Probability density function and (b) probability of exceedance, of the second order Stokes crest height and trough depth model, the Rayleigh distribution and data from the Draupner field: \diamond crest height data, \circ trough depth data ($r_+ = 0.138$).

approximative solution using series expansion must be used. For fifth order Stokes waves the dispersion relationship is also dependent on the linear amplitude, and a series expansion to find the wave number as a function of the linear amplitude is made. The resulting distribution showed that both the crest height and the trough depth tend slightly towards the Rayleigh distribution compared with the second order Stokes model. However, the extension to higher order Stokes theory is not discussed further in this work, since this model only includes the sum frequency effects. The difference between including only sum frequency effects and including both sum frequency and difference frequency effects is significant, which will be discussed in Chapter 3.6. A full second order model is therefore of more interest than including higher order terms in the Stokes model.

3.3.2 Joint distributions of successive wave crest heights and successive wave trough depths

There are several possible forms of two-dimensional distributions whose marginal distributions are given by Eqs. (3.37) and (3.43). A transformation of variables of the two-dimensional Rayleigh distribution in Eq. (3.4) gives one possible form. Let $a_1 = \eta_{a,1}/a_{\text{rms}}$ and $a_2 = \eta_{a,2}/a_{\text{rms}}$ denote the non-dimensional successive linear amplitudes $a_1 = a_j$ and $a_2 = a_{j+1}$, respectively. Similarly, let $w_{c1} = \eta_{c1}/a_{\text{rms}}$ and $w_{c2} = \eta_{c2}/a_{\text{rms}}$ denote the non-dimensional successive crest heights $w_{c1} = w_{c,j}$ and $w_{c2} = w_{c,j+1}$, respectively. Then, from Eq. (3.34) (using the positive square-root) it follows that

$$a_1 = \frac{-1 + \sqrt{1 + 2r_+ w_{c1}}}{r_+}, \quad a_2 = \frac{-1 + \sqrt{1 + 2r_+ w_{c2}}}{r_+}. \quad (3.46)$$

The bivariate transformation formula is given by

$$f_{W_{c1}, W_{c2}}(w_{c1}, w_{c2}) = f_{A_1, A_2}(a_1(w_{c1}), a_2(w_{c2})) |J|, \quad J = \begin{vmatrix} \frac{\partial a_1}{\partial w_{c1}} & \frac{\partial a_1}{\partial w_{c2}} \\ \frac{\partial a_2}{\partial w_{c1}} & \frac{\partial a_2}{\partial w_{c2}} \end{vmatrix}, \quad (3.47)$$

which results in the following two-dimensional probability density function of W_{c1} and W_{c2}

$$\begin{aligned} f_{W_{c1}, W_{c2}}(w_{c1}, w_{c2}) &= \frac{4(\sqrt{1 + 2r_+ w_{c1}} - 1)(\sqrt{1 + 2r_+ w_{c2}} - 1)}{r_+^2(1 - \kappa_{c+}^2)\sqrt{1 + 2r_+ w_{c1}}\sqrt{1 + 2r_+ w_{c2}}} \\ &\times \exp \left\{ -\frac{1}{r_+^2(1 - \kappa_{c+}^2)} \left[(\sqrt{1 + 2r_+ w_{c1}} - 1)^2 + (\sqrt{1 + 2r_+ w_{c2}} - 1)^2 \right] \right\} \\ &\times I_0 \left[\frac{2\kappa_{c+}}{r_+^2(1 - \kappa_{c+}^2)} (\sqrt{1 + 2r_+ w_{c1}} - 1)(\sqrt{1 + 2r_+ w_{c2}} - 1) \right]. \end{aligned} \quad (3.48)$$

The parameter κ_{c+} is related to the correlation coefficient, ρ_c , between W_{c1} and W_{c2} by

$$\rho_c \equiv \rho_{W_{c1}, W_{c2}} = \frac{\left(\frac{\pi}{16} + \frac{\sqrt{\pi}}{4} r_+ + \frac{1}{4} r_+^2 \right) \kappa_{c+}^2 + \frac{\pi}{256} \kappa_{c+}^4 + \frac{\pi}{1024} \kappa_{c+}^6 + O(\kappa_{c+}^8)}{1 - \frac{\pi}{4} + \frac{\sqrt{\pi}}{4} r_+ + \frac{1}{4} r_+^2}. \quad (3.49)$$

See Appendix D.1 for further details.

Similarly, for the wave trough depth, let $w_{t1} = \eta_{t1}/a_{\text{rms}}$ and $w_{t2} = \eta_{t2}/a_{\text{rms}}$ denote the non-dimensional successive trough depths $w_{t1} = w_{t,j}$ and $w_{t2} = w_{t,j+1}$, respectively. From Eq. (3.42) (using the negative square-root) it follows that

$$a_1 = \frac{1 - \sqrt{1 - 2r_+w_{t1}}}{r_+}, \quad a_2 = \frac{1 - \sqrt{1 - 2r_+w_{t2}}}{r_+}. \quad (3.50)$$

By transformation of variables of the two-dimensional Rayleigh distribution, the two-dimensional probability density function of W_{t1} and W_{t2} is obtained as

$$\begin{aligned} f_{W_{t1}, W_{t2}}(w_{t1}, w_{t2}) &= \frac{4(\sqrt{1 - 2r_+w_{t1}} - 1)(\sqrt{1 - 2r_+w_{t2}} - 1)}{r_+^2(1 - \kappa_{t+}^2)\sqrt{1 - 2r_+w_{t1}}\sqrt{1 - 2r_+w_{t2}}} \\ &\times \exp \left\{ -\frac{1}{r_+^2(1 - \kappa_{t+}^2)} \left[(\sqrt{1 - 2r_+w_{t1}} - 1)^2 + (\sqrt{1 - 2r_+w_{t2}} - 1)^2 \right] \right\} \\ &\times I_0 \left[\frac{2\kappa_{t+}}{r_+^2(1 - \kappa_{t+}^2)} (\sqrt{1 - 2r_+w_{t1}} - 1)(\sqrt{1 - 2r_+w_{t2}} - 1) \right], \end{aligned} \quad (3.51)$$

where the parameter κ_{t+} is related to the correlation coefficient, ρ_t , between W_{t1} and W_{t2} by

$$\rho_t \equiv \rho_{W_{t1}, W_{t2}} = \frac{\left(\frac{\pi}{16} - \frac{\sqrt{\pi}}{4}r_+ + \frac{1}{4}r_+^2 \right) \kappa_{t+}^2 + \frac{\pi}{256}\kappa_{t+}^4 + \frac{\pi}{1024}\kappa_{t+}^6 + O(\kappa_{t+}^8)}{1 - \frac{\pi}{4} - \frac{\sqrt{\pi}}{4}r_+ + \frac{1}{4}r_+^2} \quad (3.52)$$

The relationships between ρ_c and κ_{c+}^2 , as well as between ρ_t and κ_{t+}^2 , are illustrated in Fig. 3.8. Note that the relationships are almost linear. Thus, the method of estimating κ_{c+}^2 and κ_{t+}^2 values for general application, will be to find the correlation coefficients ρ_c and ρ_t for the actual data set and use Eqs. (3.49) and (3.52) to find the corresponding κ_{c+}^2 and κ_{t+}^2 values, respectively. Table 3.1 shows the calculated parameters for the Draupner field data.

Another quantity of interest is the conditional distribution, e.g., to know the probability density function of a wave crest given the value of the previous wave crest. The conditional probability density function of W_{c2} given W_{c1} is found by Bayes rule

$$f_{W_{c2}|W_{c1}}(w_{c2}|w_{c1}) = \frac{f_{W_{c1}, W_{c2}}(w_{c1}, w_{c2})}{f_{W_{c1}}(w_{c1})}. \quad (3.53)$$

Table 3.1: Calculated values of the Draupner field data.

r_+	[-]	0.138	ρ_c	[-]	0.291	κ_{c+}^2	[-]	0.320
$f^+(\bar{k}d)$	[-]	1.003	ρ_t	[-]	0.303	κ_{t+}^2	[-]	0.319

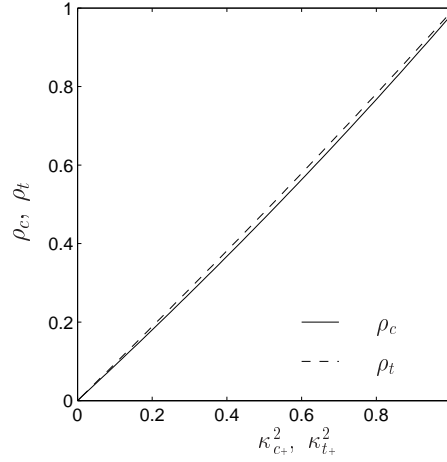


Figure 3.8: Correlation coefficients ρ_c and ρ_t as a function of the parameters κ_{c+}^2 and κ_{t+}^2 ($r_+ = 0.138$, from Draupner data).

This results in

$$\begin{aligned}
 f_{W_{c2}|W_{c1}}(w_{c2}|w_{c1}) &= \frac{f_{W_{c1},W_{c2}}(w_{c1},w_{c2})}{f_{W_{c1}}(w_{c1})} \\
 &= \frac{2(\sqrt{1+2r_+w_{c2}}-1)}{r_+(1-\kappa_{c+}^2)\sqrt{1+2r_+w_{c2}}} \\
 &\quad \times \exp \left\{ -\frac{1}{r_+^2(1-\kappa_{c+}^2)} \left[\kappa_{c+}^2 (\sqrt{1+2r_+w_{c1}}-1)^2 + (\sqrt{1+2r_+w_{c2}})^2 \right] \right\} \\
 &\quad \times I_0 \left[\frac{2\kappa_{c+}}{r_+^2(1-\kappa_{c+}^2)} (\sqrt{1+2r_+w_{c1}}-1)(\sqrt{1+2r_+w_{c2}}-1) \right].
 \end{aligned} \tag{3.54}$$

The conditional probability density function of W_{t2} given W_{t1} is

$$\begin{aligned}
 f_{W_{t2}|W_{t1}}(w_{t2}|w_{t1}) &= \frac{2(1-\sqrt{1-2r_+w_{t2}})}{r_+(1-\kappa_{t+}^2)\sqrt{1-2r_+w_{t2}}} \\
 &\quad \times \exp \left\{ -\frac{1}{r_+^2(1-\kappa_{t+}^2)} \left[\kappa_{t+}^2 (\sqrt{1-2r_+w_{t1}}-1)^2 + (\sqrt{1-2r_+w_{t2}})^2 \right] \right\} \\
 &\quad \times I_0 \left[\frac{2\kappa_{t+}}{r_+^2(1-\kappa_{t+}^2)} (\sqrt{1-2r_+w_{t1}}-1)(\sqrt{1-2r_+w_{t2}}-1) \right].
 \end{aligned} \tag{3.55}$$

3.4 Forristall distribution

Forristall (2000) suggested a parametric crest height distribution based on simulations using second order theory. The simulations are based on the theory of Sharma and Dean (1981), which are further described in Chapter 3.5. Thus the model includes both sum frequency and difference frequency effects. The simulations were done both for long-crested (2D) and short-crested (3D) random waves. A two-parameter Weibull distribution of the form

$$f_{W_c}(w_c) = \frac{\beta}{\sqrt{8\alpha}} \left(\frac{w_c}{\sqrt{8\alpha}} \right)^{\beta-1} \exp \left\{ - \left(\frac{w_c}{\sqrt{8\alpha}} \right)^{\beta} \right\}, \quad (3.56)$$

was fitted to the simulated wave data. The Weibull parameters α and β are estimated from the fit to data, and are based on the wave steepness, S_1 , and the Ursell number, U_r , defined by

$$S_1 = \frac{2\pi}{g} \frac{H_{m0}}{T_{m01}^2}, \quad (3.57)$$

and

$$U_r = \frac{H_{m0}}{\bar{k}_1^2 d^3}, \quad (3.58)$$

where \bar{k}_1 is the mean wave number corresponding to T_{m01} . Note that S_1 is based on T_{m01} rather than T_p that was used in the definition of the wave steepness in Eq. (2.6), and that U_r is based on H_{m0} and \bar{k}_1 rather than η_a and \bar{k} that was used in the definition of the Ursell number in Eq. (3.26).

The wave steepness and Ursell number characterize the degree of nonlinearity of the waves in finite water depth. At zero steepness and Ursell number the fits were forced to match the Rayleigh distribution, i.e., $\alpha = \frac{1}{\sqrt{8}} \approx 0.3536$ and $\beta = 2$. The resulting parameters for the 2D-model are

$$\begin{aligned} \alpha_{2D} &= 0.3536 + 0.2892S_1 + 0.1060U_r \\ \beta_{2D} &= 2 - 2.1597S_1 + 0.0968U_r^2, \end{aligned} \quad (3.59)$$

and for the 3D-model

$$\begin{aligned} \alpha_{3D} &= 0.3536 + 0.2568S_1 + 0.0800U_r \\ \beta_{3D} &= 2 - 1.7912S_1 - 0.5302U_r + 0.284U_r^2. \end{aligned} \quad (3.60)$$

Table 3.2 shows the calculated values based on the Draupner field data. One should note that the Ursell number will give a minor effect compared to the wave steepness in the Forristall model for these data. The wave steepness is also small, so the values for the parameters in the 2D model are almost equal to the values for the parameters in the 3D model. The Draupner data, which are described in Chapter 2.4, were sampled at water depth of 70 m, which was considered as deep water. At shallower water depths the Ursell parameter is expected to be higher.

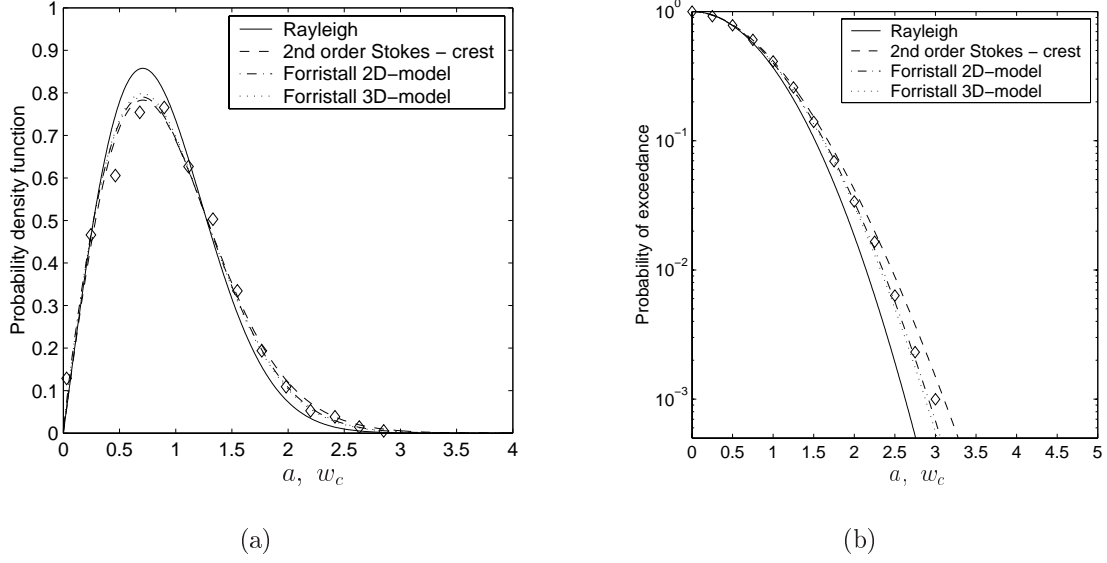


Figure 3.9: (a) Probability density function, and (b) probability of exceedance of the Forristall crest height models (2D and 3D), the second order Stokes crest height model and the Rayleigh distribution. \diamond crest height data from Draupner field ($r_+ = 0.138, \alpha_{2D} = 0.37, \beta_{2D} = 1.887, \alpha_{3D} = 0.368, \beta_{3D} = 1.902$).

Figure 3.9 (a) shows the probability density functions, both 2D- and 3D-model, compared with the Rayleigh distribution and the second order Stokes model for crest heights. The probability density functions fall between the Rayleigh distribution and the second order Stokes model. The difference between the 2D- and 3D-model is small, but the 2D-model gives a slightly more nonlinear effect. The crest height data from the Draupner field are included for comparison. Figure 3.9 (b) shows the probability of exceedance, where the difference between the models is more visible. The crest height data are quite well described by the Forristall models.

The two-dimensional probability density function of W_{c1} and W_{c2} is determined by transformation of the two-dimensional Weibull distribution (see Appendix E), which gives the following

Table 3.2: Calculated values of the Draupner field data.

S_1	[-]	0.0524	α_{3D}	[-]	0.368
U_r	[-]	0.0083	β_{3D}	[-]	1.902
α_{2D}	[-]	0.370	$\kappa_{F,2D}^2$	[-]	0.313
β_{2D}	[-]	1.887	$\kappa_{F,3D}^2$	[-]	0.313

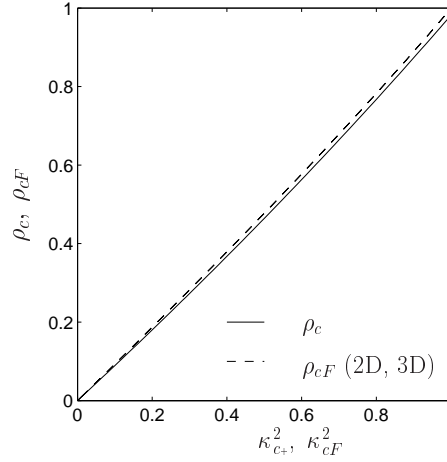


Figure 3.10: Correlation coefficients ρ_c of the second order Stokes crest height model and ρ_{cF} of the Forristall crest height models (2D and 3D) as a function of the parameters κ_{c+}^2 and κ_{cF}^2 , respectively ($r_+ = 0.138$, $\alpha_{2D} = 0.37$, $\beta_{2D} = 1.887$, $\alpha_{3D} = 0.368$, $\beta_{3D} = 1.902$, from Draupner data).

result

$$f_{W_{c1}, W_{c2}}(w_{c1}, w_{c2}) = \frac{\beta^2 w_{c1}^{\beta-1} w_{c2}^{\beta-1}}{(\sqrt{8}\alpha)^{2\beta} (1 - \kappa_{cF}^2)} \exp \left\{ -\frac{w_{c1}^\beta + w_{c2}^\beta}{(\sqrt{8}\alpha)^\beta (1 - \kappa_{cF}^2)} \right\} \times I_0 \left[\frac{2\kappa_{cF} w_{c1}^{\beta/2} w_{c2}^{\beta/2}}{(\sqrt{8}\alpha)^\beta (1 - \kappa_{cF}^2)} \right]. \quad (3.61)$$

The relationship between the parameter κ_{cF} and the correlation coefficient, ρ_{cF} , between W_{c1} and W_{c2} is given by

$$\rho_{cF} = \frac{\left[\Gamma \left(\frac{1}{\beta} \right) \right]^2}{2\beta \Gamma \left(\frac{2}{\beta} \right) - \left[\Gamma \left(\frac{1}{\beta} \right) \right]^2} \left[\frac{1}{\beta^2} \kappa_{cF}^2 + \frac{1}{4\beta^2} \left(\frac{1}{\beta} + 1 \right)^2 \kappa_{cF}^4 + \frac{1}{36\beta^2} \left(\frac{1}{\beta} + 1 \right)^2 \left(\frac{1}{\beta} + 2 \right)^2 \kappa_{cF}^6 + O(\kappa_{cF}^8) \right], \quad (3.62)$$

where Γ is the gamma function. See Appendix D.2 for further details. Figure 3.10 shows the relationships between the correlation coefficients for the Forristall crest height models (2D and 3D) and the parameter κ_{cF}^2 compared to the second order Stokes crest height model. The difference between the 2D- and 3D-model would not be distinguishable, so both models are given by the same line. The difference between the Forristall model and the Stokes model is small.

The conditional probability density function of W_{c2} given W_{c1} is obtained as

$$f_{W_{c2}|W_{c1}}(w_{c2}|w_{c1}) = \frac{\beta w_{c2}^{\beta-1}}{(\sqrt{8}\alpha)^\beta (1 - \kappa_{cF}^2)} \exp \left\{ -\frac{\kappa_{cF}^2 w_{c1}^\beta + w_{c2}^\beta}{(\sqrt{8}\alpha)^\beta (1 - \kappa_{cF}^2)} \right\} \times I_0 \left[\frac{2\kappa_{cF} w_{c1}^{\beta/2} w_{c2}^{\beta/2}}{(\sqrt{8}\alpha)^\beta (1 - \kappa_{cF}^2)} \right]. \quad (3.63)$$

3.5 Second order wave theory

The theory of second order random waves can be found in Longuet-Higgins (1963) in the case of infinite water depth. Later it has been extended to finite water depth by Sharma and Dean (1981).

Longuet-Higgins (1963) showed that the skewness of the distribution of the surface elevation is always positive. Marthinsen and Winterstein (1992) showed that the slowly varying part of the second order waves gives a negative contribution to the wave skewness in the case of a narrow-banded wave process in finite water depth, and in the general case in infinite water depth.

A short description of the second order wave theory in Marthinsen and Winterstein (1992) is given here. In Chapter 3.6 the theory for a narrow-banded wave process will be used in deriving the distribution functions for successive wave crest heights and wave trough depths.

The velocity potential and the surface elevation are found from a perturbation approach similar to the one described for second order Stokes waves in Appendix B. The surface elevation to second order is given by

$$\eta = \eta_1 + \eta_2. \quad (3.64)$$

The first order component is given in complex form by

$$\eta_1 = \sum_{n=-N}^N \frac{\eta_{a,n}}{2} e^{i\psi_n}, \quad (3.65)$$

where the phase functions are

$$\psi_n = \omega_n t - k_n x - \xi_n. \quad (3.66)$$

The second order component is given by

$$\eta_2 = \sum_{m,n=1}^N \eta_{a,m} \eta_{a,n} E_{m,n}^+ \cos(\psi_m + \psi_n) + \sum_{m,n=1}^N \eta_{a,m} \eta_{a,n} E_{m,n}^- \cos(\psi_m - \psi_n), \quad (3.67)$$

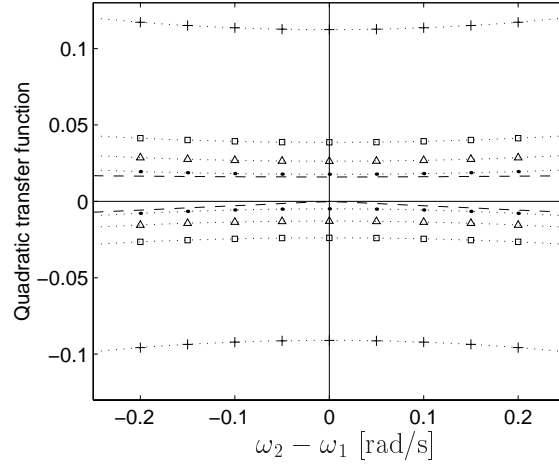


Figure 3.11: The quadratic transfer function for a fixed sum frequency $\omega_1 + \omega_2 = 1.12$ rad/s. Positive values: sum frequencies ($E_{m,n}^-$). Negative values: difference frequencies ($E_{m,n}^+$). -- deep water; $\cdot\bullet\cdot$ $d = 70$ m; $\cdot\triangle\cdot$ $d = 42$ m; $\cdot\square\cdot$ $d = 31$ m; $\cdot+\cdot$ $d = 16$ m.

where

$$E_{m,n}^+ = E_{n,m}^+ = E_{m,n} \quad (3.68)$$

$$E_{m,n}^- = E_{n,m}^- = E_{m,-n} \quad (3.69)$$

$$E_{m,n} = \frac{\frac{gk_mk_n}{2\omega_m\omega_n} - \frac{1}{4g}(\omega_m^2 + \omega_n^2 + \omega_m\omega_n) + \frac{g}{4} \frac{\omega_mk_n^2 + \omega_nk_m^2}{\omega_m\omega_n(\omega_m + \omega_n)}}{1 - g \frac{k_m + k_n}{(\omega_m + \omega_n)^2} \tanh(k_m + k_n)d} - \frac{gk_mk_n}{4\omega_m\omega_n} + \frac{1}{4g}(\omega_m^2 + \omega_n^2 + \omega_m\omega_n). \quad (3.70)$$

The quantity $E_{m,n}$ is the quadratic transfer function of the wave elevation. The $E_{m,-m}$ terms are given as the limits

$$E_{m,-m} = \lim_{\omega_n \rightarrow -\omega_m} E_{m,n} = \frac{1}{2} \frac{\frac{gk_m^2}{2\omega_m^2} - \frac{\omega_m^2}{2g} + \frac{gk_m}{\omega_m c_{g,m}}}{1 - \frac{gd}{c_{g,m}^2}} - \frac{k_m}{2 \sinh 2k_md}, \quad (3.71)$$

where

$$c_{g,m} = \left. \frac{d\omega}{dk} \right|_{\omega=\omega_m, k=k_m} = \frac{g \tanh k_md}{2\omega_m} + \frac{gk_md(1 - \tanh^2 k_md)}{2\omega_m} \quad (3.72)$$

is the wave group velocity.

Figure 3.11 shows the quadratic transfer function for a fixed sum frequency $\omega_1 + \omega_2 = 1.12$ rad/s, which corresponds to wave periods around 11 s. Along $\omega_2 - \omega_1 = 0$, then $\omega_1 = \omega_2 = 0.56$ rad/s, which corresponds to the peak frequency of the Draupner field data. Note that the second order Stokes model only includes the sum frequency terms $E_{m,m}^+$. From the figure it is clear that the second order effects increase with decreasing water depths. The difference frequency term

has almost no effect in deep water, but as the water depth decreases, this term becomes more significant, and is almost of the same magnitude as the sum frequency term. Since the difference frequency term is negative, it will give a reduction in the second order component given in Eq. (3.67). The variation of the quadratic transfer function for different values of $\omega_2 - \omega_1$ is small, which indicates that the narrow-band assumption is justified. In deep water, however, the difference frequency term is significant for large difference in ω_1 and ω_2 . This is also discussed in Myrhaug et al. (2002).

One should note that the expected value of the surface elevation is different from zero. Using a continuous representation the expected value is given by

$$\bar{\eta} = 2 \int_0^\infty E^-(\omega, \omega) S(\omega) d\omega, \quad (3.73)$$

and the variance is given by

$$\sigma^2 = \int_0^\infty S(\omega) d\omega. \quad (3.74)$$

The skewness is given by

$$\rho_3 = \frac{6}{\sigma^3} \int_0^\infty \int_0^\infty [E^+(\omega_1, \omega_2) + E^-(\omega_1, \omega_2)] S(\omega_1) S(\omega_2) d\omega_1 d\omega_2. \quad (3.75)$$

3.6 Extended second order model including sum and difference frequency effects

For a stationary narrow-banded random sea state Eqs. (3.68) - (3.70) give

$$E^+(\bar{\omega}, \bar{\omega}) = \frac{1}{2} \bar{k} \frac{\cosh \bar{k}d(2 + \cosh 2\bar{k}d)}{2 \sinh^3 \bar{k}d} \quad (3.76)$$

$$E^-(\bar{\omega}, \bar{\omega}) = -\frac{1}{2} \bar{k} \frac{2[\tanh \bar{k}d + 2\bar{k}d(1 - \tanh^2 \bar{k}d)]}{4\bar{k}d \tanh \bar{k}d - [\tanh \bar{k}d + \bar{k}d(1 - \tanh^2 \bar{k}d)]^2}. \quad (3.77)$$

The expected value and skewness given in Eqs. (3.73) and (3.75) become

$$\bar{\eta} = 2\sigma^2 E^-(\bar{\omega}, \bar{\omega}) \quad (3.78)$$

$$\rho_3 = 6\sigma [E^-(\bar{\omega}, \bar{\omega}) + E^+(\bar{\omega}, \bar{\omega})]. \quad (3.79)$$

One should note that since $E^-(\bar{\omega}, \bar{\omega}) \leq 0$, the difference frequency term will give a negative contribution to the skewness. In order to compare the distribution functions resulting from this model with the distribution functions given in Chapters 3.3 and 3.4, the mean value of the surface elevation must be zero.

Then the surface elevation at a fixed point is given by

$$\eta(t) = \eta_a \cos[\bar{\omega}t + \xi(t)] + \frac{1}{2}\bar{k}\eta_a^2 f^+(\bar{k}, d) \cos 2[\bar{\omega}t + \xi(t)] - \frac{1}{2}\bar{k}\eta_a^2 f^-(\bar{k}, d) + \frac{1}{16}\bar{k}H_{m0}^2 f^-(\bar{k}, d), \quad (3.80)$$

where

$$f^+(\bar{k}, d) = \frac{\cosh \bar{k}d(2 + \cosh 2\bar{k}d)}{2 \sinh^3 \bar{k}d} \quad (3.81)$$

$$f^-(\bar{k}, d) = \frac{2[\tanh \bar{k}d + 2\bar{k}d(1 - \tanh^2 \bar{k}d)]}{4\bar{k}d \tanh \bar{k}d - [\tanh \bar{k}d + \bar{k}d(1 - \tanh^2 \bar{k}d)]^2}. \quad (3.82)$$

The last term of Eq. (3.80) must be included in order to obtain zero expectation of the surface elevation. However, the skewness remains the same regardless of the choice of mean value. This is the same representation as used in Prevosto et al. (2000), among others. In deep water $f^-(\bar{k}, d) \rightarrow 0$, and Eq. (3.80) reduces to Eq. (3.28). See further details regarding the limitations of the wave amplitude in Appendix C.2.

The procedure of finding the distribution of the non-dimensional wave crest height is similar to the one described in Chapter 3.3. At the wave crest the nonlinear crest height, η_c , is given by

$$\eta_c = \eta_a + \frac{1}{2}\bar{k} [f^+(\bar{k}, d) - f^-(\bar{k}, d)] \eta_a^2 + \frac{1}{16}\bar{k} f^-(\bar{k}, d) H_{m0}^2. \quad (3.83)$$

The characteristic steepness of the random waves, r , is now defined as

$$r = \bar{k} a_{\text{rms}} [f^+(\bar{k}, d) - f^-(\bar{k}, d)]. \quad (3.84)$$

By using $a_{\text{rms}} = \sqrt{2m_0}$ and $H_{m0} = 4\sqrt{m_0}$, and defining

$$R = \frac{1}{2}\bar{k} a_{\text{rms}} f^-(\bar{k}, d), \quad (3.85)$$

the nonlinear non-dimensional crest height can be written as

$$w_c = a + \frac{1}{2}ra^2 + R. \quad (3.86)$$

The solution of a is

$$a = \frac{-1 \pm \sqrt{1 + 2r(w_c - R)}}{r}, \quad (3.87)$$

where only the positive square-root is a solution, because the amplitude is always positive. Since $a \geq 0$, then $w_c \geq R$. Transformation of variables using the Rayleigh distribution gives the probability density function of W_c

$$f_{W_c}(w_c) = \frac{2(\sqrt{1 + 2r(w_c - R)} - 1)}{r\sqrt{1 + 2r(w_c - R)}} \exp \left\{ -\frac{(\sqrt{1 + 2r(w_c - R)} - 1)^2}{r^2} \right\}; \quad w_c \geq R. \quad (3.88)$$

Similarly, the nonlinear trough depth, η_t is given by

$$\eta_t = \eta_a - \frac{1}{2}\bar{k} [f^+(\bar{k}, d) - f^-(\bar{k}, d)] \eta_a^2 - \frac{1}{16}\bar{k} f^-(\bar{k}, d) H_{m0}^2, \quad (3.89)$$

which gives the non-dimensional nonlinear trough depth

$$w_t = a - \frac{1}{2}ra^2 - R. \quad (3.90)$$

The solution of a is

$$a = \frac{1 \pm \sqrt{1 - 2r(w_t + R)}}{r}. \quad (3.91)$$

A similar argument as for the second order Stokes wave trough leads to the restriction $a < \frac{1}{r}$, thus only the negative square-root is a solution. See Appendix C.2 for further details. The resulting probability density function of W_t is

$$f_{W_t}(w_t) = \frac{2(1 - \sqrt{1 - 2r(w_t + R)})}{r\sqrt{1 - 2r(w_t + R)}} \exp \left\{ -\frac{(1 - \sqrt{1 - 2r(w_t + R)})^2}{r^2} \right\}; \quad w_t \geq -R. \quad (3.92)$$

Figure 3.12 shows the difference between the second order Stokes model, including sum frequency effects only, and the extended model, including both sum frequency and difference frequency effects. The Rayleigh distribution is included for comparison. Data from the Draupner field are also included. Table 3.3 shows the calculated parameters from the Draupner field.

The extended model gives a slightly lower probability of exceedance for the crest heights and a higher probability of exceedance for the trough depths. This is due to the contribution of the difference frequency term. The difference frequency term will give a negative contribution to the wave crest, and a positive contribution to the wave trough. The difference frequency term is zero in infinite water depth, and the difference between the extended model and the second order Stokes model will increase with decreasing water depth. For the Draupner data $f^+(\bar{k}d) \approx 1$ and $f^-(\bar{k}d)$ is small, which means that even at relatively deep water, the difference frequency term will give a small contribution to the surface elevation. The extended model gives a better description of the Draupner field data than the second order Stokes model.

Table 3.3: Calculated values of the Draupner field data.

r	[-]	0.119	R	[-]	0.0092
$f^+(\bar{k}d)$	[-]	1.003	$f^-(\bar{k}d)$	[-]	0.134
κ_c^2	[-]	0.319	κ_t^2	[-]	0.320

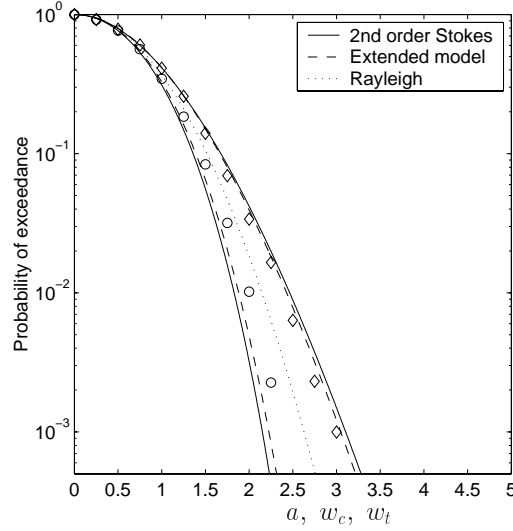


Figure 3.12: Probability of exceedance of the extended model, the second order Stokes model and the Rayleigh distribution. The lines to the right of the Rayleigh distribution are for the crest heights, and to the left are for the trough depths. \diamond crest height data and \circ trough depth data from Draupner field ($r_+ = 0.138$, $r = 0.119$, $R = 0.0092$).

Considering two successive crest heights, the joint probability density function of W_{c1} and W_{c2} is found from transformation of variables of the two-dimensional Rayleigh distribution, giving

$$\begin{aligned}
 f_{W_{c1}, W_{c2}}(w_{c1}, w_{c2}) &= \frac{4(\sqrt{1 + 2r(w_{c1} - R)} - 1)(\sqrt{1 + 2r(w_{c2} - R)} - 1)}{r^2(1 - \kappa_c^2)\sqrt{1 + 2r(w_{c1} - R)}\sqrt{1 + 2r(w_{c2} - R)}} \\
 &\times \exp \left\{ -\frac{1}{r^2(1 - \kappa_c^2)} \left[(\sqrt{1 + 2r(w_{c1} - R)} - 1)^2 \right. \right. \\
 &\quad \left. \left. + (\sqrt{1 + 2r(w_{c2} - R)} - 1)^2 \right] \right\} \\
 &\times I_0 \left[\frac{2\kappa_c}{r^2(1 - \kappa_c^2)} (\sqrt{1 + 2r(w_{c1} - R)} - 1)(\sqrt{1 + 2r(w_{c2} - R)} - 1) \right]; \\
 &\quad w_{c1}, w_{c2} \geq R,
 \end{aligned} \tag{3.93}$$

where the parameter κ_c remains the same as for the second order Stokes model defined in Eq. (3.49), but with $r_+ = r$ (see Appendix D.3). The value of κ_c^2 calculated from the Draupner field data is given in Table 3.3. Compared with the parameter κ_{c+}^2 for the second order Stokes model given in Table 3.1, it is seen that the small difference between r and r_+ gives almost no effect on κ_c^2 .

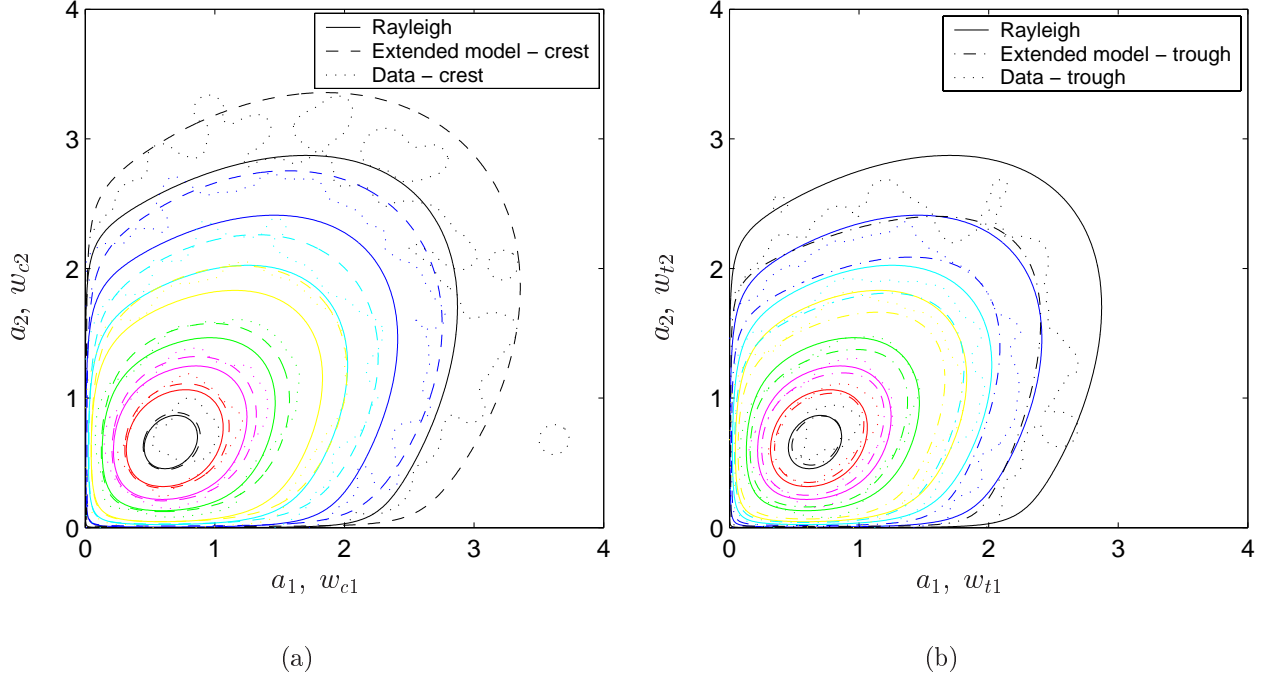


Figure 3.13: Contour plot of the two-dimensional probability density function of the extended model, the Rayleigh distribution and data from the Draupner field. (a) wave crest height, (b) wave trough depth. Percent levels the given contour lines enclose are 10, 30, 50, 70, 90, 95, 99 and 99.9. ($r = 0.119$, $R = 0.0092$, $\kappa_a^2 = 0.312$, $\kappa_c^2 = 0.319$, $\kappa_t^2 = 0.320$).

Similarly, the joint probability density function of two successive trough depths is found as

$$\begin{aligned}
 f_{W_{t1}, W_{t2}}(w_{t1}, w_{t2}) &= \frac{4(\sqrt{1 - 2r(w_{t1} + R)} - 1)(\sqrt{1 - 2r(w_{t2} + R)} - 1)}{r^2(1 - \kappa_t^2)\sqrt{1 - 2r(w_{t1} + R)}\sqrt{1 - 2r(w_{t2} + R)}} \\
 &\quad \times \exp \left\{ -\frac{1}{r^2(1 - \kappa_t^2)} \left[(\sqrt{1 - 2r(w_{t1} + R)} - 1)^2 \right. \right. \\
 &\quad \left. \left. + (\sqrt{1 - 2r(w_{t2} + R)} - 1)^2 \right] \right\} \\
 &\quad \times I_0 \left[\frac{2\kappa_t}{r^2(1 - \kappa_t^2)} (\sqrt{1 - 2r(w_{t1} + R)} - 1)(\sqrt{1 - 2r(w_{t2} + R)} - 1) \right]; \\
 &\quad w_{t1}, w_{t2} \geq -R,
 \end{aligned} \tag{3.94}$$

where the parameter κ_t is the same as in Eq. (3.52), but with $r_+ = r$. The value of κ_t^2 calculated from the Draupner field data is also given in Table 3.3.

Figure 3.13 shows the two-dimensional probability density functions of (a) two successive crest heights and (b) two successive trough depths compared with the two-dimensional Rayleigh dis-

tribution. The peaks of the distributions are almost at the same location, and the difference between the distributions is small for small wave amplitudes. However, the difference increases with increasing wave amplitudes. The Rayleigh distribution is located between the crest height and trough depth distribution, and the wave trough distribution decreases most rapidly. This is also reflected in the marginal distributions in Fig. 3.12. Data from the Draupner field are also included for comparison. The extended model gives a better agreement with the data than the Rayleigh distribution, especially for large crest heights and trough depths.

In addition to the conditional density function, it is of interest to calculate the probability of exceedance of the wave crest given that the previous wave crest exceeded a given level like a_{rms} . This is found by Bayes rule and integration of the two-dimensional probability density function. If $\eta_{c1} > a_{\text{rms}}$, then $w_{c1} > 1$, and the conditional probability of exceedance is given by

$$\begin{aligned} P(W_{c2} > w_{c2} | W_{c1} > 1) &= \frac{P(W_{c1} > 1 \cap W_{c2} > w_{c2})}{P(W_{c1} > 1)} \\ &= \frac{\int_{w_{c2}}^{\infty} \int_1^{\infty} f_{W_{c1}, W_{c2}}(w_{c1}, \tilde{w}_{c2}) dw_{c1} d\tilde{w}_{c2}}{1 - F_{W_{c1}}(1)}. \end{aligned} \quad (3.95)$$

Figure 3.14 shows the conditional probability of exceedance given that the previous non-dimensional wave crest, or wave trough, exceeded 1, compared with data from the Draupner field. The extended model agrees quite well with the data compared with the Rayleigh distribution.

The expected value of a crest height given the previous crest height is given by

$$E[W_{c2} | W_{c1} = w_{c1}] = \int_R^{\infty} w_{c2} f_{W_{c2} | W_{c1}}(w_{c2} | w_{c1}) dw_{c2}, \quad (3.96)$$

where the conditional probability density function $f_{W_{c2} | W_{c1}}(w_{c2} | w_{c1})$ is found from Bayes rule, given in Eq. (3.53).

Similarly, the expected value of a trough depth given the previous trough depth is given by

$$E[W_{t2} | W_{t1} = w_{t1}] = \int_{-R}^{\infty} w_{t2} f_{W_{t2} | W_{t1}}(w_{t2} | w_{t1}) dw_{t2}. \quad (3.97)$$

Figure 3.15 shows the conditional expectation $E[W_{c2} | W_{c1} = w_{c1}]$ versus w_{c1} , as well as the conditional expectation $E[W_{t2} | W_{t1} = w_{t1}]$ versus w_{t1} . Generally, it is observed that the wave crests have a higher expected value than the wave troughs, at least for low to moderate values of w_{c1} and w_{t1} ($w_{c1}, w_{t1} \lesssim 1.8$). For larger values the data are questionable due to few data cases in these classes of w_{c1} and w_{t1} . Overall, the deviations between the nonlinear models and linear theory are small.

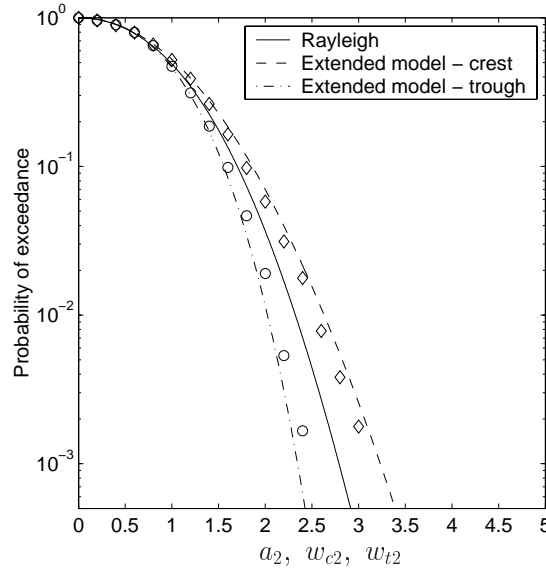


Figure 3.14: Conditional probability of exceedance of the wave amplitude given that the previous wave amplitude exceeded a_{rms} , i.e., $a_1, w_{c1}, w_{t1} > 1$. \diamond crest height data and \circ trough depth data from Draupner field ($r = 0.119$, $R = 0.0092$, $\kappa_a^2 = 0.312$, $\kappa_c^2 = 0.319$, $\kappa_t^2 = 0.320$).

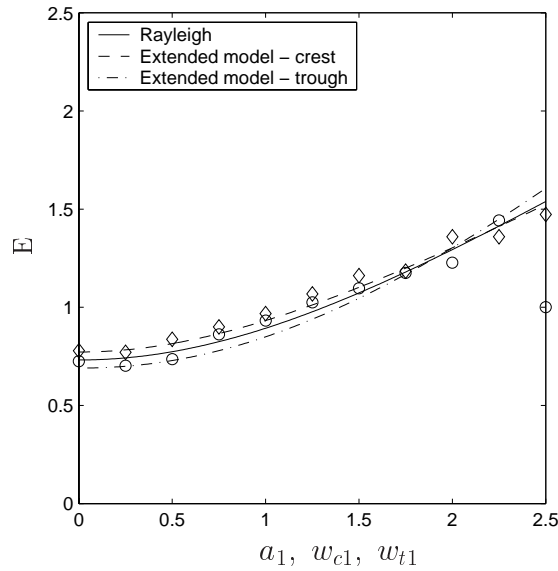


Figure 3.15: Conditional expectation of the wave amplitude given the previous wave amplitude. — $E = E[A_2|A_1 = a_1]$; -- $E = E[W_{c2}|W_{c1} = w_{c1}]$; -.- $E = E[W_{t2}|W_{t1} = w_{t1}]$; \diamond crest height data; \circ trough depth data from Draupner field ($r = 0.119$, $R = 0.0092$, $\kappa_a^2 = 0.312$, $\kappa_c^2 = 0.319$, $\kappa_t^2 = 0.320$).

3.7 Example of using the extended second order model in prediction of green water load and volume

A good model for the wave crest height can be used in many applications. In this chapter an example of predicting green water load and volume will be shown. Ogawa (2003) presented a model where the Rayleigh distribution was used as the distribution for the wave crest height. A short summary of his model is given below and the results are compared with the extended second order model. The final objective of Ogawa (2003) to give a long-term prediction method of the green water load and volume is not considered here.

Model tests were conducted in irregular waves with a domestic Japanese tanker and two cargo ships; a standard ship (Type-1) and a ship with a wider bow flare (Type-3). Measurements of the green water load and the relative water height at the stem were made. The green water volume was estimated by integrating the mean water height, measured at five cross sections on the bow deck. The results for the green water volume were only shown for the cargo ships, so the tanker will not be considered here. Table 3.4 shows the principal particulars for the cargo ships in the model tests. L_{pp} is the ship length, B is the breadth of the ship, b is the bow height at the stem, and A_d is the area of the separated fore deck.

The relationship between the maximum value of the green water load, L_{\max} , and the maximum value of the relative water height, η_{\max} , was approximated by

$$L_{\max} = \alpha_o \rho g B (\eta_{\max} - b)^2, \quad (3.98)$$

where α_o is a coefficient estimated from the model test data, and ρ is the water density. Figure 3.16 illustrates the relationship between η_{\max} and b .

By assuming that η_{\max} is distributed according to the Rayleigh distribution, a transformation of variables yields the cumulative distribution function of L_{\max}

$$F_{L_{\max}}(L_{\max}) = 1 - \exp \left\{ -\frac{(b\sqrt{\alpha_o \rho g B} + \sqrt{L_{\max}})^2}{2\alpha_o \rho g B \sigma^2} \right\}. \quad (3.99)$$

Table 3.4: Principal particulars for domestic cargo ships (left) and calculated values from model tests (right).

		Ship	Model			Type 1	Type 3
L_{pp}	[m]	78.5	4.1	α_o	[-]	0.45	0.34
B	[m]	12.8	0.669	β_o	[-]	0.31	0.18
b	[m]	5.3	0.278	σ	[m]	2.8	2.9
A_d	[m ²]	42.9	0.117				

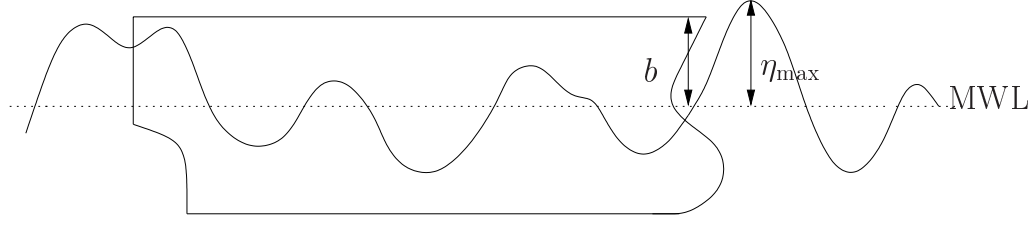


Figure 3.16: Illustration of the relationship between η_{\max} and b . The dotted line indicates the mean water level (MWL).

The measured values from the model tests were converted to full scale. Figure 3.17 shows the mean green water pressure, which is the green water load divided by the area of the separated fore deck, in terms of probability of exceedance. The Ogawa (2003) model (the solid line) underpredicts the data for both Type-1 and Type-3 cargo ship.

A new distribution function for L_{\max} can be found by using the extended second order model for the crest height. By introducing $\eta_{\max} = a_{\text{rms}} w_c$, the relationship between L_{\max} and w_c is found as

$$w_c = \frac{b\sqrt{\alpha_o \rho g B} + \sqrt{L_{\max}}}{a_{\text{rms}} \sqrt{\alpha_o \rho g B}}. \quad (3.100)$$

The cumulative distribution function of L_{\max} is found by transformation of variables using Eq. (3.88)

$$F_{L_{\max}}(L_{\max}) = 1 - \exp \left\{ - \frac{\left(\sqrt{1 + 2r \left(\frac{b\sqrt{\alpha_o \rho g B} + \sqrt{L_{\max}}}{a_{\text{rms}} \sqrt{\alpha_o \rho g B}} - R \right)} - 1 \right)^2}{r^2} \right\}. \quad (3.101)$$

The experiments were carried out in deep water, thus $f^+(\bar{k}d) = 1$ and $f^-(\bar{k}d) = 0$, giving $R = 0$. In full scale the values of H_{m0} and T_{m01} were 3.7 m and 6.7 s, respectively, giving $r = \bar{k}_1 a_{\text{rms}} = 0.116$. One should note that in Ogawa (2003) only T_{m01} was given, so that r must be based on \bar{k}_1 rather than \bar{k} . However, since a narrow-banded sea state is assumed, these values are equal.

The extended second order model is shown in Fig. 3.17 (broken line). The model overpredicts the data for both Type-1 and Type-3 cargo ship. In these cases the extended second order model and the Ogawa (2003) model give an upper and lower bound for the mean green water pressure, respectively.

The relationship between the maximum value of the green water volume, V_{\max} , and η_{\max} was approximated by

$$V_{\max} = \beta_o B (\eta_{\max} - b)^2, \quad (3.102)$$

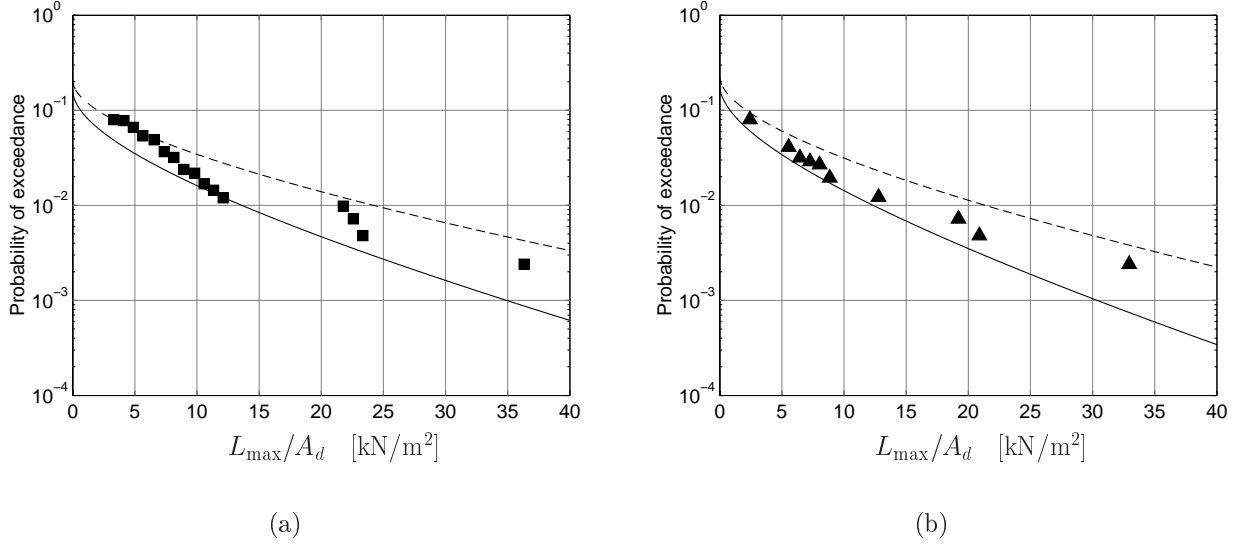


Figure 3.17: Mean green water pressure. (a) Cargo Type-1, (b) Cargo Type-3. — Ogawa (2003) method, -- extended second order model; ■ data Type-1; ▲ data Type-3.

where β_o is a coefficient estimated from the model test data.

By transformation of variables, the cumulative distribution function of V_{\max} is given by

$$F_{V_{\max}}(V_{\max}) = 1 - \exp \left\{ -\frac{(b\sqrt{\beta_o B} + \sqrt{V_{\max}})^2}{2\beta_o B \sigma^2} \right\}. \quad (3.103)$$

Figure 3.18 shows the results from the model test as the mean green water height, which is the green water volume divided by the area of the separated fore deck, in terms of probability of exceedance. The Ogawa (2003) model (the solid line) underpredicts the data for both Type-1 and Type-3 cargo ship.

Similarly to the green water load, the extended second order model can be used to obtain a new distribution for V_{\max} . The relationship between V_{\max} and w_c is given by

$$w_c = \frac{b\sqrt{\beta_o B} + \sqrt{V_{\max}}}{a_{\text{rms}}\sqrt{\beta_o B}}. \quad (3.104)$$

By transformation of variables the cumulative distribution function of V_{\max} is found as

$$F_{V_{\max}}(V_{\max}) = 1 - \exp \left\{ -\frac{\left(\sqrt{1 + 2r \left(\frac{b\sqrt{\beta_o B} + \sqrt{V_{\max}}}{a_{\text{rms}}\sqrt{\beta_o B}} - R \right)} - 1 \right)^2}{r^2} \right\}. \quad (3.105)$$

The extended second order model is shown in Fig. 3.18 (broken line). The model agrees quite

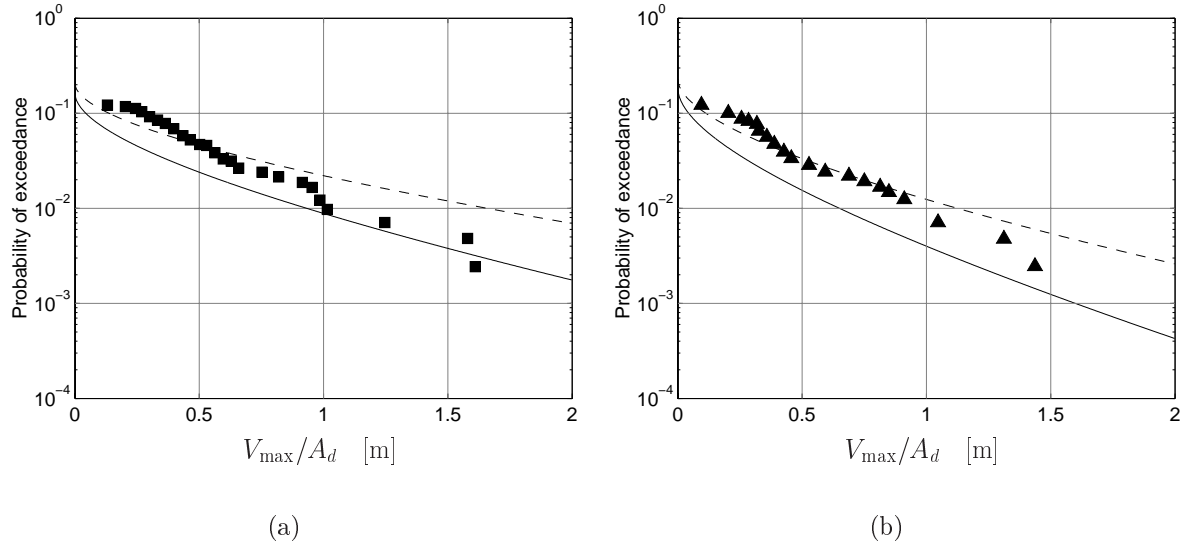


Figure 3.18: Mean green water height. (a) Cargo Type-1, (b) Cargo Type-3. — Ogawa (2003) method, -- extended second order model; ■ data Type-1; ▲ data Type-3.

well with the data for small values of the green water height for both Type-1 and Type-3 cargo ship, while it overpredicts the data for larger values of the green water height.

CHAPTER 4

Joint probability distributions for successive wave heights

4.1 Longuet-Higgins model and Næss model

According to Longuet-Higgins (1952) the wave height, η_h , is Rayleigh distributed if the wave spectrum is narrow-banded, i.e.,

$$f_H(h) = 2h \exp \{-h^2\}; \quad h = \frac{\eta_h}{\bar{h}} \geq 0, \quad (4.1)$$

where h is the dimensionless wave height. The normalizing factor, \bar{h} , was given as the root-mean-square value of η_h , which for linear waves is given by $\bar{h} = h_{\text{rms}} = 2(2m_0)^{1/2}$. Later Goda (1974), Haring et al. (1976) and Forristall (1978) among others, showed by comparison with data from the Japanese coasts and the Gulf of Mexico, respectively, that this choice of normalizing factor overpredicts the wave heights.

Forristall (1978) analyzed 116 hours of hurricane generated waves from the Gulf of Mexico, and fitted a two-parameter Weibull distribution to the data. Later Longuet-Higgins (1980) showed that the same data were well predicted by the Rayleigh distribution in Eq. (4.1), if the normalizing factor was selected as $\bar{h} = 1.85(2m_0)^{1/2}$. The reduction of \bar{h} was explained by the finite bandwidth in the field data, which also was discussed in general by Boccotti (1982).

Næss (1985) used a different approach to derive an expression for the wave height in a stationary, narrow-banded Gaussian wave train. A short description of this approach is given below. By assuming a narrow-banded process, the time interval between a maximum and a minimum is

approximately constant and equal to half the wave period τ . The expected number of simultaneous occurrences of a positive level crossing of the level ξ and a negative level crossing of the level $-\xi$ after time $\tau/2$ is given by

$$N_{\xi, -\xi} \left(\frac{\tau}{2} \right) = - \int_{-\infty}^0 \int_0^{\infty} \dot{x}_1 \dot{x}_2 f_{\mathbf{X}}(\xi, \dot{x}_1, -\xi, \dot{x}_2) d\dot{x}_1 d\dot{x}_2, \quad (4.2)$$

where \dot{x}_1 and \dot{x}_2 are the velocities at the level up-crossing and the level down-crossing, respectively. Since $X(t)$ is a Gaussian process, the joint density function is given by

$$f_{\mathbf{X}}(\mathbf{x}) = \frac{1}{(2\pi)^2 |\Sigma|^{1/2}} \exp \left\{ -\frac{1}{2} \mathbf{x}^T \Sigma^{-1} \mathbf{x} \right\}; \quad \mathbf{x} = [x_1, \dot{x}_1, x_2, \dot{x}_2]^T, \quad (4.3)$$

where

$$\Sigma = \begin{bmatrix} R_{\eta}(0) & -R'_{\eta}(0) & R_{\eta}(\frac{\tau}{2}) & R'_{\eta}(\frac{\tau}{2}) \\ R'_{\eta}(0) & -R''_{\eta}(0) & -R'_{\eta}(\frac{\tau}{2}) & -R''_{\eta}(\frac{\tau}{2}) \\ R_{\eta}(\frac{\tau}{2}) & -R'_{\eta}(\frac{\tau}{2}) & R_{\eta}(0) & -R'_{\eta}(0) \\ R'_{\eta}(\frac{\tau}{2}) & -R''_{\eta}(\frac{\tau}{2}) & R'_{\eta}(0) & -R''_{\eta}(0) \end{bmatrix}. \quad (4.4)$$

The autocorrelation function, $R_{\eta}(\tau)$, of the Gaussian wave elevation is given by

$$R_{\eta}(\tau) = E[X(t)X(t+\tau)] = \int_0^{\infty} S(\omega) e^{i\omega\tau} d\omega, \quad (4.5)$$

and ' denotes the time derivative. One should note that $R_{\eta}(0) = m_0$. Equation (4.2) can then be evaluated to

$$N_{\xi, -\xi} \left(\frac{\tau}{2} \right) = N_{0,0} \left(\frac{\tau}{2} \right) \cdot \exp \left\{ -\frac{\xi^2}{R_{\eta}(0) - R(\frac{\tau}{2})} \right\}. \quad (4.6)$$

By using $R_{\eta}(0) = m_0$ and defining $\rho_N = \frac{R_{\eta}(\tau)}{R_{\eta}(0)}$, the probability of a wave amplitude exceeding the level ξ is given by

$$P(\eta_a > \xi) = \frac{N_{\xi, -\xi}}{N_{0,0}} = \exp \left\{ -\frac{\xi^2}{m_0(1 - \rho_N)} \right\}. \quad (4.7)$$

Since the wave height is twice the amplitude, the probability of a wave height exceeding the level ξ is given by

$$P(\eta_h > \xi) = \exp \left\{ -\frac{\xi^2}{4m_0(1 - \rho_N)} \right\}. \quad (4.8)$$

Thus, the Næss (1985) approach resulted in a Rayleigh distribution as given in Eq. (4.1), with

$$\bar{h} = (2(1 - \rho_N))^{1/2} (2m_0)^{1/2}. \quad (4.9)$$

The Longuet-Higgins (1980) model corresponds to $\rho_N = -0.711$, while calculation of the Draupner data gives $\rho_N = -0.689$.

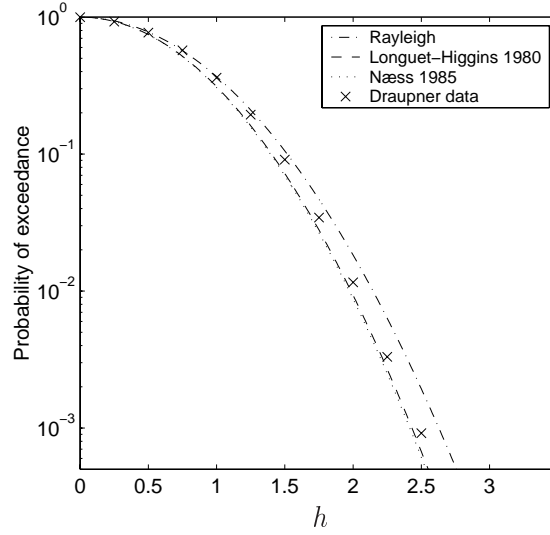


Figure 4.1: Probability of exceedance ($\rho_N = -0.689$, from Draupner data).

In the following, the wave heights will be normalized with respect to h_{rms} . With this notation the probability density function for the Næss model is given by

$$f_H(h) = \frac{4h}{1 - \rho_N} \exp \left\{ -\frac{2h^2}{1 - \rho_N} \right\}. \quad (4.10)$$

Figure 4.1 shows the difference between the Rayleigh distribution and the models proposed by Longuet-Higgins (1980) and Næss (1985). It is clear that the Rayleigh distribution predicts larger wave heights than the Longuet-Higgins (1980) and the Næss (1985) model. The two latter models give a quite similar result. Results from the Draupner field data are also included. The data fall between the Rayleigh distribution and the Næss (1985) model, but for larger values of h , the Næss (1985) model gives the best prediction of the data.

Vinje (1989) discussed these models, and compared the theoretical models with data from the Statfjord field in the North Sea. An asymptotic expansion of the Næss (1985) model was also presented.

The joint distribution function of two successive wave heights H_1 and H_2 is given by the two-dimensional Rayleigh distribution given in Eq. (3.4)

$$f_{H_1, H_2}(h_1, h_2) = \frac{4h_1 h_2}{1 - \kappa_h^2} \exp \left\{ -\frac{h_1^2 + h_2^2}{1 - \kappa_h^2} \right\} I_0 \left[\frac{2\kappa_h h_1 h_2}{1 - \kappa_h^2} \right]; \quad h_1 = \frac{\zeta_{h1}}{h_{\text{rms}}}, \quad h_2 = \frac{\zeta_{h2}}{h_{\text{rms}}}, \quad (4.11)$$

where κ_h is related to the correlation coefficient, ρ_h , between H_1 and H_2 by

$$\rho_h \equiv \rho_{H_1, H_2} = \frac{E(\kappa_h) - \frac{1}{2}(1 - \kappa_h^2)K(\kappa_h) - \frac{\pi}{4}}{1 - \frac{\pi}{4}}. \quad (4.12)$$

Note that this relationship is identical to the relationship between ρ_a and κ_a given by Eq. (3.6).

In the present notation the Næss (1985) model for two successive wave heights is given by

$$f_{H_1, H_2}(h_1, h_2) = \frac{16h_1h_2}{(1 - \kappa_h^2)(1 - \rho_N)^2} \exp \left\{ -\frac{2(h_1^2 + h_2^2)}{(1 - \kappa_h^2)(1 - \rho_N)} \right\} I_0 \left[\frac{4\kappa_h h_1 h_2}{(1 - \kappa_h^2)(1 - \rho_N)} \right]. \quad (4.13)$$

4.2 Gaussian distribution for successive wave heights using Nataf transformation

When using a marginal Rayleigh distribution or a Weibull distribution, extension to three dimensions and higher is not possible. Thus, a different approach must be used in order to derive a joint distribution function for more than two successive wave heights. The Gaussian distribution is often desirable due to its simple form in the multivariate case. This chapter discusses a method to transform the data to fit a Gaussian distribution.

4.2.1 Copulas

If the marginal distribution functions are known, then a joint distribution function can be constructed by using copulas. An introduction and overview of the subject is given in Nelsen (1999). It was Sklar who first introduced the term copula in 1959. However, earlier Fréchet (1957) among others had made important contributions to the subject. A historical development can be found in Schweizer (1991).

The basic theory of copulas is given below.

Theorem 1 (Sklar's Theorem)

Let X and Y be random variables with distribution functions F_X and F_Y , respectively, and joint distribution function $F_{X,Y}$. Then there exists a copula C such that

$$F_{X,Y}(x, y) = C(F_X(x), F_Y(y)). \quad (4.14)$$

If F_X and F_Y are continuous, then C is unique. Otherwise, C is uniquely determined on $\text{range}(F_X) \times \text{range}(F_Y)$.

Conversely, if C is a copula and F_X and F_Y are distribution functions, then the function $F_{X,Y}$ defined by Eq. (4.14) is a joint distribution function with margins F_X and F_Y .

The results can be extended to the multivariate case.

Theorem 2 (Sklar's Theorem in p dimensions)

Let X_1, X_2, \dots, X_p be random variables with distribution functions $F_{X_1}, F_{X_2}, \dots, F_{X_p}$, respectively, and joint distribution function F_{X_1, X_2, \dots, X_p} . Then there exists a p -dimensional copula C such that

$$F_{X_1, X_2, \dots, X_p}(x_1, \dots, x_p) = C(F_{X_1}(x_1), F_{X_2}(x_2), \dots, F_{X_p}(x_p)). \quad (4.15)$$

If $F_{X_1}, F_{X_2}, \dots, F_{X_p}$ are all continuous, C is unique. Otherwise, C is uniquely determined on $\text{range}(F_{X_1}) \times \text{range}(F_{X_2}) \times \dots \times \text{range}(F_{X_p})$.

Conversely, if C is a p -dimensional copula and $F_{X_1}, F_{X_2}, \dots, F_{X_p}$ are distribution functions, then the function F_{X_1, X_2, \dots, X_p} defined by Eq. (4.15) is a p -dimensional distribution function with margins $F_{X_1}, F_{X_2}, \dots, F_{X_p}$.

There are several methods to construct copulas. A straight forward method is the inversion method. Due to the fact that a marginal distribution function does not need to be strictly increasing, a definition of a quasi-inverse is needed.

Definition 1

Let F_X be a distribution function. Then a quasi-inverse of F_X is any function $F_X^{(-1)}$ with domain $[0, 1]$ such that

1. if t is in $\text{range}(F_X)$, then $F_X^{(-1)}(t)$ is any number x in \mathbb{R} such that

$$F_X(F_X^{(-1)}(t)) = t \quad (4.16)$$

2. if t is not in $\text{range}(F_X)$, then

$$F_X^{(-1)}(t) = \inf \{x | F_X(x) \geq t\} = \sup \{x | F_X(x) \leq t\} \quad (4.17)$$

If F_X is strictly increasing, then the quasi-inverse is unique, and is denoted F_X^{-1} .

The copula can be determined from

$$C(u_1, u_2, \dots, u_p) = F_{X_1, X_2, \dots, X_p}(F_{X_1}^{(-1)}(u_1), F_{X_2}^{(-1)}(u_2), \dots, F_{X_p}^{(-1)}(u_p)), \quad (4.18)$$

for any u_i in $[0, 1]$, $i = 1, \dots, p$.

4.2.2 Nataf model for successive wave heights

The Gaussian distribution is often preferable in the multivariate case. The analytical expression for the multivariate distribution allows to calculate exact statistical quantities of interest. The use of standard Gaussian distributions for the marginal distributions is often referred to as the Nataf model (see e.g. Liu and Der Kiureghian, 1986), although Nataf (1962) only described the general use of copulas.

The method of constructing a joint distribution function for the wave heights will first be shown in the bivariate case, and the extension to the multivariate case is trivial. A two-dimensional Gaussian copula is given by

$$C(u_1, u_2) = \Phi(\Phi^{-1}(u_1), \Phi^{-1}(u_2)), \quad (4.19)$$

where the standard Gaussian distribution is given by

$$\begin{aligned} \Phi(z) &= \frac{1}{\sqrt{2\pi}} \int_{-\infty}^z e^{-\frac{1}{2}t^2} dt \\ &= \frac{1}{2} \left[1 + \operatorname{erf}\left(\frac{z}{\sqrt{2}}\right) \right], \end{aligned} \quad (4.20)$$

and $\operatorname{erf}[\]$ is the error function (see Appendix F). The inverse of $\Phi(z)$ is given by

$$\Phi^{-1}(u_Z) = \sqrt{2} \operatorname{erf}^{-1}[2u_Z - 1], \quad (4.21)$$

where the random variable $U_Z = \Phi(Z)$ is uniformly distributed on $[0,1]$.

The two-dimensional distribution function of two successive wave heights H_1 and H_2 is then given by (from Eq. (4.14))

$$\begin{aligned} F_{H_1, H_2}(h_1, h_2) &= C(F_{H_1}(h_1), F_{H_2}(h_2)) \\ &= \Phi(\Phi^{-1}[F_{H_1}(h_1)], \Phi^{-1}[F_{H_2}(h_2)]), \end{aligned} \quad (4.22)$$

where the initial distributions F_{H_1} and F_{H_2} are optional.

Two different models will be presented here as initial distributions. First, the Næss (1985) model

$$F_H(h) = 1 - \exp\left\{-\frac{2h^2}{1 - \rho_N}\right\} \quad (4.23)$$

is selected to estimate the marginal probability distribution of the wave heights. Second, to improve the transformation of the data to fit the Gaussian distribution, a two-parameter Weibull distribution of the form

$$F_H(h) = 1 - \exp\left\{-\left(\frac{h}{\alpha}\right)^\beta\right\} \quad (4.24)$$

will be used. One should note that the Weibull distribution is more flexible to fit the data than the Næss (1985) model with only one parameter. The Weibull parameters α and β are found from maximum likelihood estimation.

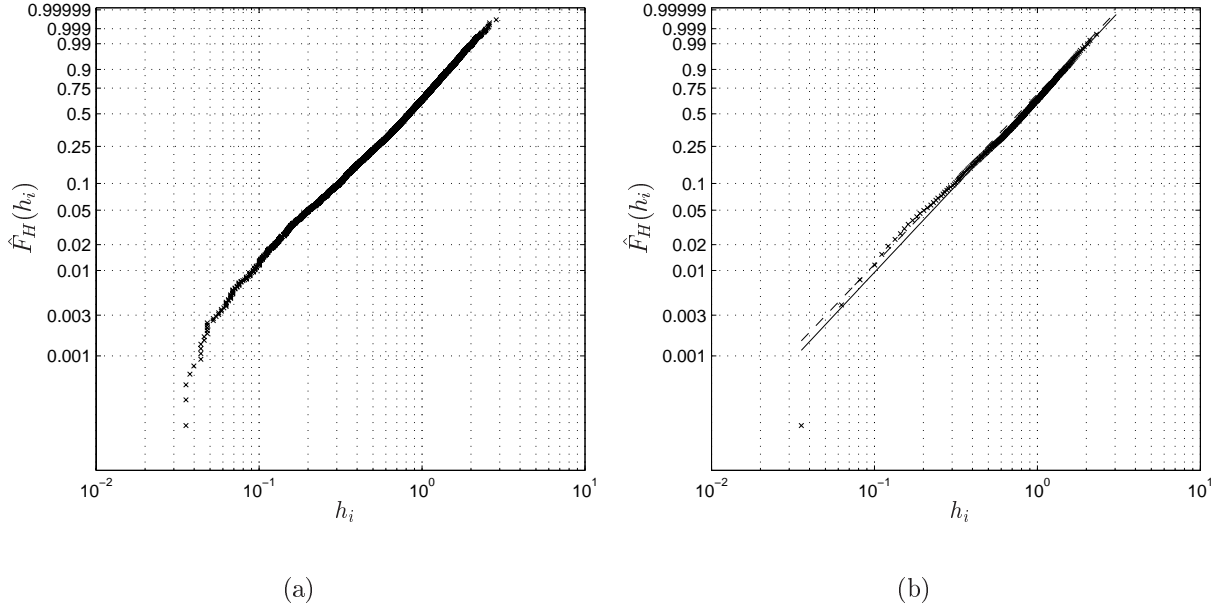


Figure 4.2: Weibull probability plot of wave height data from the Draupner field. \times data; $--$ Næss (1985) model with $\rho_N = -0.689$; $—$ fitted Weibull distribution with $\alpha = 0.978$, $\beta = 2.039$.

Figure 4.2 (a) shows a Weibull probability plot of the normalized wave heights from the Draupner field. The same data are shown in Fig. 4.2 (b), but here only every 25th data point is shown in order to illustrate where the largest amount of data is. Both the Næss (1985) model and the two-parameter Weibull distribution with $\alpha = 0.978$ and $\beta = 2.039$ are included.

Figure 4.3 (a) shows the probability density functions for the Næss (1985) model, the Weibull distribution and the Rayleigh distribution compared with data from the Draupner field. The probability of exceedance is shown in Fig. 4.3 (b). The Næss (1985) model overpredicts the peak of the density function, while the Rayleigh distribution overpredicts the data for larger values of h . The figure shows that the Weibull distribution agrees better with the data in the range $h \approx 0.5 - 2$, where the largest concentration of data points is located.

The random variable $U_H = F_H(h)$ is uniformly distributed on $[0,1]$. By using the Næss (1985) model as the initial distribution and defining $\Psi_H^N(h) = \Phi^{-1}(u_H)$, the resulting transformation is found from Eq. (4.21)

$$\Psi_H^N(h) = \sqrt{2} \operatorname{erf}^{-1} \left[2 \left(1 - \exp \left\{ -\frac{2h^2}{1 - \rho_N} \right\} \right) - 1 \right]. \quad (4.25)$$

The two-dimensional distribution function of H_1 and H_2 is found from Eq. (4.22)

$$F_{H_1, H_2}(h_1, h_2) = \Phi \left(\Psi_H^N(h_1), \Psi_H^N(h_2) \right), \quad (4.26)$$

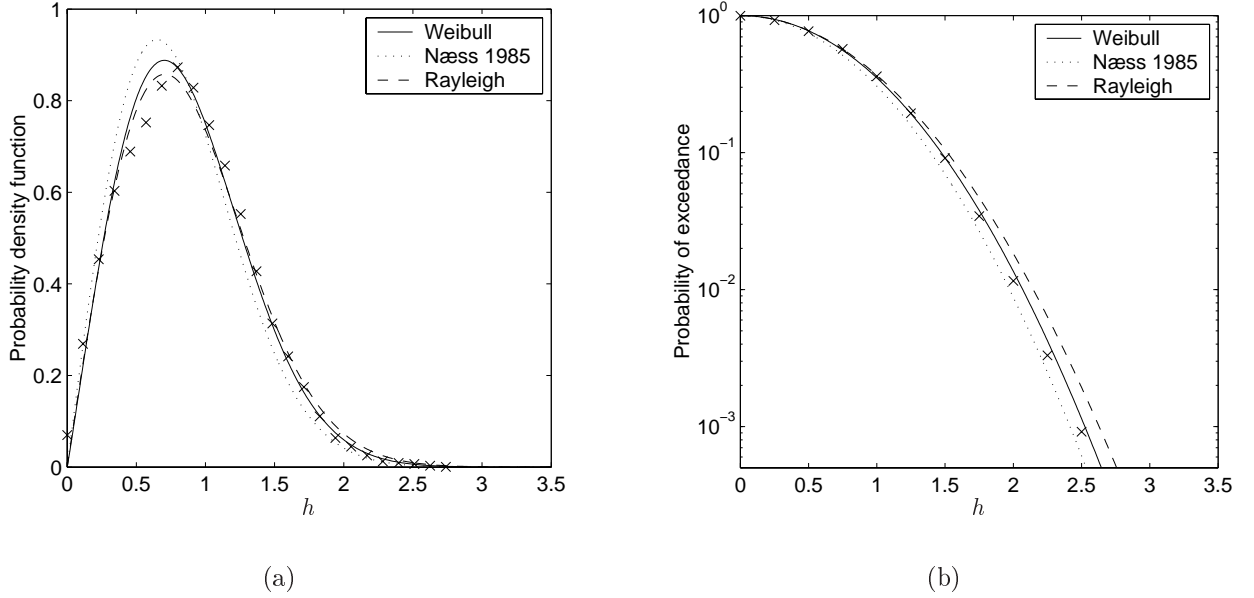


Figure 4.3: (a) Probability density function and (b) probability of exceedance for wave heights. \times data from Draupner field ($\alpha = 0.978$, $\beta = 2.039$, $\rho_N = -0.689$).

and the probability density function of H_1 and H_2 is then given by

$$f_{H_1, H_2}(h_1, h_2) = \frac{\Psi_H^{N'}(h_1) \Psi_H^{N'}(h_2)}{2\pi \sqrt{1 - \rho_{N,12}^2}} \times \exp \left\{ -\frac{1}{2(1 - \rho_{N,12}^2)} (\Psi_H^N(h_1)^2 + \Psi_H^N(h_2)^2 - 2\rho_{N,12} \Psi_H^N(h_1) \Psi_H^N(h_2)) \right\}, \quad (4.27)$$

where $\rho_{N,12}$ is the correlation coefficient between $\Psi_H^N(h_1)$ and $\Psi_H^N(h_2)$. The derivative of Ψ_H^N is found by using the properties of the error function (see Appendix F)

$$\Psi_H^{N'}(h) = \frac{4\sqrt{2\pi}h}{1 - \rho_N} \exp \left\{ \left(\operatorname{erf}^{-1} \left[1 - 2 \exp \left\{ -\frac{2h^2}{1 - \rho_N} \right\} \right] \right)^2 - \frac{2h^2}{1 - \rho_N} \right\}. \quad (4.28)$$

Next, the Weibull distribution will be used as the initial distribution. Defining $\Psi_H^W(h) = \Phi^{-1}(u_H)$ with $U_H = F_H(h)$ from Eq. (4.24), it follows from Eq. (4.21) that the transformation is

$$\Psi_H^W(h) = \sqrt{2} \operatorname{erf}^{-1} \left[2 \left(1 - \exp \left\{ -\left(\frac{h}{\alpha} \right)^\beta \right\} \right) - 1 \right], \quad (4.29)$$

with the derivative (see Appendix F)

$$\Psi_H^{W'}(h) = \sqrt{2\pi} \frac{\beta h^{\beta-1}}{\alpha^\beta} \exp \left\{ \left(\operatorname{erf}^{-1} \left[1 - 2 \exp \left\{ -\left(\frac{h}{\alpha} \right)^\beta \right\} \right] \right)^2 - \left(\frac{h}{\alpha} \right)^\beta \right\}. \quad (4.30)$$

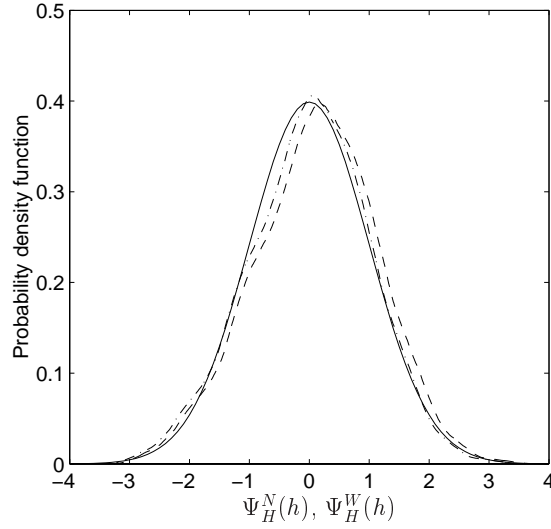


Figure 4.4: Probability density function of transformed wave height data; -- kernel density estimate of Ψ_H^N , -.- kernel density estimate of Ψ_H^W , — standard Gaussian density function. ($\alpha = 0.978$, $\beta = 2.039$, $\rho_N = -0.689$).

The two-dimensional probability density function of H_1 and H_2 will be the same as given in Eq. (4.27), with Ψ_H^W replacing Ψ_H^N and $\Psi_H^{W'}$ replacing $\Psi_H^{N'}$. The correlation coefficient $\rho_{N,12}$ must also be replaced with $\rho_{W,12}$, the correlation coefficient between $\Psi_H^W(h_1)$ and $\Psi_H^W(h_2)$.

The correlation coefficients of the transformed wave heights calculated from the Draupner field data are shown in Table 4.1. Note that the calculated values are almost identical, and they show that the dependency between the transformed wave heights decreases rapidly. The correlation coefficients of the normalized wave heights are also included for comparison. They are quite similar to the correlation coefficients of the transformed wave heights.

Figure 4.4 shows kernel density estimates of the transformed wave heights with both Ψ_H^N and Ψ_H^W compared with the standard Gaussian probability density function. The figure shows that both transformations yield an approximate standard Gaussian distribution. The transformation using the Weibull distribution as the initial distribution agrees best with the standard Gaussian distribution, while the transformation using the Næss (1985) model as the initial distribution is

Table 4.1: Correlation coefficients between $\Psi_H^N(h_1)$ and $\Psi_H^N(h_i)$ and between $\Psi_H^W(h_1)$ and $\Psi_H^W(h_i)$, and correlation coefficients of the normalized wave heights $\rho_{h,1i}$, $i = 2, 3, 4$, from Draupner data.

$\rho_{N,12}$	[-]	0.3889	$\rho_{W,12}$	[-]	0.3884	$\rho_{h,12}$	[-]	0.411
$\rho_{N,13}$	[-]	0.1164	$\rho_{W,13}$	[-]	0.1162	$\rho_{h,13}$	[-]	0.126
$\rho_{N,14}$	[-]	0.0577	$\rho_{W,14}$	[-]	0.0577	$\rho_{h,14}$	[-]	0.058

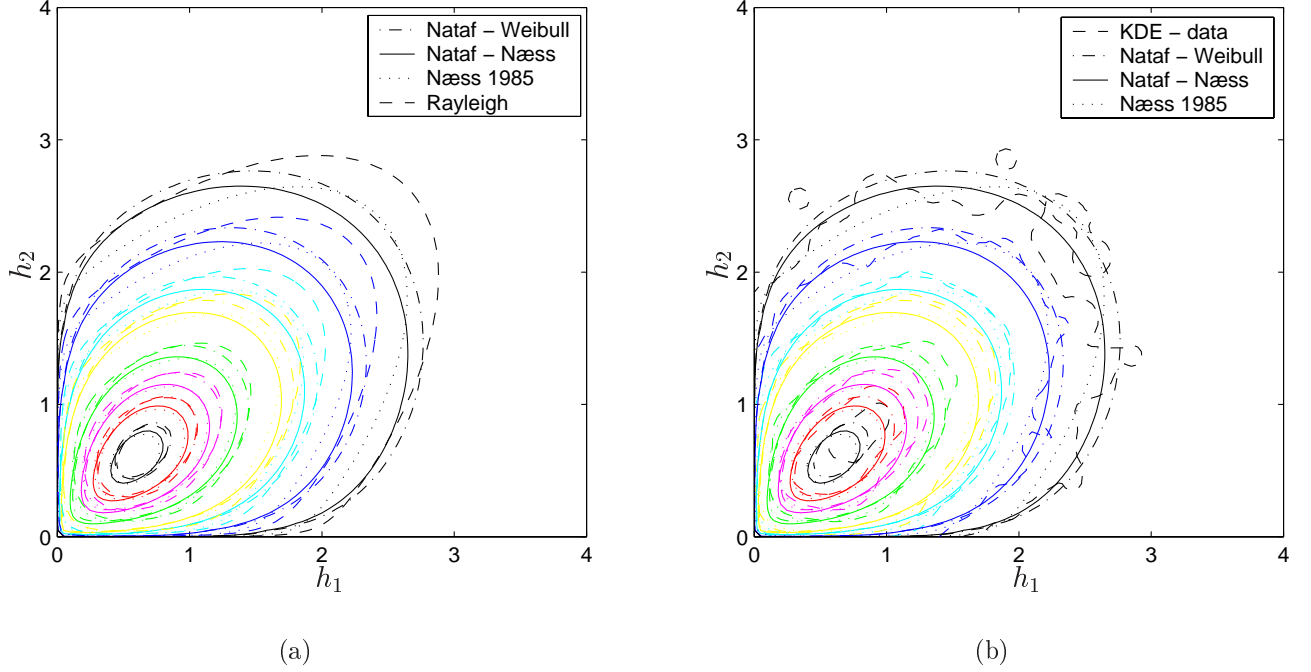


Figure 4.5: Contour plot of the two-dimensional probability density functions. The Nataf models and the Næss (1985) model are compared with (a) the Rayleigh distribution (b) kernel density estimate of the Draupner field data. Percent levels the given contour lines enclose are 10, 30, 50, 70, 90, 95, 99 and 99.9. ($\alpha = 0.978$, $\beta = 2.039$, $\rho_{W,12} = 0.388$, $\rho_N = -0.689$, $\rho_{N,12} = 0.389$, $\kappa_h^2 = 0.436$).

slightly skewed to the left ($\rho_3 < 0$).

Figure 4.5 (a) shows a contour plot of the two-dimensional Nataf model, both with using a Weibull distribution, denoted Nataf-Weibull, and the Næss (1985) model, denoted Nataf-Næss, as initial distributions. The distributions are compared with the Rayleigh distribution, given in Eq. (4.11) with $\kappa_h^2 = 0.436$, and the Næss (1985) model. The shape of the Nataf models are somewhat different from the Rayleigh distribution and the Næss (1985) model. For larger values of h the Nataf models have an almost circular shape, while the Næss (1985) model and the Rayleigh distribution have a more elliptic shape. Around the peaks, the distributions are quite similar. Along the diagonal ($h_1 = h_2$), the Nataf-Weibull model is close to the Rayleigh distribution for small values of h , but follows the Næss (1985) model for larger values of h . Outside the diagonal, the Nataf-Weibull model is closest to the Rayleigh distribution for all values of h . Along the diagonal the Nataf-Næss is close to the Næss (1985) model for small values for h , but it decreases more rapidly than the other models for larger values of h .

The Nataf models are compared with the kernel density estimate of the Draupner data in Fig. 4.5 (b). The Næss (1985) model is also included for comparison. For larger values of h , all models agree quite well with the data, but outside the diagonal, the Nataf models give a better prediction of the data. None of the distributions predict the peak of the data correctly, but the Nataf-Weibull model gives a slightly better prediction of the peak than the Nataf-Næss model. Overall, the Nataf-Weibull model gives the best agreement with the data.

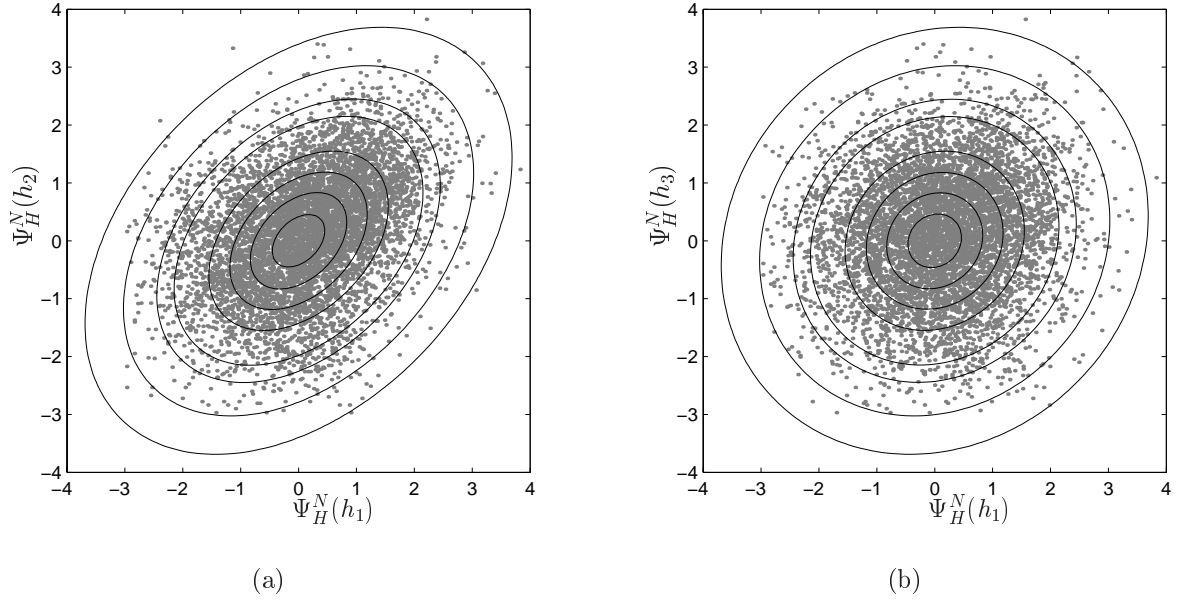


Figure 4.6: Paired plot of the transformed wave height Ψ_H^N between (a) h_1 and h_2 , (b) h_1 and h_3 , compared with a contour plot of a standard Gaussian distribution ($\rho_N = -0.689$, $\rho_{N,12} = 0.389$, $\rho_{N,13} = 0.116$). Percent levels the given contour lines enclose are 10, 30, 50, 70, 90, 95, 99 and 99.9.

When using copulas, the resulting joint distribution function always has correct marginals. However, the dependency structure should be examined by e.g. a paired plot. Figure 4.6 shows a paired plot of the transformed wave heights Ψ_H^N between (a) h_1 and h_2 and (b) h_1 and h_3 . The solid line is a contour plot of a standard Gaussian distribution. The figure shows that the dependency structure is quite similar to the one for a standard Gaussian distribution, and thus indicates that the transformation correctly takes care of the dependency structure. A paired plot of the transformed wave heights Ψ_H^W is shown in Fig. 4.7 (a) between h_1 and h_2 and (b) between h_1 and h_3 . Here also the dependency structure is quite similar to the one for a standard Gaussian distribution.

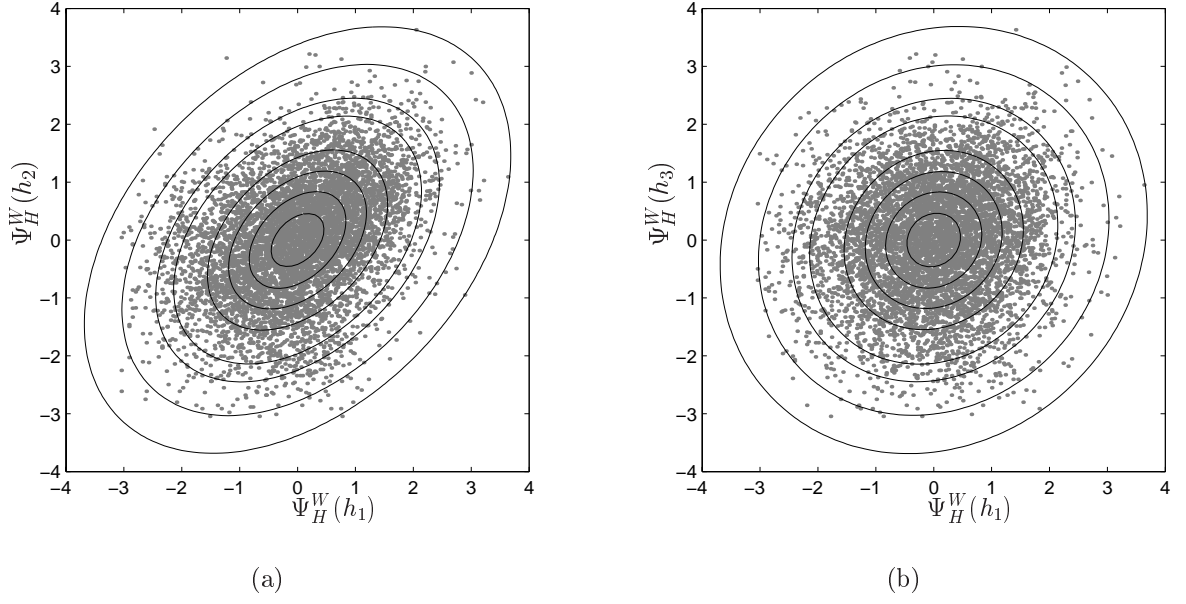


Figure 4.7: Paired plot of the transformed wave height Ψ_H^W between (a) h_1 and h_2 , (b) h_1 and h_3 , compared with a contour plot of a standard Gaussian distribution ($\alpha = 0.978$, $\beta = 2.039$, $\rho_{W,12} = 0.388$, $\rho_{W,13} = 0.116$). Percent levels the given contour lines enclose are 10, 30, 50, 70, 90, 95, 99 and 99.9.

In the following only the Nataf-Weibull model will be considered.

The extension to the multivariate case is now trivial, and the probability density function of $\mathbf{H} = [H_1, \dots, H_p]^T$ is given by

$$f_{\mathbf{H}}(\mathbf{h}) = \frac{\prod_{i=1}^p \Psi_H^{W'}(h_i)}{(2\pi)^{p/2} |\Sigma|^{1/2}} \exp \left\{ -\frac{1}{2} \Psi_H^W(\mathbf{h})^T \Sigma^{-1} \Psi_H^W(\mathbf{h}) \right\}, \quad (4.31)$$

where the covariance matrix, Σ , is given by

$$\Sigma = \begin{bmatrix} 1 & \rho_{W,12} & \cdots & \rho_{W,1p} \\ \rho_{W,12} & 1 & \cdots & \rho_{W,2p} \\ \vdots & & \ddots & \vdots \\ \rho_{W,1p} & \cdots & \cdots & 1 \end{bmatrix}. \quad (4.32)$$

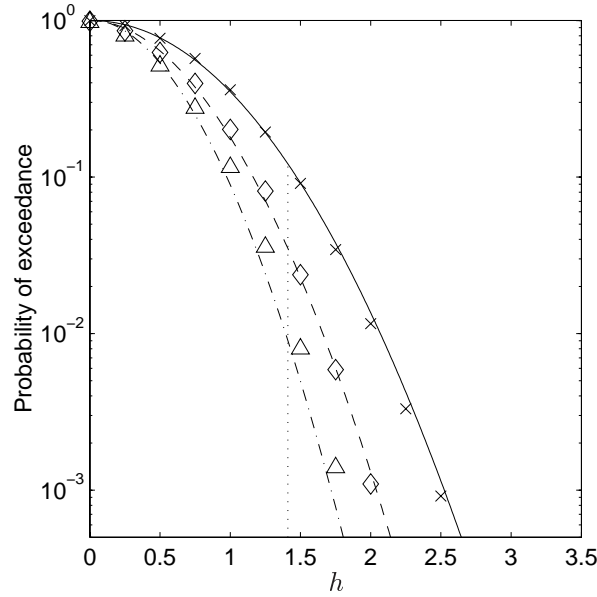


Figure 4.8: Probability of exceedance for normalized wave heights. $P(H_1 > h)$: — Nataf-Weibull model; \times data; $P(H_1 > h, H_2 > h)$: -- Nataf-Weibull model; \diamond data; $P(H_1 > h, H_2 > h, H_3 > h)$: - · - Nataf-Weibull model; \triangle data. The dotted line indicates the normalized significant wave height of 1.41. ($\alpha = 0.978$, $\beta = 2.039$, $\rho_{W,12} = 0.388$, $\rho_{W,13} = 0.116$ from Draupner field data).

Figure 4.8 shows the Nataf-Weibull model in Eq. (4.31) in terms of probability of exceedance for $p = 1, 2, 3$. The results are compared with data from the Draupner field. From the figure it is clear that the probability of p successive wave heights exceeding a value h decreases when p increases. The Nataf-Weibull model agrees quite well with the data for all values of p shown in the figure.

Thus, by using the Nataf transformation, the probability distribution for two and three successive wave heights can be modeled by a transformed multivariate Gaussian distribution. The transformed Gaussian distribution can also be applied for more than three successive wave heights, but then the dependency structure should be further examined by e.g. paired plots.

Another quantity of interest is the expected value of a wave height given the previous wave height. This is given by

$$E[H_2 | H_1 = h_1] = \int_0^\infty h_2 f_{H_2 | H_1}(h_2 | h_1) dh_2, \quad (4.33)$$

where the conditional probability density function $f_{H_2 | H_1}(h_2 | h_1)$ is found from Bayes rule in Eq. (3.53).

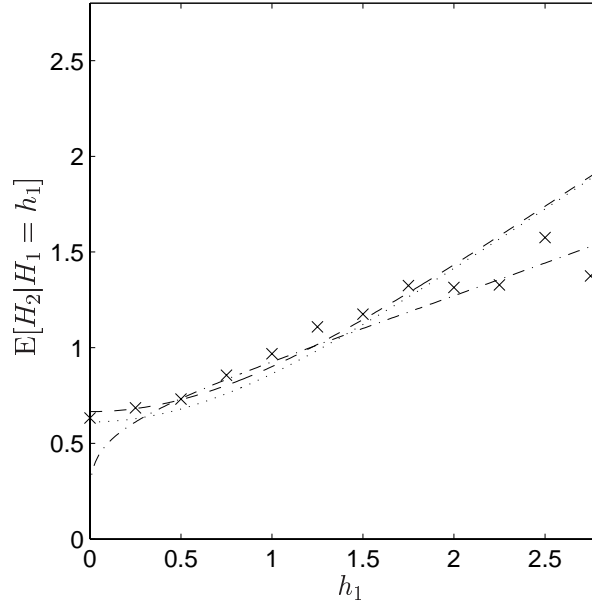


Figure 4.9: Conditional expectation of the wave height given the previous wave height. $-\cdot-$ Nataf-Weibull model; $-$ Næss (1985) model; \cdots Rayleigh distribution; \times data ($\alpha = 0.978$, $\beta = 2.039$, $\rho_{W,12} = 0.388$, $\rho_N = -0.689$ from Draupner field data).

Figure 4.9 shows the conditional expectation $E[H_2|H_1 = h_1]$ versus h_1 . The Nataf-Weibull model is compared with the Næss (1985) model and the Rayleigh distribution. Data from the Draupner field are also included. The variation in the data points is large, but overall the Nataf-Weibull model gives the best agreement with the data for large values of h_1 , while the Næss (1985) model gives the best agreement with the data for small values of h_1 .

In addition it can be of interest to calculate the probability of exceedance of the wave height given that the previous wave heights exceeded a given level, e.g. h_{rms} or H_S . The conditional probability of exceedance given that the two previous wave heights exceeded \tilde{h} is given by

$$\begin{aligned} P(H_3 > h_3 | H_2 > \tilde{h} \cap H_1 > \tilde{h}) &= \frac{P(H_1 > \tilde{h} \cap H_2 > \tilde{h} \cap H_3 > h_3)}{P(H_1 > \tilde{h} \cap H_2 > \tilde{h})} \\ &= \frac{\int_{h_3}^{\infty} \int_{\tilde{h}}^{\infty} \int_{\tilde{h}}^{\infty} f_{H_1, H_2, H_3}(h_1, h_2, \tilde{h}_3) dh_1 dh_2 d\tilde{h}_3}{\int_{\tilde{h}}^{\infty} \int_{\tilde{h}}^{\infty} f_{H_1, H_2}(h_1, h_2) dh_1 dh_2}. \end{aligned} \quad (4.34)$$

This is calculated by integration of the transformed Gaussian distribution in Eq. (4.31).

4.3 Successive wave heights modeled as a first order autoregressive (AR(1)) model

In this chapter another approach for modeling wave heights is shown by considering the successive wave heights as a time series. The theory is first presented by considering a general time series $X(t)$.

There are two useful representations of a time series $X(t)$. One is to use an autoregressive (AR) representation. The other is a moving average (MA) representation, which will not be discussed further in this thesis. It is also possible to have a combination of the two representations. The analysis of AR and MA processes are thoroughly described in Wei (1990).

In an AR representation, the value of X at time t is dependent on the values of its own past, plus a random variable. An AR process of order r of a time series with zero mean can be written

$$X(t) = \pi_1 X(t-1) + \dots + \pi_r X(t-r) + \epsilon(t), \quad (4.35)$$

where π_1, \dots, π_r are weights and $\epsilon(t)$ is a zero mean Gaussian white noise process. If a process with mean value different from zero is desired, this can be added afterwards. The weights can be related to the autocorrelations, ρ_j , and partial autocorrelations, ϕ_{jj} .

In addition to the mean and variance, a stationary time series is also characterized by ρ_j and ϕ_{jj} . The autocorrelation function (ACF) measures the correlation between $X(t)$ and $X(t+j)$ as

$$\rho_j = \frac{\text{Cov}[X(t), X(t+j)]}{\sqrt{\text{Var}[X(t)]} \sqrt{\text{Var}[X(t+j)]}}, \quad (4.36)$$

and can be estimated from data by

$$\hat{\rho}_j = \frac{\sum_{i=1}^{n-j} (x_i - \bar{\mathbf{x}})(x_{i+j} - \bar{\mathbf{x}})}{\sum_{i=1}^n (x_i - \bar{\mathbf{x}})^2}. \quad (4.37)$$

The partial autocorrelation function (PACF) measures the correlation between $X(t)$ and $X(t+j)$ after their mutual linear dependency on the intervening variables $X(t+1), \dots, X(t+j-1)$ has been removed, i.e., the conditional correlation

$$\text{Corr}[X(t), X(t+j) | X(t+1), \dots, X(t+j-1)], \quad (4.38)$$

and is calculated by

$$\hat{\phi}_{j+1,j+1} = \frac{\hat{\rho}_{j+1} - \sum_{i=1}^j \hat{\phi}_{ji} \hat{\rho}_{j+1-i}}{1 - \sum_{i=1}^j \hat{\phi}_{ji} \hat{\rho}_i} \quad (4.39)$$

$$\hat{\phi}_{j+1,i} = \hat{\phi}_{ji} - \hat{\phi}_{j+1,j+1} \hat{\phi}_{j,j+1-i}, \quad i = 1, \dots, j. \quad (4.40)$$

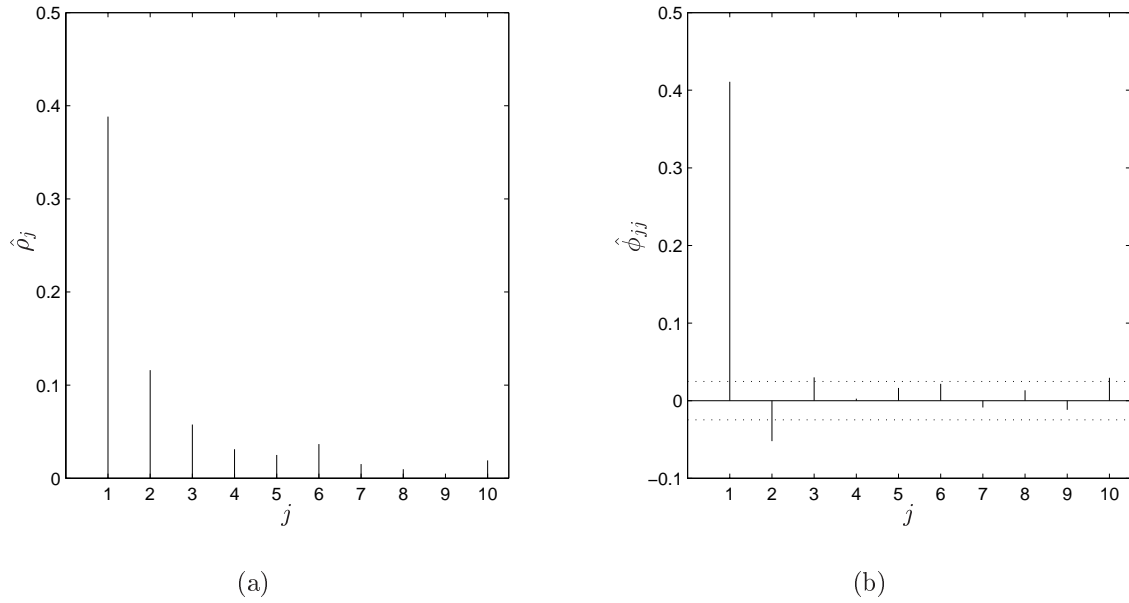


Figure 4.10: (a) Sample autocorrelation function, and (b) sample partial autocorrelation function of Ψ_H^W from Draupner data. The dotted line indicates $\pm 2(\text{Var}[\hat{\phi}_{jj}])^{1/2}$.

Under the hypothesis that the underlying process is a white noise series, the variance of $\hat{\phi}_{jj}$ can be approximated by

$$\text{Var}[\hat{\phi}_{jj}] \approx \frac{1}{n}. \quad (4.41)$$

Thus, π_1, \dots, π_r can be estimated from $\hat{\rho}_j$ and $\hat{\phi}_{j+1, j+1}$.

The first order autoregressive (AR(1)) process has the properties

$$\rho_j = \rho_1^j, \quad j \geq 1. \quad (4.42)$$

$$\phi_{jj} = \begin{cases} \rho_1 = \pi_1, & j = 1, \\ 0, & j \geq 2. \end{cases} \quad (4.43)$$

An AR(1) process has the Markov property

$$P(X(t+1) = x_{t+1} | X(0) = x_0, \dots, X(t) = x_t) = P(X(t+1) = x_{t+1} | X(t) = x_t). \quad (4.44)$$

Thus, the value of $X(t)$ is completely determined by the knowledge of $X(t-1)$. If the process can be written as an AR(1) process, then both simulations of the process and calculation of statistics are simplified.

The sample ACF and PACF of the transformed normalized wave heights Ψ_H^W from the Draupner data have been calculated, and the results are shown in Fig. 4.10 (a) and (b), respectively. The ACF decreases approximately exponentially. The PACF has one spike at $j = 1$, while the values

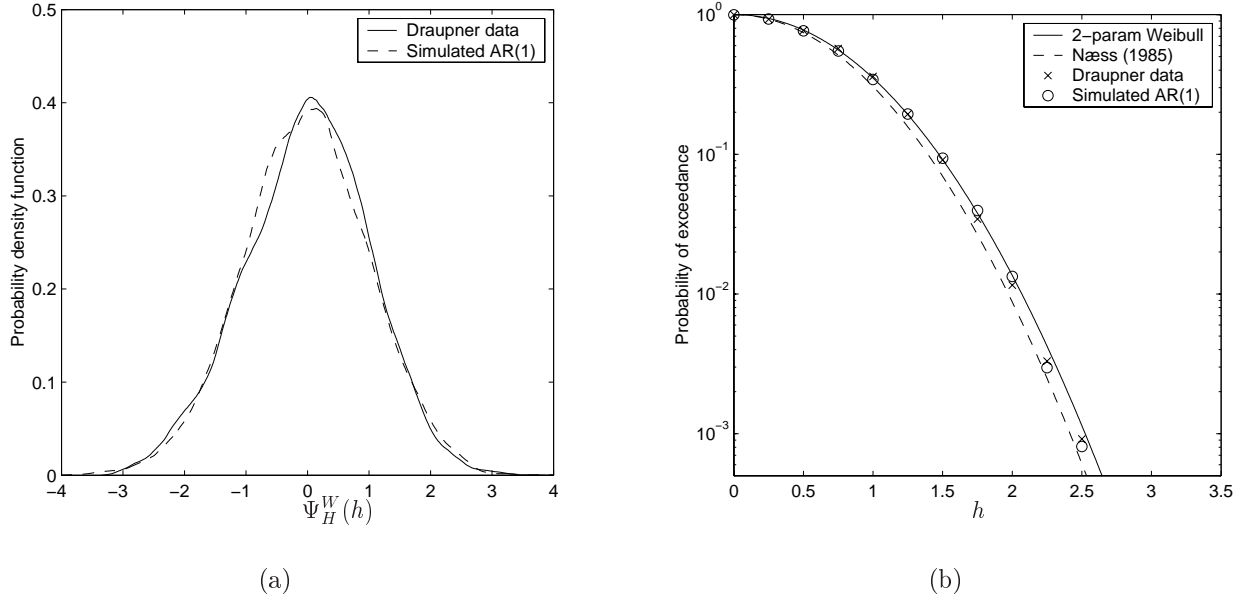


Figure 4.11: (a) Kernel density estimates of Ψ_H^W . (b) Probability of exceedance of normalized wave heights. ($\rho_1 = 0.388$, $\alpha = 0.978$, $\beta = 2.039$, $\rho_N = -0.689$).

for $j \geq 2$ are so small that they can be regarded as noise. This indicates that the process is an AR(1) process. A test to find if the process is an AR(1) process is discussed in Chapter 4.3.1.

Thus, the stochastic process of transformed successive wave heights can be written

$$\Psi_H^W(t) = \rho_1 \Psi_H^W(t-1) + \epsilon(t); \quad t = 1, 2, \dots, \quad (4.45)$$

where $\{\epsilon(t)\}$ are independent Gaussian distributed variables with zero mean and variance equal to $(1 - \rho_1^2)\text{Var}[\Psi_H^W] = 1 - \rho_1^2$. The initial value can be selected as e.g. the mean value, i.e., $\Psi_H^W(0) = 0$.

Simulations of 6400 transformed wave heights were made using the correlation coefficient $\rho_1 = \rho_{W,12}$. Figure 4.11 (a) shows the kernel density estimate of the simulated data compared with the kernel density estimate from the transformed Draupner data. The results from the simulation of an AR(1) process compare well with the transformed Draupner data.

The normalized wave height can be found from the simulated process Ψ_H^W by inverting the transformation given in Eq. (4.29), which gives

$$H = \alpha \left(-\ln \left[\frac{1}{2} \left(1 - \text{erf} \left[\frac{1}{\sqrt{2}} \Psi_H^W(h) \right] \right) \right] \right)^{1/\beta}. \quad (4.46)$$

Figure 4.11 (b) shows the probability of exceedance of the normalized wave heights from the Draupner data and the wave heights from the simulated AR(1) model, found by Eq. (4.46). The

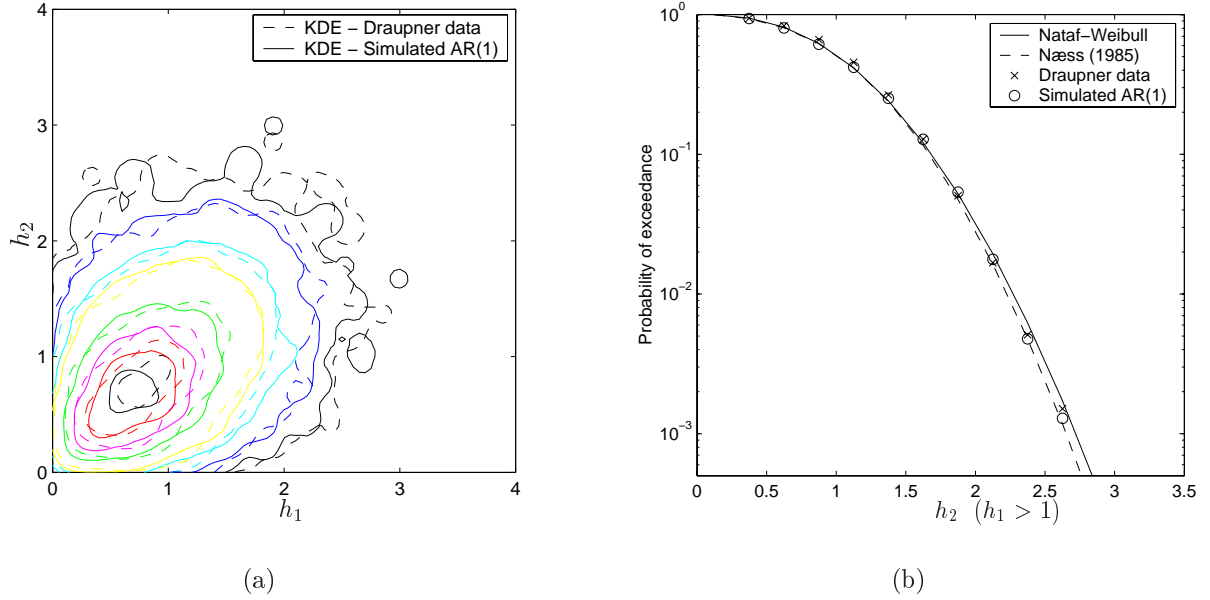


Figure 4.12: (a) Contour plot of the two-dimensional kernel density estimates. Percent levels the given contour lines enclose are 10, 30, 50, 70, 90, 95, 99 and 99.9. (b) Probability of exceedance given $h_1 > 1$ ($P(H_2 > h_2 | H_1 > h_1)$). ($\alpha = 0.978$, $\beta = 2.039$, $\rho_{W,12} = 0.388$, $\rho_N = -0.689$, $\kappa_h^2 = 0.436$).

two-parameter Weibull distribution and the Næss (1985) distribution are included for comparison. The figure shows good agreement between the Draupner data and the simulated data.

Figure 4.12 (a) shows a contour plot of the two-dimensional kernel density estimate of the Draupner data and the simulated data from the AR(1) model. The simulated data compare well with the Draupner data, which indicates that the AR(1) model retains the dependency structure. This is also shown in Fig. 4.12 (b), where the conditional probability of exceedance of h_2 is calculated, given that h_1 exceeded the rms-value, i.e., $h_1 > 1$.

4.3.1 Likelihood ratio test

In order to test if the process is an AR(1) process, a likelihood ratio test can be performed. The hypothesis that must be tested is whether the correlation coefficients are given by Eq. (4.42), i.e., if the covariance matrix has the structure

$$H_0 : \Sigma = \Sigma_0 = \begin{bmatrix} 1 & \rho & \cdots & \rho^{p-1} \\ \rho & 1 & \cdots & \rho^{p-2} \\ \vdots & & \ddots & \vdots \\ \rho^{p-1} & \rho^{p-2} & \cdots & \end{bmatrix}, \quad (4.47)$$

for a selected order p . Actually, p should be infinitely large in order to test if the process is a true AR(1) process. But, if it is of interest just to consider a given number of successive waves, then it is enough to select p as this number. The likelihood ratio statistic is given by

$$\Lambda = \frac{\max L(\Sigma_0)}{\max_{\Sigma} L(\Sigma)}, \quad (4.48)$$

where L is the likelihood function. When the sample size n is large, then $-2 \ln \Lambda$ is approximately chi-squared distributed with $p - 1$ degrees of freedom. The hypothesis is rejected at significance level α if the observed value $-2 \ln \Lambda_{obs} > \chi_{\alpha, p-1}^2$. If the hypothesis is rejected, the AR(1) process is a good approximation for the observed process at the given significance level.

When considering three successive waves, $p = 3$ is selected. The transformed variable Ψ_H^W is Gaussian distributed, and the likelihood function is given by

$$L(\Sigma) = \prod_{i=1}^n f_{\Psi_H^W}(\Psi_H^W(\mathbf{h}_i)) = \frac{1}{(2\pi)^{3n/2} |\Sigma|^{n/2}} \exp \left\{ -\frac{1}{2} \sum_{i=1}^n \Psi_H^W(\mathbf{h}_i)^T \Sigma^{-1} \Psi_H^W(\mathbf{h}_i) \right\}. \quad (4.49)$$

The maximum of the likelihood function when Σ is varied over its possible value is

$$\max_{\Sigma} L(\Sigma) = \frac{1}{(2\pi)^{3n/2} |\hat{\Sigma}|^{n/2}} e^{-3n/2}, \quad (4.50)$$

where

$$\hat{\Sigma} = \frac{1}{n} \sum_{i=1}^n (\Psi_H^W(\mathbf{h}_i) - \bar{\Psi}_H^W(\mathbf{h})) (\Psi_H^W(\mathbf{h}_i) - \bar{\Psi}_H^W(\mathbf{h}))^T. \quad (4.51)$$

Let $\hat{\Sigma}_0$ be the covariance matrix that maximizes $L(\Sigma_0)$. This is found numerically. Then the likelihood ratio statistic is given by

$$\Lambda = \frac{\max L(\Sigma_0)}{\max_{\Sigma} L(\Sigma)} = \left(\frac{|\hat{\Sigma}|}{|\hat{\Sigma}_0|} \right)^{\frac{n}{2}} \exp \left\{ \frac{3n}{2} - \frac{1}{2} \sum_{i=1}^n \Psi_H^W(\mathbf{h}_i)^T \hat{\Sigma}_0^{-1} \Psi_H^W(\mathbf{h}_i) \right\}. \quad (4.52)$$

See Johnson and Wichern (1992) for further details.

There was no overlapping of the data when constructing the triplets of wave height observations from the Draupner field. The resulting sample size was $n = 2189$ and the test result was $-2 \ln \Lambda_{obs} = 6.62$. From tables $\chi^2_{0.036,2} = 6.65$, which means that the hypothesis would not be rejected at 3.6% significance level.

4.3.2 Summary of AR(1) model

The results from the likelihood ratio test together with the sample ACF and PACF show that the wave heights from the Draupner field can be modeled as an AR(1) model. This gives two favorable results. First, the simulation of successive wave heights can be done from Eqs. (4.45) and (4.46). This is a simple and fast simulation technique. Second, the distribution of the wave height given the previous wave height is independent of the wave heights prior to the previous wave height (as in Eq. (4.44)). Thus, only a two-dimensional distribution is needed when calculating the conditional statistical properties. In practice the previous wave must be given as a small interval rather than a specific value, since this is a continuous distribution,

Figure 4.13 shows the conditional probability of h_3 in terms of probability of exceedance. The figure shows results both from conditioning on the two previous wave heights, h_1 and h_2 , being in an interval $[\tilde{h}_1, \tilde{h}_2]$ calculated from the three-dimensional distribution, and from conditioning on only the previous wave height, h_2 , being in an interval $[\tilde{h}_1, \tilde{h}_2]$ calculated from the two-dimensional distribution. The results are compared with data from the Draupner field. Here N denotes the number of field data cases in each class of h_2 . The figure shows that the results from the two-dimensional distribution are quite similar to the results from the three-dimensional distribution. This validates the hypothesis that the distribution of the wave height given the previous wave height is independent of the wave heights prior to the previous wave height. The models agree quite well with the data.

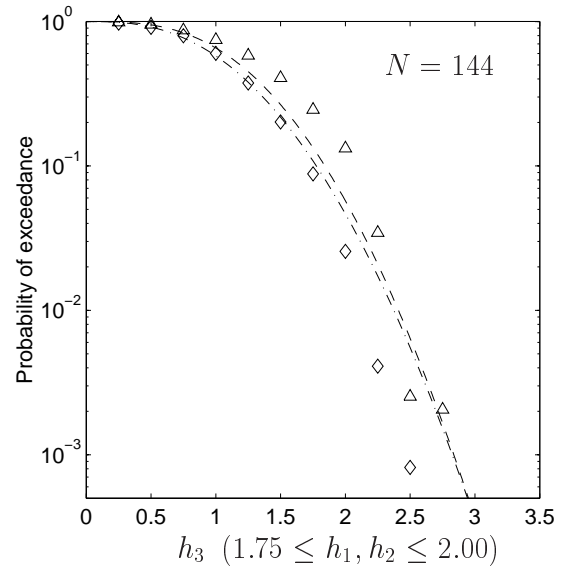
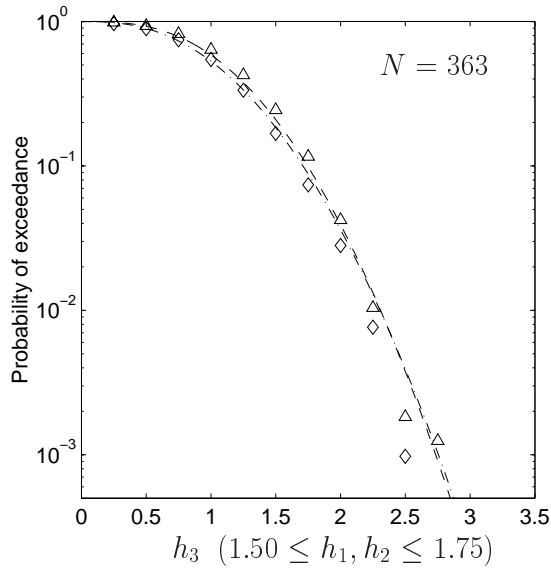
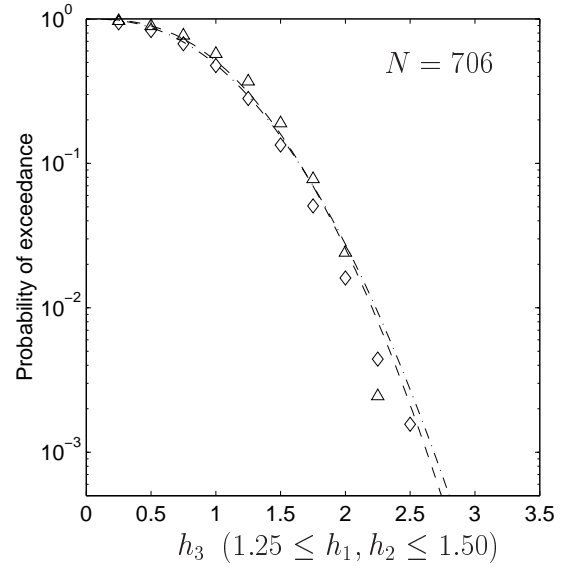
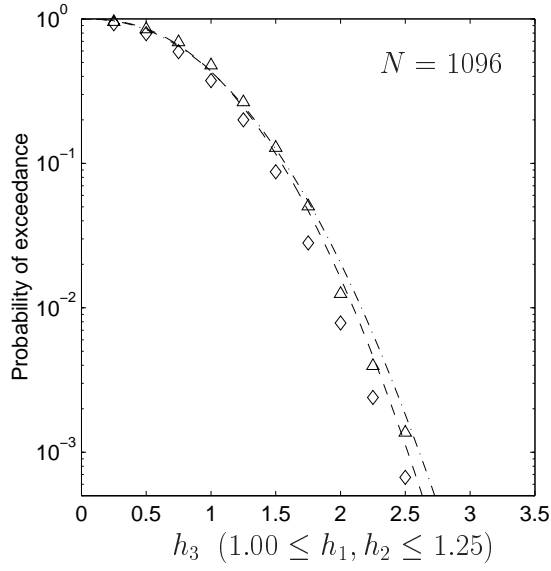


Figure 4.13: Conditional probability of exceedance of normalized wave height.
 $P(H_3 > h | \tilde{h}_1 \leq H_2 \leq \tilde{h}_2)$: -- Nataf-Weibull model; \diamond data;
 $P(H_3 > h | \tilde{h}_1 \leq H_2 \leq \tilde{h}_2, \tilde{h}_1 \leq H_1 \leq \tilde{h}_2)$: - · - Nataf-Weibull model; \triangle data.
 ($\alpha = 0.978$, $\beta = 2.039$, $\rho_{W,12} = 0.388$, $\rho_{W,13} = 0.116$ from Draupner field data).

CHAPTER 5

Joint probability distributions for successive wave periods

5.1 Marginal distributions for wave periods

Several distribution functions for the wave period, τ , have been suggested. Some of the most commonly used distributions are presented here, and they are used for comparison in the forthcoming.

The dimensionless wave period is given by $t = \tau/\bar{\tau}$, where the choice of normalizing factor, $\bar{\tau}$, varies. In the following, the wave periods will be normalized with respect to $\bar{\tau} = T_{m01}$.

Bretschneider (1959) derived a distribution for the wave period based on the distribution for the wave length. The wave length, λ_w , was assumed to be Rayleigh distributed, which was supported by comparison with data. Then by assuming that the wave length was proportional by the square of the wave period, as suggested by the dispersion relationship for linear waves in deep water ($\tau^2 = (2\pi/g)\lambda_w$), it followed that the square of the wave period was Rayleigh distributed. The normalizing factor was given as the square-root of the rms-value of τ^2 , i.e., $\bar{\tau}^2 = \zeta^2 \equiv (\tau^2)_{\text{rms}}$. In terms of the non-dimensional wave period $t = \tau/T_{m01}$, the probability density function is given by

$$f_T(t) = 4 \left(\frac{T_{m01}}{\zeta} \right)^4 t^3 \exp \left\{ - \left(\frac{T_{m01}}{\zeta} \right)^4 t^4 \right\}; \quad t \geq 0. \quad (5.1)$$

Longuet-Higgins (1975) applied a narrow-band approximation to linear theory of Gaussian noise to obtain the joint probability density function of the envelope amplitude, η_a , and the time

derivative of the envelope phase, $\dot{\psi}$, $f_{\eta_a, \dot{\psi}}(\eta_a, \dot{\psi})$. The probability density function of t was found from transformation of the marginal probability density function of $\dot{\psi}$. In the present notation the probability density function of T is given by

$$f_T(t) = \frac{1}{2\epsilon_2} \left[1 + \left(\frac{t-1}{\epsilon_2} \right)^2 \right]^{-3/2}, \quad (5.2)$$

where ϵ_2 is the spectral bandwidth parameter given by Eq. (2.13). One should note that the integral of this density function is only equal to one if negative values of t are included. The physical meaning of t , i.e., the period is always positive, indicates that a truncated version of Eq. (5.2) should be used, meaning that a normalizing factor should be included. This normalizing factor is the same as the one introduced in Longuet-Higgins (1983), given by

$$\frac{1}{2} \left(1 + (1 + \epsilon_2^2)^{-1/2} \right). \quad (5.3)$$

Longuet-Higgins (1983) used the joint density function $f_{\eta_a, \dot{\psi}}(\eta_a, \dot{\psi})$ directly to obtain the joint density function of the dimensionless wave amplitude, A , and wave period, T , by transformation of variables. A normalizing factor was introduced to take into account that the period is always positive. The marginal density function of T was found by integrating over the total domain of A , and is given by

$$f_T(t) = \frac{1}{\epsilon_2 [1 + (1 + \epsilon_2^2)^{-1/2}] t^2} \left[1 + \left(\frac{1 - \frac{1}{t}}{\epsilon_2} \right)^2 \right]^{-3/2}. \quad (5.4)$$

Cavanié et al. (1976) derived a joint density function of the wave height H and wave period T based on a narrow-band Gaussian model that accounted for the asymmetry in T . In the present notation this is given by

$$f_{H,T}(h, t) = \frac{\alpha_2^3 h^2 T_c^4}{4\sqrt{2\pi}\epsilon_4(1 - \epsilon_4^2)T_{m01}^4 t^5} \exp \left\{ -\frac{h^2 T_c^4}{8\epsilon_4^2 T_{m01}^4 t^4} \left[\left\{ \left(\frac{T_{m01}t}{T_c} \right)^2 - \alpha_2^2 \right\}^2 + \alpha_1^2 \alpha_2^4 \right] \right\}, \quad (5.5)$$

where ϵ_4 is the spectral bandwidth parameter given by Eq. (2.14) and

$$T_c = \frac{2\pi}{\alpha_2} \sqrt{\frac{m_2}{m_4}}, \quad \alpha_1^2 = \frac{\epsilon_4^2}{1 - \epsilon_4^2}, \quad \alpha_2 = \frac{1}{2} \left[1 + (1 - \epsilon_4^2)^{1/2} \right]. \quad (5.6)$$

By integration over the domain of H , the marginal density function of T is found as

$$f_T(t) = \frac{\alpha_2^3 \alpha_1^2 T_{m01}^2 t}{T_c^2} \left[\left\{ \left(\frac{T_{m01}t}{T_c} \right)^2 - \alpha_2^2 \right\}^2 + \alpha_1^2 \alpha_2^4 \right]^{-3/2}. \quad (5.7)$$

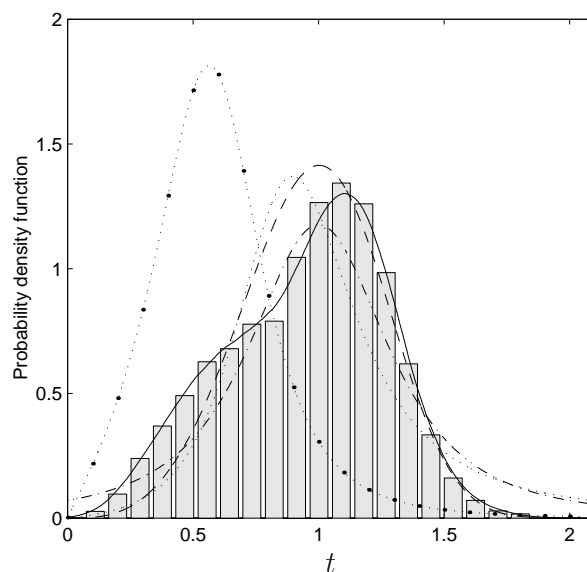


Figure 5.1: Probability density function of normalized wave periods. — kernel density estimate from Draupner data, -- Bretschneider (1959) model, -.- Longuet-Higgins (1975) model, ... Longuet-Higgins (1983) model, ··· Cavanié (1976) model. ($T_{m01} = 9.09$ s, $\zeta = 9.79$ s, $T_c = 5.80$ s, $\epsilon_2 = 0.425$, $\epsilon_4 = 0.847$, from Draupner data)

Figure 5.1 shows a histogram of the normalized wave periods from the Draupner data with the kernel density estimate. The different theoretical models are included. One should note that the shape of the data is not captured by any of the models. The value of t where the peak of the data occurs is also underestimated by all models. The Bretschneider (1959) model gives the best estimate for the largest wave periods, while the Longuet-Higgins (1975, 1983) models overpredict the large wave periods. It is clear that the Cavanié (1976) model gives a very poor estimate of the data. However, one should note that this model was only presented for combined wave height and wave period, and not for wave period alone. It is only included here for comparison.

Several comparisons between the given wave period distributions and field data have been made. Myrhaug and Rue (1993, 1998) presented field data measured at three different deep water locations on the Norwegian continental shelf; Utsira in the Central North Sea, Halten in the Norwegian Sea and Tromsøflaket in the Northern Norwegian Sea. The data included 6353 individual waves, and the data can be considered as belonging to the same statistical population. For a more thorough description of the data, see Myrhaug and Kjeldsen (1984). Data from Kjeldsen (1981) were also presented. The data included 3015 individual waves recorded in a single storm at Tromsøflaket.

Figure 5.2 shows a histogram of (a) the Myrhaug and Kjeldsen (1984) data and (b) the Kjeldsen (1981) data compared with the kernel density estimate of the Draupner field data. Note that the data are normalized with respect to ζ rather than T_{m01} , so the kernel density estimate of the Draupner data is different from Fig. 5.1. One should also note that the scale in (b) is different from (a) due to a few large observations. The Bretschneider (1959) model is also included for comparison. The Myrhaug and Kjeldsen (1984) data agree very well with the kernel density

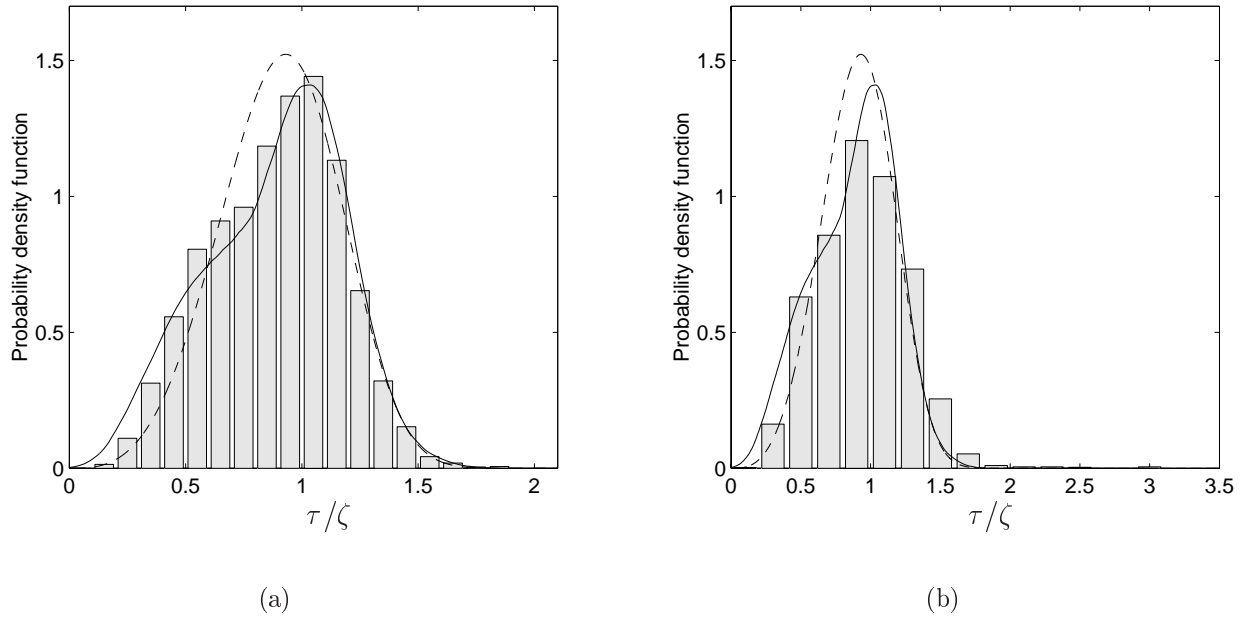


Figure 5.2: (a) Histogram of wave periods from Myrhaug and Kjeldsen (1984) and (b) histogram of wave periods from Kjeldsen (1981). — Kernel density estimate of Draupner data, - - Bretschneider (1959) model ($\zeta = 9.79$ s from Draupner data).

estimate of the Draupner field data, while the Kjeldsen (1981) data have a smaller peak and a wider spread in the data with a few large wave periods ($\tau/\zeta > 3$).

Figure 5.3 shows a Weibull plot of the Draupner field data, the Myrhaug and Kjeldsen (1984) data and the Kjeldsen (1981) data. The Bretschneider (1959) model and a Weibull distribution based on a best fit to the Draupner field data are included for comparison. Note that the Weibull parameters $\alpha = 0.982$ and $\beta = 3.422$ are based on the Draupner data normalized with respect to ζ . The figure clearly depicts the difference between the Kjeldsen (1981) data and the other two data sets, that is, the different behavior for smaller and higher periods in the Kjeldsen (1981) data. The same behavior is also shown in data from the Frigg field in the Central North Sea, which are discussed in Myrhaug and Slaattelid (1999). This phenomenon was suggested to be caused by a broad-banded wave spectrum, representing both wind waves and swell.

Rodríguez and Guedes Soares (2000) compared numerically simulated data in mixed sea states with the Longuet-Higgins (1983) model and the Cavanié et al. (1976) model. The results showed large variations in the observed probability density functions in wind-dominated sea states and swell-dominated sea states, and that the theoretical models were best suitable for predicting wave periods in the wind-dominated sea states. These results were confirmed by field measurements in mixed sea states from the Portuguese Coast (Guedes Soares and Carvalho, 2003). The Cavanié et al. (1976) model agreed apparently better with the Longuet-Higgins (1983) model and the data than observed in Fig. 5.1. This is due to the parameter T_c , which is not included in the Cavanié et al. (1976) model presented in Rodríguez and Guedes Soares (2000) and Guedes Soares and Carvalho (2003).

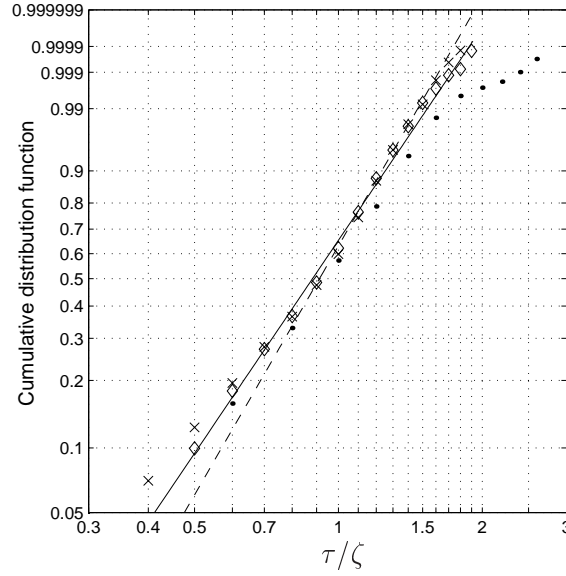


Figure 5.3: Weibull probability plot of wave periods. \times data from Draupner field; \diamond data from Myrhaug and Kjeldsen (1984); \bullet data from Kjeldsen (1981); — Weibull distribution fitted from Draupner data with $\alpha = 0.982$ and $\beta = 3.422$; -- Bretschneider (1959) model ($\zeta = 9.79$ s from Draupner data).

5.2 Joint distribution of successive wave periods

There has been less attention on joint distribution functions for successive wave periods. Kimura (1980) presented a two-dimensional Weibull distribution for two successive wave periods and compared the theoretical model with data from numerical simulations. Myrhaug and Rue (1993) presented a joint distribution function based on the Bretschneider (1959) model. This model was compared with the Kjeldsen (1981) data. Myrhaug and Rue (1998) also used a two-dimensional Weibull distribution. The model was compared with the Myrhaug and Rue (1993) model and with the same data from Tromsøflaket. It appeared that the two-dimensional Weibull distribution was in better agreement with the data.

Let $t_1 = \tau_1/T_{m01}$ and $t_2 = \tau_2/T_{m01}$ denote the non-dimensional successive wave periods $t_1 = t_j$ and $t_2 = t_{j+1}$, respectively. The two-dimensional Weibull distribution of T_1 and T_2 is given by

$$f_{T_1, T_2}(t_1, t_2) = \frac{\beta^2 (t_1 t_2)^{\beta-1}}{\alpha^{2\beta} (1 - \kappa_\tau^2)} \exp \left\{ -\frac{t_1^\beta + t_2^\beta}{\alpha^\beta (1 - \kappa_\tau^2)} \right\} I_0 \left[\frac{2\kappa_\tau (t_1 t_2)^{\beta/2}}{\alpha^{\beta/2} (1 - \kappa_\tau^2)} \right], \quad (5.8)$$

where κ_τ is related to the correlation coefficient, ρ_τ , between T_1 and T_2 by (see Appendix E)

$$\rho_\tau \equiv \rho_{T_1, T_2} = \frac{\Gamma^2 \left(\frac{1}{\beta} \right) \left[F \left(-\frac{1}{\beta}, -\frac{1}{\beta}; 1; \kappa_\tau^2 \right) - 1 \right]}{\left[2\beta \Gamma \left(\frac{2}{\beta} \right) - \Gamma^2 \left(\frac{1}{\beta} \right) \right]}. \quad (5.9)$$

One should note that the wave period is normalized w.r.t ζ in Myrhaug and Rue (1998), and the parameter α estimated there must be multiplied with ζ/T_{m01} in order to fit into the present

notation. By using the Weibull parameters $\alpha = \zeta/T_{m01}$ and $\beta = 4$, the Myrhaug and Rue (1993) model is obtained.

Myrhaug and Slaattelid (1999) presented a parametric model based on data from the Frigg field. The data included more than 3 million individual waves. The model was a combination of two two-parameter Weibull distributions, which were fitted to the data in two separate intervals. This model will not be considered in this thesis.

5.2.1 Gaussian distribution for successive wave periods using Nataf transformation

The Nataf approach presented in Chapter 4.2 can also be applied here to obtain a multivariate Gaussian distribution for the successive wave periods. The main challenge will be to select a marginal probability distribution that gives a good estimate of the wave periods.

Two distributions will be presented here as the initial distribution for the transformation. First, the Weibull distribution, given in Eq. (4.24), is used. One should note that $\alpha = \zeta/T_{m01}$ and $\beta = 4$ give the Bretschneider (1959) model. However, as the results will show, this distribution will not give a good transformation. Second, the generalized Gamma distribution will be used, which results in a better transformation.

If the two-parameter Weibull distribution is used, then the transformation to Gaussian distribution is the same as in Eq. (4.29), i.e., given by

$$\Psi_T^W(t) = \sqrt{2} \operatorname{erf}^{-1} \left[2 \left(1 - \exp \left\{ - \left(\frac{t}{\alpha} \right)^\beta \right\} \right) - 1 \right]. \quad (5.10)$$

This will be referred to as the Nataf-Weibull transformation.

Figure 5.4 shows a Weibull probability plot of the wave periods from the Draupner field, where the best fitted line is given by the parameters α and β in Table 5.1. The figure shows that the Weibull distribution deviates from the data, particularly around $t \approx 1$, and that it is not a very good fit to the data.

The generalized Gamma distribution was first used by Ochi (1992) when modeling significant wave heights in long-term statistics. The generalized Gamma probability density function is given by

$$f_T(t) = \frac{c(t - \gamma)^{c\lambda - 1}}{\Gamma(\lambda)\nu^{c\lambda}} \exp \left\{ - \left(\frac{t - \gamma}{\nu} \right)^c \right\}, \quad (5.11)$$

where λ and c are the shape coefficients, ν is the scale coefficient and γ is the location coefficient. The physical meaning of t , i.e., the wave period is always positive, implies that $\gamma = 0$. The other parameters are found from maximum likelihood estimation and given in Table 5.1 (see Appendix G for further details).

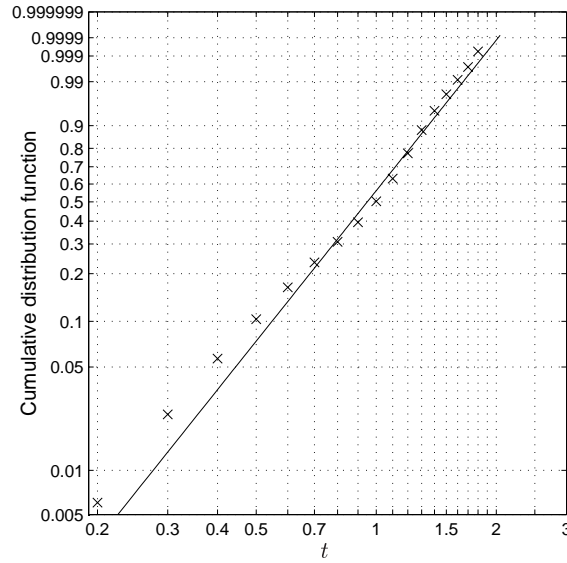


Figure 5.4: Weibull probability plot of the wave period data from the Draupner field.; \times data, — fitted Weibull distribution with $\alpha = 1.058$ and $\beta = 3.422$.

Figure 5.5 (a) shows the histogram and the kernel density estimate of the wave periods from the Draupner field compared with the Weibull distribution and the generalized Gamma distribution. The Bretschneider (1959) model is also included. The figure shows that the generalized Gamma distribution gives a better prediction of the data than both the Weibull distribution and the Bretschneider (1959) model, especially at the peak. The generalized Gamma distribution also gives a better estimate of the larger wave periods than the Weibull distribution, which slightly overpredicts the wave periods.

The probability of exceedance is shown in Fig. 5.5 (b). It shows the same results as the marginal distribution, i.e., that for almost all values of t the generalized Gamma distribution gives the best prediction of the data. However, it appears to underpredict the probability of exceedance for the largest values of t .

Table 5.1: Parameters in Weibull distribution and generalized Gamma distribution based on maximum likelihood estimation of the Draupner data.

α	[-]	1.058	λ	[-]	0.415
β	[-]	3.422	c	[-]	6.231
			ν	[-]	1.311

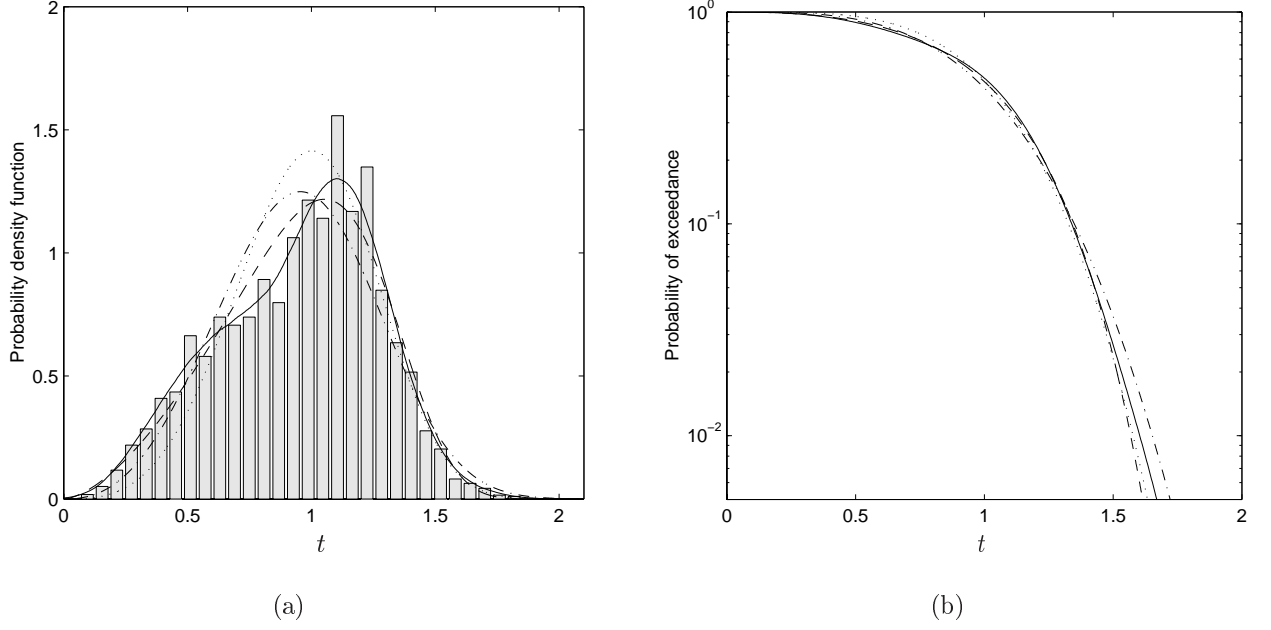


Figure 5.5: (a) A histogram of the Draupner data compared with probability density functions, and (b) probability of exceedance of the wave period with parameters from the Draupner data; — kernel density estimate of data, - - - Weibull distribution ($\alpha = 1.058$, $\beta = 3.422$), - - generalized Gamma distribution ($\lambda = 0.415$, $c = 6.231$, $\nu = 1.311$), \cdots Bretschneider (1959) model.

The cumulative generalized Gamma distribution function can be written

$$F_T(t) = I_\Gamma \left[\lambda, \left(\frac{t}{\nu} \right)^c \right], \quad (5.12)$$

where I_Γ denotes the incomplete Gamma function given by

$$I_\Gamma(\lambda, u) = \frac{1}{\Gamma(\lambda)} \int_0^u e^{-x} x^{\lambda-1} dx. \quad (5.13)$$

Defining $\Psi_T^G(t) = \Phi^{-1}(u_T)$ with $U_T = F_T(t)$ from Eq. (5.12), it follows from Eq. (4.21) that the transformation to Gaussian density function is given by

$$\Psi_T^G(t) = \sqrt{2} \operatorname{erf}^{-1} \left\{ 2I_\Gamma \left[\lambda, \left(\frac{t}{\nu} \right)^c \right] - 1 \right\}. \quad (5.14)$$

This will be referred to as the Nataf-Gamma transformation. The derivative of Ψ_T^G is given by

$$\Psi_T^{G'}(t) = \frac{\sqrt{2\pi} c}{\Gamma(\lambda)\nu} \left(\frac{t}{\nu} \right)^{c(\lambda-\frac{1}{c})} \exp \left\{ \left(\operatorname{erf}^{-1} \left[2I_\Gamma \left(\lambda, \left(\frac{t}{\nu} \right)^c \right) - 1 \right] \right)^2 - \left(\frac{t}{\nu} \right)^c \right\}. \quad (5.15)$$

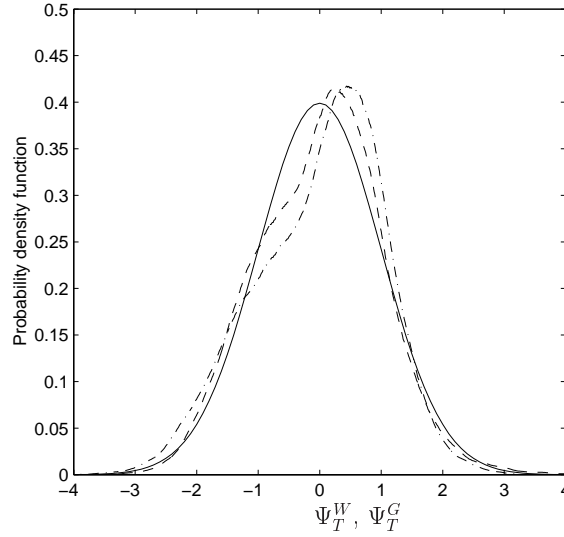


Figure 5.6: Probability density function of transformed wave height data; $-\cdot-$ KDE of Ψ_T^W , $--$ KDE of Ψ_T^G , $—$ standard Gaussian density function.

Figure 5.6 shows kernel density estimates of the transformed wave periods with both Ψ_T^W and Ψ_T^G compared with the standard Gaussian probability density function. The figure shows that both transformations give a poor approximation to a Gaussian distribution. The peak values are located too far to the right, and the shape of the density functions do not resemble the Gaussian density function. Both distributions deviate from the Gaussian distribution, but the Nataf-Gamma transformation is slightly closer to a Gaussian distribution. However, there are some differences around the peak of the density function, and this corresponds to the shape of the marginal density function for the wave period, which was shown in Fig. 5.1 (a). Unless an initial distribution that captures this feature is used, this will probably always be reflected in the transformation. Another possibility is to remove the smallest values from the data set and only consider parts of the data set, e.g., consider the wave periods where the corresponding wave heights exceed a given value. This will be discussed further in Chapter 5.3.

In the following only the Nataf-Gamma transformation will be considered.

The two-dimensional distribution of two successive wave periods T_1 and T_2 is given by

$$F_{T_1, T_2}(t_1, t_2) = \Phi(\Psi_T^G(t_1), \Psi_T^G(t_2)), \quad (5.16)$$

and the probability density function is

$$\begin{aligned} f_{T_1, T_2}(t_1, t_2) &= \frac{\Psi_T^{G'}(t_1) \Psi_T^{G'}(t_2)}{2\pi \sqrt{1 - \rho_{G,12}^2}} \\ &\times \exp \left\{ -\frac{1}{2(1 - \rho_{G,12}^2)} (\Psi_T^G(t_1)^2 + \Psi_T^G(t_2)^2 - 2\rho_{G,12} \Psi_T^G(t_1) \Psi_T^G(t_2)) \right\}, \end{aligned} \quad (5.17)$$

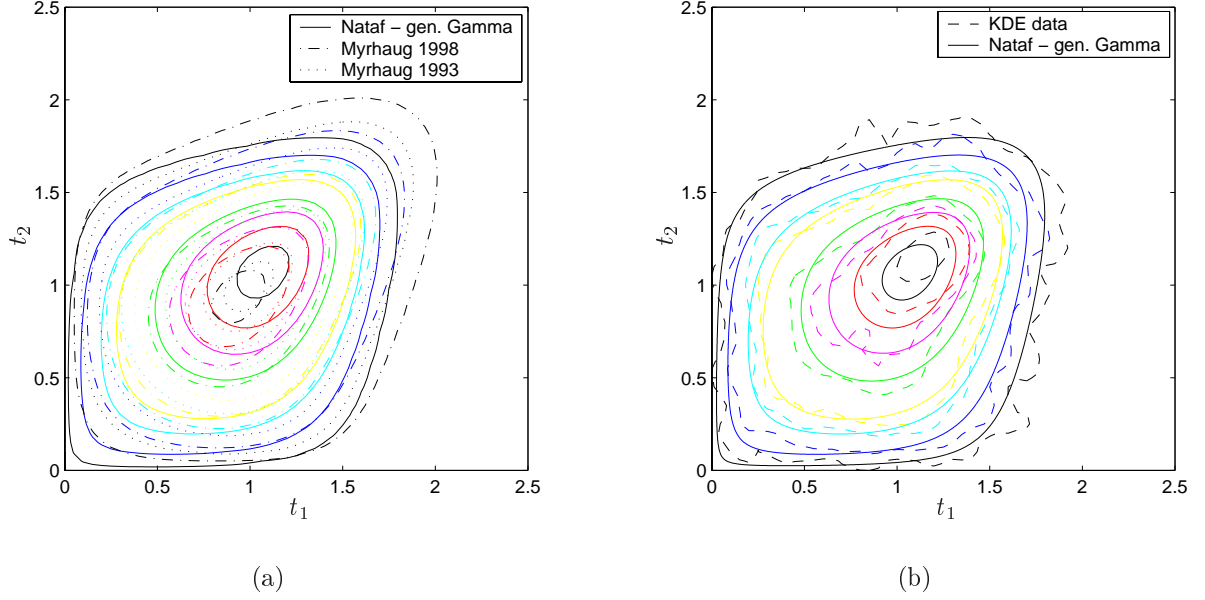


Figure 5.7: Contour plot of the two-dimensional probability density functions. Percent levels the given contour lines enclose are 10, 30, 50, 70, 90, 95, 99 and 99.9. (a) The Nataf-Gamma model compared with the Myrhaug and Rue (1993) ($\alpha = 1.077$, $\beta = 4$, $\kappa_\tau^2 = 0.404$) model and the Myrhaug and Rue (1998) ($\alpha = 1.058$, $\beta = 3.422$, $\kappa_\tau^2 = 0.391$) model. (b) The Nataf-Gamma model compared with kernel density estimate of the data. ($\lambda = 0.415$, $c = 6.231$, $\nu = 1.311$, $\rho_{G,12} = 0.325$).

where $\rho_{G,12}$ is the correlation coefficient between $\Psi_T^G(t_1)$ and $\Psi_T^G(t_2)$. Table 5.2 shows the correlation coefficients of the transformed wave periods calculated from the Draupner field data. The correlation coefficients for the normalized wave periods are included for comparison, showing that they are close to the $\rho_{G,1i}$ values. It appears that the correlation coefficients between the wave periods decrease rapidly.

Figure 5.7 (a) shows a contour plot of the two-dimensional Nataf-Gamma model. The Myrhaug and Rue (1993) ($\alpha = 1.077$, $\beta = 4$, $\kappa_\tau^2 = 0.404$) and Myrhaug and Rue (1998) ($\alpha = 1.058$, $\beta = 3.422$, $\kappa_\tau^2 = 0.391$) models are included for comparison. The peaks of the two latter distributions are located at lower values of t_1 and t_2 than the Nataf-Gamma model. They also

Table 5.2: Correlation coefficients between $\Psi_T^G(t_1)$ and $\Psi_T^G(t_i)$, and correlation coefficient of the normalized wave periods $\rho_{\tau,1i}$, $i = 2, 3, 4$, from the Draupner data.

$\rho_{G,12}$	[-]	0.325	$\rho_{\tau,12}$	[-]	0.322
$\rho_{G,13}$	[-]	0.122	$\rho_{\tau,13}$	[-]	0.118
$\rho_{G,14}$	[-]	0.073	$\rho_{\tau,14}$	[-]	0.071

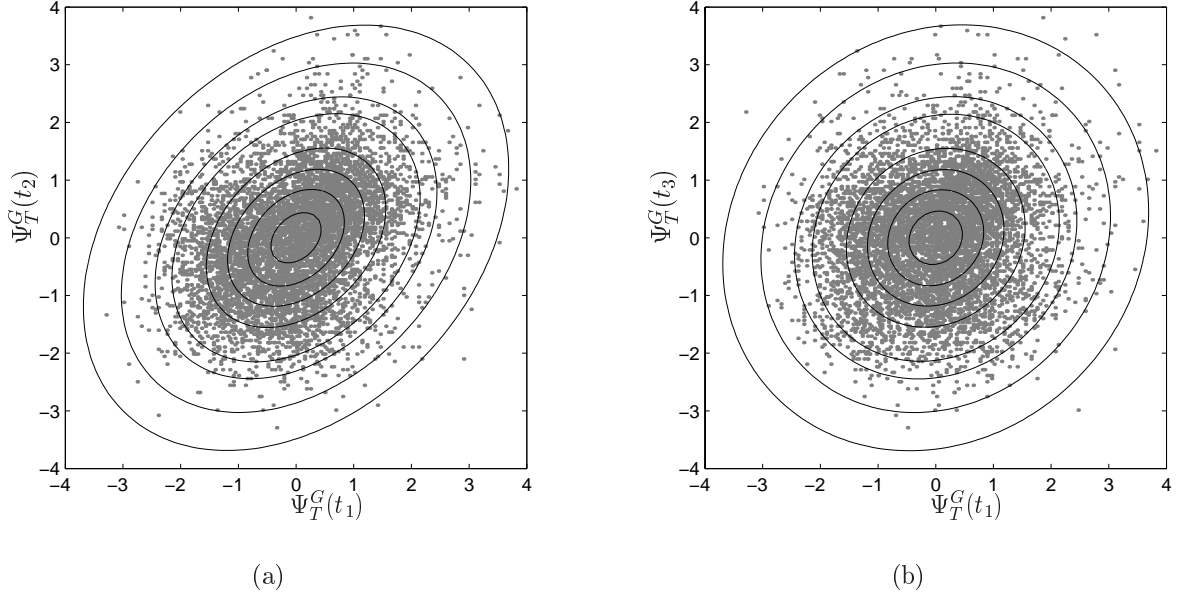


Figure 5.8: Paired plot of the transformed wave periods Ψ_T^G between (a) t_1 and t_2 , (b) t_1 and t_3 , compared with a contour plot of a standard Gaussian distribution ($\rho_{G,12} = 0.325$, $\rho_{G,13} = 0.122$, $\lambda = 0.415$, $c = 6.231$ $\nu = 1.311$). Percent levels the given contour lines enclose are 10, 30, 50, 70, 90, 95, 99 and 99.9.

decrease more slowly than the Nataf-Gamma model for large values of t_1 and t_2 . The Nataf-Gamma model is compared with the kernel density estimate of the Draupner data in Fig. 5.7 (b). The peak of the data is not correctly predicted, but generally the Nataf-Gamma model gives a good estimate of the data.

Figure 5.8 (a) and (b) show a paired plot of the transformed wave periods between t_1 and t_2 , and t_1 and t_3 , respectively. The results are compared with a contour plot of the standard Gaussian distribution. Both figures show that the dependency structure resembles the one for the Gaussian distribution.

Thus, by using the Nataf-Gamma transformation, the probability distribution for two and three successive wave periods can be modeled by a transformed Gaussian distribution. The resulting transformation is not completely Gaussian, but the results are satisfactory compared to the existing two-dimensional models. In theory, the Nataf-Gamma transformation can also be used for modeling more than three wave periods. However, the resulting dependency structure should be examined to see if the transformation correctly takes care of the correlation between the wave periods.

The probability density function for $\mathbf{T} = [T_1, \dots, T_p]^T$ is given by

$$f_{\mathbf{T}}(\mathbf{t}) = \frac{\prod_{i=1}^p \Psi_T^{G'}(t_i)}{(2\pi)^{p/2} |\Sigma|^{1/2}} \exp \left\{ -\frac{1}{2} \Psi_T^G(\mathbf{t})^T \Sigma^{-1} \Psi_T^G(\mathbf{t}) \right\}, \quad (5.18)$$

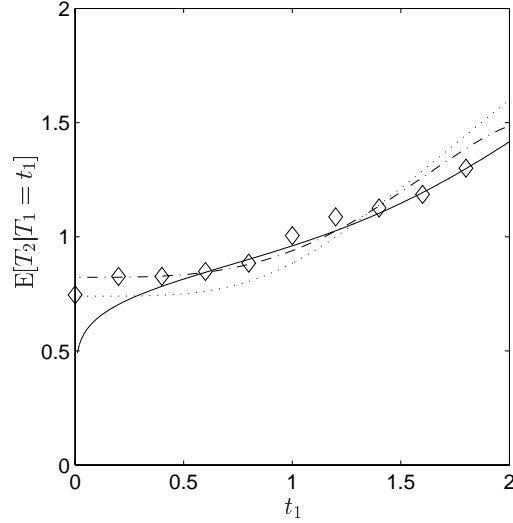


Figure 5.9: Conditional expectation of the wave period given the previous wave period. — Nataf-Gamma model ($\lambda = 0.415$, $c = 6.231$, $\nu = 1.311$, $\rho_{G,12} = 0.325$); \cdots Myrhaug and Rue (1993) model ($\alpha = 1.077$, $\beta = 4$, $\kappa_\tau^2 = 0.404$); $---$ Myrhaug and Rue (1998) model ($\alpha = 1.058$, $\beta = 3.422$, $\kappa_\tau^2 = 0.391$); \diamond field data.

where the covariance matrix, Σ , is given by

$$\Sigma = \begin{bmatrix} 1 & \rho_{G,12} & \cdots & \rho_{G,1p} \\ \rho_{G,12} & 1 & \cdots & \rho_{G,2p} \\ \vdots & & \ddots & \vdots \\ \rho_{G,1p} & & \cdots & 1 \end{bmatrix}. \quad (5.19)$$

Another quantity of interest is the expected value of a wave period given the previous wave period. This is given by

$$E[T_2|T_1 = t_1] = \int_0^\infty t_2 f_{T_2|T_1}(t_2|t_1) dt_2, \quad (5.20)$$

where the conditional probability density function $f_{T_2|T_1}(t_2|t_1)$ is found from Bayes rule in Eq. (3.53). Figure 5.9 shows the conditional expectation $E[T_2|T_1 = t_1]$ versus t_1 for the Nataf-Gamma model and the Myrhaug and Rue (1993, 1998) models. The results are compared with data from the Draupner field. The Nataf-Gamma model agrees quite well with the data except for small values of t_1 where the Myrhaug and Rue (1993, 1998) models give a better agreement with the data.

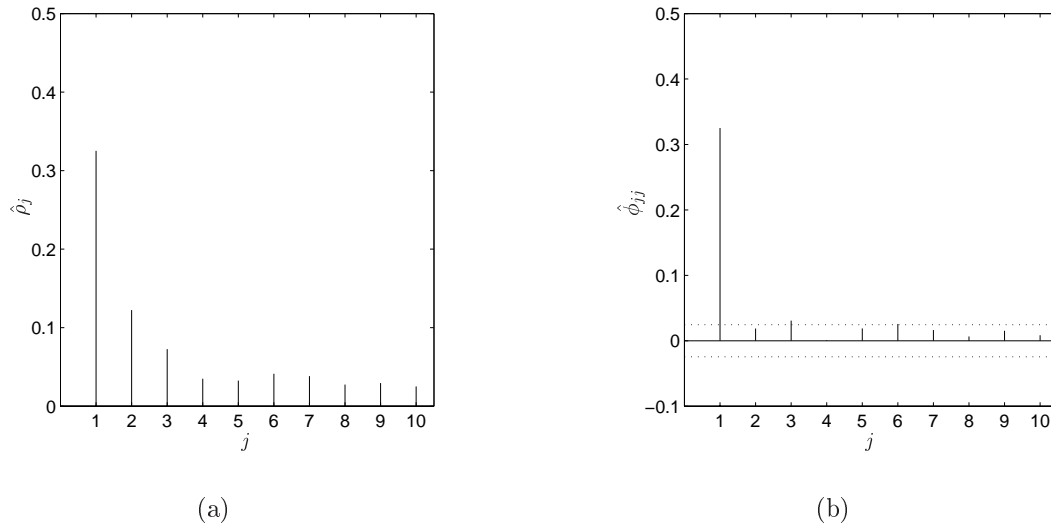


Figure 5.10: (a) Sample autocorrelation function, and (b) sample partial autocorrelation function of Ψ_T^G from Draupner data. The dotted line indicates $\pm 2(\text{Var}[\hat{\phi}_{jj}])^{1/2}$.

Successive wave periods modeled as an AR(1) model

The Nataf-Gamma transformation of the wave periods from the Draupner field can be modeled as an AR(1) model as discussed in Chapter 4.3. Figure 5.10 shows the sample ACF and PACF of Ψ_T^G . The ACF decreases approximately exponentially, and the PACF has one spike at $j = 1$. A likelihood ratio test as described in Chapter 4.3.1 gives a test result of $-2 \ln \Lambda_{obs} = 3.17$ with $n = 2208$. From tables $\chi_{0.205,2}^2 = 3.17$, which means that the hypothesis that the correlation coefficients agree with an AR(1) model (i.e., are given by Eq. (4.42)) would not be rejected at 20.5% significance level.

The simulation of successive wave periods is more difficult than for the wave heights when using the generalized Gamma distribution in the transformation. This is due to the difficulty of inverting the transformation of Ψ_T^G given in Eq. (5.14), which must be done numerically.

However, the distribution for the wave period given the previous wave period will be independent of the wave periods prior to the previous wave period. Figure 5.11 shows the probability of a wave period to be in an interval $[\tilde{t}_1, \tilde{t}_2]$ given that the previous wave period was in the same interval as a function of $x = (\tilde{t}_1 + \tilde{t}_2)/2$. Here $\tilde{t}_1 = x - 0.1$ and $\tilde{t}_2 = x + 0.1$. The Nataf-Gamma model and the Myrhaug and Rue (1993, 1998) models are included for comparison. The shape of the data is not reflected in any of the models. The Nataf-Gamma model agrees quite well with the data for large values of x , while the Myrhaug and Rue (1998) model agrees better with the data for small values of x .

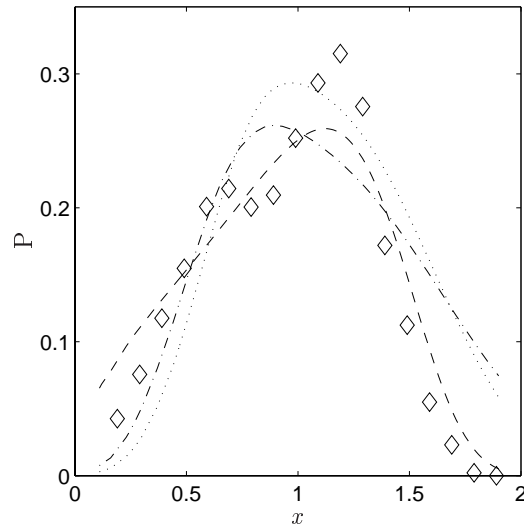


Figure 5.11: The probability of a wave period to be in an interval $[\tilde{t}_1, \tilde{t}_2]$ given that the previous wave period was in the same interval, where $\tilde{t}_1 = x - 0.1$ and $\tilde{t}_2 = x + 0.1$.
 $(P = P(x - 0.1 < T_2 < x + 0.1 | x - 0.1 < T_1 < x + 0.1))$

-- Nataf-Gamma model; \cdots Myrhaug and Rue (1993) model; $- \cdot -$ Myrhaug and Rue (1998) model; \diamond field data.

5.3 Distribution of successive wave periods for large wave heights

Usually, the most critical situations will occur when the wave height is large. That means that it is of interest to study the probability distributions for the wave period given that the corresponding wave height exceeds a given value, e.g., h_{rms} or H_S , where the latter is of most practical interest. There exist several joint distributions of wave height and corresponding wave period.

In Longuet-Higgins (1975) the joint density function of dimensionless wave height and wave period is given by

$$f_{H,T}(h, t) = \frac{2h^2}{\sqrt{\pi}\epsilon_2} \exp \left\{ -h^2 \left[1 + \left(\frac{t-1}{\epsilon_2} \right)^2 \right] \right\}. \quad (5.21)$$

The conditional probability density function of t given that h exceeds \tilde{h} is found by integration and is given by

$$f_{T|H}(t|h > \tilde{h}) = \frac{2}{\exp(-\tilde{h}^2)\sqrt{\pi}\epsilon_2} \left[\frac{1}{2} \frac{\tilde{h}}{\tilde{t}_1 e^{\tilde{t}_1 \tilde{h}^2}} + \frac{\sqrt{\pi}}{4\tilde{t}_1^{3/2}} - \frac{1}{4} \frac{\sqrt{\pi} \operatorname{erf}(\tilde{h}\sqrt{\tilde{t}_1})}{\tilde{t}_1^{3/2}} \right], \quad (5.22)$$

where

$$\tilde{t}_1 = 1 + \left(\frac{t-1}{\epsilon_2} \right)^2. \quad (5.23)$$

Similarly to the marginal density function in Eq. (5.2), the integral of the density functions in Eqs. (5.21) and (5.22) is only equal to one if negative values of t are included.

The joint density function of h and t proposed by Longuet-Higgins (1983) is given by

$$f_{H,T}(h, t) = \frac{4}{\sqrt{\pi}\epsilon_2 \left[1 + (1 + \epsilon_2^2)^{-1/2} \right]} \frac{h^2}{t^2} \exp \left\{ -h^2 \left[1 + \left(\frac{1 - \frac{1}{t}}{\epsilon_2} \right)^2 \right] \right\}, \quad (5.24)$$

and the conditional probability density function is given by

$$f_{T|H}(t|h > \tilde{h}) = \frac{4}{C_L \sqrt{\pi}\epsilon_2 \left[1 + (1 + \epsilon_2^2)^{-1/2} \right]} \frac{1}{t^2} \left[\frac{1}{2} \frac{\tilde{h}}{\tilde{t}_2 e^{\tilde{t}_2 \tilde{h}^2}} + \frac{\sqrt{\pi}}{4\tilde{t}_2^{3/2}} - \frac{1}{4} \frac{\sqrt{\pi} \operatorname{erf}(\tilde{h}\sqrt{\tilde{t}_2})}{\tilde{t}_2^{3/2}} \right], \quad (5.25)$$

where

$$\tilde{t}_2 = 1 + \left(\frac{1 - \frac{1}{t}}{\epsilon_2} \right)^2, \quad (5.26)$$

and C_L is the normalizing factor from the marginal distribution of H given by

$$C_L = \int_{\tilde{h}}^{\infty} \frac{4h}{1 + (1 + \epsilon_2^2)^{-1/2}} \exp(-h^2) \frac{1}{2} \left(1 + \operatorname{erf} \left[\frac{h}{\epsilon_2} \right] \right) dh. \quad (5.27)$$

Tayfun (1993) presented a joint probability density function of wave height and wave period that was valid for large wave heights. This was based on

$$f_{H,T}(h, t) = f_H(h)f_{T|H}(t|h), \quad (5.28)$$

and was valid for $h > \mu_h =$ the mean wave height. The marginal probability density function of H for large wave heights is given in Tayfun (1990) as

$$f_H(h) = C_{T,1}h \left(1 + \frac{1 - \kappa_a^2}{32\kappa_a h^2} \right) \exp \left\{ -\frac{2h^2}{1 + \kappa_a} \right\}; \quad h > \mu_h, \quad (5.29)$$

where $C_{T,1}$ is a normalizing factor and κ_a is the same as in the two-dimensional Rayleigh distribution. The conditional distribution of the wave period given the wave height was approximated by the Gaussian distribution, when assuming that the wave height was larger than the mean wave height

$$f_{T|H}(t|h) = C_{T,2} \exp \left\{ -\frac{1}{2} \left(\frac{t - \mu_{t|h}}{\sigma_{t|h}} \right)^2 \right\}; \quad h > \mu_h, \quad (5.30)$$

where $C_{T,2}$ is a normalizing factor and

$$\mu_{t|h} = 1 + \epsilon_2^2(1 + \epsilon_2^2)^{-3/2} \quad (5.31)$$

$$\sigma_{t|h} = \frac{2\epsilon_2}{\sqrt{8h(1 + \epsilon_2^2)}}. \quad (5.32)$$

Thus, the joint probability function is found from Eq. (5.28) as

$$f_{H,T}(h, t) = C_{T,3}h \left(1 + \frac{1 - \kappa_a^2}{32\kappa_a h^2} \right) \exp \left\{ -\frac{1}{2} \left[\frac{4h^2}{1 + \kappa_a} + \left(\frac{t - \mu_{t|h}}{\sigma_{t|h}} \right)^2 \right] \right\}, \quad (5.33)$$

where $C_{T,3}$ is a normalizing factor. The conditional probability density function given that $h > \tilde{h}$ must be calculated numerically.

Figure 5.12 shows a histogram of the wave periods from the Draupner field where the corresponding wave height is larger than h_{rms} , i.e., $h > 1$, and the kernel density estimate of the data. The data are compared with the Longuet-Higgins (1975, 1983) models and the Tayfun (1993) model. The first two models do not give a good prediction of the wave periods. The density functions are shifted towards lower values of t , and the peak value is also underestimated. The latter model gives a better estimate of the wave periods. However, this model also underestimates the peak value of the kernel density function.

The shape of the data in Fig. 5.12 indicates that a Gaussian density function would give a good description of the data. Figure 5.13 shows the data compared with a Gaussian density function with mean value and standard deviation calculated from the data, which are given in Table 5.3 for $p = 1$. The Gaussian density function agrees well with the data.

Thus, a transformation of the data is not necessary. The joint distribution of p successive wave periods $\mathbf{T} = [T_1, \dots, T_p]^T$, given the corresponding wave heights exceeding the level \tilde{h} , is then

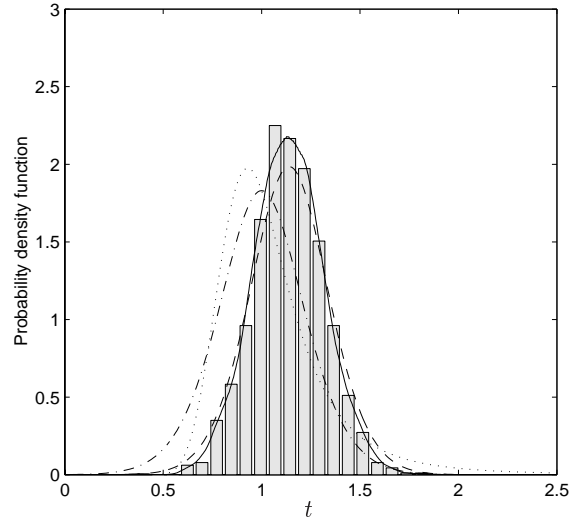


Figure 5.12: Probability density function of wave periods where the corresponding wave height is larger than h_{rms} , i.e., $h > 1$; — kernel density estimate of data, - - - Longuet-Higgins (1975), ... Longuet-Higgins (1983), -- Tayfun (1993).

given by the multivariate Gaussian distribution

$$f_{\mathbf{T}|\mathbf{H}}(\mathbf{t}|\mathbf{h} > \tilde{h}) = \frac{1}{(2\pi)^{p/2} |\Sigma_{t|\tilde{h}}|^{1/2}} \exp \left\{ -\frac{1}{2} (\mathbf{t} - \boldsymbol{\mu}_{t|\tilde{h}})^T \Sigma_{t|\tilde{h}}^{-1} (\mathbf{t} - \boldsymbol{\mu}_{t|\tilde{h}}) \right\}, \quad (5.34)$$

where $\boldsymbol{\mu}_{t|\tilde{h}} = [\mu_{t|\tilde{h},1}, \dots, \mu_{t|\tilde{h},p}]^T$ is the mean value of the wave periods given the threshold value \tilde{h} , and

$$\Sigma_{t|\tilde{h}} = \begin{bmatrix} \sigma_{t|\tilde{h},1}^2 & \text{Cov}[T_1, T_2|\tilde{h}] & \cdots & \text{Cov}[T_1, T_p|\tilde{h}] \\ \vdots & & \ddots & \vdots \\ \text{Cov}[T_1, T_p|\tilde{h}] & & \cdots & \sigma_{t|\tilde{h},p}^2 \end{bmatrix}, \quad (5.35)$$

where $\text{Cov}[T_i, T_j|\tilde{h}] = \rho_{ij} \sigma_{t|\tilde{h},i} \sigma_{t|\tilde{h},j}$.

Table 5.3: Calculated parameters for the p -dimensional Gaussian distribution with $\tilde{h} = 1$, from the Draupner field data.

	$\boldsymbol{\mu}_{t \tilde{h}}$	$\boldsymbol{\sigma}_{t \tilde{h}}$	$\boldsymbol{\rho}$	n
$p = 1$	1.14	0.18		2424
$p = 2$	$[1.18, 1.19]^T$	$[0.17, 0.17]^T$	0.245	1360
$p = 3$	$[1.18, 1.23, 1.19]^T$	$[0.17, 0.16, 0.16]^T$	$[0.287, 0.150]^T$	768

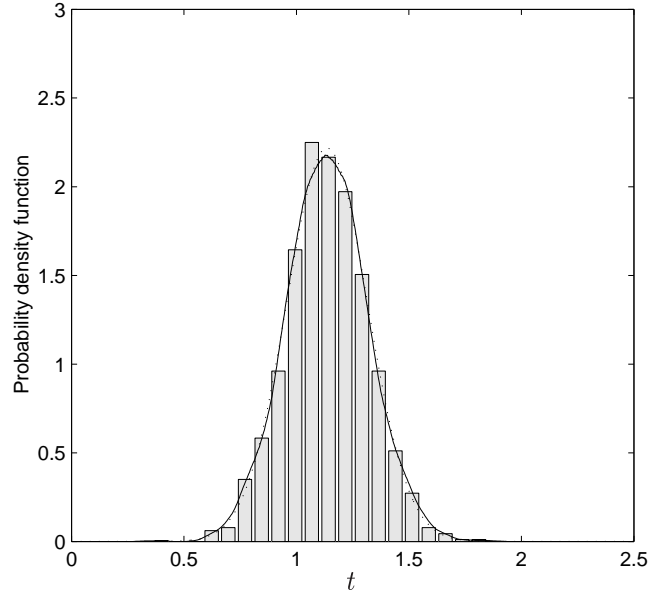


Figure 5.13: Probability density function of wave periods where the corresponding wave height is larger than h_{rms} , i.e., $h > 1$; — kernel density estimate of data, \cdots Gaussian density function ($\mu_{t|\tilde{h}} = 1.14$, $\sigma_{t|\tilde{h}} = 0.18$).

In order to compare the multivariate theory with the Draupner data, pairs and triplets of successive wave periods were formed conditioned on that the corresponding wave height was larger than h_{rms} . The mean value and standard deviation are shown in Table 5.3 for $p = 2$ and $p = 3$, respectively, and n is the number of pairs and triplets that were found. In addition, the correlation coefficients, $\boldsymbol{\rho} = [\rho_{12}, \dots, \rho_{1p}]^T$, between the successive wave periods are given. If the normalized significant wave height of 1.41 was selected as \tilde{h} , the number n would be smaller, and the number of data cases available when considering three successive wave periods would be too small. This case will instead be discussed in Chapter 6.4.1, with an increased number of data from numerical simulations.

Figure 5.14 shows a contour plot of the bivariate Gaussian distribution in Eq. (5.34) with $p = 2$ and $\tilde{h} = 1$, compared with the kernel density estimate of the Draupner data. The figure shows good correspondence between the model and the data.

In order to verify that the multivariate Gaussian distribution can be used for modeling successive wave periods, the dependency structure should be examined, e.g., by a paired plot. Figure 5.15 (a) and (b) show a paired plot of the wave periods t_1 and t_2 , and t_1 and t_3 , respectively. The figure shows that the correlation structure is correctly modeled by the bivariate Gaussian distribution.

Thus, the probability distribution for two and three successive wave periods given that the corresponding wave heights exceeded a critical level, e.g., h_{rms} , can be modeled by a multivariate Gaussian distribution. The multivariate Gaussian distribution can also be applied for more than three wave periods with corresponding large wave heights, but then the dependency structure should be further examined.

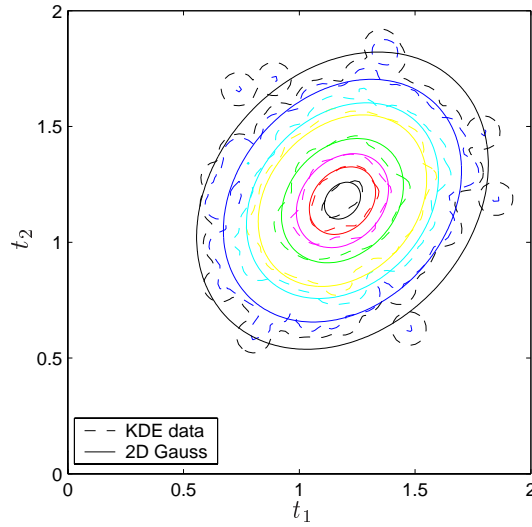


Figure 5.14: Contour plot of two successive wave periods, given that the corresponding wave heights are larger than h_{rms} , modeled by the bivariate Gaussian probability density function and compared with kernel density estimate of Draupner data. Percent levels the given contour lines enclose are 10, 30, 50, 70, 90, 95, 99 and 99.9. $(\mu_{t|\tilde{h}} = [1.18, 1.19]^T, \sigma_{t|\tilde{h}} = [0.17, 0.17]^T, \rho_{12} = 0.245)$.

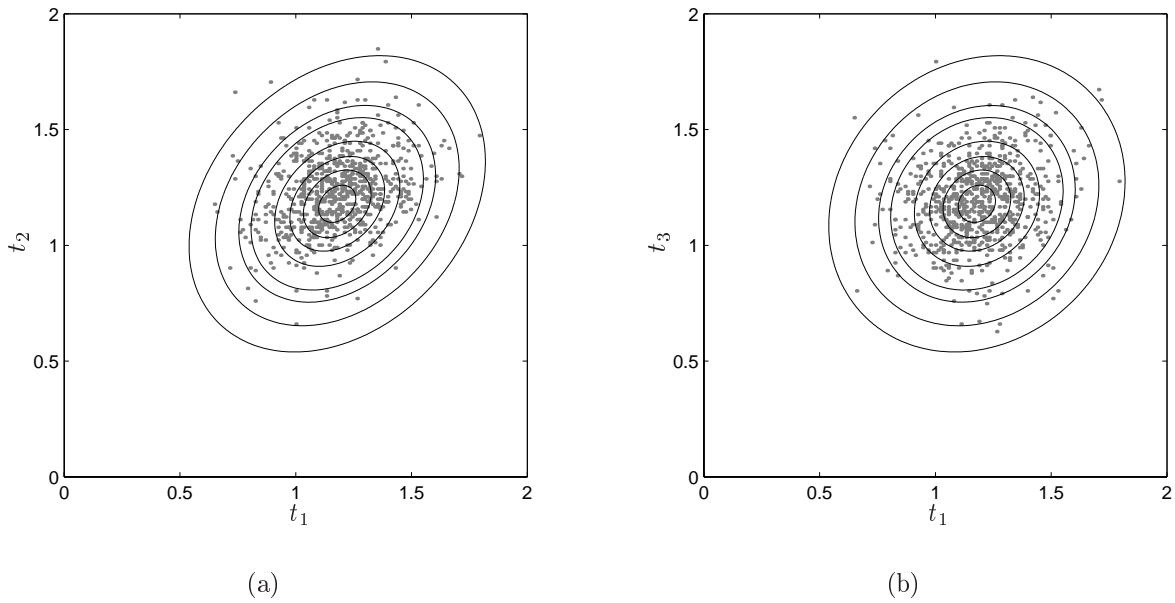


Figure 5.15: Paired plot between (a) t_1 and t_2 , and (b) t_1 and t_3 . Percent levels the given contour lines enclose are 10, 30, 50, 70, 90, 95, 99 and 99.9. $(\mu_{t|\tilde{h}} = [1.18, 1.23, 1.19]^T, \sigma_{t|\tilde{h}} = [0.17, 0.16, 0.16]^T, \rho = [0.287, 0.150]^T)$.

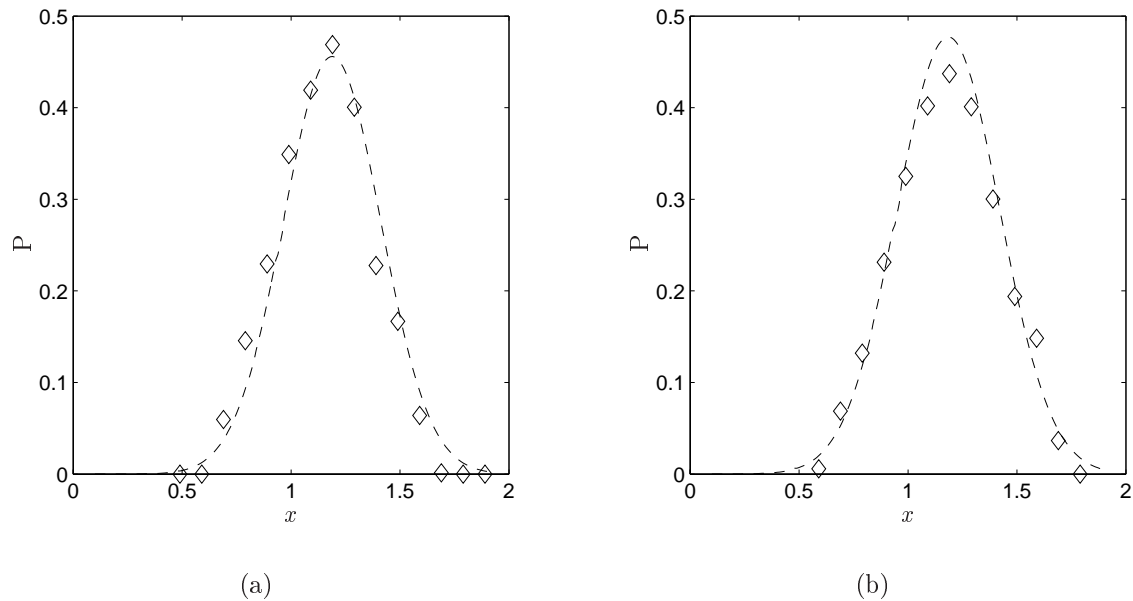


Figure 5.16: The probability of a wave period to be in an interval $[\tilde{t}_1, \tilde{t}_2]$ given that (a) the previous wave period and (b) the two previous wave periods were in the same interval, where $\tilde{t}_1 = x - 0.1$ and $\tilde{t}_2 = x + 0.1$. The corresponding wave heights are larger than h_{rms} .

-- Gaussian distribution; \diamond data from Draupner field.

(a) $P = P(\tilde{t}_1 < T_3 < \tilde{t}_2 | \tilde{t}_1 < T_2 < \tilde{t}_2, H_3 > h_{\text{rms}}, H_2 > h_{\text{rms}})$

(b) $P = P(\tilde{t}_1 < T_3 < \tilde{t}_2 | \tilde{t}_1 < T_2 < \tilde{t}_2, \tilde{t}_1 < T_1 < \tilde{t}_2, H_3 > h_{\text{rms}}, H_2 > h_{\text{rms}}, H_1 > h_{\text{rms}})$

It was shown in Chapter 5.2.1 that the Nataf-Gamma transformation of the wave periods from the Draupner field could be modeled as an AR(1) model. This means that the Markov property in Eq. (4.44) applies for all wave periods, and thus for the wave periods where the corresponding wave heights are larger than h_{rms} . Consequently, the distribution for the wave period given the previous wave period will be independent of the wave periods prior to the previous wave period, also when considering wave periods with corresponding large wave heights.

Figure 5.16 shows the probability of a wave period being in an interval $[\tilde{t}_1, \tilde{t}_2]$ given that (a) the previous wave period was in the same interval and (b) the two previous wave periods were in the same interval, as a function of $x = (\tilde{t}_1 + \tilde{t}_2)/2$. All corresponding wave heights exceeded h_{rms} . Here $\tilde{t}_1 = x - 0.1$ and $\tilde{t}_2 = x + 0.1$. The Gaussian distribution agrees quite well with the data. The results are also quite similar for both cases, which support the hypothesis that the wave periods can be modeled as an AR(1) model.

CHAPTER 6

Results and discussion

This chapter presents results both from field data and laboratory data. Numerical simulations are made for the different cases for comparison. For each case 10 simulations were made with identical input parameters in order to examine the variation in the results.

6.1 Data description

6.1.1 Draupner field

The description of the Draupner field data was given in Chapter 2.4.

Numerical simulation results

Numerical simulations of 10 time series with length equal to the total time series of the field data, i.e., 15 hours and 53 minutes, have been made. Here the time step was 0.5 s. The descriptive statistics of the wave parameters for the simulated data are given in Table 6.1. The mean values are in good agreement with the corresponding values of the field data given in Table 2.2.

Figure 6.1 (a) shows the spectral densities of each simulated time series. Compared to the spectral density of the field data in Fig. 6.1 (b), it is seen that the shape of the spectrum is quite similar, and the range of the peak periods ($11.07 \text{ s} \leq T_p \leq 11.31 \text{ s}$) corresponds well with the peak period of the field data, $T_p = 11.23 \text{ s}$.

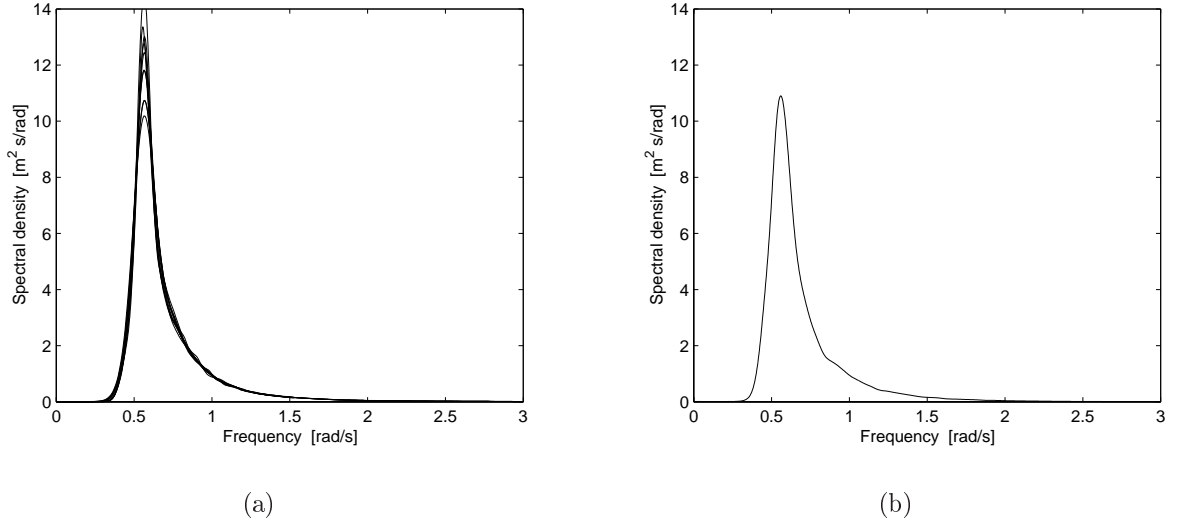


Figure 6.1: (a) Spectral densities of simulated time series. (b) The spectral density of field data.

Table 6.1: Descriptive statistics of the simulated data. Results from 10 simulations.

		Mean	Min/Max	St.dev
H_{m0}	[m]	6.77	6.69/6.90	0.07
T_{m02}	[s]	8.32	8.28/8.37	0.03
T_{m01}	[s]	8.98	8.93/9.03	0.03
T_{m24}	[s]	5.28	5.25/5.30	0.02
T_p	[s]	11.14	11.07/11.31	0.06
\bar{k}	[rad/m]	0.0582	0.0575/0.0588	0.0004
\bar{k}_1	[rad/m]	0.0500	0.0495/0.0506	0.0003
a_{rms}	[m]	2.39	2.37/2.44	0.02
σ	[m]	1.69	1.67/1.72	0.02
ρ_3	[-]	0.163	0.153/0.177	0.007
ρ_4	[-]	3.03	2.98/3.09	0.04
ϵ_2	[-]	0.407	0.404/0.411	0.002
ϵ_4	[-]	0.773	0.771/0.776	0.001
s	[-]	0.036	0.034/0.036	0.001

6.1.2 Japan Sea

Field data results

At the Poseidon platform in the Japan Sea measurements of the surface elevation were made in the period 1987-1990. Figure 6.2 is a map of the Japan Sea, and the Poseidon platform is situated 3 km off Yura. In order to investigate statistical properties of a relatively heavy sea state, a 4 hour time series measured 17th of December 1987 is considered. Three intervals containing some spurious data are removed from the data set leaving a time series of 3 hours and 51 minutes, which contains 1496 zero-upcrossing waves. The data is measured with an ultrasonic wave gauge situated at the sea floor, and the sampling frequency is 1 Hz. A cubic spline is used to interpolate the data set before further analysis. The water depth is 42 m, so a finite water depth effect is expected.

Figure 6.3 shows the spectral density for the time series. The dotted line indicates the peak frequency, $\omega_p = 0.54$ rad/s. A JONSWAP spectrum with peakedness parameter $\gamma_J = 1$ is shown in the same figure as the broken line. The JONSWAP spectrum tends to zero for small frequencies as opposed to the spectral density for the field data. The energy in the lowest part of the spectrum corresponds to the difference frequency effect, and this effect increases as the water depth decreases.

Table 6.2 shows the descriptive statistics for the time series. The measured values indicate that this sea state is quite similar to the sea state for the Draupner field data (see Table 2.2). However, the water depth of 42 m is only 3/5 of the water depth at the Draupner field, thus the nonlinear effects are expected to be more important. This is also indicated by a significantly higher value of the skewness and kurtosis. A histogram of the surface elevation compared to a Gaussian distribution with zero mean and variance equal to $(1.72 \text{ m})^2$ is shown in Fig. 6.4. It is clear from the figure that the skewness is positive.

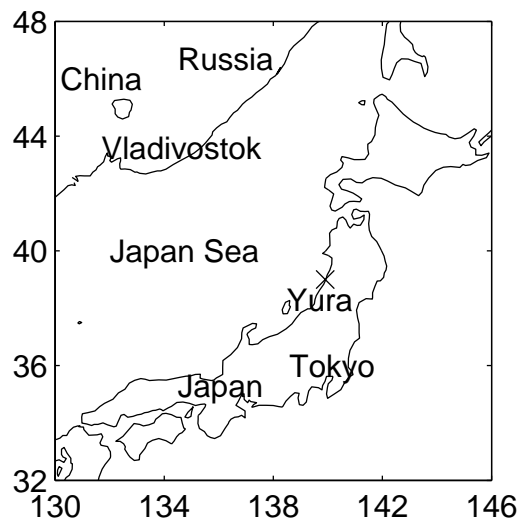


Figure 6.2: Map of the Japan Sea. The Poseidon platform is situated 3 km off Yura.

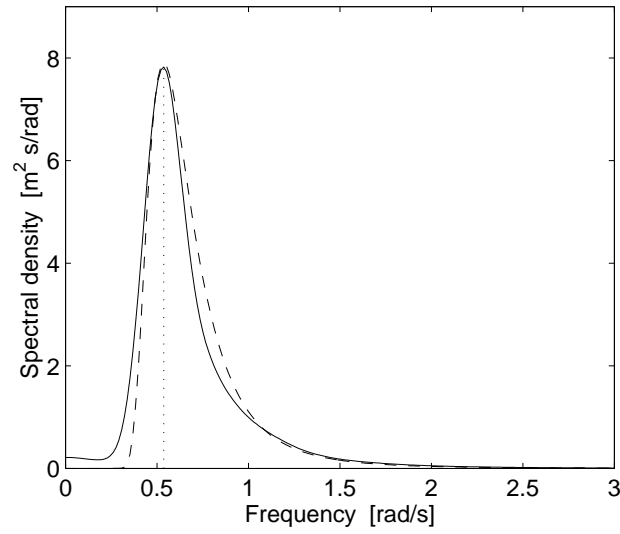


Figure 6.3: The spectral density of field data from Japan Sea (solid); JONSWAP spectrum with $\gamma_J = 1$ (broken); Peak frequency of field data $\omega_p = 0.54$ rad/s (dotted).

Table 6.2: Descriptive statistics of Japan Sea field data.

H_{m0}	[m]	6.88
T_{m02}	[s]	8.55
T_{m01}	[s]	9.45
T_{m24}	[s]	5.09
T_p	[s]	11.70
\bar{k}	[rad/m]	0.0561
\bar{k}_1	[rad/m]	0.0469
a_{rms}	[m]	2.43
σ	[m]	1.72
ρ_3	[-]	0.254
ρ_4	[-]	3.11
ϵ_2	[-]	0.470
ϵ_4	[-]	0.804
s	[-]	0.036

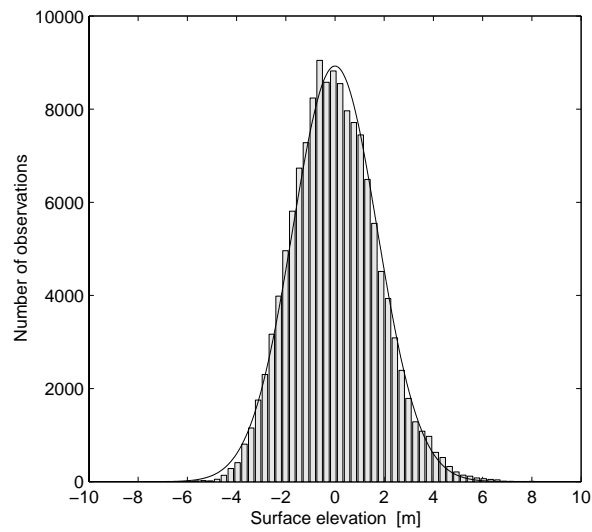


Figure 6.4: Histogram of the surface elevation from Japan Sea. The line indicates a Gaussian distribution with zero mean and variance equal to $(1.72 \text{ m})^2$.

Table 6.3: Descriptive statistics of 20 minutes intervals of Japan Sea field data.

		Mean	Min/Max	St.dev
H_{m0}	[m]	6.90	6.28/7.35	0.34
T_{m02}	[s]	8.46	8.28/8.70	0.14
T_{m01}	[s]	9.44	9.17/9.72	0.19
T_{m24}	[s]	2.43	1.41/4.93	1.09
T_p	[s]	11.74	11.38/12.05	0.32
\bar{k}	[rad/m]	0.0572	0.0542/0.0595	0.0017
\bar{k}_1	[rad/m]	0.0470	0.0447/0.0494	0.0016
a_{rms}	[m]	2.44	2.22/2.60	0.12
σ	[m]	1.73	1.57/1.84	0.09
ρ_3	[-]	0.250	0.141/0.419	0.088
ρ_4	[-]	3.06	2.66/3.82	0.29
ϵ_2	[-]	0.495	0.462/0.521	0.020
ϵ_4	[-]	0.948	0.806/0.986	0.054
s	[-]	0.036	0.032/0.041	0.003

In order to investigate the variability in the data set, the time series was divided into intervals of 20 minutes (i.e., totally 11 records) and descriptive statistics were found for each interval. The mean value, the minimum and maximum value and the standard deviation were calculated and are given in Table 6.3. The variety in the values are due to that the sea state is not completely stationary during the entire time interval. Both the significant wave height and the peak period is slightly decreasing, indicating that the storm decreases. In the following the whole time series is considered as one interval.

Numerical simulation results

Numerical simulations of 10 time series with length of 3 hours and 51 minutes corresponding to the length of the field data, have been made. The time step was 0.5 s. Since the JONSWAP spectrum did not describe the spectrum of the field data very well (see Fig. 6.3), the spectrum from the field data was used as the input spectrum for the simulations. However, since the linear component is based on the spectrum, the energy of the input spectrum should approach zero for small frequencies. Otherwise, the spectral density of the resulting simulations would correspond to both the linear component and the difference frequency component, and the value of the spectral density would be too high at low frequencies. Thus, the time series of the field data was filtered at 0.2 rad/s before the resulting spectrum was used as the input spectrum for the simulations.

The descriptive statistics of the simulated data are given in Table 6.4. The significant wave height and the peak period agrees well with the field data values in Table 6.2. The values of T_{m02} and T_{m01} are smaller than the values of the field data, thus also \bar{k} and \bar{k}_1 deviate from the field data values. The skewness is also smaller than for the field data.

Figure 6.5 (a) shows the spectral densities of each simulated time series. Both the shape of the spectra and the range of the peak frequencies ($0.52 \text{ rad/s} \leq \omega_p \leq 0.57 \text{ rad/s}$) agree well with the spectral density of the field data shown in Fig. 6.5 (b).

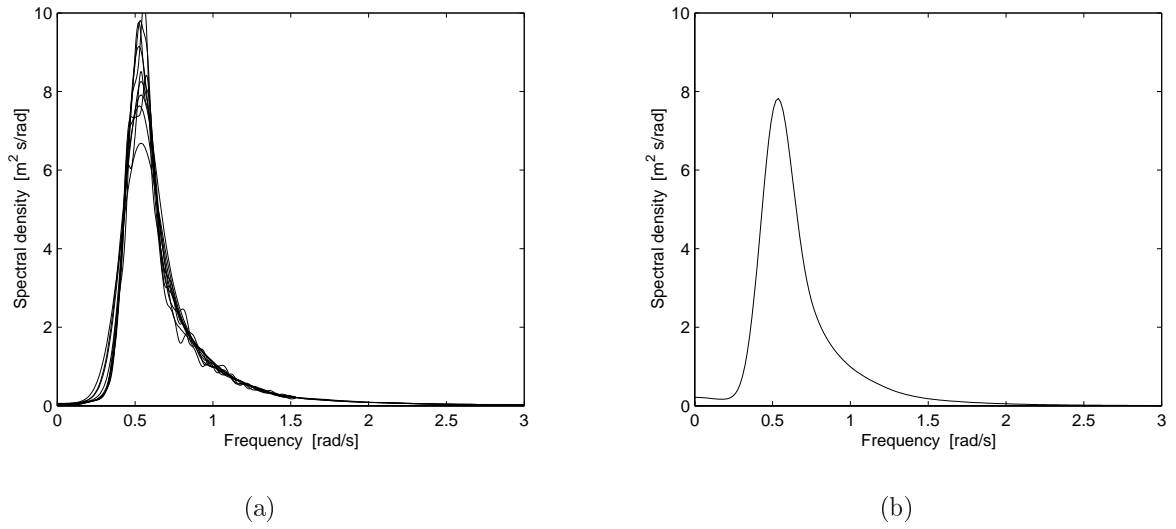


Figure 6.5: (a) Spectral densities of simulated time series. (b) The spectral density of field data.

Table 6.4: Descriptive statistics of the simulated data. Results from 10 simulations.

		Mean	Min/Max	St.dev
H_{m0}	[m]	6.97	6.76/7.14	0.11
T_{m02}	[s]	7.83	7.75/7.89	0.04
T_{m01}	[s]	8.91	8.81/9.00	0.06
T_{m24}	[s]	4.06	4.02/4.09	0.02
T_p	[s]	11.65	10.95/12.05	0.03
\bar{k}	[rad/m]	0.0662	0.0651/0.0674	0.0007
\bar{k}_1	[rad/m]	0.0520	0.0511/0.0531	0.0006
a_{rms}	[m]	2.45	2.39/2.53	0.04
σ	[m]	1.74	1.69/1.79	0.03
ρ_3	[-]	0.151	0.128/0.190	0.022
ρ_4	[-]	3.09	3.00/3.14	0.05
ϵ_2	[-]	0.544	0.538/0.558	0.007
ϵ_4	[-]	0.855	0.852/0.858	0.002
s	[-]	0.037	0.036/0.040	0.002

6.1.3 Laboratory data from HR Wallingford

In 1997 a series of experiments in the UK Coastal Research Facility (UKCRF) at HR Wallingford were made. Measurements of the surface elevation at different water depths along a beach provide useful information for validation of the finite water depth models. It should be noted that the present models cover the wave conditions at a water depth with a given constant value, and not conditions over a changing water depth. Thus, no shoaling effects are included. One should also note that the results from laboratory experiments can be influenced by effects in a closed basin, such as reflection from the edges, water flowing back from the shore or standing waves in the basin.

Experimental setup and data description

A thorough description of the UKCRF is given in Simons et al. (1995). The basin is 36 meters wide and has a maximum water depth of 80 cm. Long-crested (2D) as well as short-crested (3D) waves are generated according to a given peak period, a significant wave height and a wave spectrum. The water depth is constant for a length of 8.36 meters after the wave generator, and then the beach rises at a slope ratio of 1:20. Seven wave probes measuring the surface elevation were located at different water depths along the tank. Figure 6.6 shows the experimental setup.

Measurements made at four different water depths are analyzed; at $d = 80$ cm and $d = 78$ cm, which represent relatively deep water; and at $d = 41$ cm and $d = 31$ cm, representing intermediate water depths. The main focus will be on the deep water data (80 m, 78 m). However, the other data (41 m, 31 m) will be included for comparison. Only long-crested (2D) waves are considered. Other aspects of data collected during the same experiments are given in Memos (2002).

A time series of irregular waves was generated from a JONSWAP spectrum with spectral parameter $\gamma_J = 3$. The peak period was $T_p = 1.2$ s, and the significant wave height was $H_S = 9$ cm. In full scale, typically 1:100, this corresponds to a sea state with $T_p = 12$ s, and $H_S = 9$ m. The following results will be presented in full scale 1:100. The sampling frequency was 25 Hz with a sampling interval of 1020 s, corresponding to 2 hours 50 minutes in full scale.

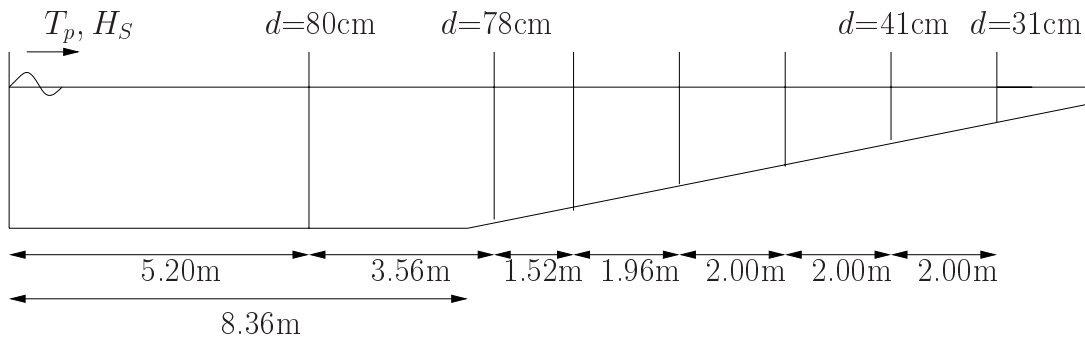


Figure 6.6: Experimental setup at HR Wallingford.

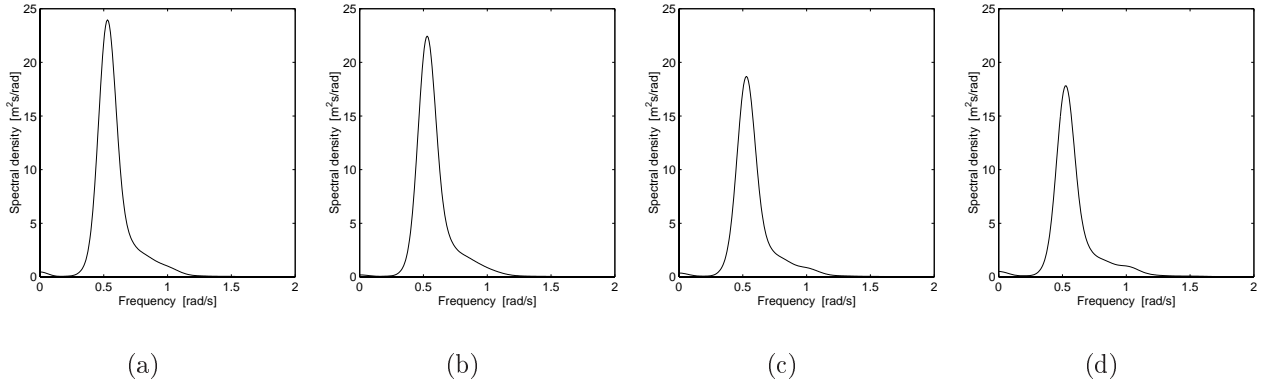


Figure 6.7: The spectral density. (a) $d = 80$ m, (b) $d = 78$ m, (c) $d = 41$ m, (d) $d = 31$ m.

Figure 6.7 shows the spectral density at the different water depths. The peak frequencies are the same at the different water depths, i.e., $\omega_p = 0.53$ rad/s. The spectra are quite similar except for more energy in deep water. This is to be expected since the significant wave height will decrease with decreasing water depth, which is confirmed by the data in Table 6.5.

A closer look at the spectral density in the lower tail is shown in Fig. 6.8. The energy in this part of the spectrum corresponds to the difference-frequency effects, and should increase with decreasing water depth. However, the figure shows that the spectral density for $d = 80$ m has a large peak around $\omega \approx 0.044$ rad/s, which is not physically correct. The amount of energy in this low frequency part of the spectrum is larger at $d = 80$ m than the energy at both $d = 78$ m and $d = 41$ m. The spectral density for $d = 78$ is expected to be quite similar to the spectral density for $d = 80$ m. Thus, the data at $d = 80$ m and $d = 78$ m are filtered at 0.2 rad/s before proceeding with the analysis. This gave only minor changes in the descriptive statistics (at second decimal).

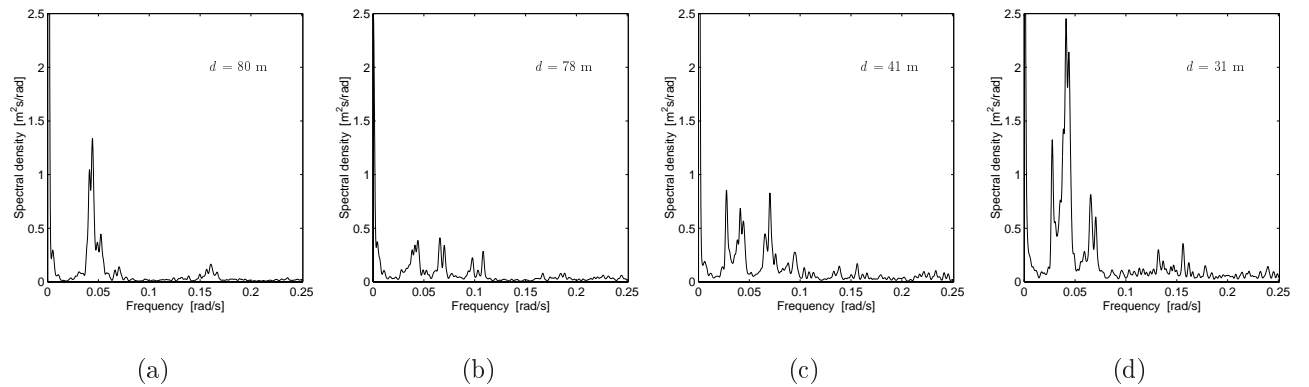


Figure 6.8: Low frequency part of spectral density. (a) $d = 80$ m, (b) $d = 78$ m, (c) $d = 41$ m, (d) $d = 31$ m.

The descriptive statistics of the data at the different water depths are shown in Table 6.5. The data for $d = 80$ m and $d = 78$ m are calculated from the filtered time series. One should note that the significant wave height decreases with decreasing water depth, while the peak period is constant. The mean period between maxima is significantly reduced at intermediate water depths, which indicates that the surface elevation is more broad-banded, and that nonlinear effects become more important. This is also indicated by the increase in both skewness and kurtosis. There appear to be more secondary peaks in the time series at $d = 41$ m and $d = 31$ m than at $d = 80$ m and $d = 78$ m. In the zero-crossing analysis, wave of amplitude less than $1/10$ of the standard deviation above or below the zero line are neglected. Some of the secondary peaks at $d = 41$ m and $d = 31$ m occur around the zero line with amplitude larger than $1/10$ of the standard deviation, and thus the number of waves with small wave period and corresponding small wave height is larger than expected. This is observed in Fig. 6.9. It is uncertain if this is caused by physical effects or by the instrumentation. One should also note that in the water depth $d = 31$ m, the wave steepness for a few individual waves is quite large ($k\eta_{a,\max} = 0.51$). The second order Stokes criterion, which at this water depth is given by the criterion for no bump in the trough in Eq. (3.20), leads to $\bar{k}\eta_a < 0.38$. So, obviously there will be a few individual waves at this water depth not satisfying the second order Stokes criterion. Despite of all the

Table 6.5: Descriptive statistics of laboratory data.

		$d = 80$ m	$d = 78$ m	$d = 41$ m	$d = 31$ m
H_{m0}	[m]	9.10	8.87	8.25	8.12
T_{m02}	[s]	10.34	10.35	8.72	8.88
T_{m01}	[s]	10.75	10.76	10.38	10.38
T_{m24}	[s]	7.65	7.60	1.86	2.05
T_p	[s]	11.87	11.87	11.87	11.87
\bar{k}	[rad/m]	0.0378	0.0377	0.0542	0.0546
\bar{k}_1	[rad/m]	0.0351	0.0351	0.0402	0.0430
a_{rms}	[m]	3.22	3.14	2.92	2.87
σ	[m]	2.28	2.22	2.06	2.03
ρ_3	[-]	0.250	0.236	0.270	0.405
ρ_4	[-]	3.04	3.15	3.24	3.50
ϵ_2	[-]	0.284	0.283	0.646	0.603
ϵ_4	[-]	0.673	0.679	0.977	0.973
s	[-]	0.042	0.041	0.043	0.046

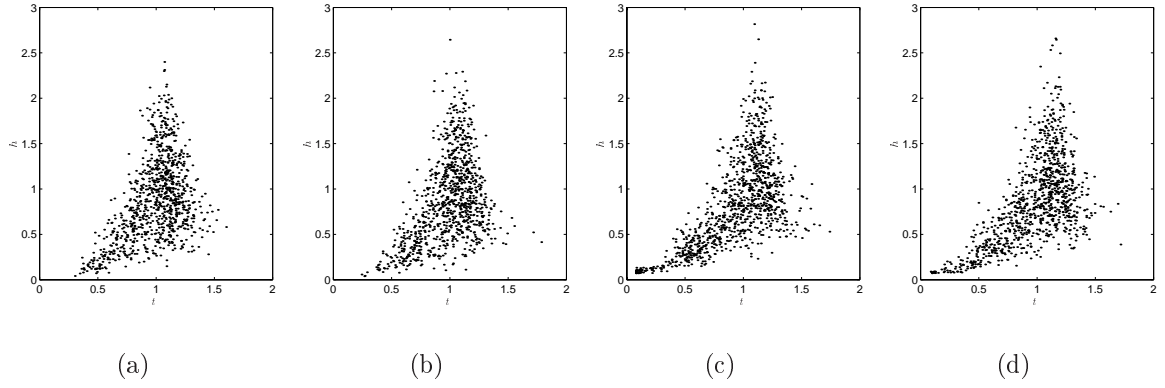


Figure 6.9: Paired plot of the normalized wave period and the corresponding normalized wave height from the laboratory data. (a) $d = 80$ m, (b) $d = 78$ m, (c) $d = 41$ m, (d) $d = 31$ m.

concerns associated with the data at $d = 41$ m and $d = 31$ m, they are included for comparison. However, the comments given above should be kept in mind when considering the results for all the data (crests, troughs, heights and periods).

Numerical simulation results

Numerical simulations of 10 time series with length of 3 hours have been made. The time step was 0.4 s. Similarly to the simulations of the Japan field data, the spectra from the filtered laboratory data were used as input spectra for the simulations.

The descriptive statistics of the simulated data are shown in Table 6.6. The significant wave height and the peak period correspond well with the laboratory data given in Table 6.5, while the wave periods T_{m01} , T_{m02} and T_{m24} deviate slightly. There is a large difference in the parameters ρ_3 and ρ_4 , for which the values are almost equal at the different water depths as opposed to the laboratory data where the values increase with decreasing water depths. One should recall that the simulations are based on wave conditions at a water depth with a given constant value. The simulations also only include second order nonlinear effects. Thus, the laboratory data can include other nonlinear effects in the intermediate water depths $d = 41$ m and $d = 31$ m, which are not captured by the second order model.

Table 6.6: Descriptive statistics of simulated data for comparison with laboratory data.

		$d = 80$ m	$d = 78$ m	$d = 41$ m	$d = 31$ m
H_{m0} [m]	Mean	9.17	8.97	8.32	8.26
	Min/Max	8.86/9.31	8.67/9.12	8.04/8.46	7.98/8.39
	St.dev	0.16	0.15	0.15	0.15
T_{m02} [s]	Mean	10.14	10.14	9.17	9.04
	Min/Max	10.02/10.20	10.02/10.19	9.05/9.24	8.94/9.10
	St.dev	0.06	0.06	0.06	0.06
T_{m01} [s]	Mean	10.63	10.63	10.30	10.14
	Min/Max	10.51/10.69	10.51/10.69	10.18/10.36	10.02/10.19
	St.dev	0.06	0.06	0.06	0.06
T_{m24} [s]	Mean	7.30	7.23	2.97	3.25
	Min/Max	7.00/7.44	6.94/7.38	2.91/3.02	3.19/3.31
	St.dev	0.14	0.14	0.04	0.04
T_p [s]	Mean	11.83	11.83	11.85	11.96
	Min/Max	11.64/12.05	11.64/12.05	11.64/12.05	11.77/12.19
	St.dev	0.12	0.12	0.12	0.12
\bar{k} [rad/m]	Mean	0.0393	0.0393	0.0495	0.0530
	Min/Max	0.039/0.040	0.039/0.040	0.049/0.051	0.053/0.054
	St.dev	0.0005	0.0005	0.0006	0.0005
a_{rms} [m]	Mean	3.24	3.17	2.94	2.92
	Min/Max	3.13/3.29	3.07/3.22	2.84/2.99	2.82/2.97
	St.dev	0.06	0.05	0.05	0.05
σ [m]	Mean	2.29	2.24	2.08	2.07
	Min/Max	2.22/2.33	2.17/2.28	2.01/2.11	1.99/2.10
	St.dev	0.04	0.04	0.04	0.04
ρ_3 [-]	Mean	0.174	0.172	0.163	0.157
	Min/Max	0.143/0.201	0.142/0.198	0.126/0.194	0.112/0.193
	St.dev	0.018	0.017	0.022	0.027
ρ_4 [-]	Mean	3.07	3.07	3.07	3.09
	Min/Max	2.90/3.31	2.91/3.31	2.90/3.31	2.91/3.32
	St.dev	0.13	0.13	0.13	0.13
ϵ_2 [-]	Mean	0.315	0.316	0.512	0.506
	Min/Max	0.310/0.320	0.310/0.321	0.505/0.518	0.499/0.511
	St.dev	0.003	0.004	0.004	0.004
ϵ_4 [-]	Mean	0.694	0.700	0.946	0.933
	Min/Max	0.680/0.720	0.687/0.726	0.945/0.947	0.932/0.935
	St.dev	0.013	0.013	0.001	0.001
s [-]	Mean	0.043	0.042	0.043	0.046
	Min/Max	0.042/0.044	0.041/0.043	0.042/0.045	0.045/0.047
	St.dev	0.001	0.001	0.001	0.001

6.2 Results for wave crest heights and wave trough depths

6.2.1 Results for Draupner field data

The sum frequency and difference frequency components were discussed in Chapter 3.5, and the magnitude of these effects was illustrated in Fig. 3.11. This discussion will be continued here by looking at the composition of the wave from a simulated time series.

In order to see the influence of the different second order terms, the surface elevation is decomposed into the linear part, the sum frequency part and the difference frequency part. The results shown in Figs. 6.10 and 6.11 are from one of the simulated time series corresponding to the Draupner field data, which can be considered as deep water waves since the effect of water depth is insignificant (see Chapter 2.4). The simulations corresponding to the other data sets give similar results.

Figure 6.10 shows a part of a simulated time series with a detailed composition of the wave. The total second order wave is also shown together with the result from combining only the linear part and the sum frequency part. From the figure it is clear that the sum frequency component is locally quite significant, especially when the linear amplitude is high, and it will give a large contribution to the total wave crest height. At the same time, the difference frequency component will reduce this effect. The largest contribution from the sum frequency and difference frequency terms is for the highest wave amplitudes. Thus, the nonlinearity of the waves will increase with increasing crest height and trough depth.

Figure 6.11 shows the different components of the spectral density from a simulated time series. One should note the different scale of the spectral density compared to Fig. 6.1 (a), where the spectral density for the sum frequency and difference frequency component would not have been visible at all. The sum frequency component has no contribution for low frequencies, and due to the large linear component, it will not give any significant influence around the peak frequency of the second order spectral density spectrum. However, for higher frequencies, $\omega \gtrsim 2$, it is of the same magnitude as the linear component and will give a significant contribution. For very high frequencies, $\omega \gtrsim 3$, the linear component is almost zero, and the second order spectral density is only dependent on the sum frequency component. The difference frequency component gives only a contribution for the lowest frequencies.

The variation with water depth of the sum and difference frequency effects will be discussed in Chapter 6.2.3.

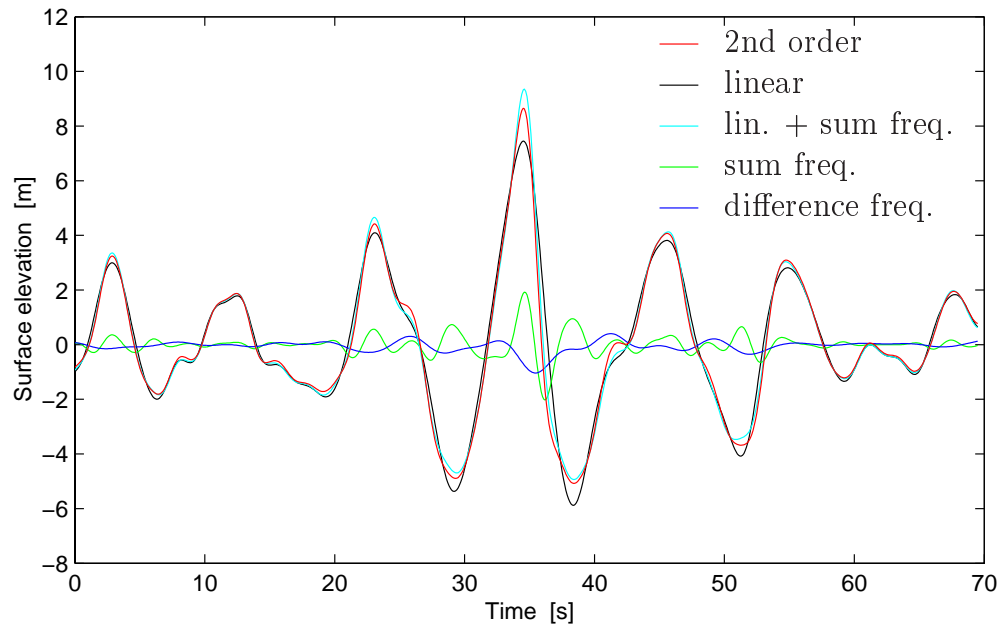


Figure 6.10: Different components of the surface elevation in a simulated time series.

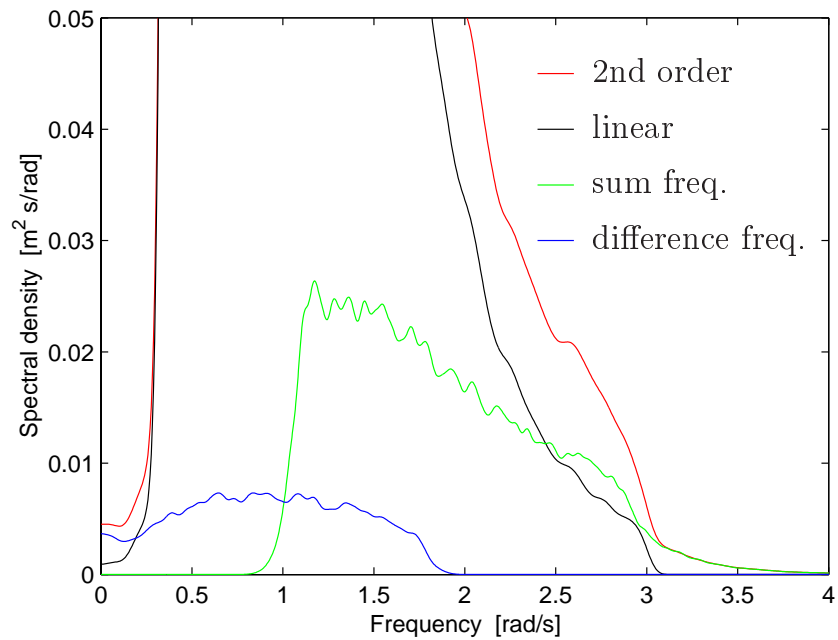


Figure 6.11: Different components of the spectral density in a simulated time series ($\omega_p = 0.56$ rad/s).

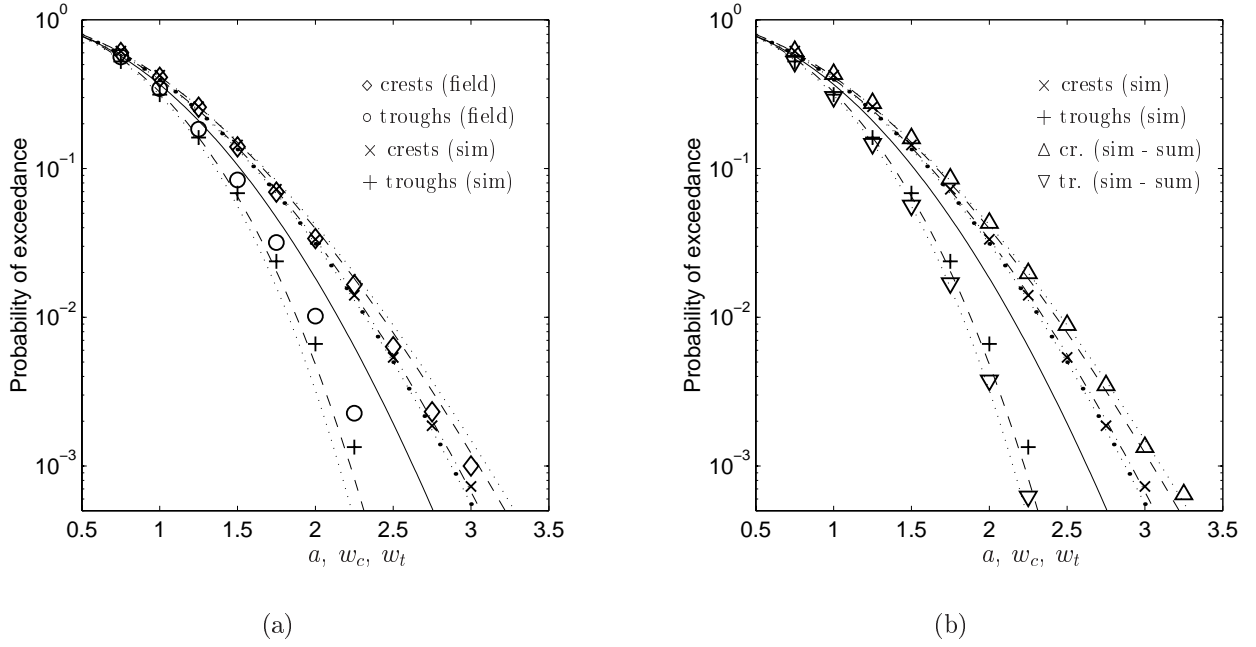


Figure 6.12: Marginal distributions; — Rayleigh distribution, — — extended second order model, \cdots second order Stokes model, — \cdot — Forristall 2D-model, $\cdot \bullet \cdots$ Forristall 3D-model. The lines to the right and left of the Rayleigh distribution corresponds to the crest height and trough depth, respectively.

Figure 6.12 shows the marginal distributions of the crest heights and trough depths in terms of probability of exceedance. In (a) the field data are compared with the simulated data, which are based on the second order wave theory. In (b) the simulated data using the full second order surface are compared with the simulated data where only the linear and the sum frequency components are included, which will be referred to as the simulated sum frequency data. Each simulated data point is the mean value of 10 data points based on the kernel density estimate of the 10 simulations.

The results of the field data compared with the theoretical distributions were discussed in Figs. 3.9 (b) and 3.12. From Fig. 6.12 (a) it is clear that the simulated wave crest data agrees well with the field data. For the highest wave amplitudes the simulated wave crests slightly underpredict the field data. They fall between the Rayleigh distribution and the extended second order model, while the Forristall models agree well with the data. The simulated wave trough data underpredicts the field data, and the extended second order model agrees quite well with the simulated data.

The results in Fig. 6.12 (b) clearly show the difference between using only the linear and sum frequency components and using the full second order surface including difference frequency components. The results support the observations of the surface elevation in Fig. 6.10, i.e., by including difference frequency terms the nonlinearity of the waves is decreased. Thus the simulated sum frequency data deviate more from the Rayleigh distribution, and these simulated

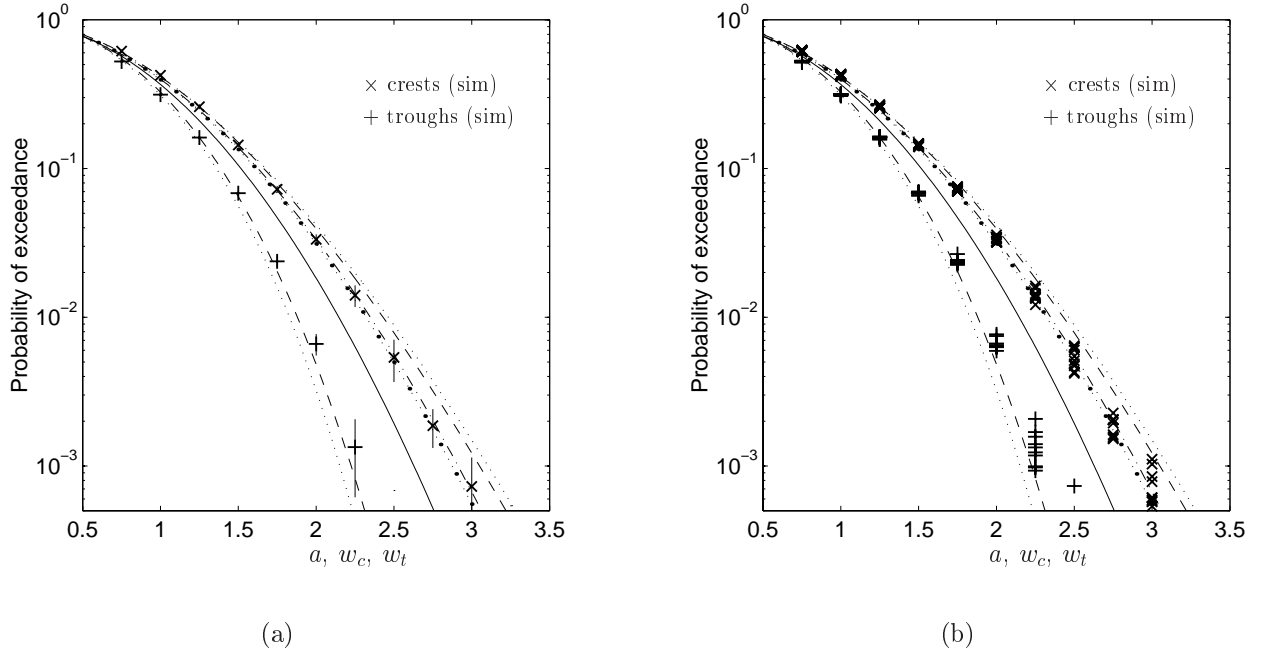


Figure 6.13: Marginal distributions; — Rayleigh distribution, -- extended second order model, ... second order Stokes model, -.- Forristall 2D-model, ··· Forristall 3D-model. The lines to the right and left of the Rayleigh distribution corresponds to the crest height and trough depth, respectively. (a) Mean values from simulations with confidence intervals. (b) Results from the individual simulations.

data are also well described by the second order Stokes model. One should remember that the extended second order model only includes the difference frequency component in a simplified manner, i.e., the narrow-band approximation, as mentioned earlier (see Fig. 3.11).

The variation in the simulated data is shown in Fig. 6.13. The mean values of the 10 simulations are shown in Fig. 6.13 (a). Confidence intervals given by $\pm 2\text{Var}[x]^{1/2}$, where x is a vector of the 10 simulation points, are indicated for each mean value. Figure 6.13 (b) show the results from the individual simulations.

Figure 6.14 shows the conditional distribution of w_{c2} and w_{t2} given w_{c1} and w_{t1} , respectively, in terms of the probability of exceedance. Here N_c and N_t denote the number of field data cases in each class of w_{c1} and w_{t1} , respectively. The results show similar behavior as observed in Fig. 6.12 (a), although the data show larger variation. Overall, the crest data are fairly well described by the second order Stokes model and the extended second order model. In the lower two figures the data fall between the extended second order model and the Forristall models for larger values of w_{c2} and w_{t2} . In the interval $1.75 < w_{c1}, w_{t1} < 2.0$, the data are questionable for large values of w_{c2} and w_{t2} due to few data cases. The trough data, on the other hand, fall between the Rayleigh distribution and the extended second order model. The simulated data agrees fairly well with the field data, but gives a small underprediction of both crest data and trough data for large values of w_{c2} and w_{t2} .

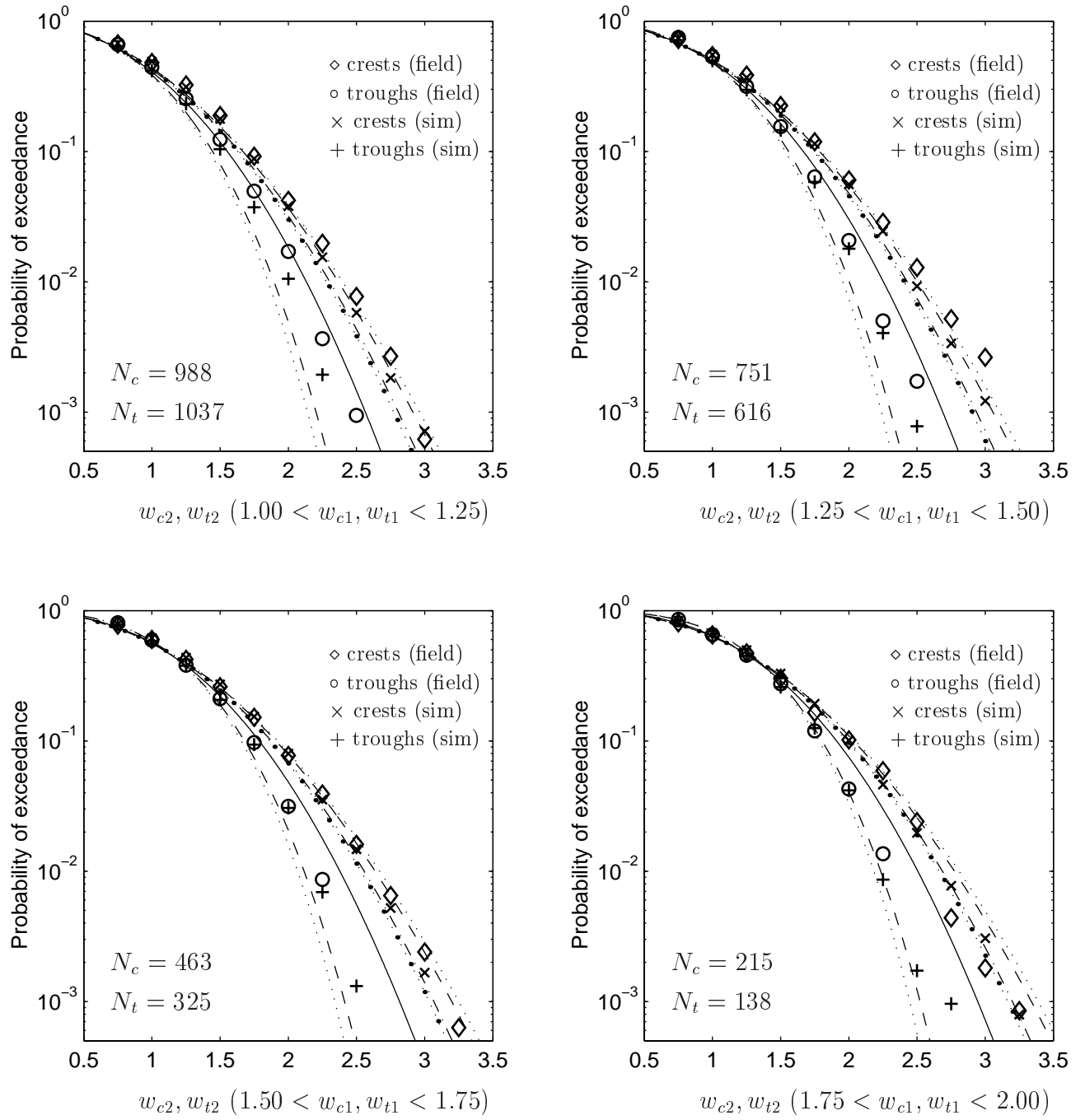


Figure 6.14: Conditional distributions; — Rayleigh distribution, -- extended second order model, ... second order Stokes model, - · - Forristall 2D-model, · · · Forristall 3D-model. The lines to the right and left of the Rayleigh distribution corresponds to the crest height and trough depth, respectively.

6.2.2 Results for Japan Sea field data

The calculated values of the wave parameters for the field data from Japan sea are shown in Table 6.7. Compared to the calculated values of the Draupner field data in Tables 3.1, 3.2 and 3.3 the term $f^-(\bar{k}d)$ is much higher, which leads to a larger difference in the characteristic steepness parameters r and r_+ . This indicates a larger difference between including the difference frequency terms and only using the sum frequency terms. This is to be expected since the water depth is shallower, and the nonlinear effects are expected to be larger. Also the correlation coefficients, and thereby the parameters κ_c^2 and κ_t^2 , are smaller. The parameters S_1 and U_r are of same magnitude, as opposed to the parameters for the Draupner field data, where $U_r \approx 1/6 S_1$. This is due to the change in water depth. However, the Forristall parameters still remain quite similar.

Figure 6.15 shows a histogram of the field data and the corresponding kernel density estimate for (a) the wave crest heights and (b) the wave trough depths, compared with the probability density function of the Rayleigh distribution, the second order Stokes model and the extended second order model. The Forristall models are not included in (a) because it would be difficult to see the difference between them and the second order models. However, they are included in the probability of exceedance in Fig. 6.16, where the difference is more visible. The second order Stokes model and the extended second order model agree well with the wave crest data. They also agree well with the trough data for $w_t \gtrsim 1$, but there are some discrepancies for smaller values of w_t .

Figure 6.16 shows the probability of exceedance of the wave crest heights and the wave trough depths. In (a) the field data are compared with the simulated data, and in (b) the simulated data (full second order) are compared with the simulated sum frequency data. Both the crest height and the trough depth field data are well described by the extended second order model except for the largest wave crest heights, where the data follows the second order Stokes model. This is different from the Draupner field data, where the second order models appeared to be more nonlinear than the data. As already discussed, it is clear that the difference between the second order Stokes model and the extended model is larger than it was in Fig. 6.12. This is consistent

Table 6.7: Calculated values of the Japan Sea field data.

r	[-]	0.108	ρ_c	[-]	0.227	κ_c^2	[-]	0.249
r_+	[-]	0.147	ρ_t	[-]	0.174	κ_t^2	[-]	0.186
R	[-]	0.019	$f^+(\bar{k}d)$	[-]	1.074	$f^-(\bar{k}d)$	[-]	0.283
S_1	[-]	0.0493	U_r	[-]	0.0422	$\kappa_{F,2D}^2$	[-]	0.244
α_{2D}	[-]	0.372	β_{2D}	[-]	1.893	$\kappa_{F,3D}^2$	[-]	0.244
α_{3D}	[-]	0.370	β_{3D}	[-]	1.890			

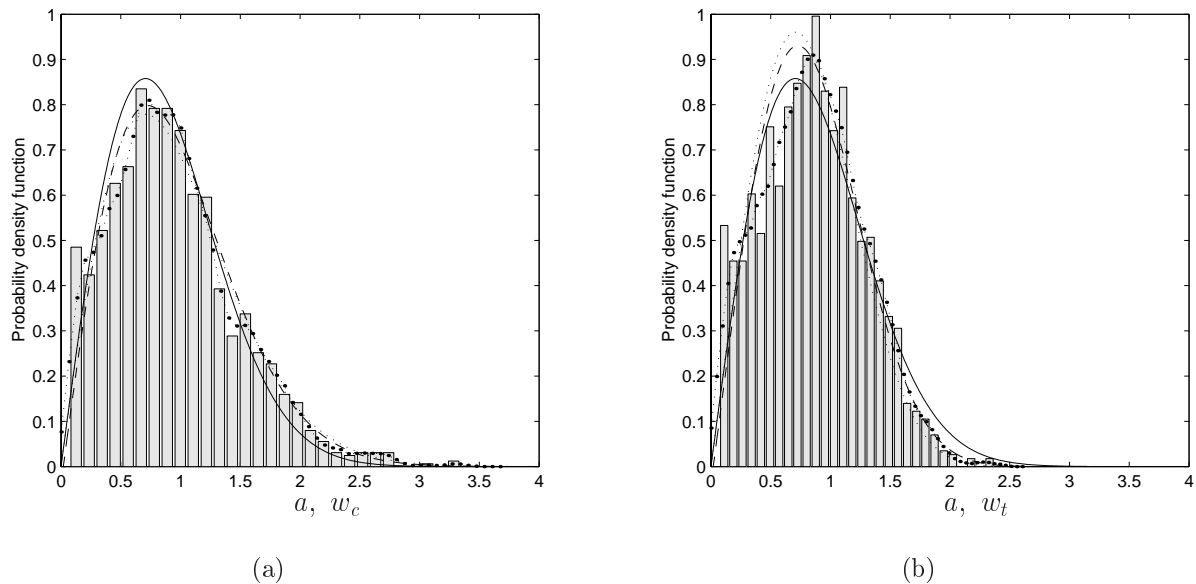


Figure 6.15: Marginal probability density functions and histogram of the field data (a) wave crest height (b) wave trough depth; $\cdot \bullet \cdots$ kernel density estimate, — Rayleigh distribution, — — extended second order model, \cdots second order Stokes model.

with that the effect of only including sum frequency effects will be amplified when the nonlinear effects are expected to increase as the water depth decreases, as compared with the results by the extended model. There is almost no difference between the Forristall models, which fall between the Rayleigh distribution and the extended second order model. The difference between the Forristall models and the extended second order model is slightly less than it was in Fig. 6.12. The simulations agree well with the field data for low and moderate values of w_c and w_t ($w_c, w_t \lesssim 2$). Similar to the Draupner data, the simulations underpredict the wave crest height for large values of w_c . On the other hand, the simulations overpredicts the wave trough depths for large values of w_t , as opposed to the Draupner data. The simulated wave crest heights are well predicted by the Forristall models. Since the parameters in the Forristall models are based upon second order simulations, this is to be expected.

Figure 6.17 shows the conditional probability of exceedance. Only two intervals are considered since the number of crest heights and trough depths in the intervals with higher values of w_{c1} and w_{t1} were below 100. The data show similar behavior as observed in Fig. 6.16 (a), although not so clearly. The second order Stokes model and the extended second order model agree fairly well with the data, but seem to underpredict the data for large values of w_{c2} . The simulated data do not show the same strong nonlinear behavior as the laboratory data. Overall the simulated wave crest data are well described by the extended second order model and the Forristall models, while the simulated wave trough data fall between the Rayleigh distribution and the extended second order model.

The conditional expectation of the wave amplitude given the previous wave amplitude is shown in Appendix H.1, and the results are similar to the results for the Draupner field data.

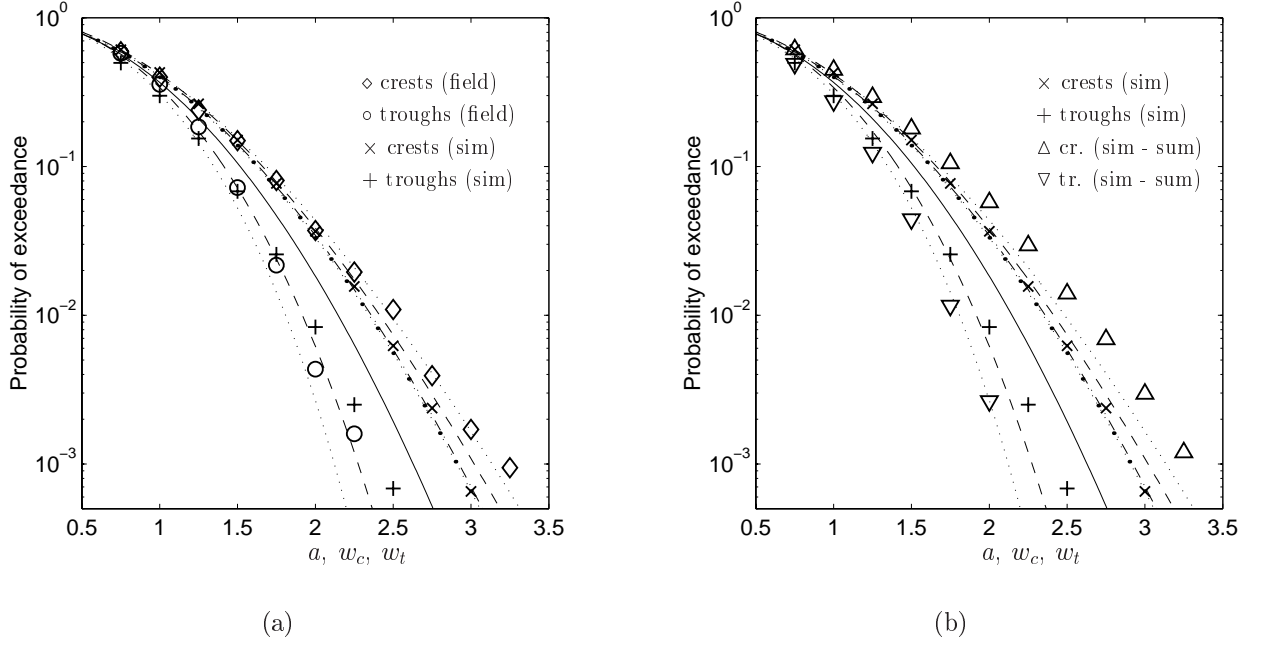


Figure 6.16: Marginal distributions; — Rayleigh distribution, -- extended second order model, ... second order Stokes model, - · - Forristall 2D-model, · · · Forristall 3D-model. The lines to the right and left of the Rayleigh distribution corresponds to the crest height and trough depth, respectively.

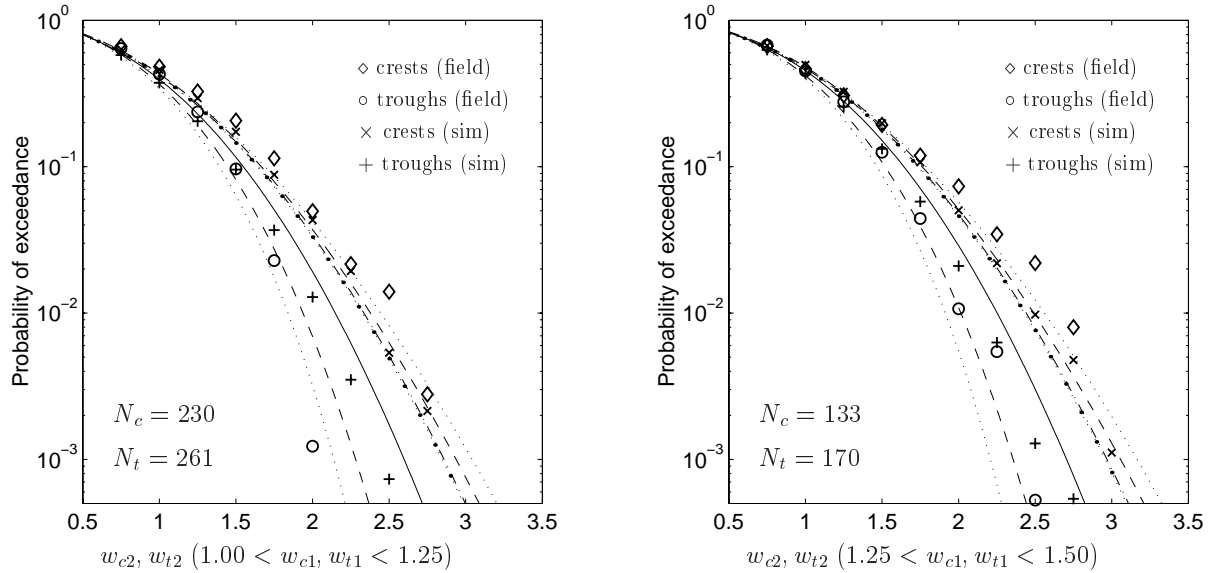


Figure 6.17: Conditional distributions; — Rayleigh distribution, -- extended second order model, ... second order Stokes model, - · - Forristall 2D-model. The lines to the right and left of the Rayleigh distribution corresponds to the crest height and trough depth, respectively.

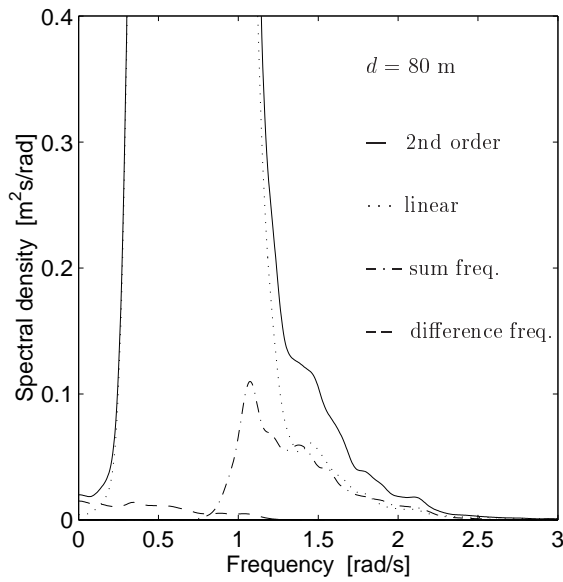
6.2.3 Results for laboratory data

The calculated values of the wave parameters for the laboratory data from HR Wallingford are shown in Table 6.8. One should note that the characteristic steepness parameter r is higher at the intermediate water depths than in deep water. This is also the case for r_+ , and the difference between r and r_+ increases with decreasing water depth. This indicates that including the difference-frequency effect in the theoretical models is more important when the water depth decreases. One should also note the significant increase in U_r with decreasing water depth.

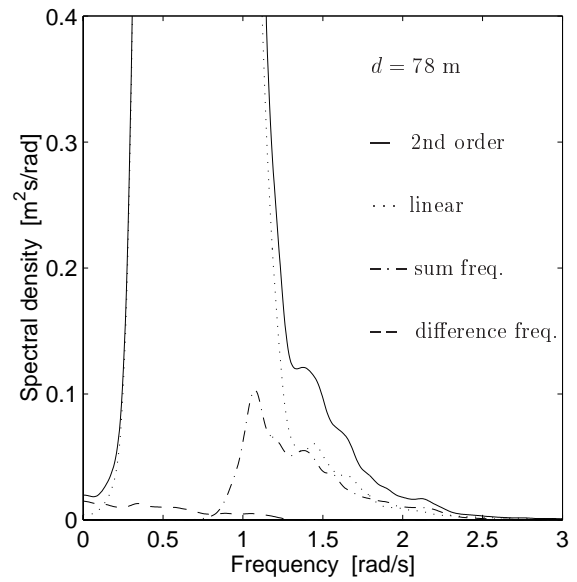
Figure 6.18 shows the different components of the spectral density from a simulated time series for the different water depths. Overall, the spectral density components show the same behavior as in Fig. 6.11, i.e., the sum frequency component has no contribution for low frequencies, while the difference frequency component only gives a contribution for the lowest frequencies. It is clear from the figure that the contributions for the different components increase with decreasing water depth. Especially the contribution from the difference frequency component increases significantly from $d = 80$ m to $d = 31$ m. This supports the importance of including the nonlinear effects, which become more important as the water depth decreases.

Table 6.8: Calculated values of the laboratory data.

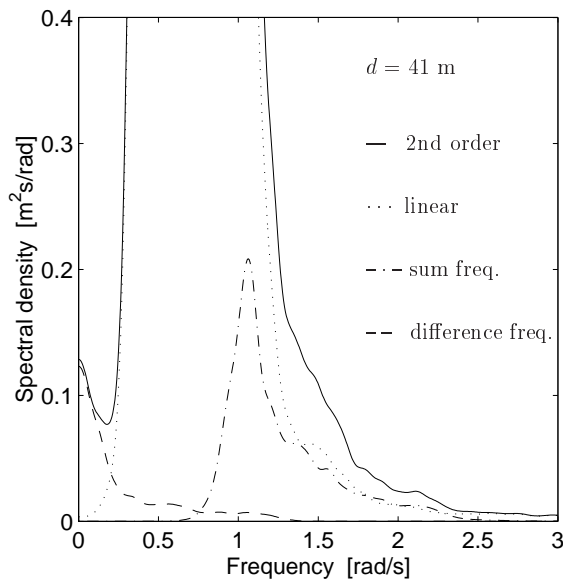
		$d = 80$ m	$d = 78$ m	$d = 41$ m	$d = 31$ m
r	[-]	0.101	0.097	0.124	0.119
r_+	[-]	0.124	0.121	0.174	0.204
$f^+(\bar{k}d)$	[-]	1.019	1.023	1.098	1.303
$f^-(\bar{k}d)$	[-]	0.192	0.200	0.314	0.545
R	[-]	0.012	0.012	0.025	0.043
ρ_c	[-]	0.446	0.436	0.453	0.490
ρ_t	[-]	0.396	0.391	0.484	0.450
κ_c^2	[-]	0.478	0.479	0.487	0.525
κ_t^2	[-]	0.416	0.399	0.505	0.470
S_1	[-]	0.0504	0.0491	0.0490	0.0483
U_r	[-]	0.0144	0.0152	0.0741	0.1474
α_{2D}	[-]	0.370	0.369	0.376	0.383
β_{2D}	[-]	1.891	1.895	1.895	1.898
$\kappa_{F,2D}^2$	[-]	0.477	0.478	0.485	0.524



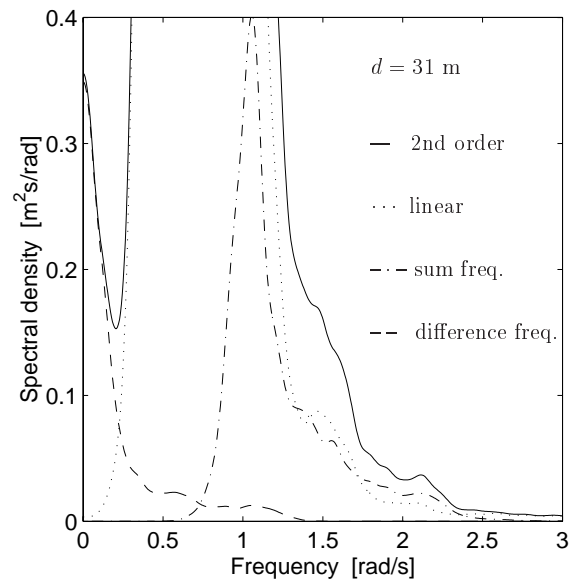
(a)



(b)



(c)



(d)

Figure 6.18: Different components of the spectral density in a simulated time series. (a) $d = 80$ m; (b) $d = 78$ m; (c) $d = 41$ m; (d) $d = 31$ m.

Figure 6.19 shows the marginal distributions of the crest heights and trough depths in terms of probability of exceedance. The laboratory data are compared with the simulated data for different water depths. The data are also compared with the second order models, the Rayleigh distribution and the Forristall 2D-model. The generated laboratory waves are two-dimensional, thus only the Forristall crest height model for 2D waves is considered. It is clear from the figure that the second order models, and in particular the second order Stokes model, exhibit a more nonlinear behavior with decreasing water depth. The laboratory data show a strong nonlinear behavior, and the wave crest data are slightly underpredicted by the second order Stokes model for $d = 80$ m and $d = 78$ m. However, the crest data are fairly well predicted by the second order Stokes model for $d = 41$ m and $d = 31$ m. The wave trough data generally fall between the second order Stokes model and the extended second order model.

The simulated wave data show a slightly less nonlinear behavior than the laboratory data. They underpredict the wave crest data, while they slightly overpredict the wave trough data. The simulated data are well described by the extended second order model and the Forristall 2D-model.

One should also note that the theory for the second order models is valid for horizontal sea bed, while the measurements are taken where the sea bed is rising.

Figure 6.20 shows the difference between the simulated data and the simulated sum frequency data for the different water depths. It is clear that by using only the linear and the sum frequency component, the wave crests are higher and the trough depths are shallower than by using the full model. This is in good agreement with the discussion of the influence of the different second order terms in Chapter 6.2.1. The difference increases with decreasing water depth. Overall, the simulated sum frequency data are well described by the second order Stokes model.

Figures 6.21 and 6.22 show the conditional distribution of w_{c2} and w_{t2} given w_{c1} and w_{t1} , respectively, in terms of the probability of exceedance. Only two intervals are considered since the number of crest heights or trough depths in the intervals with higher values of w_{c1} and w_{t1} were below 100. Both the laboratory data and the simulated data show a large variation. Overall the wave crest heights are fairly well predicted or slightly underpredicted by the second order models and the Forristall 2D-model. For the wave trough depths it is difficult to make a firm conclusion.

The conditional expectation of the wave amplitude given the previous wave amplitude is shown in Appendix H.1, and the results are similar to the results for the Draupner field data and the Japan Sea field data.

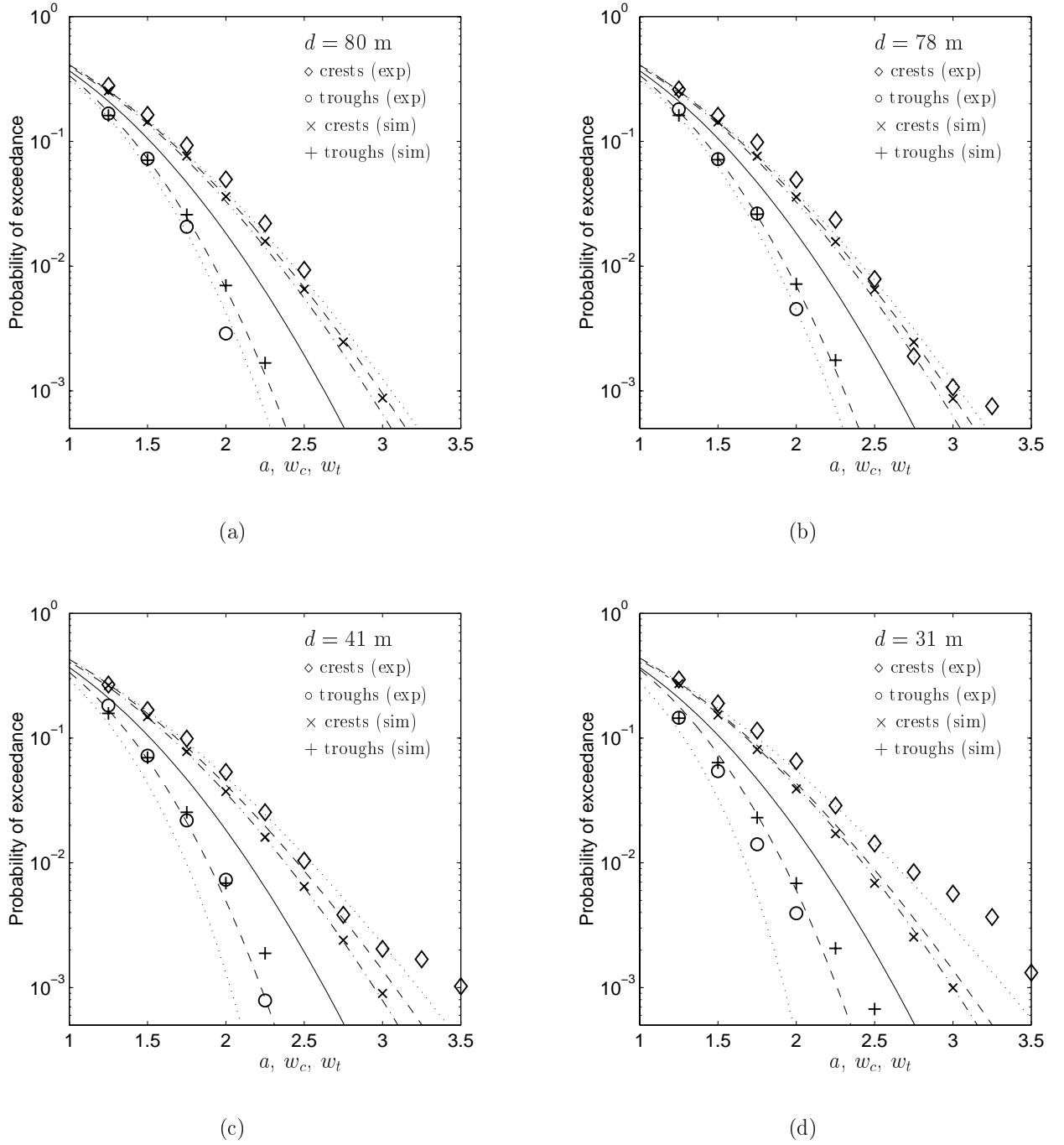


Figure 6.19: Marginal distributions of laboratory data compared with simulated data. — Rayleigh distribution, -- extended second order model, \cdots second order Stokes model, -.- Forristall 2D-model. The lines to the right and left of the Rayleigh distribution corresponds to the crest height and trough depth, respectively. (a) $d = 80$ m; (b) $d = 78$ m; (c) $d = 41$ m; (d) $d = 31$ m.

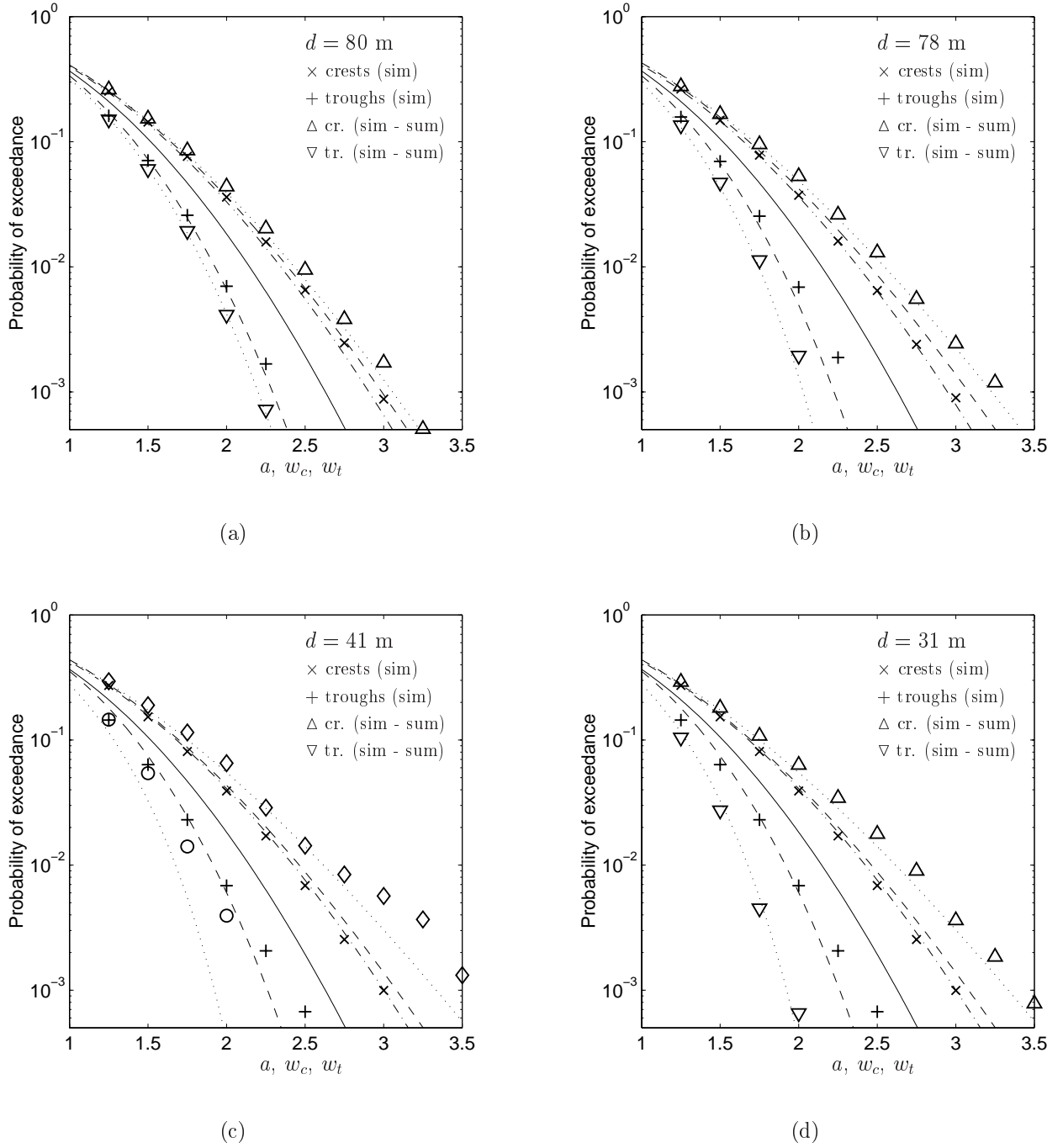


Figure 6.20: Marginal distributions of the simulated data compared with the simulated sum frequency data. — Rayleigh distribution, - - extended second order model, \cdots second order Stokes model, - · - Forristall 2D-model. The lines to the right and left of the Rayleigh distribution corresponds to the crest height and trough depth, respectively. (a) $d = 80$ m; (b) $d = 78$ m; (c) $d = 41$ m; (d) $d = 31$ m.

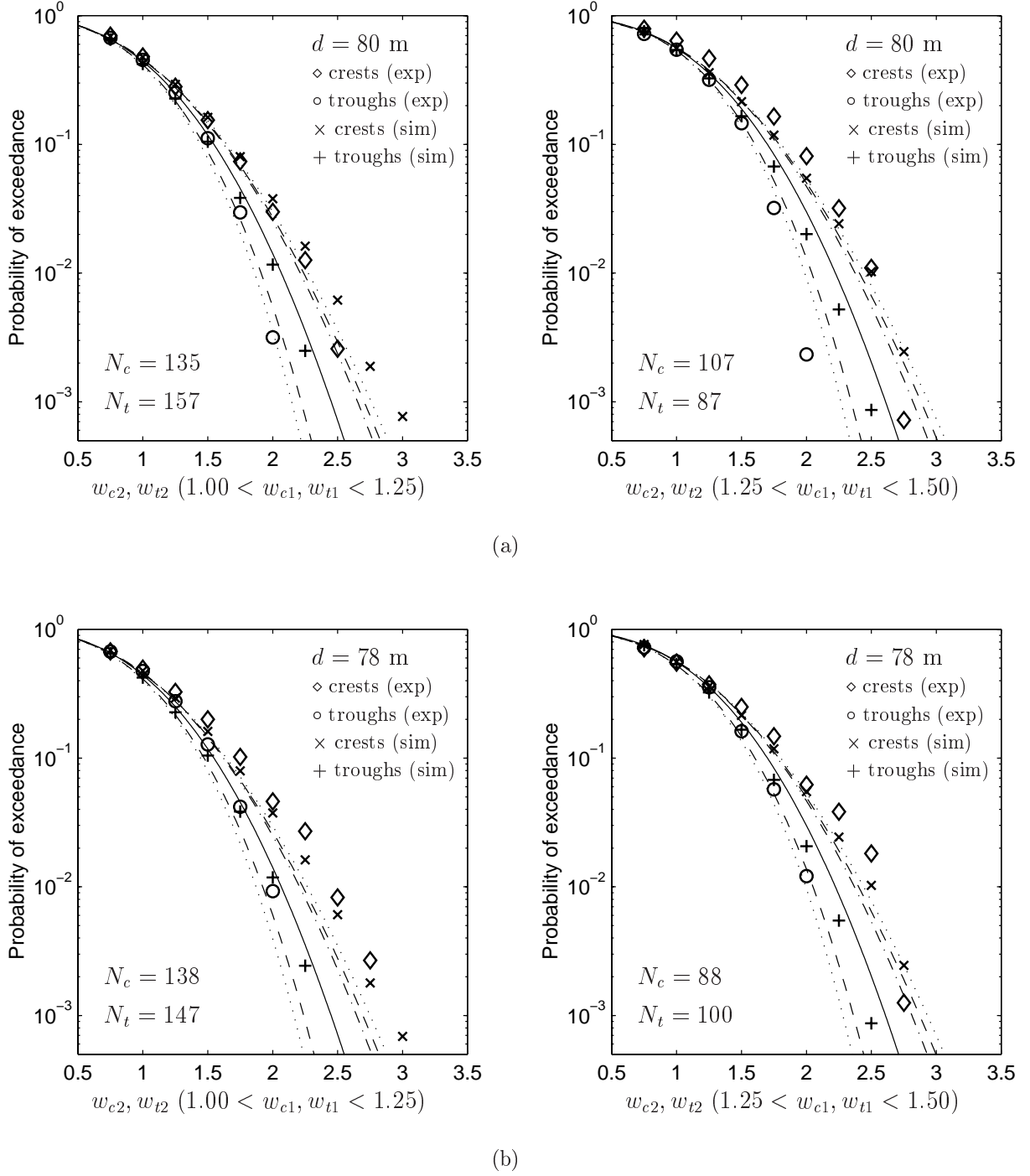
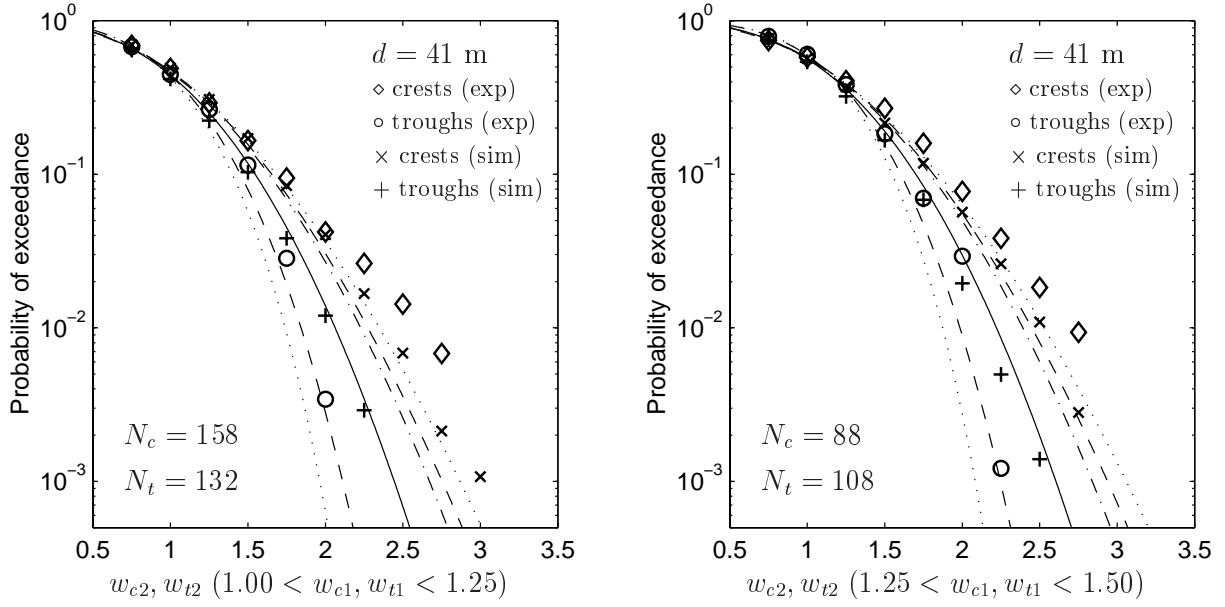
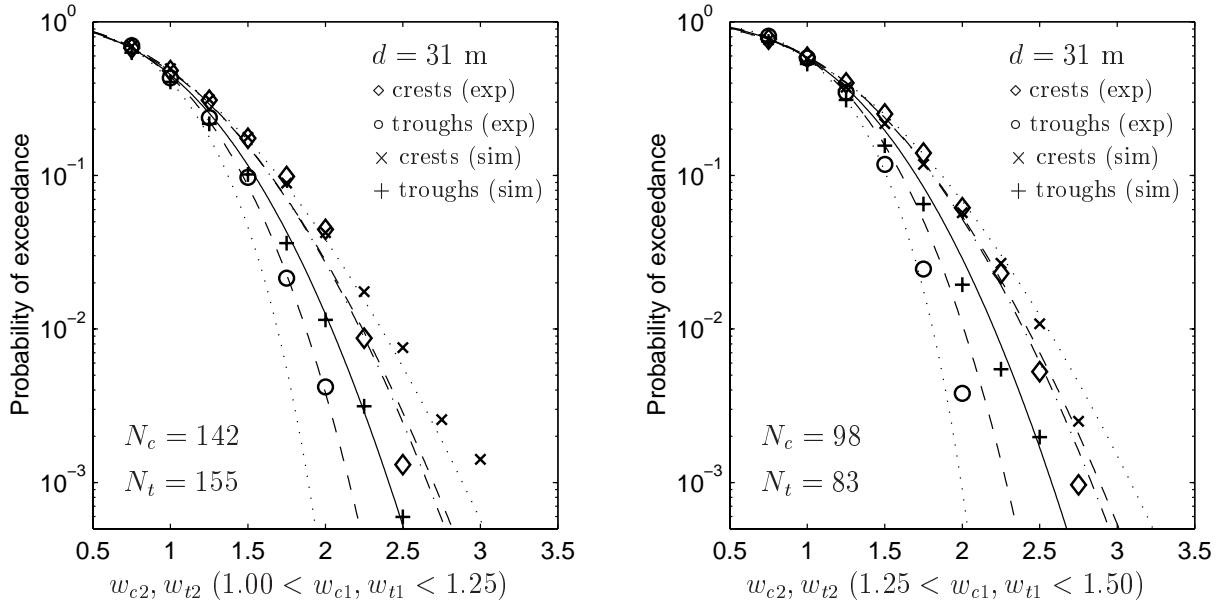


Figure 6.21: Conditional distributions; — Rayleigh distribution, -- second order model, ... second order Stokes model, --- Forristall 2D-model. The lines to the right and left of the Rayleigh distribution corresponds to the crest height and trough depth, respectively. (a) $d = 80$ m (b) $d = 78$ m.



(a)



(b)

Figure 6.22: Conditional distributions; — Rayleigh distribution, -- second order model, \cdots second order Stokes model, --- Forristall 2D-model. The lines to the right and left of the Rayleigh distribution corresponds to the crest height and trough depth, respectively. (a) $d = 41$ m (b) $d = 31$ m.

6.3 Results for wave heights

6.3.1 Wave height results for Draupner field data

The results for the wave heights from the Draupner field data were described in the discussion of the Nataf transformation in Chapter 4.2. In this chapter these results will be compared with data from the numerical simulations. The calculated values of the wave parameters from the Draupner field data are summarized in Table 6.9. The correlation coefficients were given in Table 4.1.

Figure 6.23 (a) shows the marginal distribution of the normalized wave heights in terms of the probability of exceedance. The simulated data agree well with the field data, but for larger values of h ($h \gtrsim 2$) they slightly underpredict the field data. The data are well described by the Nataf model for low values of h , and they fall between the Nataf model and the Næss (1985) model for larger values of h .

In order to see the difference between the probability of occurrence of an individual wave height and two successive wave heights, the probability of two successive wave heights exceeding the value h is shown in Fig. 6.23 (b). The simulated data agree very well with the field data, and they are both well described by the Nataf model. For larger values of h the Næss (1985) model also agrees well with the data. From the figures it is clear that the probability of exceedance of a given value is reduced when considering two successive waves, as would be expected. The probability of an individual wave height exceeding e.g. the normalized significant wave height (indicated by the vertical dotted line) is in the range $[0.095, 0.137]$, depending on the model considered, while when considering two successive wave heights exceeding the same value it is reduced to $[0.027, 0.052]$.

Table 6.9: Calculated values of the Draupner field data.

h_{rms}	[m]	4.78	α	[-]	0.978
ρ_N	[-]	-0.689	β	[-]	2.039
ρ_h	[-]	0.411	κ_h^2	[-]	0.436

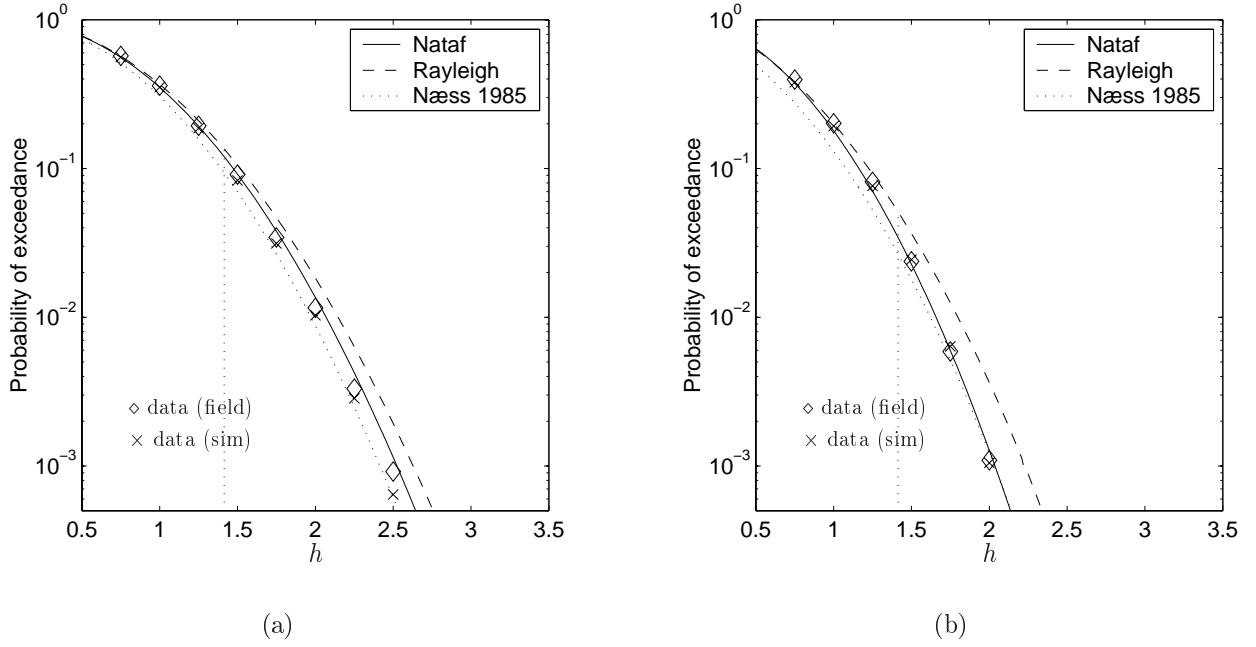
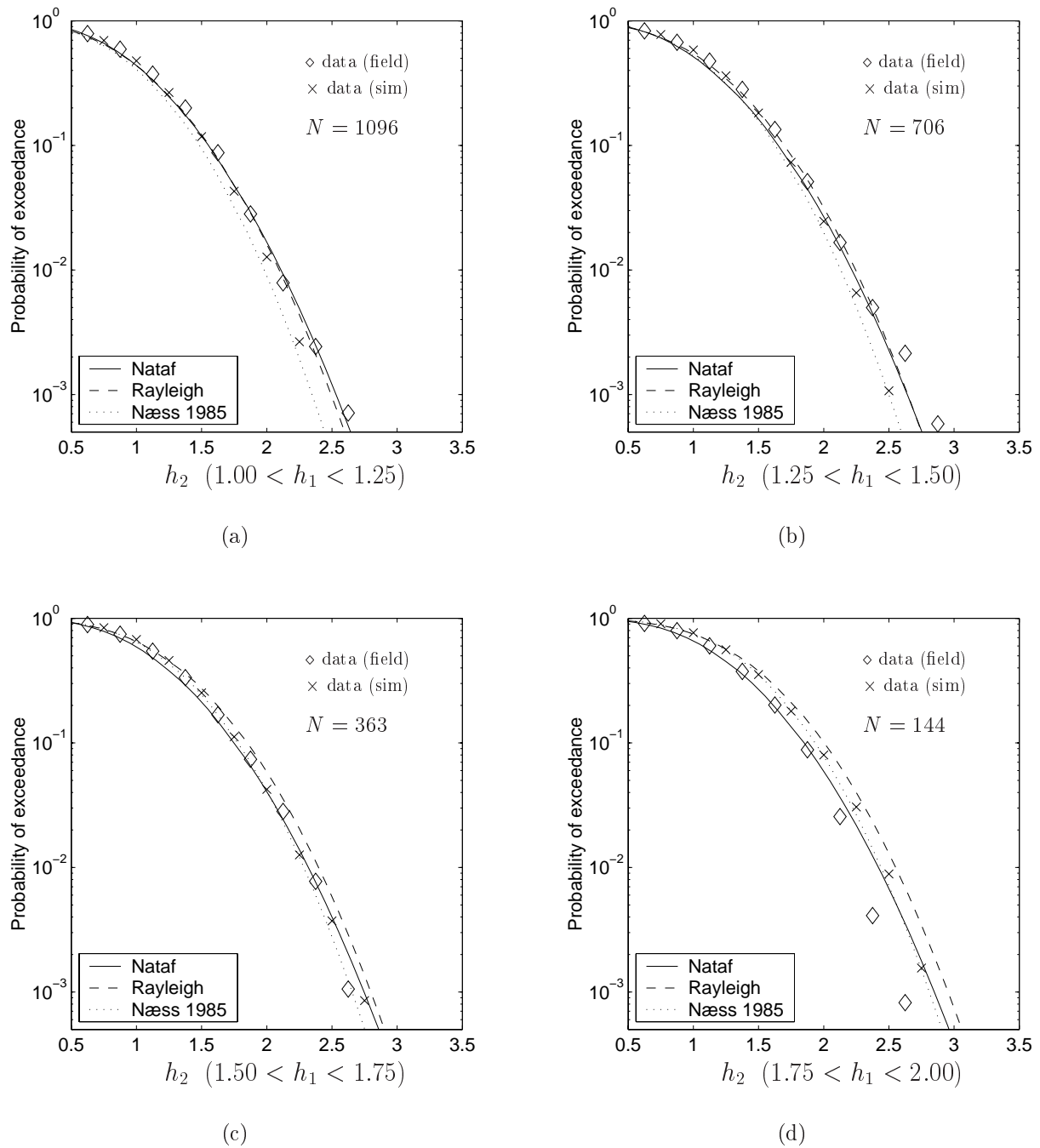


Figure 6.23: (a) Probability of exceedance for an individual wave ($P(H > h)$); (b) Probability of exceedance for two successive waves ($P(H_1 > h, H_2 > h)$). The normalized significant wave height of 1.41 is indicated by the vertical dotted line.

Figure 6.24 shows the conditional distribution of h_2 given h_1 in terms of probability of exceedance. Here N denotes the number of field data cases in each class of h_1 . Overall the simulated data agree well with the field data, but in (d) they overpredict the field data. The Nataf model gives a good prediction of the data except for larger values of h_2 in (d). The other models have a different behavior than the Nataf model. In (a) and (b) the Rayleigh distribution gives the best prediction of the data compared with the Næss (1985) model, while in (c) and (d) it is the opposite.

Figure 6.24: Conditional distributions of h_2 given h_1 .

6.3.2 Wave height results for Japan Sea field data

The calculated values of the field data from the Japan Sea are given in Table 6.10. Compared to the values from the Draupner field data, the correlation coefficients are smaller, but the other parameter values are quite similar. The correlation coefficients for the transformed wave heights, $\rho_{W,12}$, $\rho_{W,13}$ and $\rho_{W,14}$, show the same behavior as for the Draupner field data, i.e., that the dependency between the wave heights decreases rapidly.

Figure 6.25 (a) shows a histogram of the wave heights with the kernel density estimate compared with the probability density functions of the Rayleigh distribution, the Næss (1985) model and the Nataf model, which for the marginal distribution is the two-parameter Weibull distribution. The Nataf model lies between the Rayleigh distribution and the Næss (1985) model. For larger values of h ($h \gtrsim 1.5$) both the Nataf model and the Næss (1985) model agree well with the data, while the Rayleigh distribution overpredicts the wave heights.

Figure 6.25 (b) shows the marginal distributions in terms of probability of exceedance. The field data are compared with the simulated data, the Rayleigh distribution, the Næss (1985) model and the Nataf model. The simulated data agree well with the field data, and both fall between the Nataf model and the Næss (1985) model.

A histogram of the transformed wave heights is shown in Fig. 6.26 (a). The data are compared with a standard Gaussian probability density function. The figure shows that the resulting transformation is slightly skewed to the left, but overall the resulting distribution is approximately Gaussian. The dependency structure is examined by a paired plot of the transformed wave heights h_1 and h_2 , which is shown in Fig. 6.26 (b). The solid line is a contour plot of the standard Gaussian distribution. The dependency structure of the transformed wave heights of h_1 and h_2 is quite similar to the one for a standard Gaussian distribution. Thus, from Fig. 6.26 (a) and (b) it is seen that the Nataf model is suitable, and that it correctly takes care of the dependency structure.

Table 6.10: Calculated values of the Japan Sea field data.

h_{rms}	[m]	4.87	α	[-]	0.969
ρ_N	[-]	-0.630	β	[-]	2.071
ρ_h	[-]	0.321	$\rho_{W,12}$	[-]	0.294
κ_h^2	[-]	0.343	$\rho_{W,13}$	[-]	0.078
			$\rho_{W,14}$	[-]	0.026

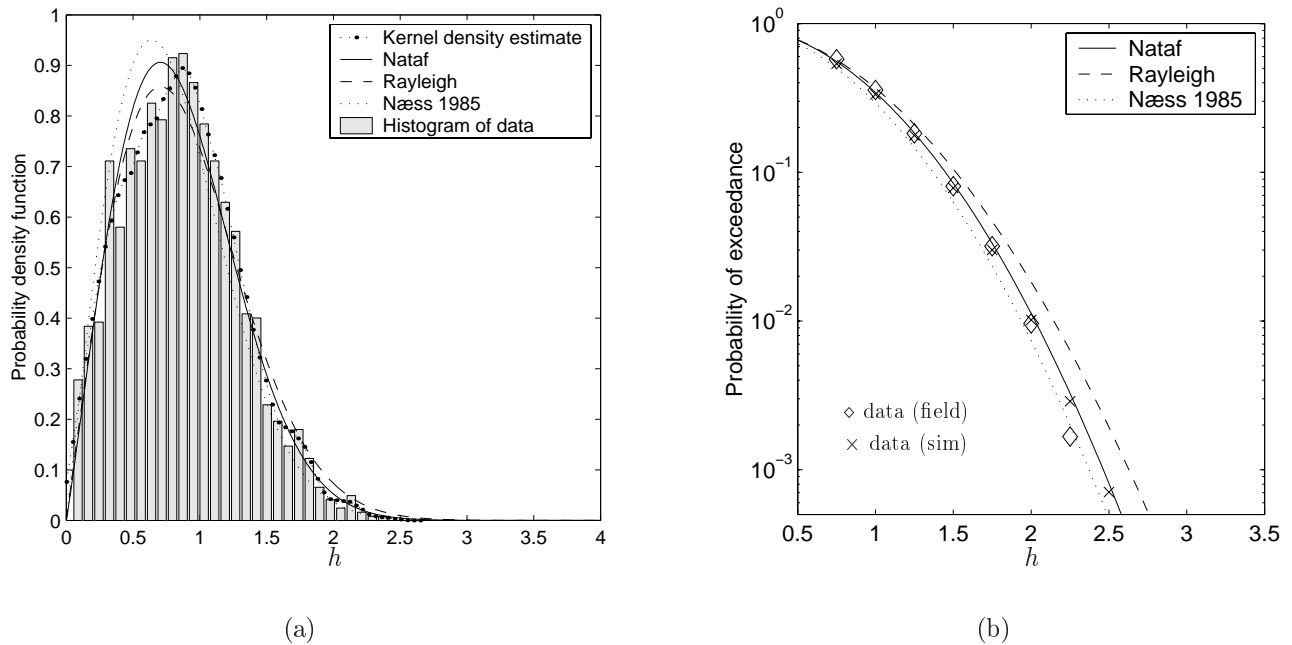


Figure 6.25: (a) Marginal probability density functions of the normalized wave heights. (b) Marginal distributions in terms of probability of exceedance.

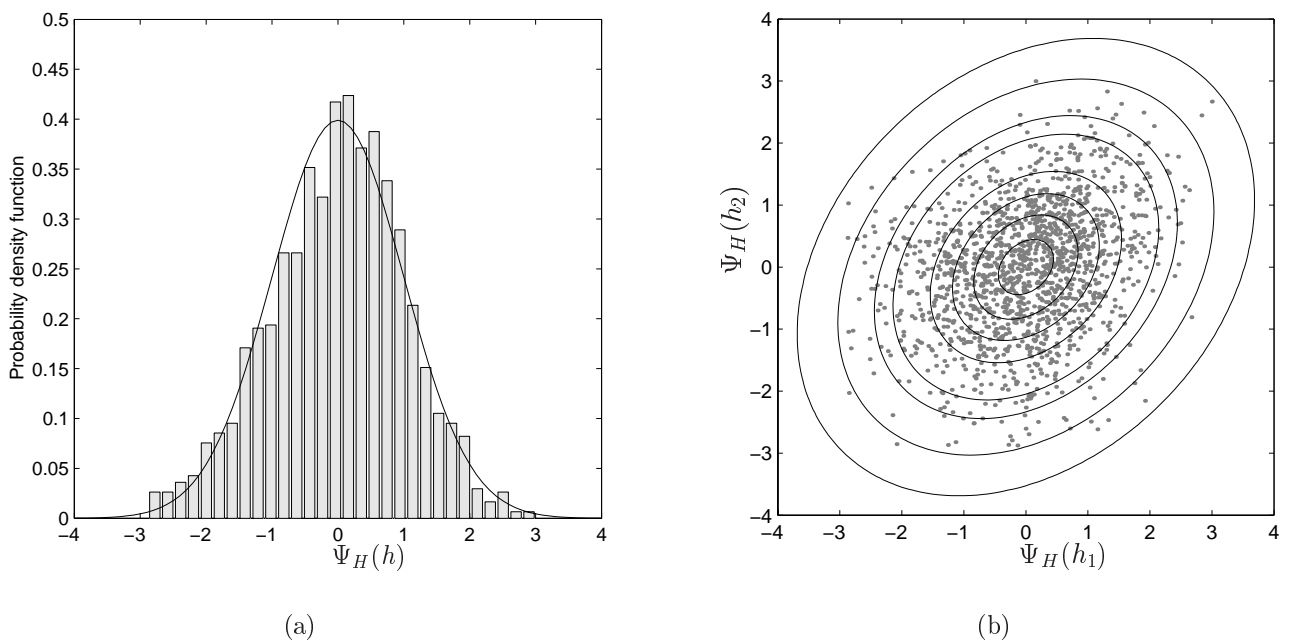


Figure 6.26: (a) Histogram of the transformed wave height data. The solid line is the standard Gaussian probability density function. (b) Paired plot of the transformed wave height between h_1 and h_2 compared with a contour plot of a standard Gaussian distribution.

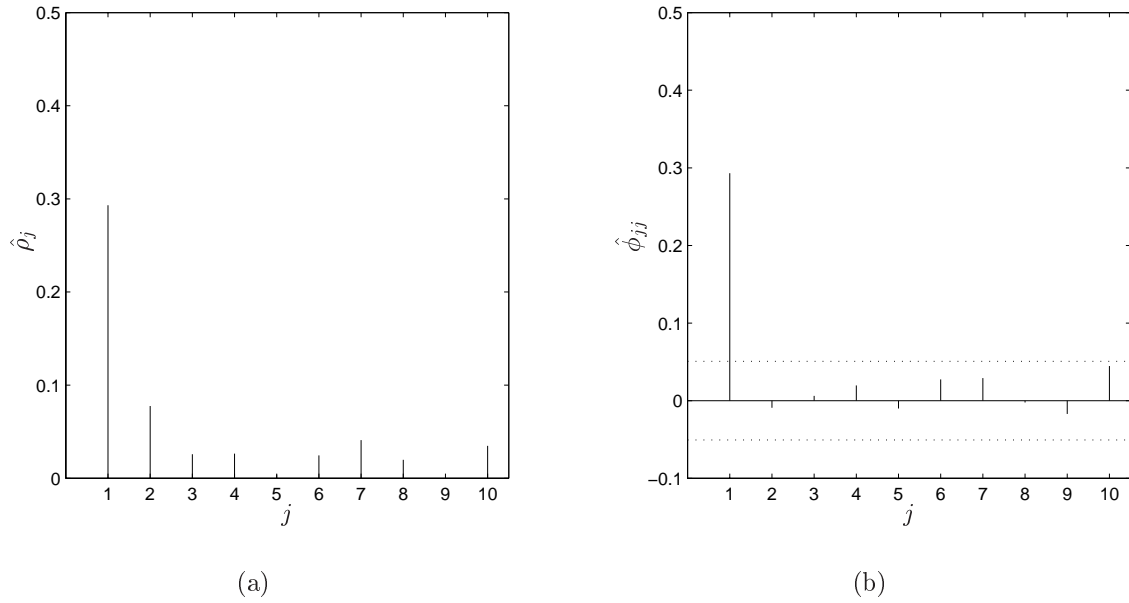


Figure 6.27: (a) Sample autocorrelation function, and (b) sample partial autocorrelation function of the transformed wave heights. The dotted line indicates $\pm 2(\text{Var}[\hat{\phi}_{jj}])^{1/2}$.

Figure 6.27 shows the sample ACF (a) and PACF (b) of the transformed wave heights. Since the ACF decreases approximately exponentially, and the PACF has one spike at $j = 1$, the process appears to be an AR(1) process. A likelihood ratio test with $p = 3$ as described in Chapter 4.3.1 resulted in $n = 518$, and the observed value of the likelihood ratio statistic was $-2 \ln \Lambda_{obs} = 6.22$. From tables $\chi^2_{0.044,2} = 6.25$, which means that the hypothesis that the correlation coefficients agree with an AR(1) model (i.e., are given by Eq. (4.42)) would not be rejected at 4.4% significance level.

Figure 6.28 shows the conditional distribution of h_2 given h_1 in terms of probability of exceedance. Only two intervals are considered since the number of wave heights in the intervals with higher values of h_1 were below 100. The simulated data agree well with the field data. The Nataf model gives a good prediction of the data. While the Næss (1985) model slightly underpredicts the data in (a), it agrees well with the data in (b). The Rayleigh distribution slightly overpredicts the data in both (a) and (b).

The conditional expectation of the wave height given the previous wave height is shown in Appendix H.2, and the results are similar to the results for the Draupner field data.

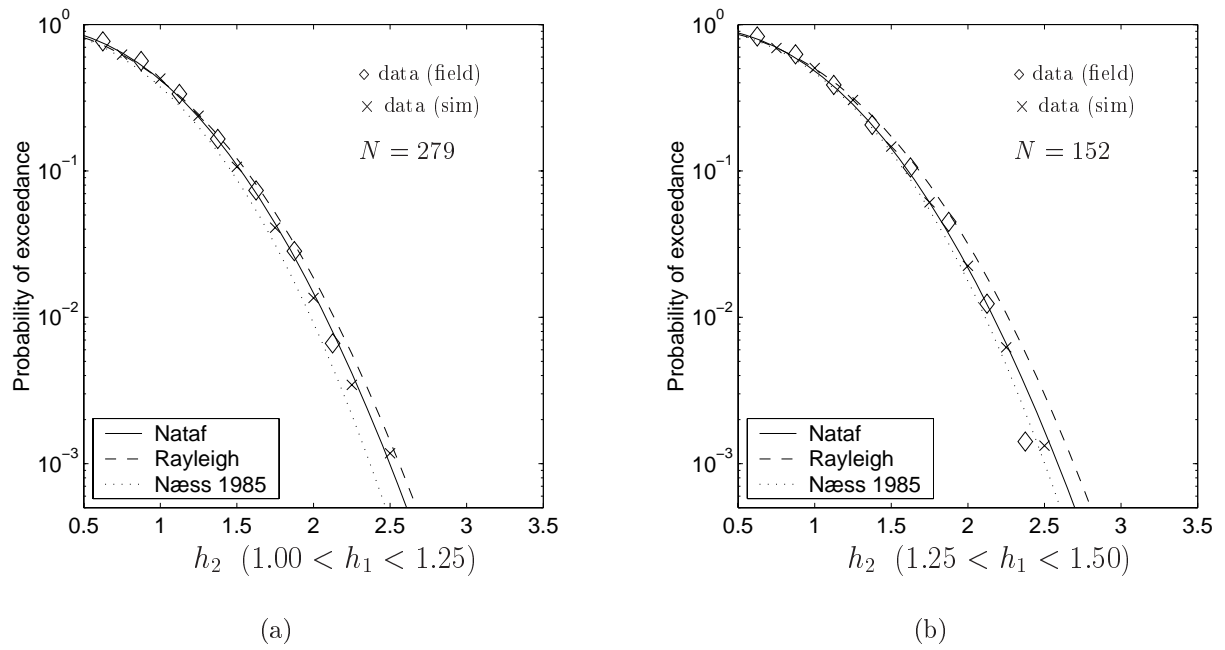


Figure 6.28: Conditional distributions of h_2 given h_1 in terms of probability of exceedance.

6.3.3 Wave height results for laboratory data

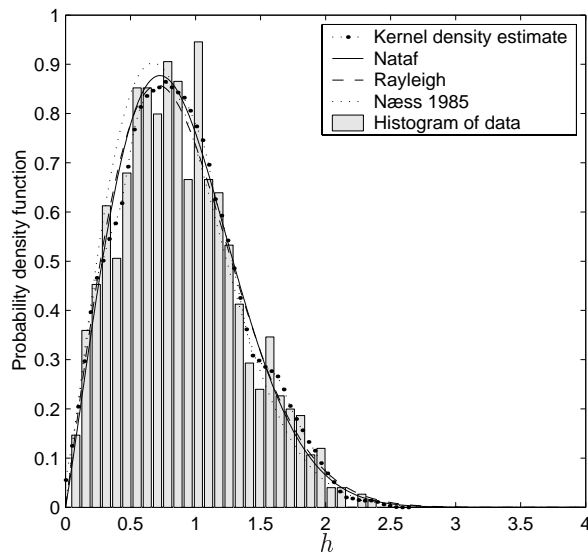
The calculated values of the wave parameters for the laboratory data are given in Table 6.11. The correlation coefficients are larger compared with both the Draupner field data and the Japan Sea field data. The parameters ρ_N are also larger in magnitude. The variation with water depth is quite small. One should note that the comments given earlier regarding the shoaling effects, which is not included, are still valid.

Figure 6.29 shows a histogram of the wave heights with the kernel density estimate compared with the Nataf model, the Næss (1985) model and the Rayleigh distribution for the different water depths. The Nataf model agrees well with the data for $d = 80$ m and $d = 78$ m, and the difference between the models is small. For $d = 41$ m and $d = 31$ m the figures show that there is a large number of waves with small wave heights. This is probably due to that secondary peaks in the time series give a larger number of waves with small wave period and corresponding small wave height than expected, which was discussed in Chapter 6.1.3 and illustrated in Fig. 6.9. The fitted Weibull distribution, and thus the Nataf model, is then slightly skewed to the right compared with the other models. This will also influence the two-dimensional results that will be discussed in the following.

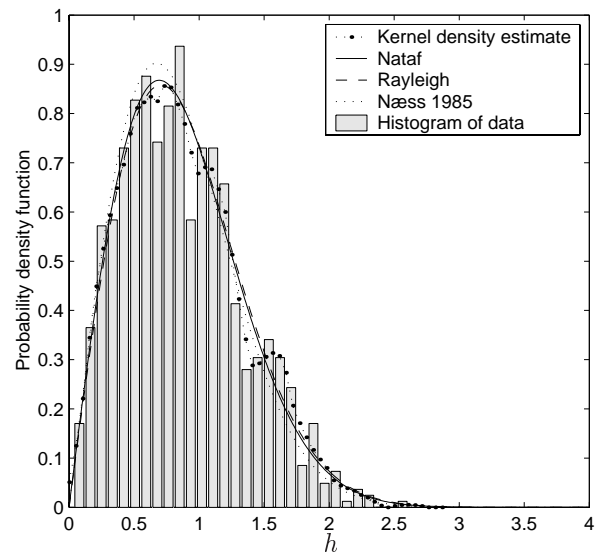
The marginal distributions in terms of the probability of exceedance are shown in Fig. 6.30. The laboratory data are compared with the simulated data, the Nataf model, the Næss (1985) model and the Rayleigh distribution for the different water depths. The simulated data agree quite well with the laboratory data except for larger values of h at $d = 31$ m, where they underpredict the laboratory data. The variation in the data points is large, and it is difficult to draw a firm conclusion regarding the agreement with the models.

Table 6.11: Calculated values of the laboratory data.

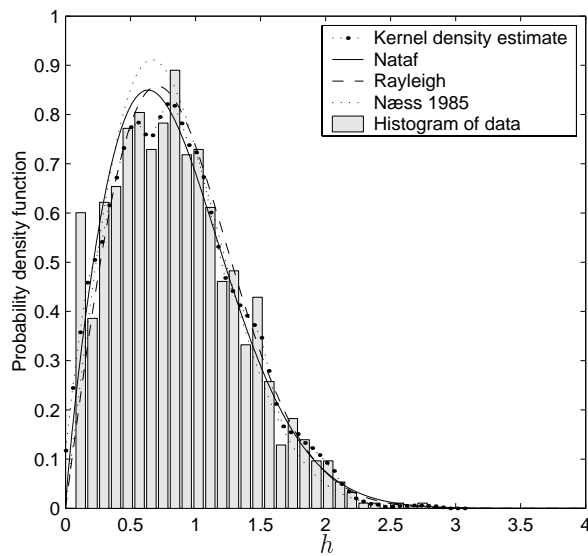
		$d = 80$ m	$d = 78$ m	$d = 41$ m	$d = 31$ m
h_{rms}	[m]	6.43	6.272	5.84	5.74
ρ_N	[-]	-0.806	-0.808	-0.772	-0.742
ρ_h	[-]	0.533	0.516	0.572	0.593
κ_h^2	[-]	0.560	0.543	0.600	0.621
α	[-]	1.000	0.985	0.964	0.971
β	[-]	2.067	1.985	1.856	1.826
$\rho_{W,12}$	[-]	0.514	0.484	0.533	0.558
$\rho_{W,13}$	[-]	0.204	0.152	0.226	0.215
$\rho_{W,14}$	[-]	0.063	0.074	0.068	0.061



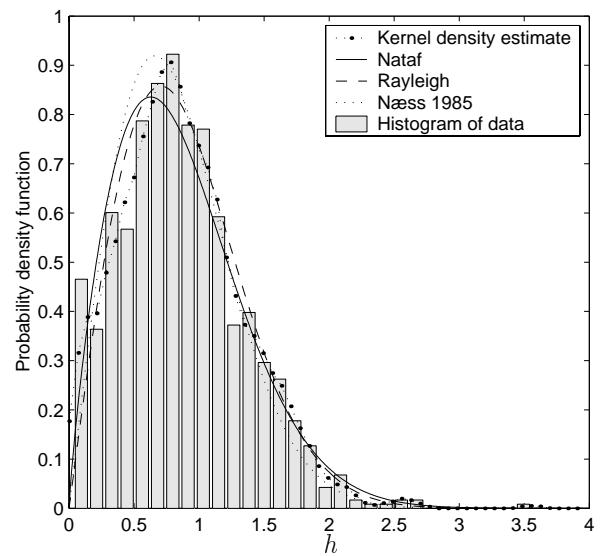
(a)



(b)

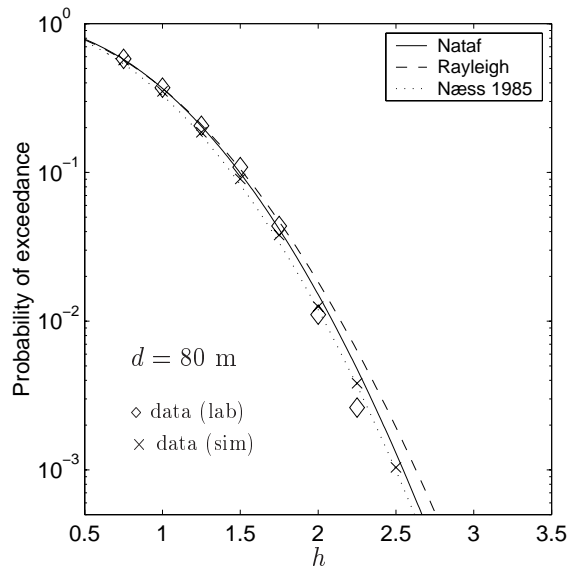


(c)

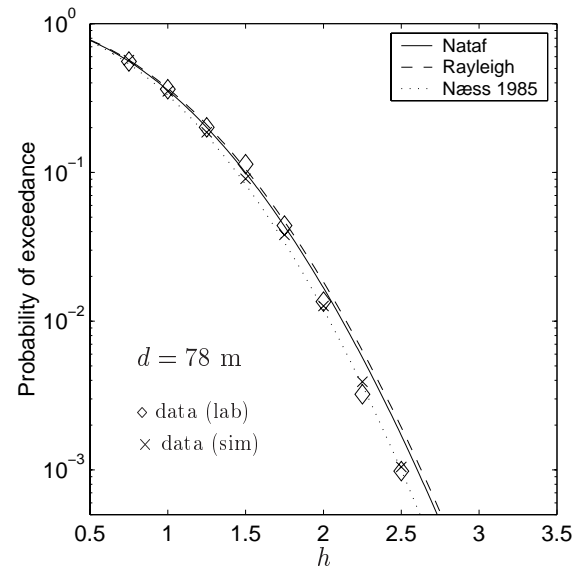


(d)

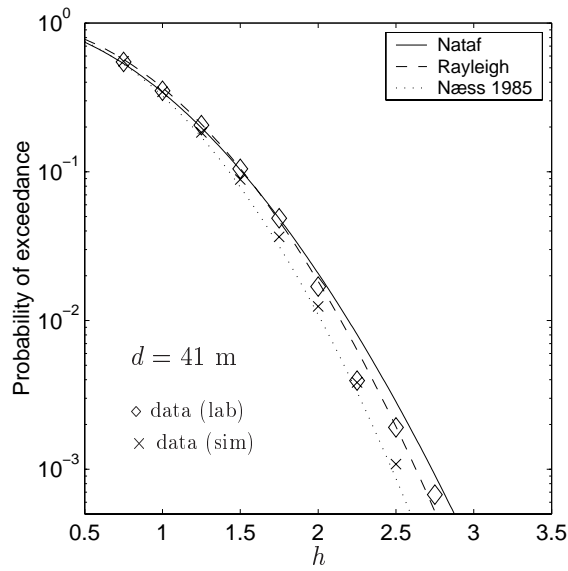
Figure 6.29: Marginal probability density functions of the normalized wave heights. (a) $d = 80$ m, (b) $d = 78$ m, (c) $d = 41$ m (d) $d = 31$ m.



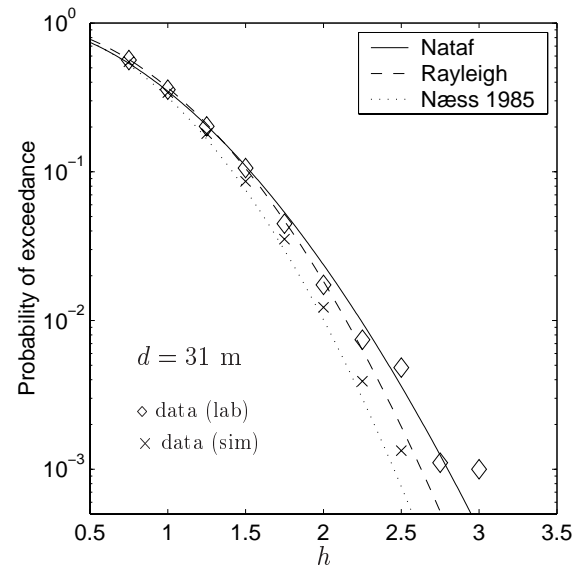
(a)



(b)



(c)



(d)

Figure 6.30: Marginal distributions of the wave heights in terms of probability of exceedance.

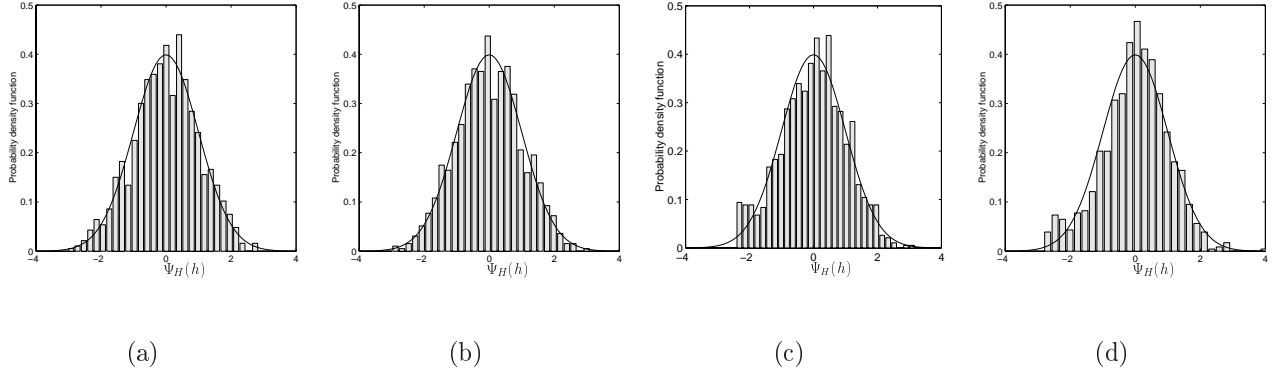


Figure 6.31: Histogram of the transformed wave heights (a) $d = 80$ m, (b) $d = 78$ m, (c) $d = 41$ m, (d) $d = 31$ m. The solid line is the standard Gaussian probability density function.

Figure 6.31 shows a histogram of the transformed wave heights for the different water depths. The data are compared with a standard Gaussian probability density function. For $d = 80$ m and $d = 78$ m the transformations resemble a Gaussian distribution. The data show a larger variation for $d = 41$ m and $d = 31$ m, but overall the resulting transformations are approximatively Gaussian.

A paired plot of the transformed wave heights h_1 and h_2 is shown in Fig. 6.32 for the different water depths compared with a contour plot of the standard Gaussian distribution. The concentration of data points is slightly higher in the lower left part for $d = 41$ m and $d = 31$ m, but overall the figure shows that the Nataf model correctly takes care of the dependency structure.

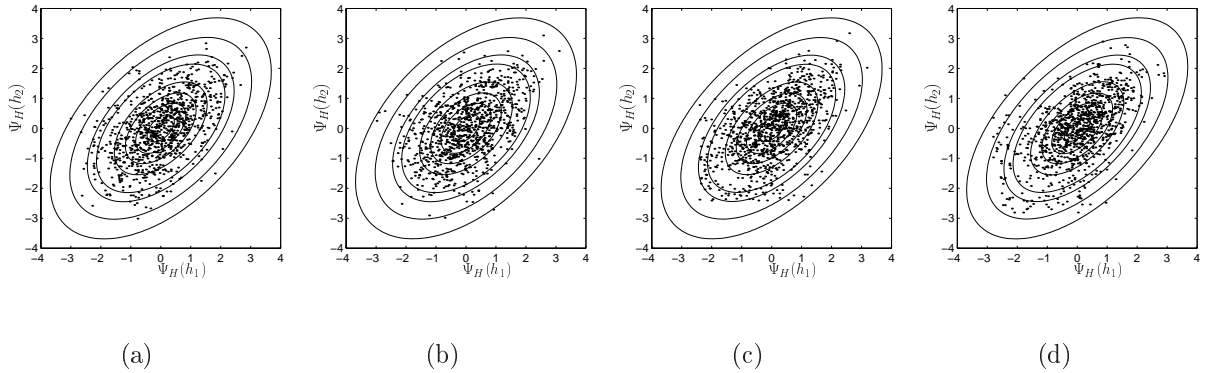


Figure 6.32: Paired plots of the transformed wave heights between h_1 and h_2 compared with a contour plot of the standard Gaussian distribution (a) $d = 80$ m, (b) $d = 78$ m, (c) $d = 41$ m, (d) $d = 31$ m.

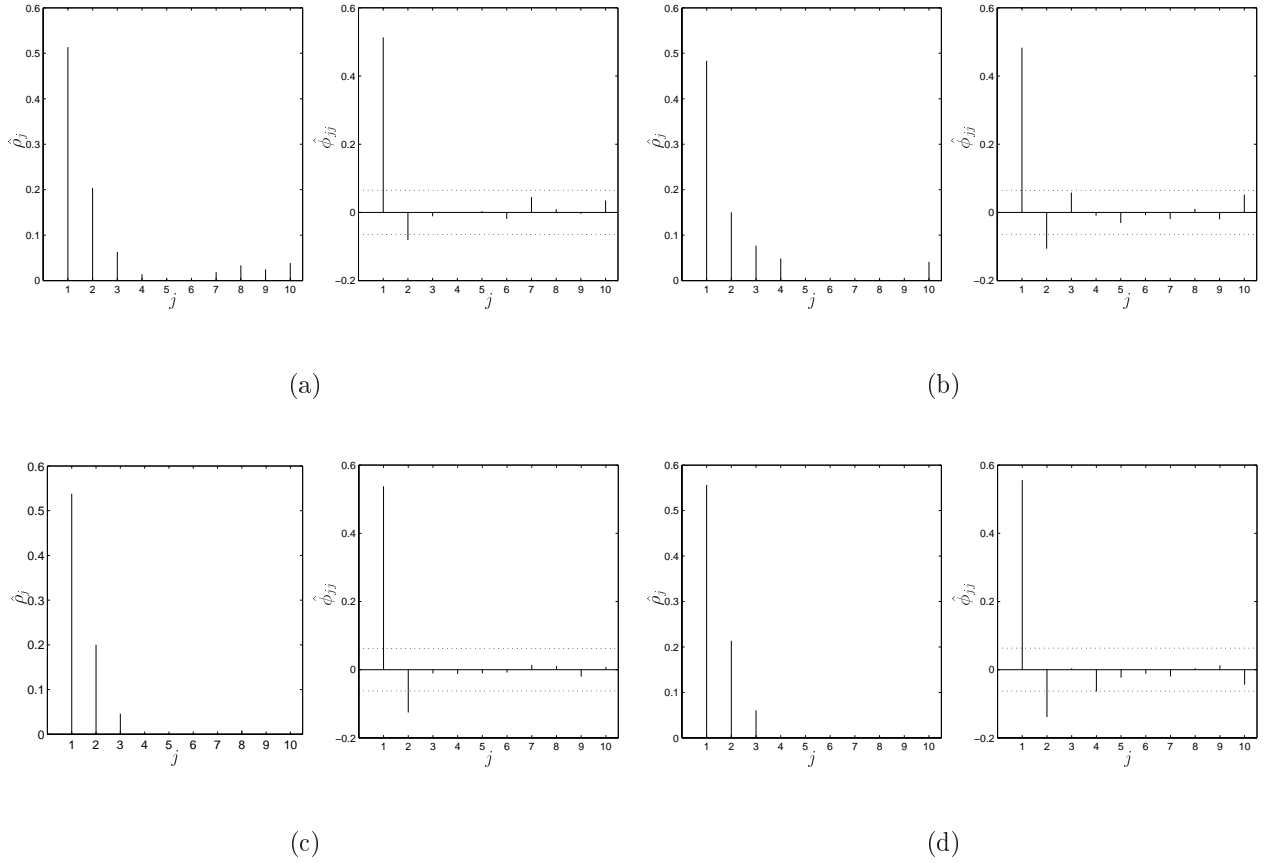


Figure 6.33: Sample autocorrelation function $\hat{\rho}_j$ and sample partial autocorrelation function $\hat{\phi}_{jj}$ at (a) $d = 80$ m, (b) $d = 78$ m, (c) $d = 41$ m and (d) $d = 31$ m, of the transformed wave heights. The dotted line indicates $\pm 2(\text{Var}[\hat{\phi}_{jj}])^{1/2}$.

Figure 6.33 shows the sample ACF and PACF of the transformed wave heights for the different water depths. The ACF decreases approximatively exponentially. For $d = 80$ m and $d = 78$ m the PACF has one spike at $j = 1$, while for $d = 41$ m and $d = 31$ m the PACF also has a distinct spike at $j = 2$. This indicates that the process is an AR(1) process for $d = 80$ m and $d = 78$ m, while it is less probable for $d = 41$ m and $d = 31$ m.

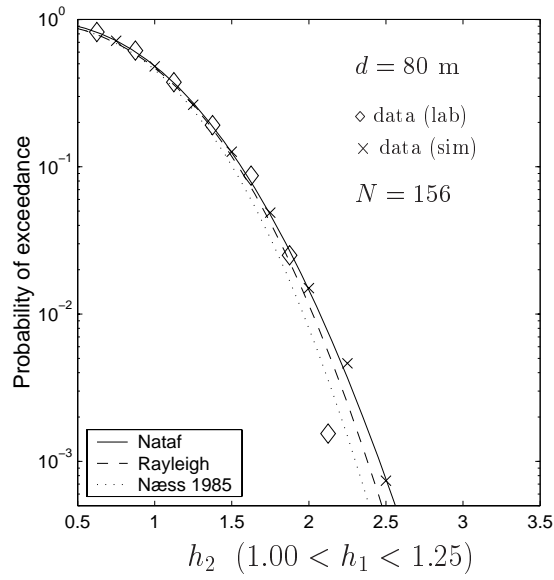
The results from the likelihood ratio tests are shown in Table 6.12. The hypothesis that the successive wave heights can be modeled as an AR(1) model (the correlation coefficients are given by Eq. (4.42)) would not be rejected at the given significance levels. It is clear from the likelihood ratio test and Fig. 6.33 (d) that the wave heights is not an AR(1) process at $d = 31$ m.

Figures 6.34 and 6.35 show the conditional distribution of h_2 given h_1 in terms of probability of exceedance. The number of wave heights in the interval $1.25 < h_1 < 1.50$ is quite small, but the figures are included for comparison. The simulated data agree fairly well with the laboratory data. The large variation in the data points makes it difficult to draw any firm conclusions. However, the Nataf model overpredicts the wave heights for $d = 41$ m and $d = 31$ m. This is due to the fitted Weibull distribution being skewed to the right, causing a larger tail in the distribution. Thus the Nataf model is more influenced by the given data set.

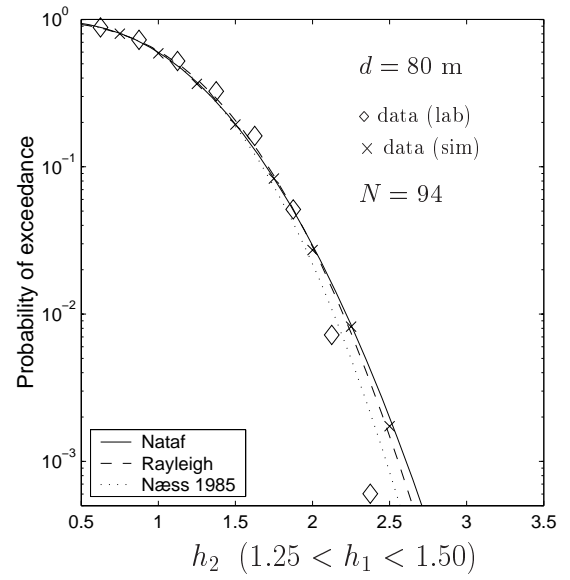
The conditional expectation of the wave height given the previous wave height is shown in Appendix H.2, and the results are similar to the results for the Draupner field data and the Japan Sea field data.

Table 6.12: Likelihood ratio test with $p = 3$ of the transformed wave heights from the laboratory data.

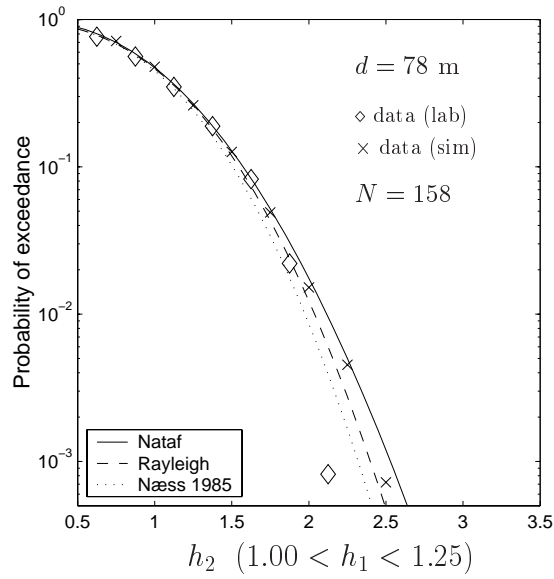
	$d = 80$ m	$d = 78$ m	$d = 41$ m	$d = 31$ m
n	318	319	343	336
$-2 \ln \Lambda_{obs}$	2.47	3.34	7.55	29.34
significance level	29.1%	18.8%	2.2%	0%



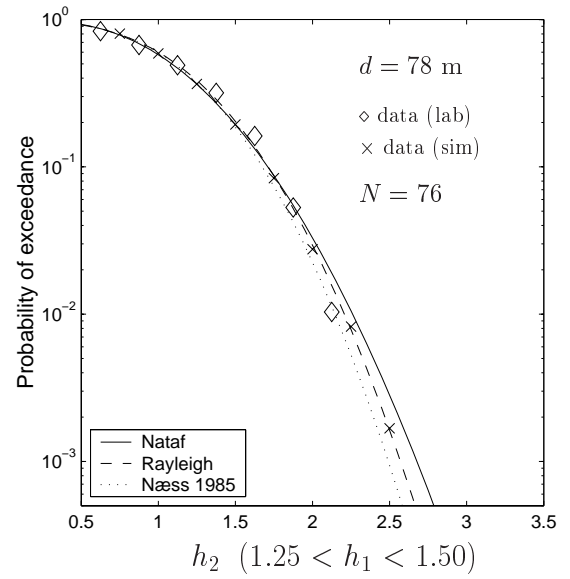
(a)



(b)

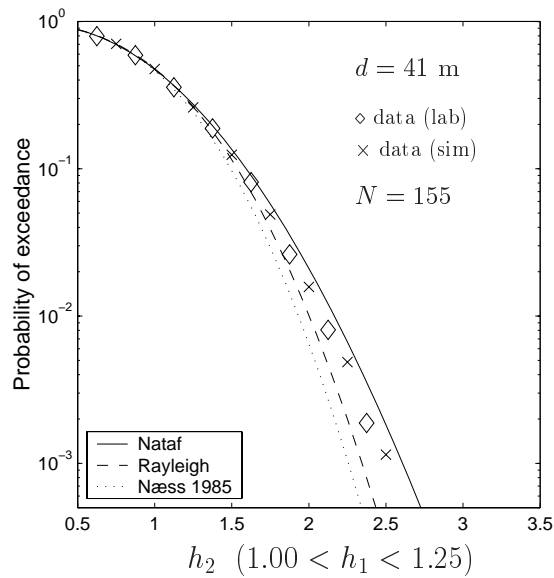


(c)

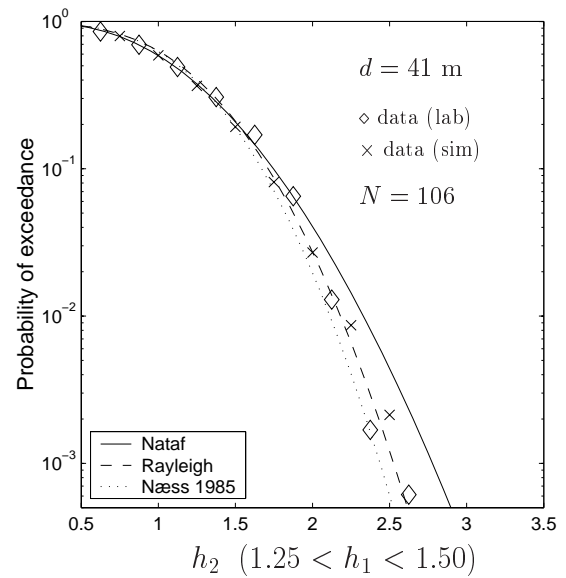


(d)

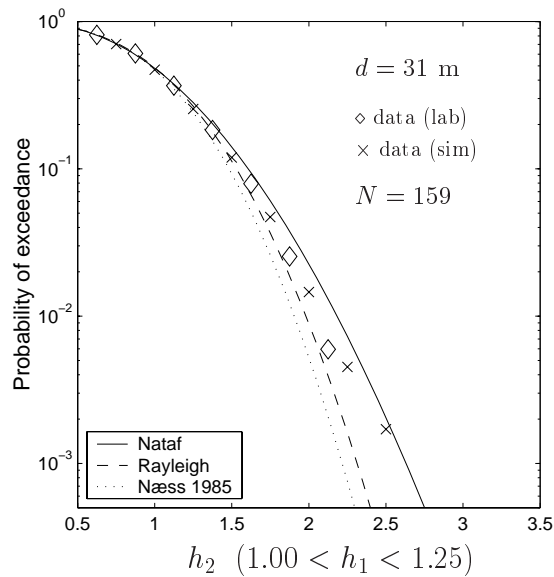
Figure 6.34: Conditional distributions of h_2 given h_1 in terms of probability of exceedance. (a) - (b) $d = 80 \text{ m}$, (c) - (d) $d = 78 \text{ m}$.



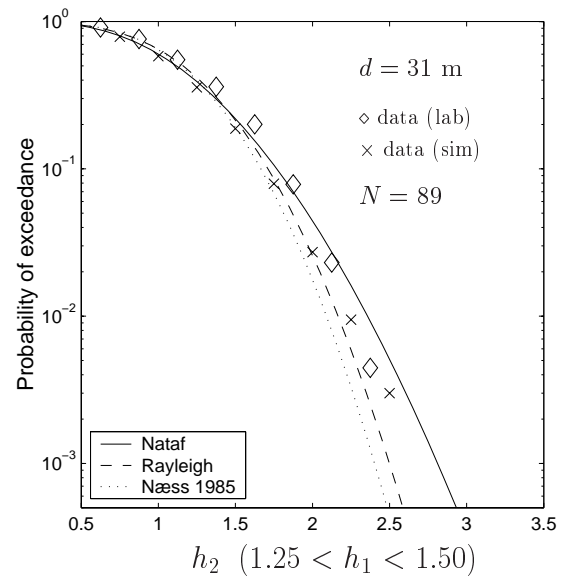
(a)



(b)



(c)



(d)

Figure 6.35: Conditional distributions of h_2 given h_1 in terms of probability of exceedance. (a) - (b) $d = 41 \text{ m}$, (c) - (d) $d = 31 \text{ m}$.

6.4 Results for wave periods

6.4.1 Wave period results for Draupner field data

The wave period results from the Draupner field data were shown in Chapter 5. In this chapter the results will be compared with results from the numerical simulations. Table 6.13 summarizes the calculated parameters for the wave periods from the Draupner field data.

Figure 6.36 shows the kernel density estimates of the field data and the 10 numerical simulations. The results are compared with the Bretschneider (1959) model and the generalized Gamma distribution. From the figure it is clear that the simulated data show the same behavior as the field data.

The probability that a wave period is in an interval $[\tilde{t}_1, \tilde{t}_2]$ given that the previous wave period was in the same interval is shown in Fig. 6.37 (a) as a function of $x = (\tilde{t}_1 + \tilde{t}_2)/2$. Here $\tilde{t}_1 = x - 0.1$ and $\tilde{t}_2 = x + 0.1$. The results are compared with the Nataf model and the Myrhaug and Rue (1993, 1998) models. The simulated data are also included, and they agree fairly well with the field data. The models do not reflect the shape of the data, which have an indication of a second peak around $x \approx 0.7$. While the Nataf model is in better agreement with the data for large values of x , the Myrhaug and Rue (1998) model agrees better with the data for small values of x .

Figure 6.37 (b) shows the variation in the simulated data. The mean values of the 10 simulations are shown with a confidence interval given by $\pm 2\text{Var}[y]^{1/2}$, where y is a vector of the 10 simulation points. The confidence intervals cover some of the field data points, but not all of them.

Table 6.13: Calculated values of the Draupner field data.

ζ	[s]	9.79	λ	[-]	0.415
T_c	[s]	5.80	c	[-]	6.231
α_1	[-]	1.60	ν	[-]	1.311
α_2	[-]	0.766	$\rho_{G,12}$	[-]	0.325
T_{m01}	[s]	9.09	$\rho_{G,13}$	[-]	0.122

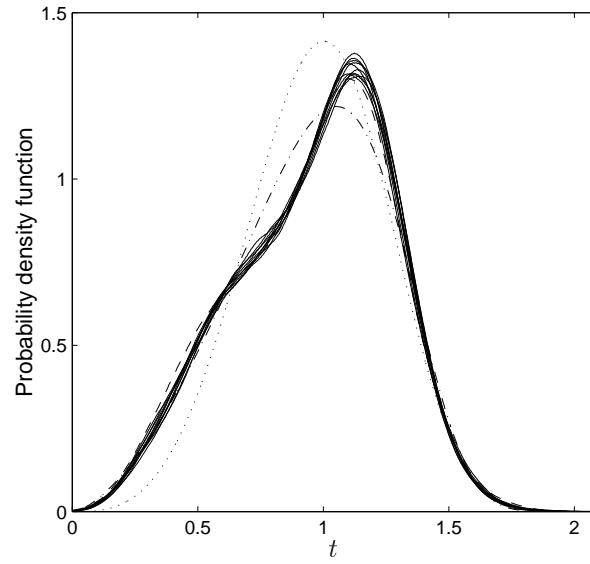


Figure 6.36: Marginal probability density function of the normalized wave periods. -- KDE data; — KDE simulations; ... Bretschneider (1959) model; -·- generalized Gamma distribution.

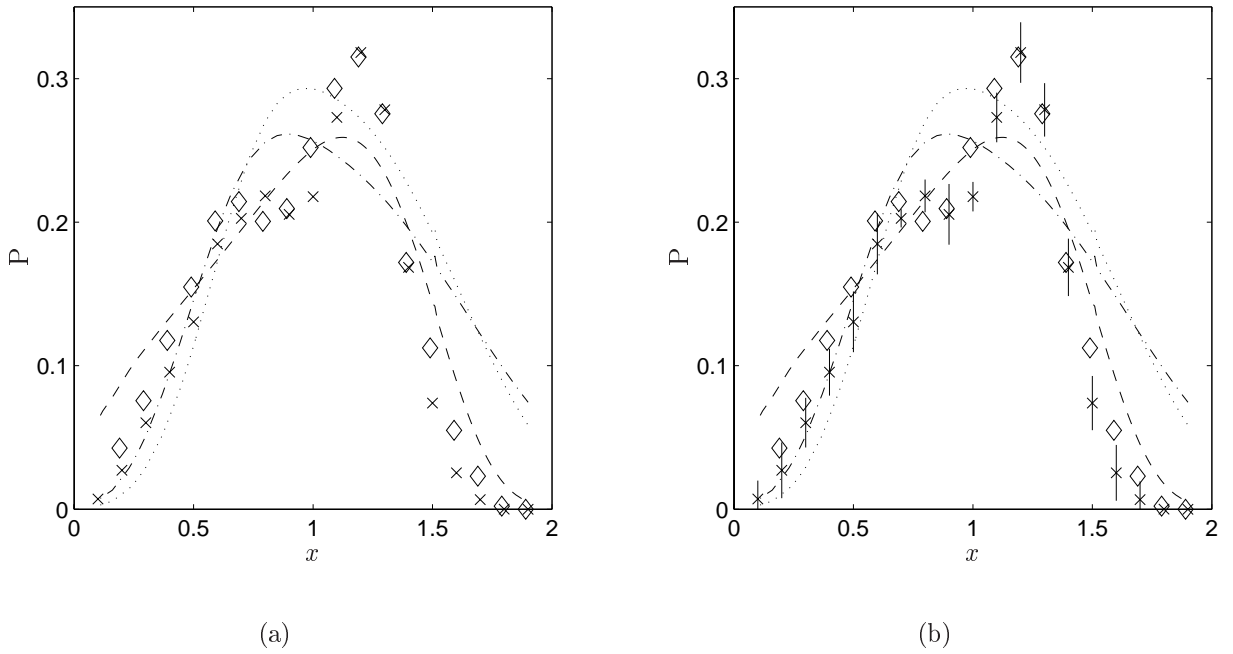


Figure 6.37: The probability that a wave period is in an interval $[\tilde{t}_1, \tilde{t}_2]$ given that the previous wave period was in the same interval, where $\tilde{t}_1 = x - 0.1$ and $\tilde{t}_2 = x + 0.1$. -- Nataf model; ... Myrhaug and Rue (1993) model; -·- Myrhaug and Rue (1998) model; \diamond field data; \times simulated data. (a) Data and mean values of simulations. (b) Simulations including confidence intervals. ($P = P(x - 0.1 < T_2 < x + 0.1 | x - 0.1 < T_1 < x + 0.1)$).

Successive wave periods for large wave heights

Wave heights exceeding h_{rms}

Figure 6.38 (a) shows the probability that a wave period is in an interval $[\tilde{t}_1, \tilde{t}_2]$ of size 0.2 given that the previous wave period was in the same interval, and given that the two corresponding wave heights exceeded h_{rms} . This is shown as a function of $x = (\tilde{t}_1 + \tilde{t}_2)/2$. The simulated data show fairly good agreement with the field data. The results show good agreement between the data and the model. Figure 6.38 (b) shows the variation in the simulated data, where the confidence intervals are given by $\pm 2\text{Var}[y]^{1/2}$, where y is a vector of the 10 simulation points. The confidence intervals are larger than when all wave periods were considered in Fig. 6.37 (b). This is due to the reduction in the number of data cases available when conditioning on the corresponding wave height, as discussed in Chapter 5.3.

The probability of a wave period to be in an interval $[\tilde{t}_1, \tilde{t}_2]$ of size 0.2 given that the two previous wave periods were in the same interval, and given that the three corresponding wave heights exceeded h_{rms} is shown in Fig. 6.39 (a). The results are quite similar to the results in Fig. 6.38, which support the hypothesis that the wave periods can be modeled as an AR(1) model as discussed in Chapter 5.3. The confidence intervals of the simulations are included in (b).

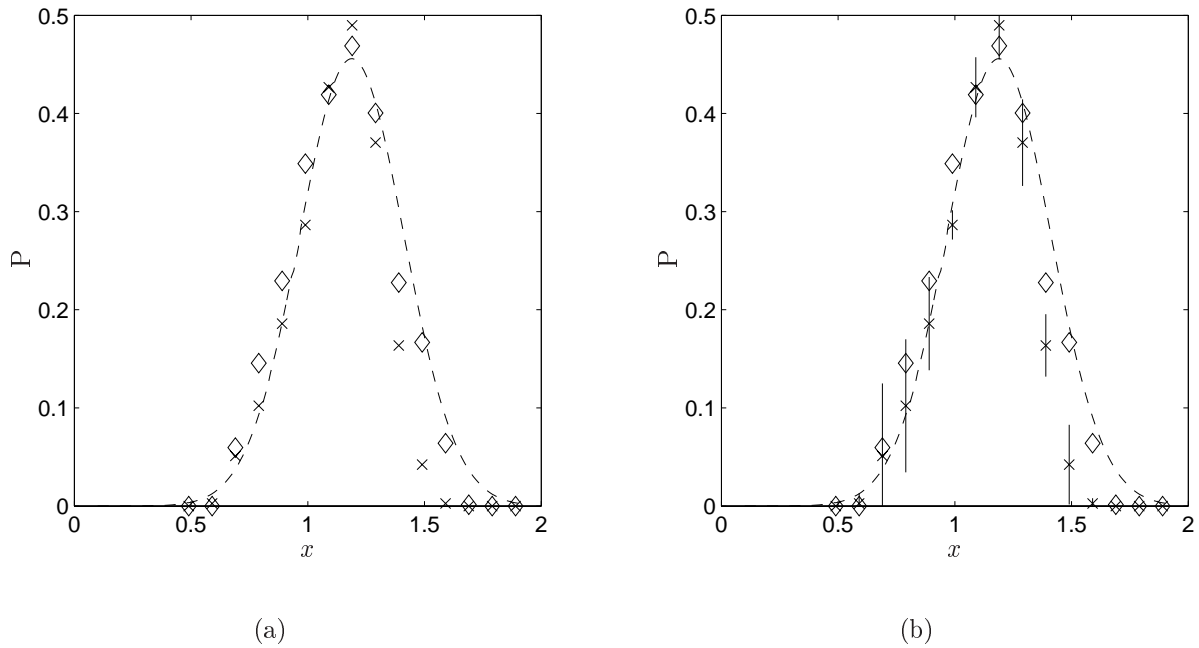


Figure 6.38: The probability that a wave period is in an interval $[\tilde{t}_1, \tilde{t}_2]$ given that the previous wave period was in the same interval, where $\tilde{t}_1 = x - 0.1$ and $\tilde{t}_2 = x + 0.1$, and given that the two corresponding wave heights exceeded h_{rms} . -- Nataf model; \diamond field data; \times simulated data.

(a) Data and mean values of simulations. (b) Simulations including confidence intervals.

($P = P(x - 0.1 < T_2 < x + 0.1 | x - 0.1 < T_1 < x + 0.1, H_1 > 1, H_2 > 1)$).

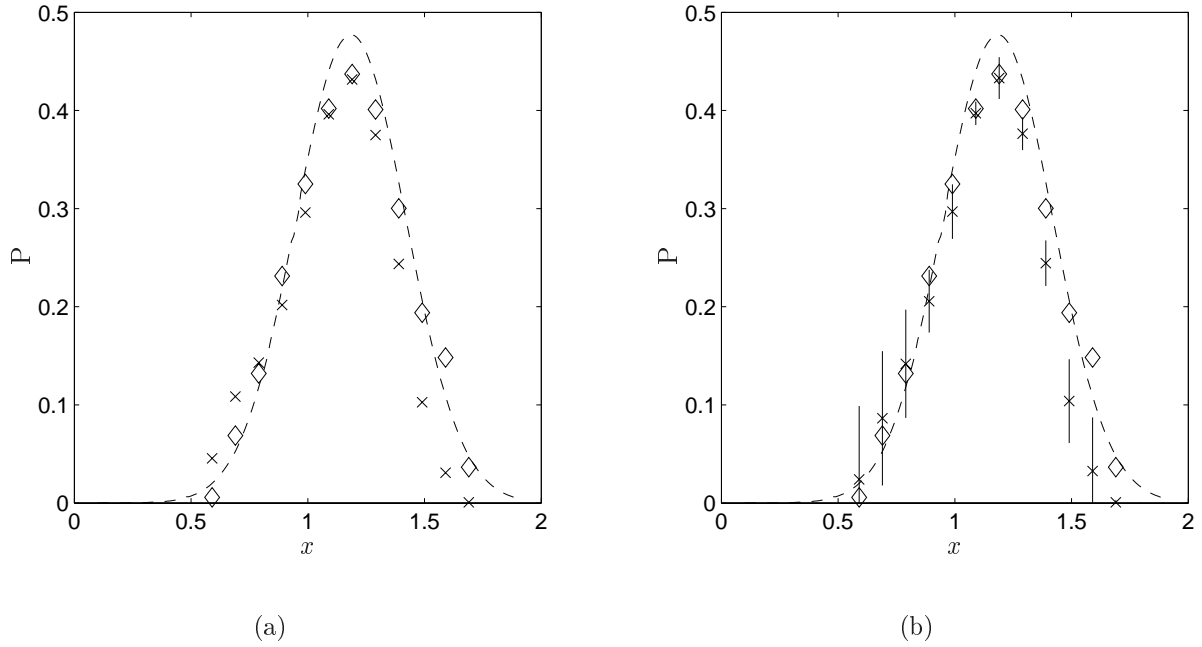


Figure 6.39: The probability that a wave period is in an interval $[\tilde{t}_1, \tilde{t}_2]$ given that the two previous wave periods were in the same interval, where $\tilde{t}_1 = x - 0.1$ and $\tilde{t}_2 = x + 0.1$, and given that the three corresponding wave heights exceeded h_{rms} . -- Nataf model; \diamond field data; \times simulated data.

(a) Data and mean values of simulations. (b) Simulations including confidence intervals.

Wave heights exceeding H_{m0}

For practical purposes, it is of more interest to study the wave periods for wave heights exceeding the significant wave height. The calculated parameters from the Draupner field data when constructing pairs and triplets of wave periods conditioned on the corresponding wave heights exceeding H_{m0} are shown in Table 6.14. Compared to the values in Table 5.3, where the corresponding wave heights exceeded h_{rms} , the difference in the parameters for the Gaussian distribution is small, but the number n has decreased significantly. Thus, in order to compare with data, especially if two or three successive wave periods are considered, a long time series is needed, as mentioned in Chapter 5.3. When considering three successive waves with corresponding wave heights exceeding H_{m0} , the time series of the Draupner field data, which was nearly 16 hours, only resulted in 80 data cases.

Figure 6.40 (a) shows the probability that a wave period is in an interval $[\tilde{t}_1, \tilde{t}_2]$ of size 0.2 given that the previous wave period were in the same interval, and given that the two corresponding wave heights exceeded H_{m0} . The results show fairly good agreement between the data and the model. The confidence intervals of the simulations are included in (b). The confidence intervals cover the field data for smaller values of x , but there is larger difference between the field data and the simulations for large values of x .

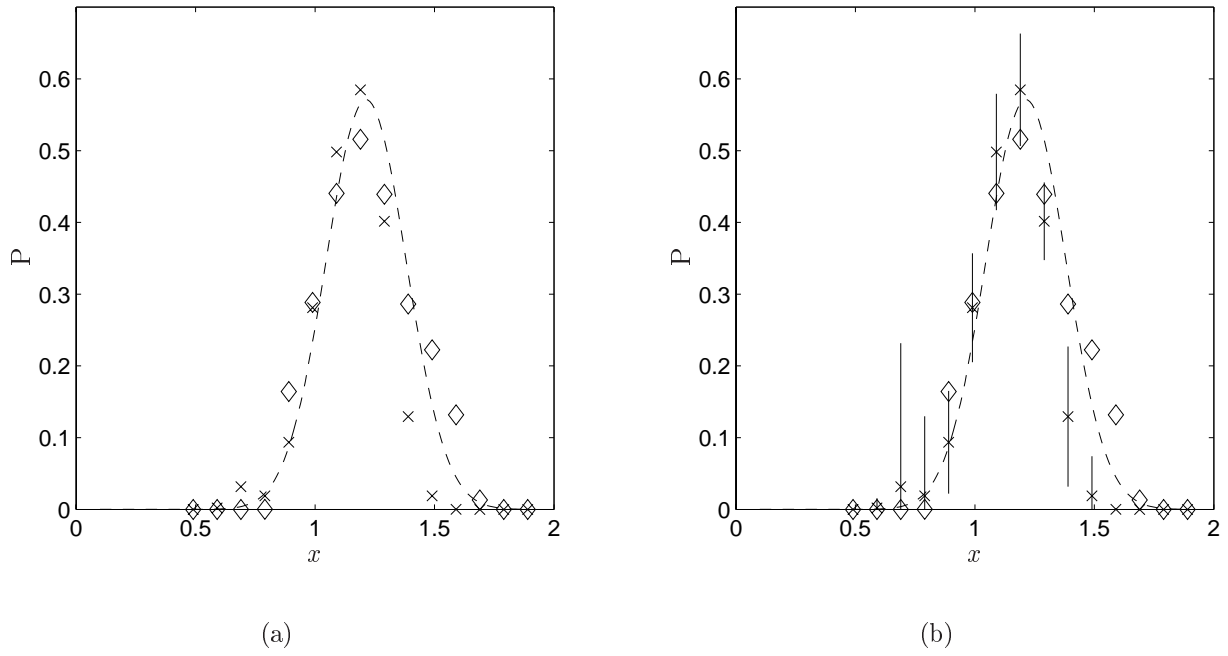


Figure 6.40: The probability that a wave period is in an interval $[\tilde{t}_1, \tilde{t}_2]$ given that the previous wave period was in the same interval, where $\tilde{t}_1 = x - 0.1$ and $\tilde{t}_2 = x + 0.1$, and given that the two corresponding wave heights exceeded the normalized value of H_{m0} , 1.41.

($P = P(x - 0.1 < T_2 < x + 0.1 | x - 0.1 < T_1 < x + 0.1, H_1 > 1.41, H_2 > 1.41)$).

-- Nataf model; \diamond field data; \times simulated data.

(a) Data and mean values of simulations. (b) Simulations including confidence intervals.

Table 6.14: Calculated parameters for the p -dimensional Gaussian distribution with $\tilde{h} = 1.41$ (normalized value of H_{m0}), from the Draupner field data.

	$\boldsymbol{\mu}_{t \tilde{h}}$	$\boldsymbol{\sigma}_{t \tilde{h}}$	$\boldsymbol{\rho}$	n
$p = 1$	1.15	0.15		798
$p = 2$	$[1.210, 1.213]^T$	$[0.147, 0.129]^T$	0.217	251
$p = 3$	$[1.204, 1.256, 1.212]^T$	$[0.154, 0.139, 0.110]^T$	$[0.361, 0.196]^T$	80

6.4.2 Wave period results for Japan Sea field data

The calculated wave parameters from the Japan Sea field data are shown in Table 6.15. Compared with the values from the Draupner field data the correlation coefficients are smaller. The parameter c in the generalized Gamma distribution is higher, which means that the distribution will be skewed further to the left.

Figure 6.41 shows a histogram of the normalized wave periods from the field data with the kernel density estimate. The Bretschneider (1959) model, the Longuet-Higgins (1975, 1983) models and the Cavanié (1976) model are included for comparison. The models show a similar behavior as discussed for the Draupner field data in Fig. 5.1. The field data have a similar shape as the Draupner field data, but for the Japan Sea data there is a more distinct second peak around $t \approx 0.6$. Figure 6.41 also includes the generalized Gamma distribution that will be used in the Nataf transformation. The distribution agrees quite well with the data, and around the peak of the data it gives a much better prediction than any of the other models. However, it does not capture the behavior of the data with a second peak.

Figure 6.42 (a) shows a histogram of the transformed wave periods and the corresponding kernel density estimate compared with the standard Gaussian probability density function. The transformation of the Japan Sea field data yields the same problems as for the Draupner field data due to the shape of the marginal distribution.

A paired plot of the transformed wave periods between t_1 and t_2 is shown in Fig. 6.42 (b) compared with a contour plot of the standard Gaussian distribution. The figure shows that the correlation of the transformed wave periods resembles the one for the Gaussian distribution.

Figures 6.41 and 6.42 thus indicate that the Nataf transformation does not give a perfect result, but the results are at least as good as the existing models. The dependency structure is preserved, so the results for the two-dimensional model should be satisfactory.

Table 6.15: Calculated values of the Japan Sea field data.

ζ	[s]	10.16	λ	[-]	0.247
T_c	[s]	6.38	c	[-]	8.972
α_1	[-]	1.35	ν	[-]	1.392
α_2	[-]	0.798	$\rho_{G,12}$	[-]	0.259
T_{m01}	[s]	9.45	$\rho_{G,13}$	[-]	0.094

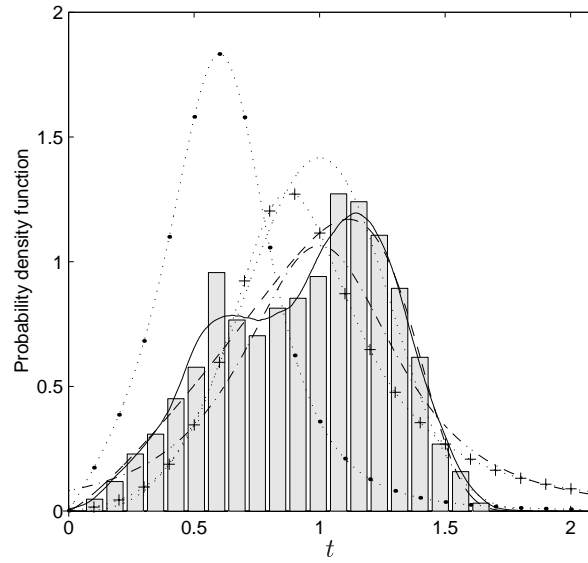


Figure 6.41: Probability density function of the normalized wave periods. — Generalized Gamma distribution; — KDE Japan Sea data; \cdots Bretschneider (1959) model; $-\cdot-$ Longuet-Higgins (1975) model; $+ \cdots$ Longuet-Higgins (1983) model; $\bullet \cdots$ Cavanié (1976) model.

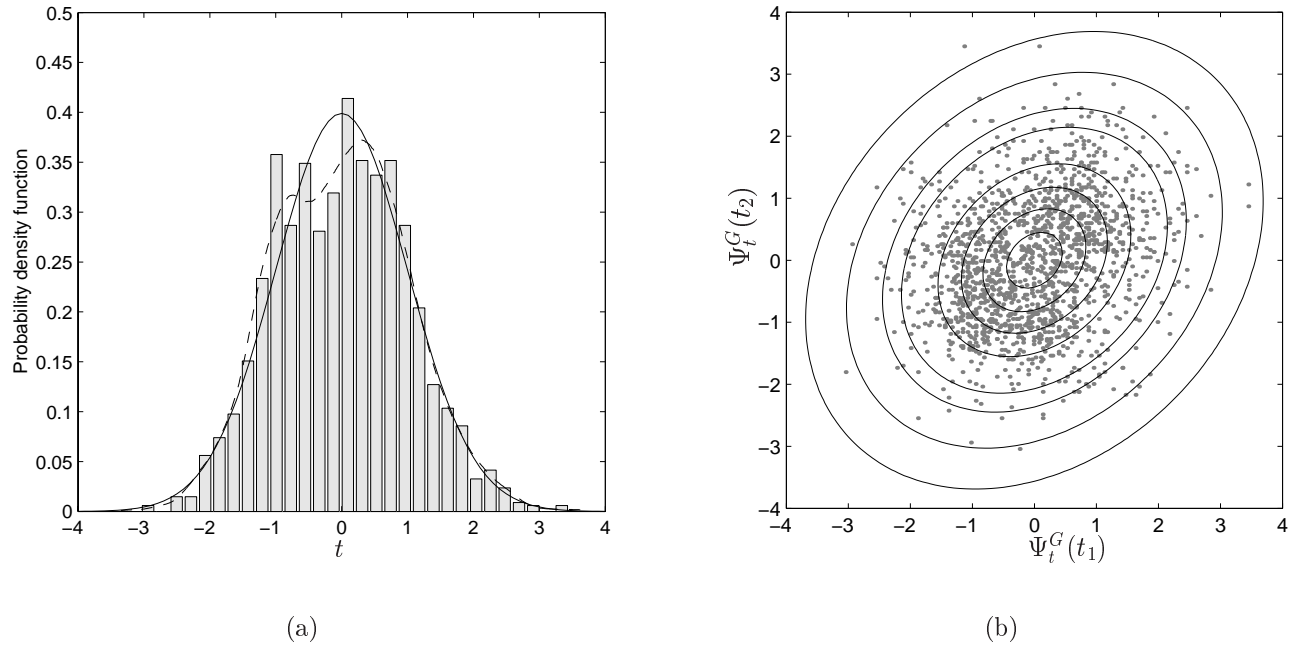


Figure 6.42: (a) Histogram of transformed wave period field data. — standard Gaussian probability density function; $-\cdot-$ KDE of the transformed wave period data. (b) Paired plot of the transformed wave periods between t_1 and t_2 compared with a contour plot of the standard Gaussian distribution.

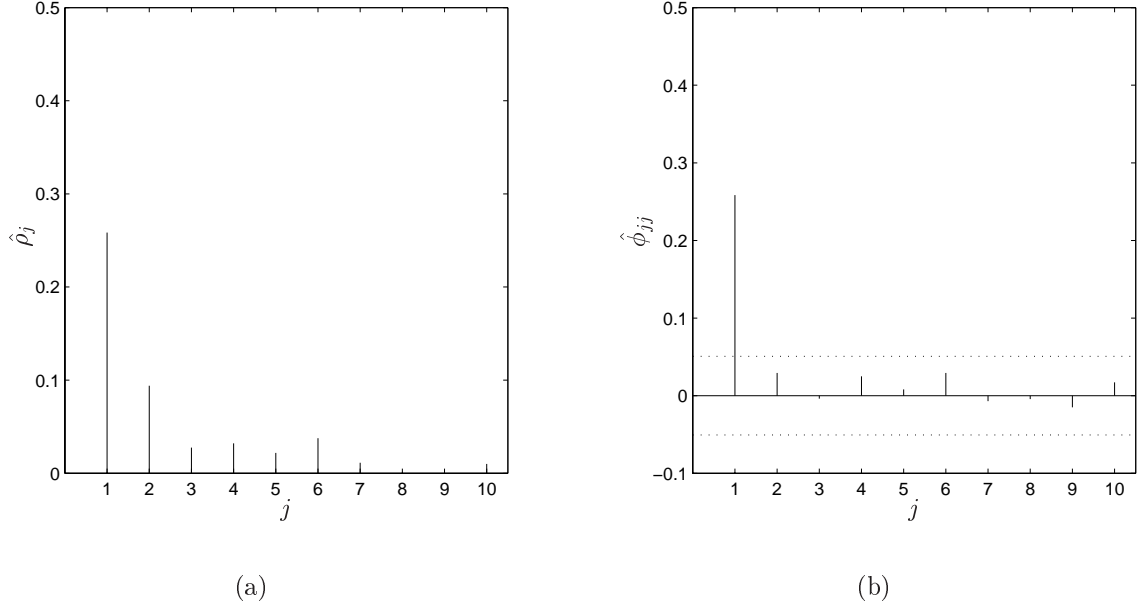


Figure 6.43: (a) Sample autocorrelation function, and (b) sample partial autocorrelation function of Ψ_T^G from Japan Sea data. The dotted line indicates $\pm(\text{Var}[\hat{\phi}_{jj}])^{1/2}$.

Figure 6.43 shows the sample ACF (a) and PACF (b) of the transformed wave periods from the Japan Sea field data. The ACF decreases approximately exponentially and the PACF has one spike at $j = 1$, which indicates that the process is an AR(1) process. A likelihood ratio test with $p = 3$ resulted in $n = 521$, and the observed value of the likelihood ratio statistic was $-2\ln\Lambda_{obs} = 1.65$. From tables $\chi_{0.437,2}^2 = 1.66$, which means that the hypothesis that the correlation coefficients agree with an AR(1) process would not be rejected at 43.7% significance level.

The probability that a wave period is in an interval $[\tilde{t}_1, \tilde{t}_2]$ of size 0.2 given that the previous wave period was in the same interval is shown in Fig. 6.44 (a) as a function of $x = (\tilde{t}_1 + \tilde{t}_2)/2$. The field data have two very distinct peaks, while the simulated data have much smaller peaks. None of the models capture the behavior of the data, but overall the Nataf model is in better agreement with the data than the Myrhaug and Rue (1993, 1998) models. Figure 6.44 (b) shows the variation in the simulated data, where the confidence intervals are given by $\pm 2\text{Var}[y]^{1/2}$, where y is a vector of the 10 simulation points.

The conditional expectation of the wave period given the previous wave period is shown in Appendix H.3.1, and the results are similar to the results for the Draupner field data.

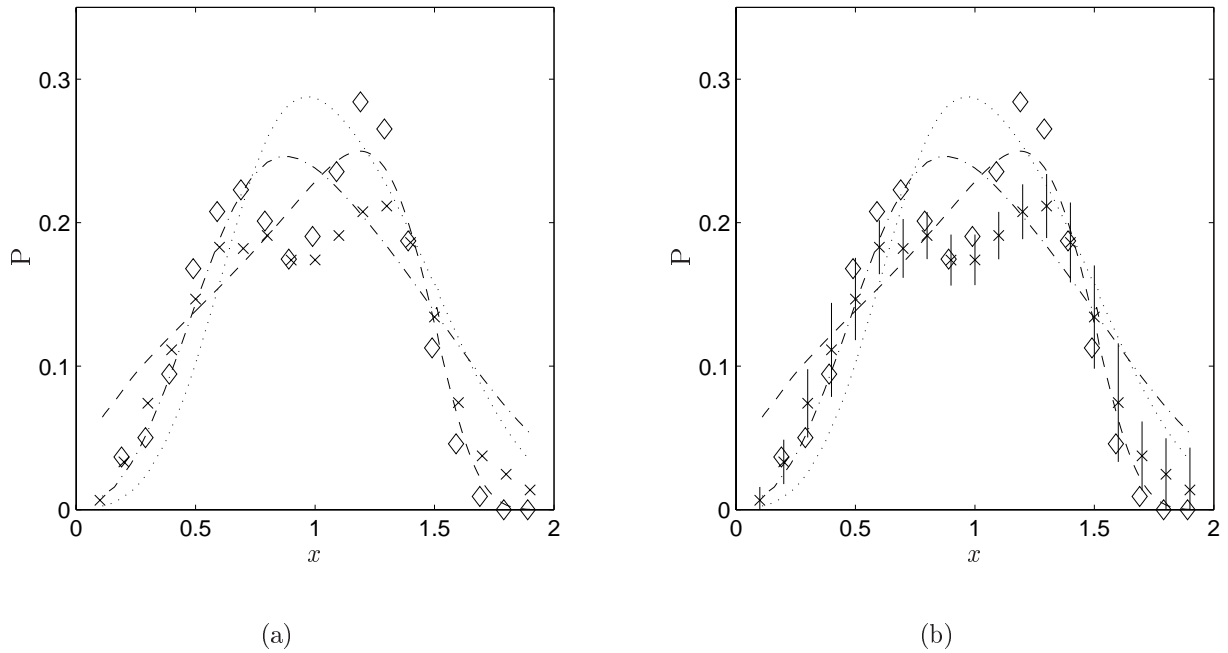


Figure 6.44: The probability that a wave period is in an interval $[\tilde{t}_1, \tilde{t}_2]$ given that the previous wave period was in the same interval, where $\tilde{t}_1 = x - 0.1$ and $\tilde{t}_2 = x + 0.1$. -- Nataf model; \cdots Myrhaug and Rue (1993) model; $-\cdot-$ Myrhaug and Rue (1998) model; \diamond field data; \times simulated data. (a) Data and mean values of simulations. (b) Simulations including confidence intervals. ($P = P(x - 0.1 < T_2 < x + 0.1 | x - 0.1 < T_1 < x + 0.1)$).

Successive wave periods for large wave heights

Table 6.16 shows the calculated parameters for the Gaussian distribution conditioned on the corresponding p successive wave heights exceeding h_{rms} . The number of waves that are found in the time series that fulfills this requirement decreases rapidly when considering several successive waves. Thus, a long time series is requested when considering three or more successive waves where the corresponding wave heights exceeds h_{rms} . In the following the emphasis will be on two successive wave periods. However, finally an example of three successive wave periods will be given. The expected values and standard deviation remain quite constant with different values of p .

Figure 6.45 shows a histogram and the corresponding kernel density estimate of the wave periods where the corresponding wave heights are larger than h_{rms} . Figure 6.45 (a) shows the first wave period t_1 , while (b) shows the successive wave period t_2 . The data are compared with the Longuet-Higgins (1975, 1983) models, the Tayfun (1993) model and the Gaussian probability density function. The results show that the data agree very well with the Gaussian distribution. The Tayfun (1993) model also agree well with the data, but underpredicts the peak value, while the Longuet-Higgins (1975, 1983) models are shifted towards lower values of t . The lack of values in the histogram for $t \gtrsim 1.6$ is due to that the largest wave periods with corresponding wave heights exceeding h_{rms} are almost equal (see Appendix H.3.1). Since n is small, this has a large influence on the resulting histogram.

A paired plot of the wave periods t_1 and t_2 for the field data is shown in Fig. 6.46 (a) compared with a contour plot of the bivariate Gaussian distribution. The number of data points is small, but the correlation coefficients seems to be correctly modeled by the Gaussian distribution. In order to increase the number of data points, the results for the simulations are added in Fig. 6.46 (b). Here it is clear that the dependency structure is correctly modeled by the bivariate Gaussian distribution.

Table 6.16: Calculated parameters for the p -dimensional Gaussian distribution with $\tilde{h} = 1$, from the Japan Sea field data.

	$\boldsymbol{\mu}_{t \tilde{h}}$	$\boldsymbol{\sigma}_{t \tilde{h}}$	$\boldsymbol{\rho}$	n
$p = 1$	1.15	0.18		555
$p = 2$	$[1.21, 1.19]^T$	$[0.16, 0.17]^T$	0.09	279
$p = 3$	$[1.19, 1.24, 1.18]^T$	$[0.16, 0.14, 0.17]^T$	$[0.14, 0.05]^T$	149

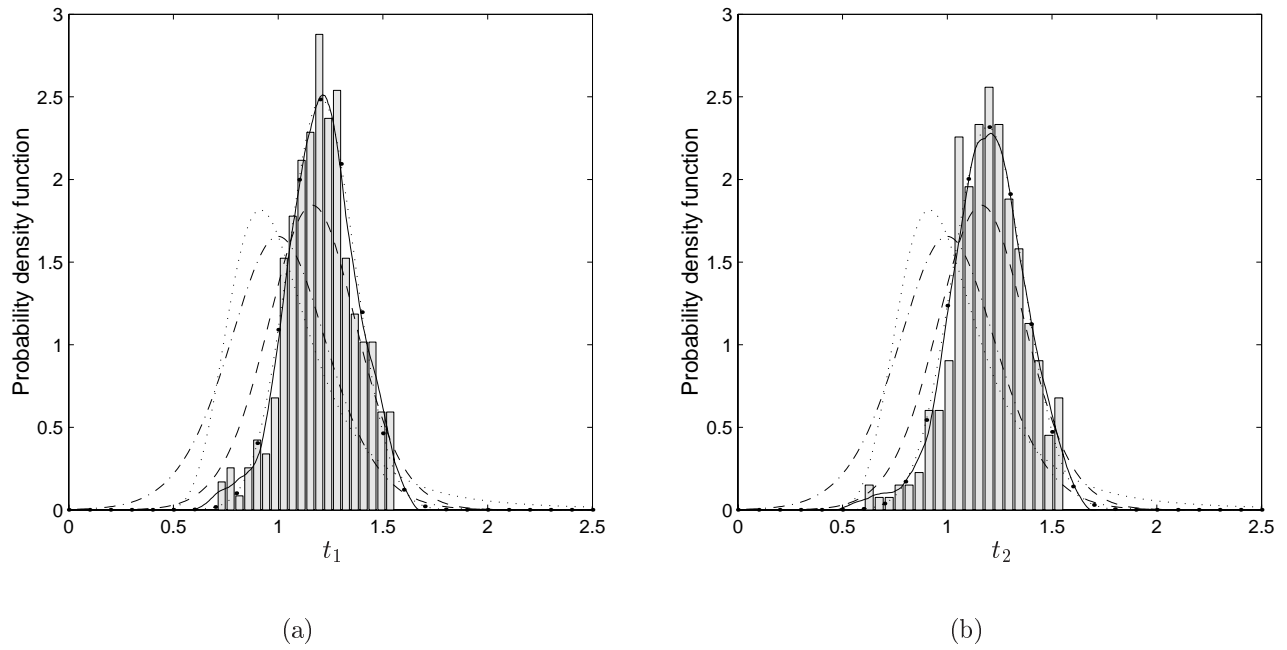


Figure 6.45: Probability density function of wave periods where the corresponding wave height is larger than h_{rms} , i.e., $h > 1$; — KDE Japan Sea data; -- Tayfun (1993) model; \cdots Longuet-Higgins (1983) model; - \cdot - Longuet-Higgins (1975) model; $\cdot \bullet \cdots$ Gaussian density function.

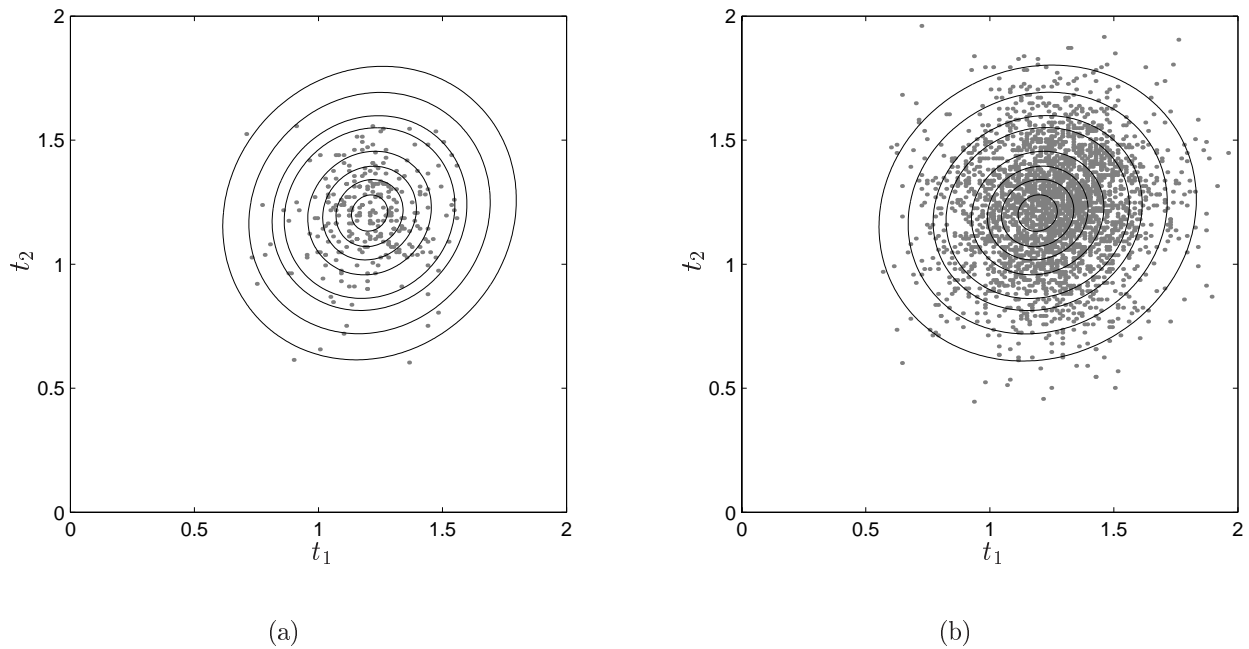


Figure 6.46: Paired plot between t_1 and t_2 compared with a contour plot of the bivariate Gaussian distribution. (a) Japan Sea data, (b) Simulated data.

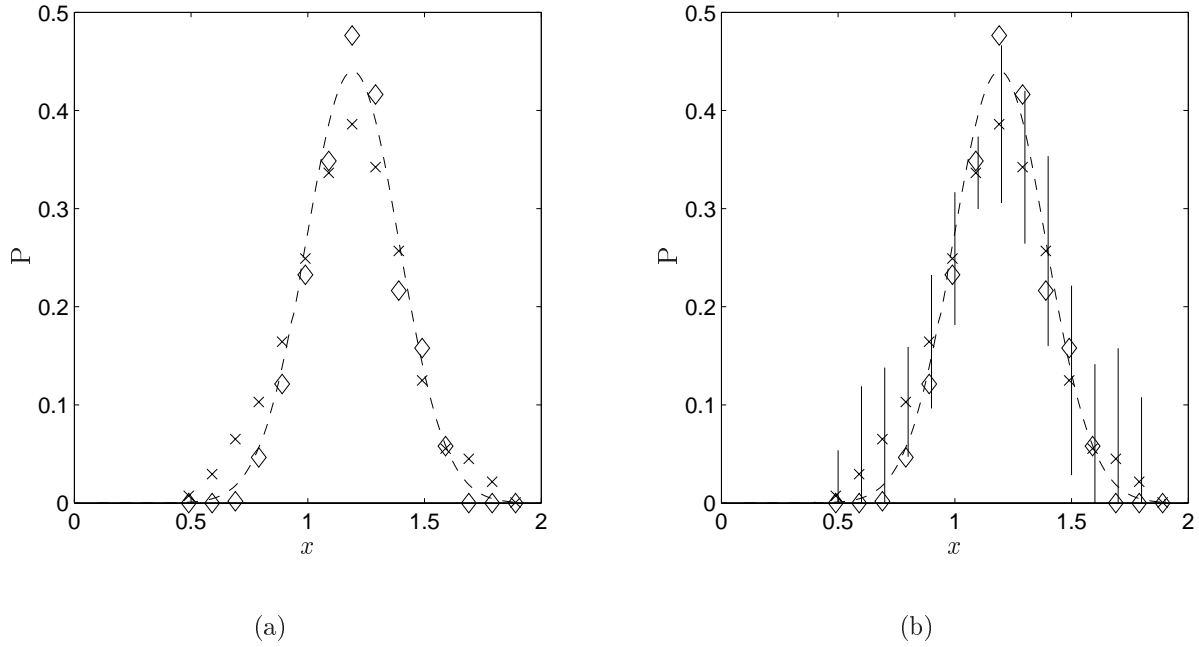


Figure 6.47: The probability that a wave period is in an interval $[\tilde{t}_1, \tilde{t}_2]$ given that the previous wave period was in the same interval, where $\tilde{t}_1 = x - 0.1$ and $\tilde{t}_2 = x + 0.1$, and given that the two corresponding wave heights exceeded h_{rms} . -- Nataf model; \diamond field data; \times simulated data. (a) Data and mean values of simulations. (b) Simulations including confidence intervals.

($P = P(x - 0.1 < T_2 < x + 0.1 | x - 0.1 < T_1 < x + 0.1, H_1 > h_{\text{rms}}, H_2 > h_{\text{rms}})$).

Figure 6.47 (a) shows the probability that a wave period is in an interval $[\tilde{t}_1, \tilde{t}_2]$ of size 0.2 given that the previous wave period was in the same interval, and given that the two corresponding wave heights exceeded h_{rms} . This is shown as a function of $x = (\tilde{t}_1 + \tilde{t}_2)/2$. The field data have a larger peak than the simulated data. However, due to the large variation in the simulated data the field data agree well with the simulated data. The results show a good agreement between the data and the model. The confidence intervals of the simulations are included in (b). The intervals are quite large, and they cover the field data for almost all values of x .

Figure 6.48 (a) shows the probability of a wave period to be in an interval $[\tilde{t}_1, \tilde{t}_2]$ of size 0.2 given that the two previous wave periods were in the same interval, and given that the three corresponding wave heights exceeded h_{rms} . The results are quite similar to the results in Fig. 6.47. Thus, the results barely change by conditioning on the two previous wave periods compared to only conditioning on the previous wave period. The confidence intervals of the simulations are included in (b). There are some very large intervals due to the small number of data cases.

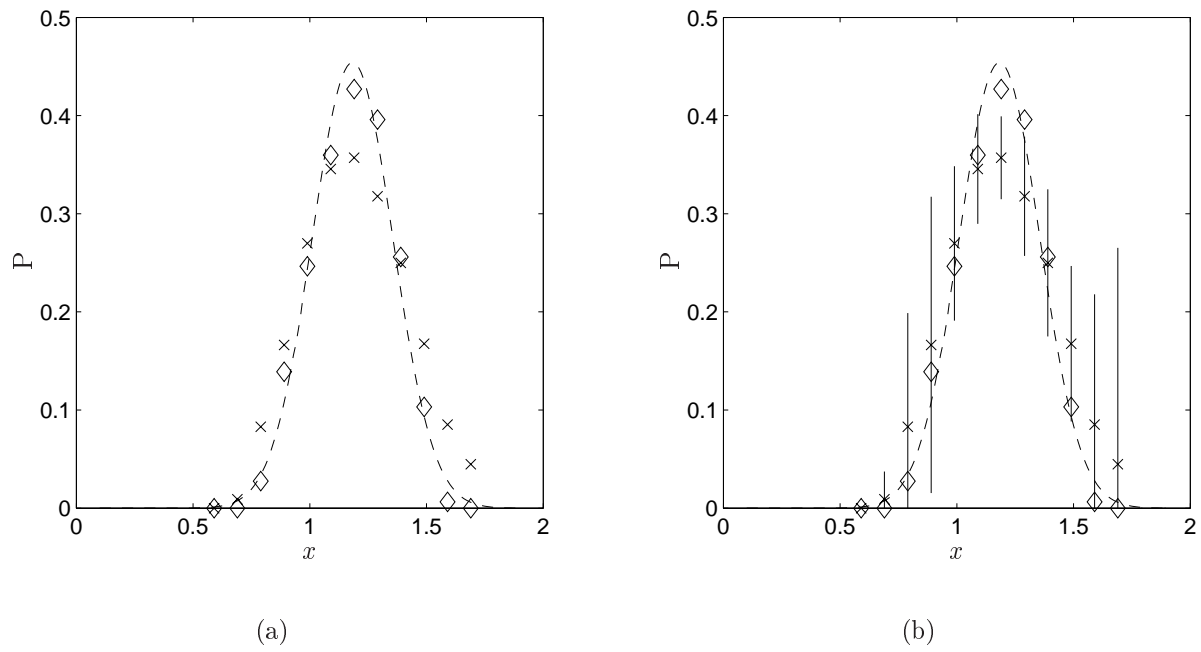


Figure 6.48: The probability that a wave period is in an interval $[\tilde{t}_1, \tilde{t}_2]$ given that the two previous wave periods were in the same interval, where $\tilde{t}_1 = x - 0.1$ and $\tilde{t}_2 = x + 0.1$, and given that the three corresponding wave heights exceeded h_{rms} . -- Nataf model; \diamond field data; \times simulated data.

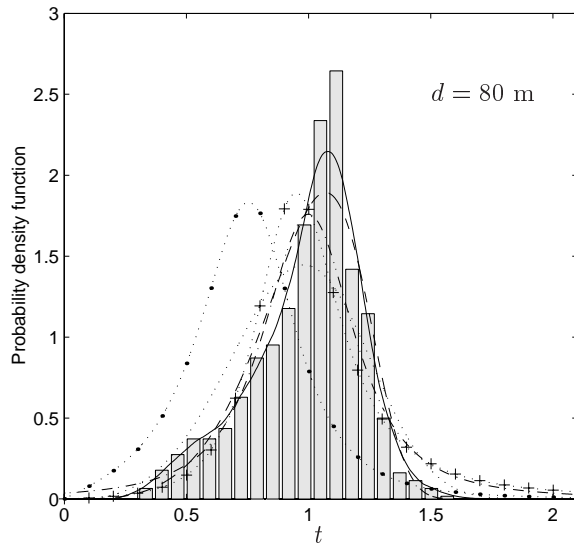
6.4.3 Wave period results for laboratory data

The calculated wave parameters from the laboratory data are shown in Table 6.17. The changes in T_c , α_1 and α_2 are due to the change in the spectral bandwidth parameters ϵ_2 and ϵ_4 , see Table 6.5, which increase significantly with decreasing water depth. The parameters for the generalized Gamma distribution are sensitive to the variations in the data sets, and thus they vary significantly at the different water depths.

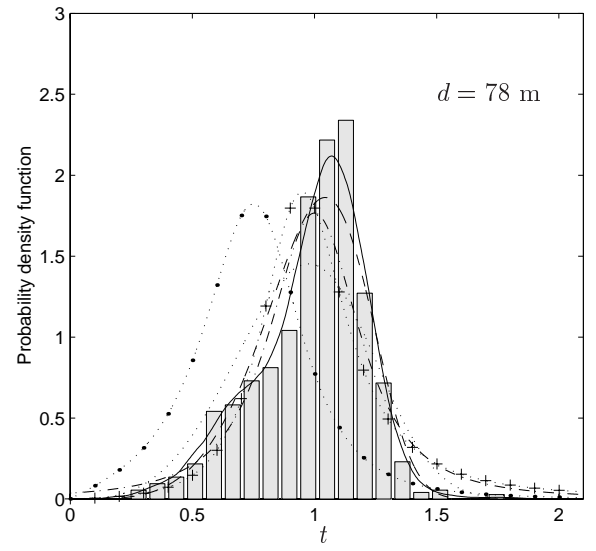
Figures 6.49 (a), (b), (c) and (d) show a histogram of the normalized wave periods from the laboratory data with the kernel density estimate for the water depths 80 m, 78 m, 41 m and 31 m, respectively. The Bretschneider (1959) model, the Longuet-Higgins (1975, 1983) models and the Cavanié (1976) model are included for comparison. The laboratory data at $d = 80$ m and $d = 78$ m show the same qualitative behaviour as the Draupner field data and the Japan Sea field data. The indication of a second peak is most visible at $d = 78$ m. It is observed that the wave period distribution changes significantly from $d = 80, 78$ m to $d = 41, 31$ m. However, this is contrary to what is expected; the wave period distribution is expected to be invariant with respect to the water depth. At $d = 41$ m and $d = 31$ m there appear to be a large number of small wave periods. This is consistent with the observations in Chapter 6.1.3, that secondary peaks in the time series give a larger number of waves with small wave period and corresponding small wave height than expected. This was also illustrated in Fig. 6.9. The Cavanié (1976) model differs significantly from the results in deep water, since this model is dependent on ϵ_4 . The difference in the Longuet-Higgins (1975, 1983) models are due to the change in ϵ_2 . The Bretschneider (1959) model is similar at all water depths, since this model is only dependent on the parameters ζ and T_{m01} that do not vary much for the different water depths. The figures

Table 6.17: Calculated values of the laboratory data.

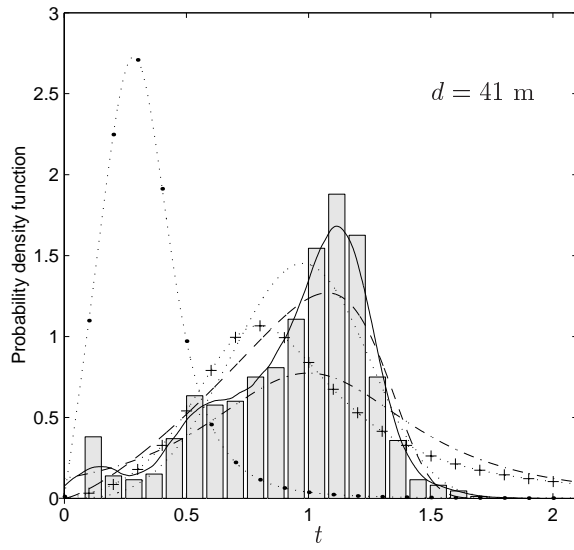
		$d = 80$ m	$d = 78$ m	$d = 41$ m	$d = 31$ m
ζ	[s]	11.32	11.28	10.89	11.13
T_c	[s]	8.79	8.77	3.06	3.33
α_1	[-]	0.910	0.925	4.59	4.22
α_2	[-]	0.870	0.867	0.607	0.615
λ	[-]	0.582	0.779	0.264	0.313
c	[-]	7.737	6.235	8.962	9.178
ν	[-]	1.185	1.127	1.329	1.317
$\rho_{G,12}$	[-]	0.286	0.231	0.313	0.342
$\rho_{G,13}$	[-]	0.088	0.077	0.108	0.091



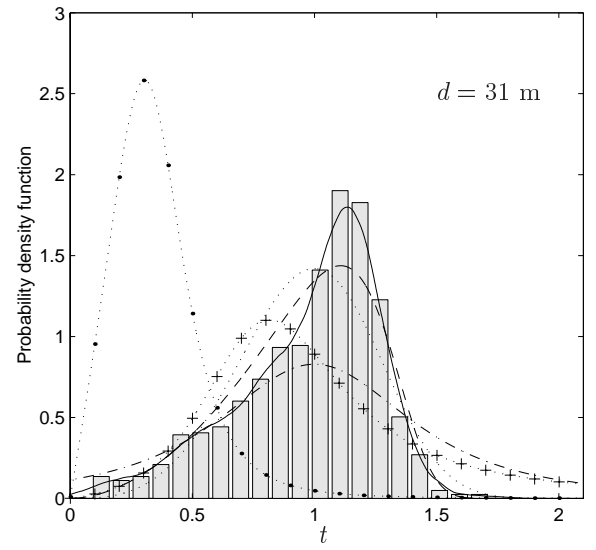
(a)



(b)



(c)



(d)

Figure 6.49: Probability density function of the normalized wave periods. — Generalized Gamma distribution; — KDE laboratory data; \cdots Bretschneider (1959) model; $-\cdot-$ Longuet-Higgins (1975) model; $\cdot + \cdot$ Longuet-Higgins (1983) model; $\cdot \bullet \cdots$ Cavanié (1976) model. (a) $d = 80$ m. (b) $d = 78$ m. (c) $d = 41$ m. (d) $d = 31$ m.

include the generalized Gamma distribution that will be used in the Nataf transformation. The distribution agrees better with the data than the other models, since the parameters are based on the given data sets. However, since the generalized Gamma distribution, and thus the Nataf transformation, will be influenced by the large number of small waves at $d = 41$ m and $d = 31$ m, these results are only shown in Appendix H.3.2 for comparison. The comments given in Chapter 6.1.3 regarding the concerns associated with the data at $d = 41$ m and $d = 31$ m should be kept in mind when considering the results.

The results for $d = 78$ m are quite similar to the results for $d = 80$ m. Thus, these results are shown in Appendix H.3.2. The comments regarding the results for $d = 80$ m will also be valid for the results for $d = 78$ m.

Figure 6.50 (a) shows a histogram of the transformed wave periods and the corresponding kernel density estimate for $d = 80$ m compared with the standard Gaussian probability density function. The transformations yield the same qualitative behaviour as the Draupner field data and Japan Sea field data, and they are significantly different from a Gaussian distribution. The paired plots of the transformed wave periods between t_1 and t_2 in Fig. 6.50 (b) for $d = 80$ m, show that the dependency structure between the two successive wave periods is fairly well described by the bivariate Gaussian distribution.

Thus, from Fig. 6.50 it is clear that the results from the Nataf transformation are not expected to agree very well with the data. However, the results will be as satisfactory as for any of the existing models.

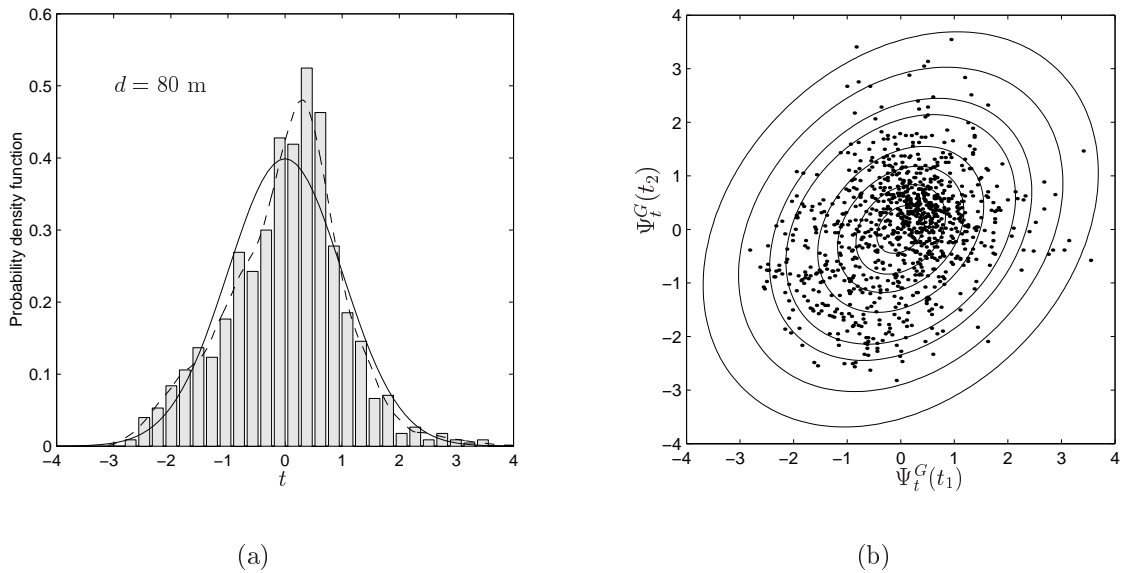


Figure 6.50: (a) Histogram of transformed wave period data. — standard Gaussian probability density function; -- KDE of the transformed wave period data. (b) Paired plot of the transformed wave periods between t_1 and t_2 compared with a contour plot of the standard Gaussian distribution. $d = 80$ m.

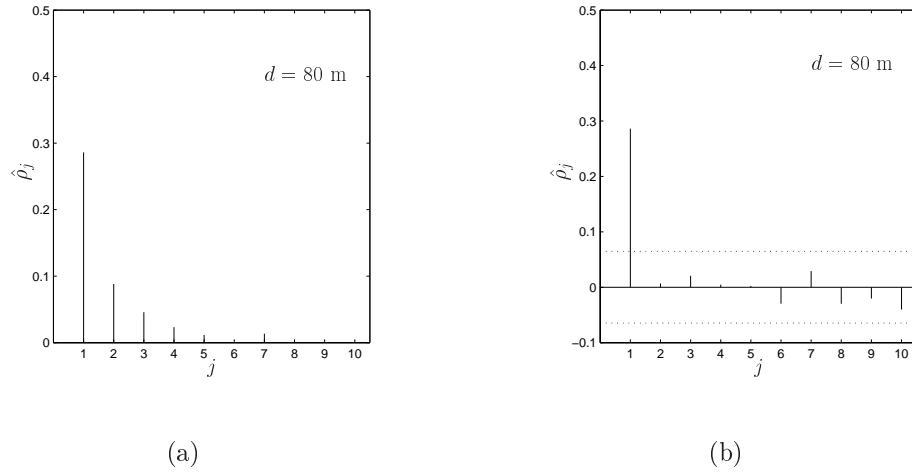


Figure 6.51: (a) Sample autocorrelation function, and (b) sample partial autocorrelation function at $d = 80$ m of Ψ_T^G from laboratory data. The dotted line indicates $\pm(\text{Var}[\hat{\phi}_{jj}])^{1/2}$.

Fig. 6.51 shows the sample ACF and PACF of the transformed wave periods for $d = 80$ m. A likelihood ratio test with $p = 3$ resulted in $n = 318$, and the observed value of the likelihood ratio statistic was $-2 \ln \Lambda_{obs} = 6.38$. From tables $\chi_{0.041,2}^2 = 6.39$, which means that the hypothesis that the correlation coefficients agree with an AR(1) process would not be rejected at 4.1% significance

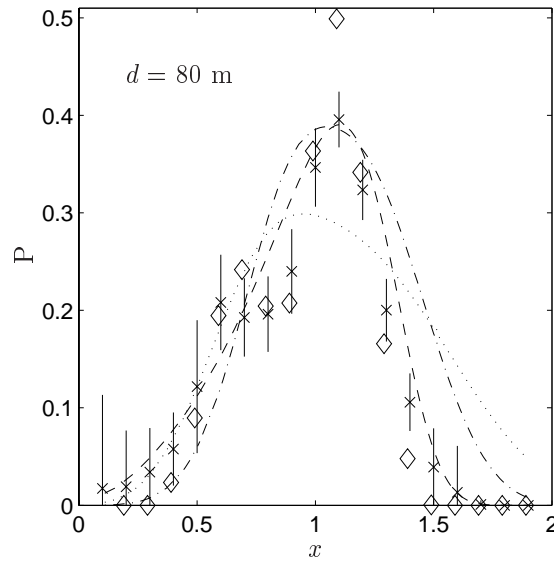


Figure 6.52: The probability that a wave period is in an interval $[\tilde{t}_1, \tilde{t}_2]$ given that the previous wave period was in the same interval, where $\tilde{t}_1 = x - 0.1$ and $\tilde{t}_2 = x + 0.1$. -- Nataf model; \cdots Myrhaug and Rue (1993) model; $-\cdot-$ Myrhaug and Rue (1998) model; \diamond laboratory data; \times simulated data. ($P = P(x - 0.1 < T_2 < x + 0.1 | x - 0.1 < T_1 < x + 0.1)$).

level. Thus, the stochastic process for the transformed wave periods can be approximated by an AR(1) process at the given significance level.

Figure 6.52 shows the probability that a wave period is in an interval $[\tilde{t}_1, \tilde{t}_2]$ of size 0.2 given that the previous wave period was in the same interval, and given that the two corresponding wave heights exceeded h_{rms} . This is shown as a function of $x = (\tilde{t}_1 + \tilde{t}_2)/2$. The confidence intervals of the simulations are also included. The laboratory data have a larger peak than the simulated data. However, due to the large variation in the simulated data the laboratory data agree fairly well with the simulated data for almost all values of x . The results show that the Nataf model agrees well with the data, but it is not able to capture the behaviour with a second peak at $x \approx 0.6$.

The conditional expectation of the wave period given the previous wave period is shown in Appendix H.3.2, and the results are quite similar to the results for the Draupner field data and the Japan Sea field data.

Successive wave periods for large wave heights

In most practical applications, it is of interest to consider wave periods with corresponding large wave heights. When considering wave periods where the corresponding wave height is larger than a given threshold, there are no longer any problems regarding the large number of small wave periods at $d = 41$ m and $d = 31$ m. Then it appears that the distributions for the wave period are quite similar for all water depths, as would be expected (see Fig. 6.9).

The calculated parameters for the Gaussian distribution conditioned on the corresponding p successive wave periods exceeding h_{rms} are shown in Table 6.18. The number n decreases when

Table 6.18: Calculated parameters for the p -dimensional Gaussian distribution with $\tilde{h} = 1$, from the laboratory data.

	$\mu_{t \tilde{h}}$		$\sigma_{t \tilde{h}}$		ρ		n	
	$d = 80\text{m}$	$d = 31\text{m}$	$d = 80\text{m}$	$d = 31\text{m}$	$d = 80\text{m}$	$d = 31\text{m}$	$d = 80\text{m}$	$d = 31\text{m}$
$p = 1$	1.06	1.12	0.107	0.118			360	363
$p = 2$	$\begin{bmatrix} 1.09 \\ 1.10 \end{bmatrix}$	$\begin{bmatrix} 1.16 \\ 1.14 \end{bmatrix}$	$\begin{bmatrix} 0.10 \\ 0.09 \end{bmatrix}$	$\begin{bmatrix} 0.10 \\ 0.11 \end{bmatrix}$	-0.02	0.02	215	233
$p = 3$	$\begin{bmatrix} 1.09 \\ 1.11 \\ 1.11 \end{bmatrix}$	$\begin{bmatrix} 1.16 \\ 1.17 \\ 1.14 \end{bmatrix}$	$\begin{bmatrix} 0.10 \\ 0.07 \\ 0.09 \end{bmatrix}$	$\begin{bmatrix} 0.11 \\ 0.10 \\ 0.11 \end{bmatrix}$	$\begin{bmatrix} -0.04 \\ 0.05 \end{bmatrix}$	$\begin{bmatrix} -0.10 \\ -0.17 \end{bmatrix}$	133	152

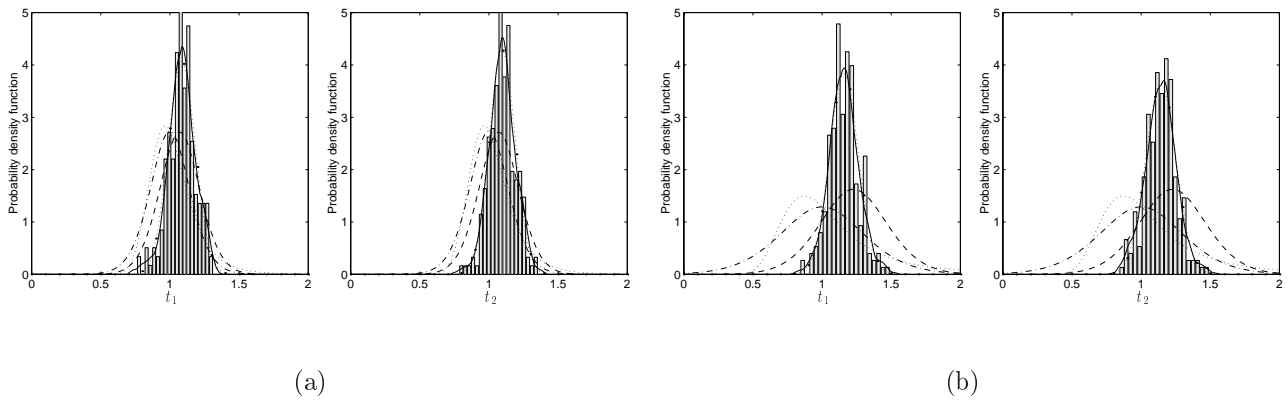


Figure 6.53: Probability density function of wave periods where the corresponding wave height is larger than h_{rms} , i.e., $h > 1$; — KDE laboratory data; -- Tayfun (1993) model; \cdots Longuet-Higgins (1983) model; - \cdot - Longuet-Higgins (1975) model; $\cdot \cdots$ Gaussian density function. (a) $d = 80$ m. (b) $d = 31$ m.

p increases, and the number for $p = 3$ is small. Thus, only two successive wave periods will be considered in the following. However, the number of data cases is also small for $p = 2$, and a longer time series should be considered in order to draw any firm conclusions. Results will only be presented for $d = 80$ m and $d = 31$ m.

Figures 6.53 (a) and (b) show a histogram and the corresponding kernel density estimate of the two successive wave periods with corresponding wave heights larger than h_{rms} for $d = 80$ m and $d = 31$ m, respectively. The data are compared with the Longuet-Higgins (1975, 1983) models, the Tayfun (1993) model and the Gaussian probability density function. The peaks of the data are much larger than any of the models, especially at $d = 31$ m, and the distributions of the data appear to be similar at the two water depths, which was expected. There is a large variation in the data, but the results show that the data agree well with the Gaussian distribution. The difference in the models at $d = 80$ m and $d = 31$ m is due to the change in the parameter ϵ_2 .

Figures 6.54 (a) and (b) show a paired plot of the wave periods t_1 and t_2 compared with a contour plot of the bivariate Gaussian distribution for $d = 80$ m and $d = 31$ m, respectively. The dependency structure resembles the one for the bivariate Gaussian distribution, but the number of data points is too small to make any firm conclusion.

The probability that a wave period is in an interval $[\tilde{t}_1, \tilde{t}_2]$ of size 0.2 given that the previous wave period was in the same interval, and given that the two corresponding wave heights exceeded h_{rms} is shown in Fig. 6.55 (a) and (b) for $d = 80$ m and $d = 31$ m, respectively. This is shown as a function of $x = (\tilde{t}_1 + \tilde{t}_2)/2$. The confidence intervals for the simulations are also included. Due to the large variation in the simulated data, the laboratory data agree well with the simulated data for almost all values of x . The results show a good agreement between the data and the model.

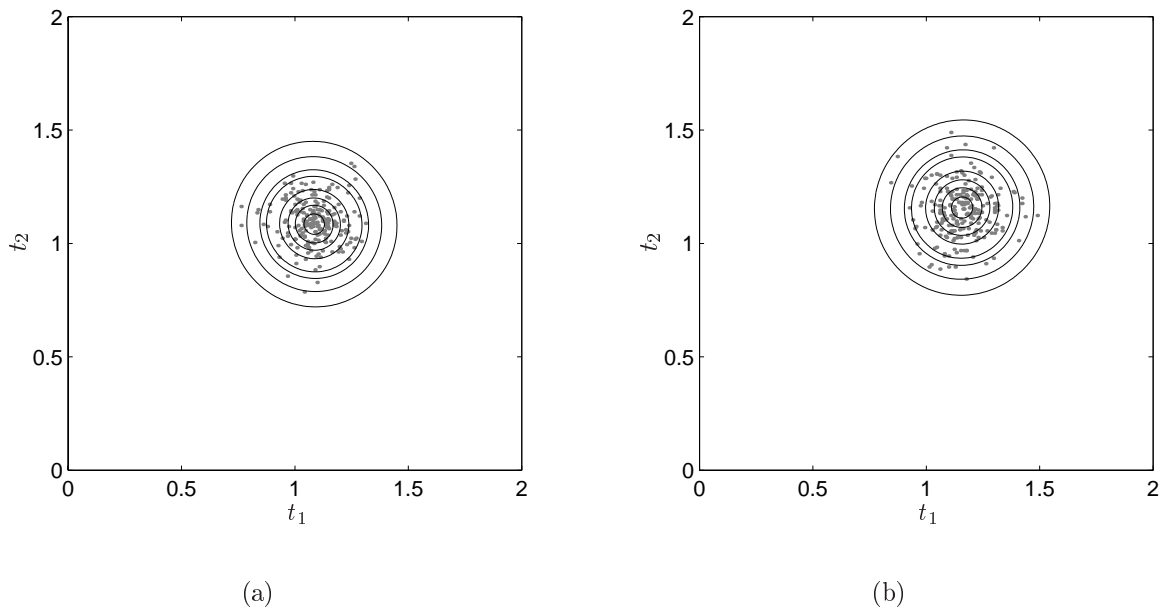


Figure 6.54: Paired plot between t_1 and t_2 compared with a contour plot of the bivariate Gaussian distribution. (a) $d = 80$ m. (b) $d = 31$ m.

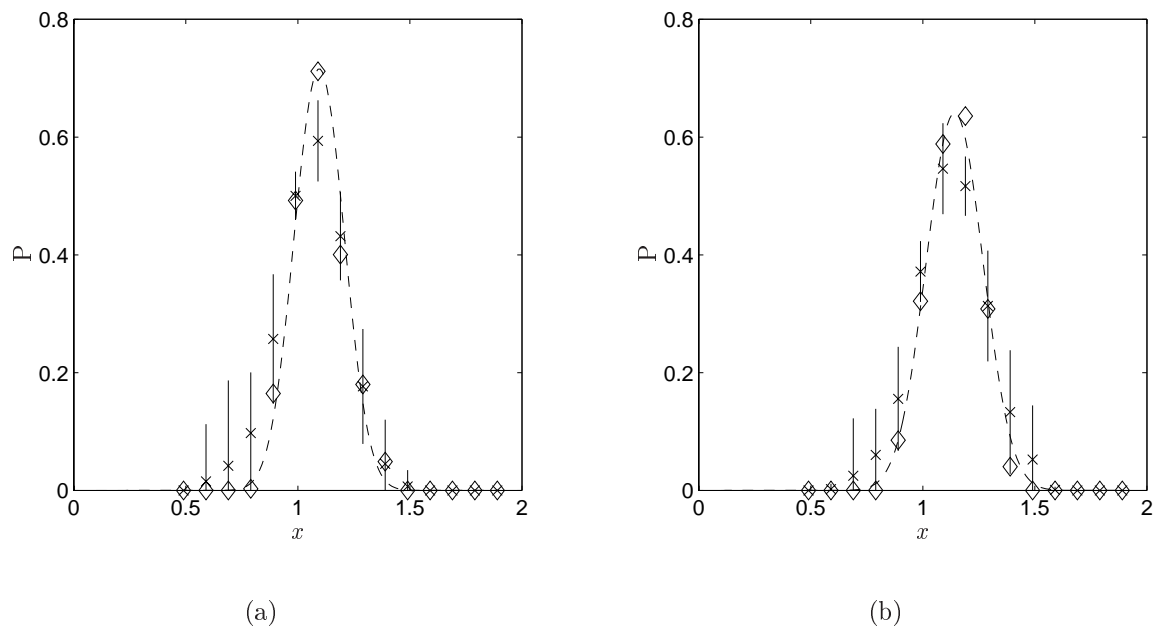


Figure 6.55: The probability that a wave period is in an interval $[\tilde{t}_1, \tilde{t}_2]$ given that the two previous wave periods were in the same interval, where $\tilde{t}_1 = x - 0.1$ and $\tilde{t}_2 = x + 0.1$, and given that the three corresponding wave heights exceeded h_{rms} . -- Nataf model; \diamond laboratory data; \times simulated data. (a) $d = 80$ m. (b) $d = 31$ m.

Conclusions and future perspectives

7.1 Summary and conclusions

The main objective of this work has been to study the statistical properties of parameters for individual successive waves; the wave crest height, the wave height and the wave period. Marginal probability distributions and joint probability distributions of the parameter in successive waves have been presented.

Wave crest heights

In most mild to moderate sea states, the wave crest height can be approximated by half the wave height, and statistics can be determined from the Rayleigh distribution. However, in more severe sea states, which are of interest for design purposes, the wave crest heights are usually larger than half the wave height. Thus, the statistical models must reflect the nonlinearity in the waves. The use of second order Stokes-type nonlinearity have been discussed by several authors. This approach has been adopted here. By transformation of the two-dimensional Rayleigh distribution, a joint probability distribution for two successive wave crest heights is obtained. One should note that the model is based on a narrow-band assumption, and that only sum frequency effects are included. The model is valid in finite water depth. Another wave crest height model is based on the second order wave theory in Marthinsen and Winterstein (1992) for a narrow-banded random sea state. The effect of finite water depth is included. This model includes both sum frequency and difference frequency effects. A parametric wave crest height distribution proposed by Forristall (2000) is also discussed. The model is based on

simulations using second order theory, both for long-crested and short-crested random waves. A two-parameter Weibull distribution is fitted to the simulations. The model has been extended to two dimensions by transformation of the two-dimensional Weibull distribution. Although the wave crest height is the quantity of primary interest in engineering applications, the results for the wave trough depth are included to illustrate the nonlinearity of the waves.

Results for the different wave crest height models are compared with field data from the Draupner field and the Japan Sea, and with laboratory data from experiments at HR Wallingford measured at different water depths. Data from numerical simulations based on second order wave theory, including both sum frequency and difference frequency effects, are also included. It should be noted that the present models are valid for a given constant water depth and do not include shoaling effects. This also applies for the numerical simulations, so any shoaling effects in the laboratory data are not reflected in the simulations that are used for comparison.

The observed data from field measurements and laboratory tests clearly show nonlinear wave effects that should be included in the statistical models. The sum frequency effect has an amplifying effect, which means that the wave crest heights are higher, and the wave trough depths are shallower than in linear theory. The difference frequency term is negative and thus has a reducing effect. The magnitude of the second order effects is illustrated in terms of the quadratic transfer function. It demonstrates the importance of including both sum and difference frequency effects, since both terms are almost of the same magnitude, especially in finite water. The narrow-band assumption, however, may not be that critical since the off-diagonal variation is small, except for difference frequencies in deep water. The second order Stokes model, which only includes the sum frequency effect, overpredicts the data, and should be used in deep water or almost deep water only, where the difference frequency effects are small. The parametric Forristall (2000) model appears to predict the crest heights quite well. This is possibly due to that the simulations, which the model is based upon, include both sum frequency and difference frequency effects.

Wave heights

The existing wave height models are applicable when modeling only two successive wave heights. The models considered here are the Rayleigh distribution and the Næss (1985) model, where the latter distribution was in best agreement with the data.

In this thesis a Gaussian copula, which is often referred to as the Nataf model, is used for modeling three successive wave heights. The difficulty is to find the initial distribution for which the transformation is approximately Gaussian. Both the Næss (1985) model and a two-parameter Weibull distribution have been used in the transformation. The Weibull distribution was in best agreement with the data. However, the parameters in the Weibull distribution must be estimated for each data set. The transformed multivariate Gaussian distribution can in theory be applied for modeling more than three successive wave heights, but then the dependency structure should be examined in order to validate that the correlation between the wave heights is correctly taken care of during the transformation. The results show that the Nataf model is more sensitive to

variation in the data set than the existing models. Thus, the parameter estimation is crucial for the behavior of the distribution.

Results have shown that the Nataf transformation of successive wave heights can be approximated by a first order autoregressive (AR(1)) model. This gives two major advantages. Firstly, the time series has the Markov property, i.e., the distribution of the wave height given the previous wave height is independent of the wave heights prior to the previous wave height. Secondly, the simulation of successive wave heights can be done directly by simulating a series of transformed wave heights and then find the wave heights by inverting the transformation. This is a simple and fast simulation technique, which is useful when the time series of the complete surface elevation is not needed.

Wave periods

Several models exist for modeling a single wave period. The Bretschneider (1959) model, the Longuet-Higgins (1975, 1983) models and the Cavanié (1976) model are presented here. None of them capture the shape of the probability density function of the data, but the Bretschneider (1959) model agrees quite well with the data for large wave periods. Fewer models exist for modeling two successive wave periods. The models considered here are the two-dimensional Weibull distribution (Myrhaug and Rue, 1998) and the special case where the Weibull parameters correspond to the Bretschneider (1959) model (Myrhaug and Rue, 1993).

The Nataf transformation can also be used when modeling more than two successive wave periods. The shape of the probability density function of the data, however, makes it difficult to select an initial distribution so that the transformation is approximately Gaussian. Results from using a two-dimensional Weibull distribution and a generalized Gamma distribution show that the latter distribution yields the best results. The model gives satisfactory results compared with the existing models. The Nataf transformation of successive wave periods can also be approximated by an AR(1) model, which means that the time series has the Markov property. However, the simulation of successive wave periods is not possible in the same way as for the wave heights when using the generalized Gamma distribution in the transformation, since the transformation can not be inverted analytically. Thus, this must be done numerically.

When considering successive wave periods for large waves, the probability density function for the wave periods can be approximated by a Gaussian density function. This means that a transformation is not necessary, and three successive wave periods with corresponding large wave heights can be modeled by the three-dimensional Gaussian distribution. The multivariate Gaussian distribution can also be applied for more than three wave periods with corresponding large wave heights, but then the dependency structure should be further examined. When comparing with data, the number of data cases decreases rapidly both if the selected level of the corresponding wave height increases and if the number of successive periods of interest increases. Thus, a long time series is needed in order to obtain enough data cases.

7.2 Recommendation for further work

The wave crest height and wave trough depth models discussed in this thesis are valid for a given constant water depth and do not include shoaling effects. Thus, it would be of interest to establish a wave crest height model that is valid for varying water depth.

The Nataf model gives the possibility to explore probability distributions for more than two successive waves. The initial distributions explored in this thesis that gave the best results are the Weibull distribution and the generalized Gamma distribution for the wave heights and wave periods, respectively. However, the parameters in the distributions must be estimated from data sets, and the parameters are not related to any of the sea state parameters. Thus, for obtaining a more general method, it would be of interest to establish parameters based on different sea state parameters, similar to the parameters in the Forristall (2000) model. This can be obtained by numerical simulations and validated by comparison with field data.

When considering successive wave periods with corresponding large wave heights, it is of most practical interest to select the corresponding wave height to exceed H_S . This requires a long time series in order to obtain enough data cases for comparison. In this thesis this was only considered for the Draupner field data and the corresponding numerical simulations. The results showed that the multivariate Gaussian distribution was in good agreement with the data. This should be examined further with other large data sets in addition to numerically simulated data.

References

- ABRAMOWITZ, M. AND I. A. STEGUN (1965). *Handbook of mathematical functions*. Dover Publications, New York.
- AL-HUMOUD, J., M. A. TAYFUN, AND H. ASKAR (2002). Distribution of nonlinear wave crests. *Ocean Engineering* 29(15), 1929–1943.
- ARHAN, M. AND R. EZRATY (1978). Statistical relations between successive wave heights. *Oceanologica Acta* 1(2), 151–158.
- ARHAN, M. AND R. O. PLAISTED (1981). Non-linear deformation of sea-wave profiles in intermediate and shallow water. *Oceanologica Acta* 4(2), 107–115.
- BARNDORFF-NIELSEN, O. E. AND D. R. COX (1989). *Asymptotic techniques for use in statistics*. Monographs on statistics and applied probability; 31. Chapman and Hall, London.
- BITNER, E. M. (1980). Non-linear effects of the statistical model of shallow-water wind waves. *Applied Ocean Research* 2(2), 63–73.
- BOCCOTTI, P. (1982). Relations between characteristic sea wave parameters. *Journal of Geophysical Research* 87(C6), 4267–4268.
- BRETSCHNEIDER, C. L. (1959). Wave variability and wave spectra for wind-generated gravity waves. Beach Erosion Board, U.S. Army Corps of Engineers. Technical Memorandum 118.
- BRODTKORB, P. A., D. MYRHAUG, AND H. RUE (2000). Joint distributions of wave height and wave steepness parameters. In *Proceedings 27th International Conference on Coastal Engineering*, Vol 1, Sydney, Australia, pp. 545–558.
- CARTWRIGHT, D. E. AND M. S. LONGUET-HIGGINS (1956). The statistical distribution of the maxima of a random function. *Proc. R. Soc. Lond. A* 237, 212–232.
- CAVANIÉ, A., M. ARHAN, AND R. EZRATY (1976). A statistical relationship between individual heights and periods of storm waves. In *Proceedings First International Conference on Behaviour of Off-Shore Structures*, Vol 2, Trondheim, Norway, pp. 354–360.

- DAWSON, T. H. (2001). Rayleigh law and Stokes correction for high waves in heavy seas. In *Ocean wave measurement and analysis: Proceedings of the fourth international symposium WAVES 2001*, Vol 1, San Francisco, California, pp. 484–493.
- DEAN, R. G. AND R. A. DALRYMPLE (1984). *Water wave mechanics for engineers and scientists*. Prentice-Hall, Englewood Cliffs, New Jersey.
- DEAN, R. G. AND J. N. SHARMA (1981). Simulation of wave systems due to nonlinear directional spectra. In *Int. Symp. on Hydrodynamics in Ocean Engineering*, Vol 2, Trondheim, Norway, pp. 1211–1222.
- EPANECHNIKOV, V. A. (1969). Non-parametric estimation of a multivariate probability density. *Theory of probability and its applications* 14, 153–158.
- EWING, J. A. (1973). Mean length of runs of high waves. *Journal of Geophysical Research* 78(12), 1933–1936.
- FORRISTALL, G. Z. (1978). On the statistical distribution of wave heights in a storm. *Journal of Geophysical Research* 83(C5), 2353–2358.
- FORRISTALL, G. Z. (1998). Wave crest distributions: Observations and second order theory. In *Ocean Wave Kinematics, Dynamics and Load on Structures, Proc. of 1998 Int. OTRC Symposium*, Houston, Texas, pp. 372–395.
- FORRISTALL, G. Z. (2000). Wave crest distributions: Observations and second-order theory. *Journal of Physical Oceanography* 30(8), 1931–1943.
- FRANCE, W. N., M. LEVADOU, T. W. TRAKLE, J. R. PAULLING, R. K. MICHEL, AND C. MOORE (2003). An investigation of head-sea parametric rolling and its influence on container lashing systems. *Marine Technology* 40(1), 1–19.
- FRÉCHET, M. (1957). Les tableaux de corrélation et les programmes linéaires. *Revue de l'Institut international de statistique* 25, 23–40.
- GODA, Y. (1970). Numerical experiments on wave statistics with spectral simulation. *Report of The Port and Harbour Research Institute* 9(3), 3–57.
- GODA, Y. (1974). Estimation of wave statistics from spectral information. In *Proceedings of the International Symposium on Ocean Wave Measurement and Analysis*, Vol 1, New Orleans, Louisiana, pp. 320–337. ASCE.
- GUEDES SOARES, C. (1984). Representation of double-peaked sea wave spectra. *Ocean Engineering* 11(2), 185–207.
- GUEDES SOARES, C. AND A. N. CARVALHO (2003). Probability distributions of wave heights and periods in measured combined sea-states from the Portuguese Coast. *Journal of Off-shore Mechanics and Arctic Engineering* 125, 198–204.
- HARING, R. E., A. R. OSBORNE, AND L. P. SPENCER (1976). Extreme wave parameters based on continental shelf storm wave records. In *Proceedings of the Fifteenth Coastal Engineering Conference*, Honolulu, Hawaii, pp. 151–170.
- JHA, A. K. AND S. R. WINTERSTEIN (2000). Nonlinear random ocean waves: Prediction and comparison with data. In *Proceedings of ETCE/OMAE2000 Joint Conference Energy for the New Millenium*, New Orleans, Louisiana. OMAE2000/S&R-6125.

- JOHNSON, N. L. AND S. KOTZ (1970). *Distributions in statistics: Continuous univariate distributions*, Vol 1. John Wiley & Sons.
- JOHNSON, R. A. AND D. W. WICHERN (1992). *Applied multivariate statistical analysis* (3 ed.). Prentice-Hall, Englewood Cliffs, New Jersey.
- KAPLAN, P. (1992). Wave impact forces on offshore structures: Re-examination and new interpretations. In *Proc. of the 24th Offshore Technology Conference*, Houston, Texas, pp. 79–86. OTC 6814.
- KAPLAN, P., J. J. MURRAY, AND W. C. YU (1995). Theoretical analysis of wave impact forces on platform deck structures. In *Proc. of the 14th Int. Conf. on Offshore Mechanics and Arctic Engineering*, Vol 1-A, Copenhagen, Denmark, pp. 189–198. ASME.
- KIMURA, A. (1980). Statistical properties of random wave groups. In *Proceedings of the 17th Coastal Engineering Conference*, Vol III, Sydney, Australia, pp. 2955–2973. ASCE.
- KJELDSSEN, S. P. (1981). Design waves. Technical Report NHL 181008, Norwegian Hydrodynamic Laboratories, Trondheim, Norway.
- KRIEBEL, D. L. AND T. H. DAWSON (1991). Nonlinear effects on wave groups in random seas. *Journal of Offshore Mechanics and Arctic Engineering* 113(2), 142–147.
- KRIEBEL, D. L. AND T. H. DAWSON (1993). Nonlinearity in wave crest statistics. In *Proc. of the 2nd Int. Symp. on Ocean Wave Measurement and Analysis, Waves '93*, New Orleans, Louisiana, pp. 61–75. ASCE.
- LINDGREN, G. AND I. RYCHLIK (1982). Wave characteristic distributions for Gaussian waves - wave-length, amplitude and steepness. *Ocean Engineering* 9(5), 411–432.
- LIU, P.-L. AND A. DER KIUREGHIAN (1986). Multivariate distribution models with prescribed marginals and covariances. *Probabilistic Engineering Mechanics* 1(2), 105–112.
- LONGUET-HIGGINS, M. S. (1952). On the statistical distribution of the heights of sea waves. *Journal of Marine Research* 11(3), 245–266.
- LONGUET-HIGGINS, M. S. (1957). The statistical analysis of a random, moving surface. *Phil. Trans. R. Soc. Lond. A.* 249(966), 321–387.
- LONGUET-HIGGINS, M. S. (1963). The effect of non-linearities on statistical distributions in the theory of sea waves. *Journal of Fluid Mechanics* 17(3), 459–480.
- LONGUET-HIGGINS, M. S. (1975). On the joint distribution of the periods and amplitudes of sea waves. *Journal of Geophysical Research* 80(18), 2688–2694.
- LONGUET-HIGGINS, M. S. (1980). On the distribution of the heights of sea waves: Some effects of nonlinearity and finite band width. *Journal of Geophysical Research* 85(C3), 1519–1523.
- LONGUET-HIGGINS, M. S. (1983). On the joint distribution of wave periods and amplitudes in a random wave field. *Proc. R. Soc. Lond. A.* 389, 241–258.
- LONGUET-HIGGINS, M. S. (1984). Statistical properties of wave groups in a random sea state. *Phil. Trans. R. Soc. Lond. A.* 312, 219–250.

- LONGUET-HIGGINS, M. S. (1986). Wave group statistics. In E. C. MONAHAN AND G. MAC NIOCAILL (Eds.), *Oceanic Whitecaps*, pp. 15–35. D. Reidel Publishing Company, Dordrecht.
- MACHADO, U. B. (2003). Probability density functions for non-linear random waves and responses. *Ocean Engineering* 30(8), 1027–1050.
- MARTHINSEN, T. AND S. R. WINTERSTEIN (1992). On the skewness of random surface waves. In *Proc. of the Second Int. Offshore and Polar Engineering Conference*, Vol 3, San Francisco, USA, pp. 472–478.
- MASSEL, S. R. (1996). *Ocean surface waves: Their physics and prediction*. Advanced series on ocean engineering; 11. World Scientific Publishing, Singapore.
- MEMOS, C. (2002). Stochastic description of sea waves. *Journal of Hydraulic Research* 40(3), 265–274. With contributions by Tzanis, K. and Zographou, K.
- MIDDLETON, D. (1960). *An introduction to statistical communication theory*. McGraw-Hill Company, Inc., New York.
- MYRHAUG, D., E. A. DAHLE, AND H. RUE (1995). A two-dimensional Weibull distribution and its application to rolling. *Journal of Offshore Mechanics and Arctic Engineering* 117(3), 178–182.
- MYRHAUG, D., E. A. DAHLE, H. RUE, AND O. H. SLAATTELID (2000). Statistics of successive wave periods with application to rolling of ships. *International Shipbuilding Progress: Marine Technology Quarterly* 47(451), 253–266.
- MYRHAUG, D. AND S. P. KJELDSSEN (1984). Parametric modelling of joint probability density distributions for steepness and asymmetry in deep water waves. *Applied Ocean Research* 6(4), 207–220.
- MYRHAUG, D. AND H. RUE (1993). Note on a joint distribution of successive wave periods. *Journal of Ship Research* 37(3), 208–212.
- MYRHAUG, D. AND H. RUE (1998). Joint distribution of successive wave periods revisited. *Journal of Ship Research* 42(3), 199–206.
- MYRHAUG, D. AND O. H. SLAATTELID (1999). Statistical properties of successive wave periods. *Journal of Offshore Mechanics and Arctic Engineering* 121, 166–171.
- MYRHAUG, D., C. T. STANSBERG, AND H. T. WIST (2002). Aspects of nonlinear random wave kinematics. In *Proc. of OMAE'02, 21st Int. Conf. on Offshore Mechanics and Arctic Engineering*, Oslo, Norway. OMAE2002-28205.
- NÆSS, A. (1985). On the distribution of crest to trough wave heights. *Ocean Engineering* 12(3), 221–234.
- NATAF, A. (1962). Détermination des distributions de probabilités dont les marges sont données. *Comptes Rendus Hebdomadaires des Séances de l'Académie des Sciences* 255, 42–43.
- NELSEN, R. B. (1999). *An introduction to copulas*. Lecture notes in statistics; 139. Springer-Verlag, New York.

- NERZIC, R. AND M. PREVOSTO (1997). A Weibull-Stokes model for the distribution of maximum wave and crest heights. In *Proc. of the Seventh Int. Offshore and Polar Engineering Conf*, Vol 3, Honolulu, USA, pp. 367–377.
- NERZIC, R. AND M. PREVOSTO (1998). A Weibull-Stokes model for the distribution of maximum wave and crest heights. *Journal of Offshore and Polar Engineering* 8(2), 90–101.
- NEWLAND, D. E. (1993). *An introduction to random vibrations, spectral and wavelet analysis* (3 ed.). Longman, Harlow.
- NOLTE, K. G. AND F. H. HSU (1972). Statistics of ocean wave groups. In *Preprint Proc. of Fourth Offshore Technology Conference*, Houston, Texas, pp. 637–644. OTC-1688.
- OCHI, M. K. (1992). New approach for estimating the severest sea state from statistical data. In *Coastal Engineering 1992: Proc. 23rd Int. Conf.*, Vol 1, Venice, Italy, pp. 512–525.
- OCHI, M. K. (1998). *Ocean waves*. Cambridge University Press, Cambridge.
- OGAWA, Y. (2003). Long-term prediction method for the green water load and volume for an assessment of the load line. *Journal of Marine Science and Technology* 7, 137–144.
- PEARSON, K. (1895). Contributions to the mathematical theory of evolution. II Skew variations in homogeneous material. *Philos. Trans. Roy. Soc. London, Ser. A* 186, 343–414.
- PREVOSTO, M. AND G. Z. FORRISTALL (2002). Statistics of wave crests from models vs. measurements. In *Proc. of OMAE'02, 21st Int. Conf. on Offshore Mechanics and Arctic Engineering*, Oslo, Norway. OMAE2002-28443.
- PREVOSTO, M., H. E. KROGSTAD, AND A. ROBIN (2000). Probability distributions for maximum wave and crest heights. *Coastal Engineering* 40, 329–360.
- RAYLEIGH, L. (1880). On the resultant of a large number of vibrations of the same pitch and of arbitrary phase. *Philosophical Magazine*, 73–78. In *Scientific papers by John William Strutt, Baron Rayleigh*, Vol I. 1869–1881, pp. 491–496. Cambridge University Press (1899).
- RICE, S. O. (1945). Mathematical analysis of random noise. *Bell System Technical Journal* 24, 46–156.
- RODRÍGUEZ, G. AND C. GUEDES SOARES (1999). The bivariate distribution of wave heights and periods in mixed sea states. *Journal of Offshore Mechanics and Arctic Engineering* 121, 102–108.
- RODRÍGUEZ, G., C. GUEDES SOARES, M. PACHECO, AND E. PÉREZ-MARTELL (2002). Wave height distribution in mixed sea states. *Journal of Offshore Mechanics and Arctic Engineering* 124, 34–40.
- RODRÍGUEZ, G. R. AND C. GUEDES SOARES (2000). Wave period distribution in mixed sea states. In *Proceedings of ETCE/OMAE2000 Joint Conference Energy for the New Millenium*, New Orleans, Louisiana. OMAE2000/S&R-6132.
- RYCHLIK, I., P. JOHANNESSON, AND M. R. LEADBETTER (1997). Modelling and statistical analysis of ocean-wave data using transformed Gaussian processes. *Marine Structures* 10, 13–47.

- RYE, H. (1977). The stability of some currently used wave parameters. *Coastal Engineering* 1, 17–30.
- RYE, H. AND R. SVEE (1976). Parametric representation of a wind-wave field. In *Proceedings of the 15th Coastal Engineering Conference*, Honolulu, Hawaii, pp. 183–199.
- SCHWEIZER, B. (1991). Thirty years of copulas. In *Advances in probability distributions with given marginals*, Rome, Italy, pp. 13–50.
- SHARMA, J. N. AND R. G. DEAN (1981). Second-order directional seas and associated wave forces. *Society of Petroleum Engineers Journal* 21, 129–140.
- SILVERMAN, B. W. (1986). *Density estimation for statistics and data analysis*. Monographs on statistics and applied probability; 26. Chapman & Hall, London.
- SIMONS, R. R., R. J. WHITEHOUSE, R. D. MACIVER, J. PEARSON, P. B. SAYERS, Y. ZHAO, AND A. R. CHANNELL (1995). Evaluation of the UK Coastal Research Facility. In *Coastal dynamics '95 : proceedings of the Int. Conf. on Coastal Research in Terms of Large Scale Experiments*, Gdansk, Poland, pp. 161–172.
- SKJELBREIA, L. AND J. HENDRICKSON (1960). Fifth order gravity wave theory. In *Proceedings of Seventh Conference on Coastal Engineering*, Hague, Netherlands, pp. 184–196.
- SOBEY, R. J. (1996). Correlation between individual waves in a real sea state. *Coastal Engineering* 27, 223–242.
- SOULSBY, R. (1997). *Dynamics of marine sands: A manual for practical applications*. Thomas Telford, London.
- SROKOSZ, M. A. (1998). A new statistical distribution for the surface elevation of weakly nonlinear water waves. *Journal of Physical Oceanography* 28(1), 149–155.
- STANSBERG, C. T. (1993). Second-order numerical reconstruction of laboratory generated random waves. In *Proc. of OMAE'93, 12th Int. Conf. on Offshore Mechanics and Arctic Engineering*, Vol 2, Glasgow, Scotland, pp. 143–151.
- STANSBERG, C. T. (1998). Non-Gaussian extremes in numerically generated second-order random waves on deep water. In *Proc. of the Eighth Int. Offshore and Polar Engineering Conference*, Vol 3, Montréal, Canada, pp. 103–110.
- STANSBERG, C. T. AND S. I. KARLSEN (2001). Green sea and water impact on FPSO in steep random waves. In *Proc. of the Eighth Int. Symp. on Practical Design of Ships and Other Floating Structures, PRADS*, Vol 1, Shanghai, China, pp. 593–601.
- STOKES, G. G. (1847). On the theory of oscillatory waves. *Trans. of the Cambridge Philosophical Society* 8, 441–455.
- SUNDE, A. (1995). Kjempebølger i Nordsjøen. *Vær og klima* 18(1), 17–23. In Norwegian.
- SWEETMAN, B. AND S. R. WINTERSTEIN (2003). Non-Gaussian air gap response models for floating structures. *Journal of Engineering Mechanics* 129(3), 302–309.
- TAYFUN, M. A. (1980). Narrow-band nonlinear sea waves. *Journal of Geophysical Research* 85(C3), 1548–1552.

- TAYFUN, M. A. (1990). Distribution of large wave heights. *Journal of Waterway, Port, Coastal, and Ocean Engineering* 116(6), 686–707.
- TAYFUN, M. A. (1993). Joint distribution of large wave heights and associated periods. *Journal of Waterway, Port, Coastal, and Ocean Engineering* 119(3), 261–273.
- TAYFUN, M. A. (1994). Distributions of envelope and phase in weakly nonlinear random waves. *Journal of Engineering Mechanics* 120(5), 1009–1025.
- TUNG, C. C. AND N. E. HUANG (1985). Peak and trough distributions of nonlinear waves. *Ocean Engineering* 12(3), 201–209.
- VINJE, T. (1989). The statistical distribution of wave heights in a random seaway. *Applied Ocean Research* 11(3), 143–152.
- WEI, W. W. S. (1990). *Time series analysis: Univariate and multivariate methods*. Addison-Wesley Publishing Company, Redwood City, California.
- WIST, H. T., D. MYRHAUG, AND H. RUE (2001). Nonlinearity in successive wave crest height statistics. In *Ocean wave measurement and analysis: Proceedings of the fourth international symposium WAVES 2001*, Vol 1, San Francisco, California, pp. 464–473.
- WIST, H. T., D. MYRHAUG, AND H. RUE (2002a). Joint distributions of successive wave crest heights and successive wave trough depths for second-order nonlinear waves. *Journal of Ship Research* 46(3), 175–185.
- WIST, H. T., D. MYRHAUG, AND H. RUE (2002b). Nonlinearity in successive wave crest height statistics in finite water depths. In *Proc. of 28th Int. Conf. on Coastal Eng. ICCE 2002*, Vol 1, Cardiff, Wales, pp. 601–613.

APPENDIX A

Properties of the Rayleigh distribution

A.1 The marginal Rayleigh distribution

The Rayleigh probability density function of a dimensionless variable A is given by (Rayleigh, 1880)

$$f_A(a) = 2a \exp \{-a^2\}; \quad a \geq 0. \quad (\text{A.1})$$

The expected value and variance are given by

$$\text{E}[A] = \frac{1}{2}\sqrt{\pi} \quad (\text{A.2})$$

$$\text{Var}[A] = 1 - \frac{\pi}{4}. \quad (\text{A.3})$$

A.2 A two-dimensional Rayleigh distribution

There are several number of possible forms of two-dimensional distributions whose marginal probability density function is given by Eq. (A.1). A possible two-dimensional Rayleigh distribution is given by (see Kimura (1980) or Longuet-Higgins (1986))

$$f_{A_1, A_2}(a_1, a_2) = \frac{4a_1 a_2}{1 - \kappa_a^2} \exp \left\{ -\frac{a_1^2 + a_2^2}{1 - \kappa_a^2} \right\} I_0 \left[\frac{2\kappa_a a_1 a_2}{1 - \kappa_a^2} \right], \quad (\text{A.4})$$

where a_1 and a_2 are nondimensional variables and I_0 is the modified Bessel function of zeroth order. The parameter κ_a is related to the correlation coefficient ρ_a between A_1 and A_2 by

$$\rho_a = \frac{E(\kappa_a) - \frac{1}{2}(1 - \kappa_a^2)K(\kappa_a) - \frac{\pi}{4}}{1 - \frac{\pi}{4}}, \quad (\text{A.5})$$

where $K(\kappa_a)$ and $E(\kappa_a)$ are complete elliptic integrals of the first and second kind, respectively, defined by (Abramowitz and Stegun, 1965)

$$K(\kappa_a) = \int_0^{\pi/2} (1 - \kappa_a^2 \sin^2 \theta)^{-\frac{1}{2}} d\theta \quad (\text{A.6})$$

$$E(\kappa_a) = \int_0^{\pi/2} (1 - \kappa_a^2 \sin^2 \theta)^{\frac{1}{2}} d\theta. \quad (\text{A.7})$$

The elliptic functions can also be expressed by the hypergeometric function $F(a, b; c; x)$,

$$K(\kappa_a) = \frac{1}{2}\pi F\left(\frac{1}{2}, \frac{1}{2}; 1; \kappa_a^2\right) \quad (\text{A.8})$$

$$E(\kappa_a) = \frac{1}{2}\pi F\left(-\frac{1}{2}, \frac{1}{2}; 1; \kappa_a^2\right), \quad (\text{A.9})$$

where

$$F(a, b; c; x) = \frac{\Gamma(c)}{\Gamma(a)\Gamma(b)} \sum_{n=0}^{\infty} \frac{\Gamma(a+n)\Gamma(b+n)}{\Gamma(c+n)} \frac{x^n}{n!}. \quad (\text{A.10})$$

The correlation coefficient ρ_a can then be expressed by

$$\rho_a = \frac{\frac{\pi}{4}F\left(-\frac{1}{2}, -\frac{1}{2}; 1; \kappa_a^2\right) - \frac{\pi}{4}}{1 - \frac{\pi}{4}}. \quad (\text{A.11})$$

Calculation of the expected values is performed by expanding the Bessel function (Middleton, 1960)

$$\begin{aligned} E[A_1^\nu A_2^\mu] &= \int_0^\infty \int_0^\infty a_1^\nu a_2^\mu f_{A_1, A_2}(a_1, a_2) da_1 da_2 \\ &= \int_0^\infty \int_0^\infty a_1^\nu a_2^\mu \frac{4a_1 a_2}{1 - \kappa_a^2} \exp\left(-\frac{a_1^2 + a_2^2}{1 - \kappa_a^2}\right) \sum_{m=0}^{\infty} \frac{\left(\frac{2\kappa_a a_1 a_2}{1 - \kappa_a^2}\right)^{2m}}{2^{2m} m! \Gamma(m+1)} da_1 da_2 \\ &= \sum_{m=0}^{\infty} \frac{1}{(m!)^2} \kappa_a^{2m} (1 - \kappa_a^2)^{\nu/2 + \mu/2 + 1} \Gamma\left(\frac{\nu}{2} + m + 1\right) \Gamma\left(\frac{\mu}{2} + m + 1\right) \\ &= (1 - \kappa_a^2)^{\nu/2 + \mu/2 + 1} \Gamma\left(\frac{\nu}{2} + 1\right) \Gamma\left(\frac{\mu}{2} + 1\right) F\left(\frac{\nu}{2} + 1, \frac{\mu}{2} + 1; 1; \kappa_a^2\right). \end{aligned} \quad (\text{A.12})$$

This gives the following expected values

$$\mathbb{E}[A_1] = \mathbb{E}[A_2] = \frac{1}{2}\sqrt{\pi} \quad (\text{A.13})$$

$$\mathbb{E}[A_1^2] = \mathbb{E}[A_2^2] = 1 \quad (\text{A.14})$$

$$\mathbb{E}[A_1^3] = \mathbb{E}[A_2^3] = \frac{3}{4}\sqrt{\pi} \quad (\text{A.15})$$

$$\mathbb{E}[A_1^4] = \mathbb{E}[A_2^4] = 2 \quad (\text{A.16})$$

$$\mathbb{E}[A_1 A_2] = \frac{\pi}{4}(1 - \kappa_a^2)^2 F\left(\frac{3}{2}, \frac{3}{2}; 1; \kappa_a^2\right) \quad (\text{A.17})$$

$$\mathbb{E}[A_1 A_2^2] = \mathbb{E}[A_1^2 A_2] = \frac{1}{4}\sqrt{\pi}(2 + \kappa_a^2) \quad (\text{A.18})$$

$$\mathbb{E}[A_1^2 A_2^2] = 1 + \kappa_a^2 \quad (\text{A.19})$$

These properties of the Rayleigh distribution are needed for calculation the correlation coefficients in Appendix D.

APPENDIX B

Perturbation technique in second order Stokes theory

A description of the perturbation approach of Stokes (1847) is given in e.g. Dean and Dalrymple (1984). However, some steps in the deduction of the second order solution is not straight forward, thus a more thorough description is given below.

The governing differential equation (GE) is given by

$$\nabla^2 \phi = 0, \quad (\text{B.1})$$

with bottom boundary condition (BBC)

$$\frac{\partial \phi}{\partial z} = 0; \quad z = -d. \quad (\text{B.2})$$

The dynamic free surface condition (DFSC) is given by

$$\frac{p}{\rho} + \frac{\partial \phi}{\partial t} + \frac{1}{2} \left[\left(\frac{\partial \phi}{\partial x} \right)^2 + \left(\frac{\partial \phi}{\partial z} \right)^2 \right] + gz = C_B; \quad z = \eta(x, t), \quad (\text{B.3})$$

where C_B is the Bernoulli constant. The kinematic free surface condition (KFSC) is given by

$$\frac{\partial \eta}{\partial t} + \frac{\partial \phi}{\partial x} \frac{\partial \eta}{\partial x} - \frac{\partial \phi}{\partial z} = 0; \quad z = \eta(x, t). \quad (\text{B.4})$$

By introducing dimensionless variables

$$\begin{aligned} X &= kx & \Phi &= \frac{k\phi}{\eta_a \sqrt{kg}} \\ Z &= kz & \Omega &= \frac{\omega}{\sqrt{kg}} \\ A &= \frac{\eta}{\eta_a} & P &= \frac{kp}{\rho g} \\ T &= \sqrt{kg} t & Q &= \frac{k}{g} C_B, \end{aligned}$$

the boundary value problem is given by

$$\begin{aligned} \text{(GE)} \quad & \nabla^2 \Phi = 0 \\ \text{(BBC)} \quad & \frac{\partial \Phi}{\partial Z} = 0; \quad Z = -kd \\ \text{(DFSC)} \quad & P + \eta_a k \frac{\partial \Phi}{\partial T} + \frac{1}{2} (\eta_a k)^2 \left[\left(\frac{\partial \Phi}{\partial X} \right)^2 + \left(\frac{\partial \Phi}{\partial Z} \right)^2 \right] + Z = Q; \quad Z = \eta_a k A \\ \text{(KFSC)} \quad & \frac{\partial A}{\partial T} + \eta_a k \frac{\partial \Phi}{\partial X} \frac{\partial A}{\partial X} - \frac{\partial \Phi}{\partial Z} = 0; \quad Z = \eta_a k A. \end{aligned} \tag{B.5}$$

The exact free surface is not known, and by a Taylor expansion about $\eta_a k A$, the free surface conditions are transferred from the free surface position $Z = \eta_a k A$ to the mean free surface at $Z = 0$. Also Q is selected so that $P = 0$ on the free surface.

$$\begin{aligned} \text{(DFSC)} \quad & \frac{\partial \Phi}{\partial T} + \frac{1}{2} \eta_a k \left[\left(\frac{\partial \Phi}{\partial X} \right)^2 + \left(\frac{\partial \Phi}{\partial Z} \right)^2 \right] + \eta_a k A \frac{\partial^2 \Phi}{\partial Z \partial T} + A + \mathcal{O}((\eta_a k)^2) = Q; \quad Z = 0 \\ \text{(KFSC)} \quad & \frac{\partial A}{\partial T} + \eta_a k \frac{\partial \Phi}{\partial X} \frac{\partial A}{\partial X} - \frac{\partial \Phi}{\partial Z} + \eta_a k A \frac{\partial^2 A}{\partial Z \partial T} - \eta_a k A \frac{\partial^2 \Phi}{\partial Z^2} + \mathcal{O}((\eta_a k)^2) = 0; \quad Z = 0 \end{aligned} \tag{B.6}$$

By using $\eta_a k$ as an expansion parameter, i.e. assuming $\eta_a k$ is small, the different quantities can be decomposed into power series

$$\begin{aligned} \Phi &= \Phi_1 + \eta_a k \Phi_2 + (\eta_a k)^2 \Phi_3 + \dots \\ A &= A_1 + \eta_a k A_2 + (\eta_a k)^2 A_3 + \dots \\ Q &= Q_1 + \eta_a k Q_2 + (\eta_a k)^2 Q_3 + \dots \\ \Omega &= \Omega_1 + \eta_a k \Omega_2 + (\eta_a k)^2 \Omega_3 + \dots \end{aligned} \tag{B.7}$$

The boundary value problem is then given by

$$\begin{aligned}
(\text{GE}) \quad & \nabla^2 \Phi_1 + \eta_a k \nabla^2 \Phi_2 + \mathcal{O}((\eta_a k)^2) = 0 \\
(\text{BBC}) \quad & \frac{\partial \Phi_1}{\partial Z} + \eta_a k \frac{\partial \Phi_2}{\partial Z} + \mathcal{O}((\eta_a k)^2) = 0; \quad Z = -kd \\
(\text{DFSC}) \quad & \frac{\partial \Phi_1}{\partial T} + \eta_a k \frac{\partial \Phi_2}{\partial T} + \frac{1}{2} \eta_a k \left[\left(\frac{\partial \Phi_1}{\partial x} \right)^2 + \left(\frac{\partial \Phi_1}{\partial Z} \right)^2 \right] \\
& + \eta_a k A_1 \frac{\partial^2 \Phi_1}{\partial Z \partial T} + A_1 + \eta_a k A_2 + \mathcal{O}((\eta_a k)^2) = Q_1 + \eta_a k Q_2; \quad Z = 0 \\
(\text{KFSC}) \quad & \frac{\partial A_1}{\partial T} + \eta_a k \frac{\partial A_2}{\partial T} + \eta_a k \frac{\partial \Phi_1}{\partial X} \frac{\partial A_1}{\partial X} - \frac{\partial \Phi_1}{\partial Z} - \eta_a k \frac{\partial \Phi_2}{\partial Z} \\
& + \eta_a k A_1 \frac{\partial^2 A_1}{\partial Z \partial T} - \eta_a k A_1 \frac{\partial^2 \Phi_1}{\partial Z^2} + \mathcal{O}((\eta_a k)^2) = 0; \quad Z = 0.
\end{aligned} \tag{B.8}$$

The first order equations are given by keeping the terms of order $(\eta_a k)^0$.

$$\begin{aligned}
(\text{GE}) \quad & \nabla^2 \Phi_1 = 0 \\
(\text{BBC}) \quad & \frac{\partial \Phi_1}{\partial Z} = 0; \quad Z = -kd \\
(\text{DFSC}) \quad & \frac{\partial \Phi_1}{\partial T} + A_1 = Q_1; \quad Z = 0 \\
(\text{KFSC}) \quad & \frac{\partial A_1}{\partial T} - \frac{\partial \Phi_1}{\partial Z} = 0; \quad Z = 0
\end{aligned} \tag{B.9}$$

The solution is found by the method of separating variables

$$\Phi_1(X, Z, T) = \cosh(Z + kd) \left[B_1 \cos(\Omega T - X) + \tilde{B}_1 \sin(\Omega T - X) \right], \tag{B.10}$$

where B_1 and \tilde{B}_1 are constants that are found from the DFSC. Since A_1 has a zero spatial and temporal mean, then $Q_1 = 0$, and the solution is

$$\Phi_1(X, Z, T) = -\frac{\cosh(Z + kd)}{\Omega \cosh kd} \sin(\Omega T - X) \tag{B.11}$$

$$A_1 = \cos(\Omega T - X) \tag{B.12}$$

$$\Omega_1^2 = \tanh kd. \tag{B.13}$$

In dimensional form the first order solution is

$$\phi_1(x, z, t) = -\frac{\eta_a g \cosh k(z + d)}{\omega \cosh kd} \sin(\omega t - kx) \tag{B.14}$$

$$\eta_1 = \eta_a \cos(\omega t - kx) \tag{B.15}$$

$$\omega_1^2 = kg \tanh kd. \tag{B.16}$$

The second order equations are given by the terms of order $(\eta_a k)^1$

$$\begin{aligned}
(\text{GE}) \quad & \nabla^2 \Phi_2 = 0 \\
(\text{BBC}) \quad & \frac{\partial \Phi_2}{\partial Z} = 0; \quad Z = -kd \\
(\text{DFSC}) \quad & \frac{\partial \Phi_2}{\partial T} + \frac{1}{2} \left[\left(\frac{\partial \Phi_1}{\partial X} \right)^2 + \left(\frac{\partial \Phi_1}{\partial Z} \right)^2 \right] + A_1 \frac{\partial^2 \Phi_1}{\partial Z \partial T} + A_2 = Q_2; \quad Z = 0 \\
(\text{KFSC}) \quad & \frac{\partial A_2}{\partial T} + \frac{\partial \Phi_1}{\partial X} \frac{\partial A_1}{\partial X} - \frac{\partial \Phi_2}{\partial Z} + A_1 \frac{\partial^2 A_1}{\partial Z \partial T} - A_1 \frac{\partial^2 \Phi_1}{\partial Z^2} = 0; \quad Z = 0.
\end{aligned} \tag{B.17}$$

The DFSC and KFSC can be combined by eliminating A_2 and inserting the expressions for Φ_1 and A_1

$$\begin{aligned}
& \frac{\partial Q_2}{\partial T} - \frac{\partial^2 \Phi_2}{\partial T^2} - \frac{\partial \Phi_2}{\partial Z} \\
&= \frac{1}{2} \frac{\partial}{\partial T} \left[\left(\frac{\partial \Phi_1}{\partial X} \right)^2 + \left(\frac{\partial \Phi_1}{\partial Z} \right)^2 \right] + \frac{\partial A_1}{\partial T} \frac{\partial^2 \Phi_1}{\partial Z \partial T} + A_1 \frac{\partial}{\partial Z} \left[\frac{\partial^2 \Phi_1}{\partial T^2} + \frac{\partial \Phi_1}{\partial Z} \right] - \frac{\partial \Phi_1}{\partial X} \frac{\partial A_1}{\partial X} \\
&= \left[\frac{-1 - 2 \cosh^2 kd + 2\Omega^2 \sinh kd \cosh kd}{2\Omega \cosh^2 kd} \right] \sin 2(\Omega T - X) \\
&= \left[\frac{-3}{2\Omega \cosh^2 kd} - \frac{\tanh^2 kd}{\Omega} + \Omega \tanh kd \right] \sin 2(\Omega T - X).
\end{aligned} \tag{B.18}$$

By using

$$\begin{aligned}
\Omega &= \Omega_1 + \eta_a k \Omega_2 + \dots \\
\Omega_1^2 &= \tanh kd \\
\left(1 + \eta_a k \frac{\Omega_2}{\Omega_1} + \dots \right)^{-1} &= 1 - \eta_a k \frac{\Omega_2}{\Omega_1} + \dots,
\end{aligned} \tag{B.19}$$

the combined free surface condition is simplified to

$$\begin{aligned}
& \frac{\partial Q_2}{\partial T} - \frac{\partial^2 \Phi_2}{\partial T^2} - \frac{\partial \Phi_2}{\partial Z} \\
&= \left[-\frac{3\Omega_1}{2\Omega_1(\Omega_1 + \eta_a k \Omega_2 + \dots) \cosh^2 kd} - \frac{\Omega_1^4}{(\Omega_1 + \eta_a k \Omega_2 + \dots)} \right. \\
&\quad \left. + (\Omega_1 + \eta_a k \Omega_2 + \dots) \Omega_1^2 \right] \sin 2(\Omega T - X) \\
&= -\frac{3\Omega_1}{\sinh 2kd} \sin 2(\Omega T - X) + \mathcal{O}(\eta_a k).
\end{aligned} \tag{B.20}$$

One solution that satisfies Laplace equation and the bottom boundary condition is

$$\Phi_2 = B_2 \cosh 2(Z + kd) \sin 2(\Omega T - X). \quad (\text{B.21})$$

The constant B_2 is found from the combined free surface condition.

$$\begin{aligned} \frac{\partial Q_2}{\partial T} + [4B_2\Omega^2 \cosh 2(Z + kd) - 2B_2 \sinh 2(Z + kd)] \sin 2(\Omega T - X) = \\ -\frac{3\Omega_1}{\sinh 2kd} \sin 2(\Omega T - X); \quad Z = 0. \end{aligned} \quad (\text{B.22})$$

Since Q_2 is only dependent on T , $\frac{\partial Q_2}{\partial T}$ can not be a function of $\sin 2(\Omega T - X)$, thus $\frac{\partial Q_2}{\partial T} = 0$, meaning $Q_2 = \text{constant}$. Then the combined free surface condition is

$$\begin{aligned} [4B_2\Omega^2 \cosh 2kd - 2B_2 \sinh 2kd] \sin 2(\Omega T - X) = -\frac{3\Omega_1}{\sinh 2kd} \sin 2(\Omega T - X) \\ B_2 \left[\frac{\Omega^2}{\tanh^3 kd} + \frac{\Omega^2}{\tanh kd} - \frac{1}{\tanh^2 kd} \right] = -\frac{3\Omega_1}{8 \sinh^4 kd}. \end{aligned} \quad (\text{B.23})$$

By using the relationships in Eq. (B.19) this is reduced to

$$B_2 \left[\frac{1}{\Omega_1^4} + 1 - \frac{1}{\Omega_1^4} + \mathcal{O}(\eta_a k) \right] = -\frac{3\Omega_1}{8 \sinh^4 kd}. \quad (\text{B.24})$$

Since $\Omega_1 = \Omega - \eta_a k \Omega_2 - \dots$, the constant B_2 is to order $\mathcal{O}(\eta_a k)$ given by

$$B_2 = -\frac{3\Omega}{8 \sinh^4 kd}. \quad (\text{B.25})$$

The second order potential is then given by

$$\Phi_2 = -\frac{3\Omega}{8 \sinh^4 kd} \cosh 2(Z + kd) \sin 2(\Omega T - X). \quad (\text{B.26})$$

Then the (DFSC) is used to find A_2 .

$$\begin{aligned} A_2 = Q_2 - \frac{\partial \Phi_2}{\partial T} - \frac{1}{2} \left[\left(\frac{\partial \Phi_1}{\partial X} \right)^2 + \left(\frac{\partial \Phi_1}{\partial Z} \right)^2 \right] - A_1 \frac{\partial^2 \Phi_1}{\partial Z \partial T}; \quad Z = 0 \\ = Q_2 - \frac{1}{4\Omega^2} - \frac{\sinh^2 kd}{4\Omega^2 \cosh^2 kd} + \frac{\sinh kd}{2 \cosh kd} \\ + \left[\frac{3\Omega^2 \cosh 2kd}{4 \sinh^4 kd} - \frac{1}{4\Omega^2} + \frac{\sinh^2 kd}{4\Omega^2 \cosh^2 kd} + \frac{\sinh kd}{2 \cosh kd} \right] \cos 2(\Omega T - X) \end{aligned} \quad (\text{B.27})$$

$$A_2 = Q_2 - \frac{\cosh 2kd}{4\Omega^2 \sinh^2 kd} \tanh^2 kd + \frac{1}{2} \tanh kd + \left[\frac{3\Omega^2 \cosh 2kd}{4 \sinh^4 kd} - \frac{\tanh^2 kd}{4\Omega^2 \sinh^2 kd} + \frac{1}{2} \tanh kd \right] \cos 2(\Omega T - X). \quad (\text{B.28})$$

By inserting $\Omega^2 = \tanh kd + \mathcal{O}(\eta_a k)$, A_2 can be written as

$$A_2 = Q_2 - \frac{\Omega^2 \cosh 2kd}{4 \sinh^2 kd} + \frac{1}{2} \Omega^2 + \left[\frac{3\Omega^2 \cosh 2kd}{4 \sinh^4 kd} - \frac{\Omega^2}{4 \sinh^2 kd} + \frac{1}{2} \Omega^2 \right] \cos 2(\Omega T - X), \quad (\text{B.29})$$

which can reduced to

$$A_2 = Q_2 - \frac{1}{2 \sinh 2kd} + \frac{\cosh kd(2 + \cosh 2kd)}{4 \sinh^3 kd} \cos 2(\Omega T - X). \quad (\text{B.30})$$

The combined free surface condition to order $\mathcal{O}((\eta_a k)^2)$ is given by

$$\begin{aligned} \frac{\partial Q_2}{\partial T} - \frac{\partial^2 \Phi_2}{\partial T^2} - \frac{\partial \Phi_2}{\partial Z} = & - \frac{3\Omega_1}{\sinh 2kd} \sin 2(\Omega T - X) \\ & + \eta_a k \Omega_2 \left(\frac{3}{\sinh 2kd} + 2\Omega_1^2 \right) \sin 2(\Omega T - X); \quad Z = 0. \end{aligned} \quad (\text{B.31})$$

Since $\frac{\partial Q_2}{\partial T} = 0$, the contribution from the last term to the solution of Φ_2 is given from

$$\frac{\partial^2 \Phi_2}{\partial T^2} + \frac{\partial \Phi_2}{\partial Z} = -\eta_a k \Omega_2 \left(\frac{3}{\sinh 2kd} + 2\Omega_1^2 \right) \sin 2(\Omega T - X); \quad Z = 0. \quad (\text{B.32})$$

The solution is

$$\Phi_2 = \frac{\tilde{B}_2 T \cosh 2(Z + kd)}{\Omega \cosh 2kd} \cos 2(\Omega T - X), \quad (\text{B.33})$$

where

$$\tilde{B}_2 = \frac{1}{4} \eta_a k \Omega_2 \left(\frac{3}{\sinh 2kd} + 2\Omega_1^2 \right). \quad (\text{B.34})$$

Since Eq. (B.33) is unbounded with T , Φ_2 will increase to infinity. Therefore $\tilde{B}_2 \equiv 0$, which means that $\Omega_2 \equiv 0$. Thus,

$$\Omega = \Omega_1 + \mathcal{O}((\eta_a k)^2), \quad (\text{B.35})$$

so the dispersion relationship does not change at second order.

The second order solution is then

$$\Phi_2 = -\frac{3\Omega}{8 \sinh^4 kd} \cosh 2(Z + kd) \sin 2(\Omega T - X) \quad (\text{B.36})$$

$$A_2 = Q_2 - \frac{1}{2 \sinh 2kd} + \frac{\cosh kd(2 + \cosh 2kd)}{4 \sinh^3 kd} \cos 2(\Omega T - X) \quad (\text{B.37})$$

$$\Omega^2 = \tanh kd. \quad (\text{B.38})$$

In dimensional form the second order solution is

$$\phi_2 = -\frac{3}{8} \frac{\eta_a \omega \cosh 2k(z+d)}{k \sinh^4 kd} \sin 2(\omega t - kx) \quad (\text{B.39})$$

$$\eta_2 = \tilde{C}_{B2} - \frac{1}{2} \eta_a \frac{1}{\sinh 2kd} + \frac{1}{2} \eta_a \frac{\cosh kd(2 + \cosh 2kd)}{2 \sinh^3 kd} \cos 2(\omega t - kx) \quad (\text{B.40})$$

$$\omega^2 = kg \tanh kd. \quad (\text{B.41})$$

APPENDIX C

Limitations of wave amplitude in second order Stokes model and extended second order model

C.1 Second order Stokes model

In deep water the wave steepness criterion, $k\eta_a < \frac{\pi}{7}$, is the most restrictive. The nonlinear crest height and trough depth is then given by

$$k\eta_c = k\eta_a + \frac{1}{2}(k\eta_a)^2 = \frac{\pi}{7} + \frac{1}{2}\left(\frac{\pi}{7}\right)^2 \quad (\text{C.1})$$

$$k\eta_t = k\eta_a - \frac{1}{2}(k\eta_a)^2 = \frac{\pi}{7} - \frac{1}{2}\left(\frac{\pi}{7}\right)^2, \quad (\text{C.2})$$

which gives

$$\frac{\eta_c}{\eta_t} = \frac{k\eta_c}{k\eta_t} = \frac{14 + \pi}{14 - \pi}. \quad (\text{C.3})$$

The ratio of the nonlinear crest height to trough depth expressed by the linear dimensionless amplitude a is given by

$$\frac{\eta_c}{\eta_t} = \frac{\frac{\eta_c}{a_{\text{rms}}}}{\frac{\eta_t}{a_{\text{rms}}}} = \frac{w_c}{w_t} = \frac{a + \frac{1}{2}r_+a^2}{a - \frac{1}{2}r_+a^2} = \frac{1 + \frac{1}{2}r_+a}{1 - \frac{1}{2}r_+a}. \quad (\text{C.4})$$

Comparing these two equations gives the criterion for the maximum value of a , a_{\max} ,

$$\frac{1 + \frac{1}{2}r_+a_{\max}}{1 - \frac{1}{2}r_+a_{\max}} = \frac{14 + \pi}{14 - \pi} \quad (\text{C.5})$$

$$a_{\max} = \frac{\pi}{7r_+}. \quad (\text{C.6})$$

In shallow water the criterion for no bump in the trough, $k\eta_a < \frac{(kd)^3}{3}$, is the most restrictive. The nonlinear crest height and trough depth in shallow water is given by

$$\eta_c = \eta_a + \frac{3}{4} \frac{k}{(kd)^3} \eta_a^2 \quad (\text{C.7})$$

$$\eta_t = \eta_a - \frac{3}{4} \frac{k}{(kd)^3} \eta_a^2, \quad (\text{C.8})$$

which gives

$$k\eta_c = k\eta_a + \frac{3}{4} \frac{(k\eta_a)^2}{(kd)^3} = \frac{(kd)^3}{3} + \frac{3}{4} \frac{(kd)^6}{3^2(kd)^3} = \frac{5}{12}(kd)^3 \quad (\text{C.9})$$

$$k\eta_t = k\eta_a - \frac{3}{4} \frac{(k\eta_a)^2}{(kd)^3} = \frac{(kd)^3}{3} - \frac{3}{4} \frac{(kd)^6}{3^2(kd)^3} = \frac{3}{12}(kd)^3. \quad (\text{C.10})$$

The criterion for the maximum value of a is then given by

$$\frac{1 + \frac{1}{2}r_+a_{\max}}{1 - \frac{1}{2}r_+a_{\max}} = \frac{5}{3} \quad (\text{C.11})$$

$$a_{\max} = \frac{1}{2r_+}. \quad (\text{C.12})$$

C.2 Extended second order model

The difference between the expression of the surface elevation for the second order Stokes model and the extended second order model is two constant terms. This means that the criterion for no bump in the trough will be the same for both models.

In deep water the wave steepness criterion, $k\eta_a < \frac{\pi}{7}$, is the most restrictive. The parameters $f^+(k, d) \rightarrow 1$ and $f^-(k, d) \rightarrow 0$, and the result will be the same as for the second order Stokes model, i.e., a_{\max} is given by Eq. (C.6).

In shallow water the criterion for no bump in the trough, $k\eta_a < \frac{(kd)^3}{3}$, is the most restrictive. The parameters $f^+(k, d) \rightarrow \frac{3}{2}(kd)^{-3}$ and $f^-(k, d) \rightarrow \frac{3}{2}(kd)^{-3}$, thus the nonlinear crest height and trough depth are given by

$$\eta_c = \eta_a + \frac{1}{16} k f^-(k, d) H_{m0}^2 \quad (\text{C.13})$$

$$\eta_t = \eta_a - \frac{1}{16} k f^-(k, d) H_{m0}^2. \quad (\text{C.14})$$

By using $H_{m0} = 4\sqrt{m_0} = \sqrt{8}a_{\text{rms}}$ and $\eta_{a,\text{max}} = a_{\text{rms}}\sqrt{\ln N}$, where N is the number of waves in the duration of the given sea state, Eqs. (C.13) and (C.14) can be transformed to

$$k\eta_c = \frac{(kd)^3}{3} + \frac{(kd)^3}{12 \ln N} \quad (\text{C.15})$$

$$k\eta_t = \frac{(kd)^3}{3} - \frac{(kd)^3}{12 \ln N}. \quad (\text{C.16})$$

Typically $N = 1000$ in a sea state of duration 3 hours, giving $\ln N \approx 6.9$. If $\ln N = 7$ is selected, the ratio of crest height to trough depth is given by

$$\frac{\eta_c}{\eta_t} = \frac{29}{27}. \quad (\text{C.17})$$

In terms of the linear dimensionless amplitude the ratio is given by

$$\frac{\eta_c}{\eta_t} = \frac{w_c}{w_t} = \frac{a + \frac{1}{2}ra^2 + R}{a - \frac{1}{2}ra^2 - R}, \quad (\text{C.18})$$

which inserted in Eq. (C.17) gives

$$28ra^2 - 2a + 56R = 0. \quad (\text{C.19})$$

The criterion for the maximum value of a , a_{max} , is then given by

$$a_{\text{max}} = \frac{1 + \sqrt{1 - 1568rR}}{28r}. \quad (\text{C.20})$$

Since r and R are small, a series expansion can be used, giving

$$a_{\text{max}} = \frac{1}{14r} - 28R - \dots < \frac{1}{14r}. \quad (\text{C.21})$$

APPENDIX D

Correlation coefficients

D.1 Correlation coefficients in the second order Stokes model

The nonlinear non-dimensional crest height is expressed in terms of the linear non-dimensional amplitude as

$$w_c = a + \frac{1}{2}r_+a^2. \quad (\text{D.1})$$

The linear amplitude is Rayleigh distributed, and the properties are discussed in appendix A. Then the expected values of W_c and W_c^2 are given by

$$\text{E}[W_c] = \text{E}[A] + \frac{1}{2}r_+\text{E}[A^2] = \frac{\sqrt{\pi}}{2} + \frac{1}{2}r_+ \quad (\text{D.2})$$

$$\text{E}[W_c^2] = \text{E}[A^2] + r_+\text{E}[A^3] + \frac{1}{4}r_+^2\text{E}[A^4] = 1 + \frac{3}{4}\sqrt{\pi}r_+ + \frac{1}{2}r_+^2, \quad (\text{D.3})$$

and the variance is given by

$$\begin{aligned} \text{Var}[W_c] &= \text{E}[W_c^2] - \text{E}[W_c]^2 \\ &= (\text{E}[A^2] - \text{E}[A]^2) + r_+ (\text{E}[A^3] - \text{E}[A]\text{E}[A^2]) + \frac{1}{4}r_+^2 (\text{E}[A^4] - \text{E}[A^2]^2) \\ &= 1 - \frac{\pi}{4} + \frac{\sqrt{\pi}}{4}r_+ + \frac{1}{4}r_+^2. \end{aligned} \quad (\text{D.4})$$

Considering two successive crest heights W_{c1} and W_{c2} , the covariance is given by

$$\begin{aligned}
\text{Cov}[W_{c1}, W_{c2}] &= E[W_{c1}W_{c2}] - E[W_{c1}]E[W_{c2}] \\
&= E \left[\left(A_1 + \frac{1}{2}r_+A_1^2 \right) \left(A_2 + \frac{1}{2}r_+A_2^2 \right) \right] \\
&\quad - E \left[A_1 + \frac{1}{2}r_+A_1^2 \right] E \left[A_2 + \frac{1}{2}r_+A_2^2 \right] \\
&= E[A_1A_2] - E[A_1]E[A_2] + \frac{1}{2}r_+ (E[A_1A_2^2] - E[A_1]E[A_2^2]) \\
&\quad + \frac{1}{2}r_+ (E[A_1^2A_2] - E[A_1^2]E[A_2]) + \frac{1}{4}r_+^2 (E[A_1^2A_2^2] - E[A_1^2]E[A_2^2]) \\
&= \frac{\pi}{4}(1 - \kappa_{c+}^2)^2 F \left(\frac{3}{2}, \frac{3}{2}; 1; \kappa_{c+}^2 \right) - \frac{\pi}{4} + \frac{\sqrt{\pi}}{4}r_+\kappa_{c+}^2 + \frac{1}{4}r_+^2\kappa_{c+}^2
\end{aligned} \tag{D.5}$$

An expansion of the hypergeometric function F gives

$$F \left(\frac{3}{2}, \frac{3}{2}; 1; \kappa_{c+}^2 \right) = 1 + \frac{9}{4}\kappa_{c+}^2 + \frac{225}{64}\kappa_{c+}^4 + \frac{1225}{256}\kappa_{c+}^6 + \mathcal{O}(\kappa_{c+}^8). \tag{D.6}$$

Then the covariance can be written as

$$\text{Cov}[W_{c1}, W_{c2}] = \left(\frac{\pi}{16} + \frac{\sqrt{\pi}}{4}r_+ + \frac{1}{4}r_+^2 \right) \kappa_{c+}^2 + \frac{\pi}{256}\kappa_{c+}^4 + \frac{\pi}{1024}\kappa_{c+}^6 + \mathcal{O}(\kappa_{c+}^8). \tag{D.7}$$

The correlation coefficient between W_{c1} and W_{c2} is given by

$$\begin{aligned}
\rho_c &= \frac{\text{Cov}[W_{c1}, W_{c2}]}{\text{Var}[W_{c1}]^{1/2}\text{Var}[W_{c2}]^{1/2}} \\
&= \frac{\left(\frac{\pi}{16} + \frac{\sqrt{\pi}}{4}r_+ + \frac{1}{4}r_+^2 \right) \kappa_{c+}^2 + \frac{\pi}{256}\kappa_{c+}^4 + \frac{\pi}{1024}\kappa_{c+}^6 + \mathcal{O}(\kappa_{c+}^8)}{1 - \frac{\pi}{4} + \frac{\sqrt{\pi}}{4}r_+ + \frac{1}{4}r_+^2}.
\end{aligned} \tag{D.8}$$

The correlation coefficient between the successive trough depths is found following the same procedure. The nonlinear non-dimensional trough depth is expressed in terms of the linear non-dimensional amplitude as

$$w_t = a - \frac{1}{2}r_+a^2, \tag{D.9}$$

with expected value and variance equal to

$$E[W_t] = \frac{\sqrt{\pi}}{2} - \frac{1}{2}r_+ \tag{D.10}$$

$$\text{Var}[W_t] = 1 - \frac{\pi}{4} - \frac{\sqrt{\pi}}{4}r_+ + \frac{1}{4}r_+^2. \tag{D.11}$$

The covariance between two successive trough depths W_{t1} and W_{t2} can be written as

$$\text{Cov}[W_{t1}, W_{t2}] = \left(\frac{\pi}{16} - \frac{\sqrt{\pi}}{4}r_+ + \frac{1}{4}r_+^2 \right) \kappa_{t+}^2 + \frac{\pi}{256}\kappa_{t+}^4 + \frac{\pi}{1024}\kappa_{t+}^6 + \mathcal{O}(\kappa_{t+}^8), \tag{D.12}$$

which gives the following correlation coefficient between W_{t1} and W_{t2}

$$\begin{aligned}\rho_t \equiv \rho_{W_{t1}, W_{t2}} &= \frac{\text{Cov}[W_{t1}, W_{t2}]}{\text{Var}[W_{t1}]^{1/2} \text{Var}[W_{t2}]^{1/2}} \\ &= \frac{\left(\frac{\pi}{16} - \frac{\sqrt{\pi}}{4} r_+ + \frac{1}{4} r_+^2 \right) \kappa_{t+}^2 + \frac{\pi}{256} \kappa_{t+}^4 + \frac{\pi}{1024} \kappa_{t+}^6 + \mathcal{O}(\kappa_{t+}^8)}{1 - \frac{\pi}{4} - \frac{\sqrt{\pi}}{4} r_+ + \frac{1}{4} r_+^2}.\end{aligned}\tag{D.13}$$

D.2 Correlation coefficient in the Forristall model

The Forristall distribution is a two-parameter Weibull distribution. The properties of the Weibull distribution are given in Appendix E. The correlation coefficient is found by Eq. (E.5) with $\beta_1 = \beta_2 = \beta$ and $\kappa = \kappa_{cF}$. By expanding the hypergeometric function the resulting correlation coefficient is

$$\begin{aligned}\rho_{cF} &= \frac{\left[\Gamma\left(\frac{1}{\beta}\right) \right]^2}{2\beta \Gamma\left(\frac{2}{\beta}\right) - \left[\Gamma\left(\frac{1}{\beta}\right) \right]^2} \left[\frac{1}{\beta^2} \kappa_{cF}^2 + \frac{1}{4\beta^2} \left(\frac{1}{\beta} + 1 \right)^2 \kappa_{cF}^4 \right. \\ &\quad \left. + \frac{1}{36\beta^2} \left(\frac{1}{\beta} + 1 \right)^2 \left(\frac{1}{\beta} + 2 \right)^2 \kappa_{cF}^6 + O(\kappa_{cF}^8) \right].\end{aligned}\tag{D.14}$$

D.3 Correlation coefficients in the extended second order model

The nonlinear non-dimensional crest heights is expressed in terms of the linear non-dimensional amplitude as

$$w_c = a + \frac{1}{2} r a^2 + R.\tag{D.15}$$

Considering two successive wave crest heights W_{c1} and W_{c2} , the covariance is given by

$$\begin{aligned}\text{Cov}[W_{c1}, W_{c2}] &= \text{E} \left[\left(A_1 + \frac{1}{2} r A_1^2 + R \right) \left(A_2 + \frac{1}{2} r A_2^2 + R \right) \right] \\ &\quad - \text{E} \left[A_1 + \frac{1}{2} r A_1^2 + R \right] \text{E} \left[A_2 + \frac{1}{2} r A_2^2 + R \right] \\ &= \text{E}[A_1 A_2] - \text{E}[A_1] \text{E}[A_2] + \frac{1}{2} r (\text{E}[A_1 A_2^2] - \text{E}[A_1] \text{E}[A_2^2]) \\ &\quad + \frac{1}{2} r (\text{E}[A_1^2 A_2] - \text{E}[A_1^2] \text{E}[A_2]) + \frac{1}{4} r^2 (\text{E}[A_1^2 A_2^2] - \text{E}[A_1^2] \text{E}[A_2^2]),\end{aligned}\tag{D.16}$$

which is the same as for the second order Stokes model in Eq. (D.5). Thus, the correlation coefficient between W_{c1} and W_{c2} becomes

$$\rho_c = \frac{\left(\frac{\pi}{16} + \frac{\sqrt{\pi}}{4}r + \frac{1}{4}r^2\right) \kappa_c^2 + \frac{\pi}{256} \kappa_c^4 + \frac{\pi}{1024} \kappa_c^6 + \mathcal{O}(\kappa_c^8)}{1 - \frac{\pi}{4} + \frac{\sqrt{\pi}}{4}r + \frac{1}{4}r^2}. \quad (\text{D.17})$$

Similarly, the correlation coefficient between two successive trough depths is found. The nonlinear non-dimensional crest heights is expressed in terms of the linear non-dimensional amplitude as

$$w_t = a - \frac{1}{2}ra^2 - R. \quad (\text{D.18})$$

The covariance between two successive trough depths W_{t1} and W_{t2} is the same as for the second order Stokes model in Eq. (D.12), which gives the following correlation coefficient

$$\rho_t = \frac{\left(\frac{\pi}{16} - \frac{\sqrt{\pi}}{4}r + \frac{1}{4}r^2\right) \kappa_t^2 + \frac{\pi}{256} \kappa_t^4 + \frac{\pi}{1024} \kappa_t^6 + \mathcal{O}(\kappa_t^8)}{1 - \frac{\pi}{4} - \frac{\sqrt{\pi}}{4}r + \frac{1}{4}r^2}. \quad (\text{D.19})$$

APPENDIX E

Properties of the two-parameter Weibull distribution

E.1 The marginal Weibull distribution

The two-parameter Weibull probability density function of a dimensionless variable X is given by

$$f_X(x) = \frac{\beta x^{\beta-1}}{\alpha^\beta} \exp \left\{ - \left(\frac{x}{\alpha} \right)^\beta \right\}; \quad x \geq 0, \quad (\text{E.1})$$

where α and β are the Weibull parameters. The expected value and variance are given by

$$\text{E}[X] = \alpha \Gamma \left(\frac{1}{\beta} + 1 \right) \quad (\text{E.2})$$

$$\text{Var}[X] = \alpha^2 \left[\Gamma \left(\frac{2}{\beta} + 1 \right) - \Gamma^2 \left(\frac{1}{\beta} + 1 \right) \right]. \quad (\text{E.3})$$

E.2 A two-dimensional Weibull distribution

One possible form of the two-dimensional Weibull distribution whose marginal distribution is given by Eq. (E.1) is given in Myrhaug et al. (1995)

$$f_{X_1, X_2}(x_1, x_2) = \frac{\beta_1 \beta_2 x_1^{\beta_1-1} x_2^{\beta_2-1}}{\alpha_1^{\beta_1} \alpha_2^{\beta_2} (1 - \kappa^2)} \exp \left\{ -\frac{1}{1 - \kappa^2} \left[\left(\frac{x_1}{\alpha_1} \right)^{\beta_1} + \left(\frac{x_2}{\alpha_2} \right)^{\beta_2} \right] \right\} \\ \times I_0 \left[\frac{2\kappa}{1 - \kappa^2} \left(\frac{x_1}{\alpha_1} \right)^{\beta_1/2} \left(\frac{x_2}{\alpha_2} \right)^{\beta_2/2} \right]. \quad (\text{E.4})$$

The parameter κ is related to the correlation coefficient between X_1 and X_2 by

$$\rho_{X_1, X_2} = \frac{\Gamma\left(\frac{1}{\beta_1}\right) \Gamma\left(\frac{1}{\beta_2}\right) \left[F\left(-\frac{1}{\beta_1}, -\frac{1}{\beta_2}; 1; \kappa^2\right) - 1 \right]}{\left[2\beta_1 \Gamma\left(\frac{2}{\beta_1}\right) - \Gamma^2\left(\frac{1}{\beta_1}\right) \right]^{1/2} \left[2\beta_2 \Gamma\left(\frac{2}{\beta_2}\right) - \Gamma^2\left(\frac{1}{\beta_2}\right) \right]^{1/2}}. \quad (\text{E.5})$$

APPENDIX F

Properties of the Gaussian distribution

F.1 The multivariate Gaussian distribution

The p -dimensional Gaussian distribution for the vector \mathbf{X} of p random variables is given by

$$f_{\mathbf{X}}(\mathbf{x}) = \frac{1}{(2\pi)^{p/2} |\boldsymbol{\Sigma}|^{1/2}} \exp \left\{ -\frac{1}{2} (\mathbf{x} - \boldsymbol{\mu})^T \boldsymbol{\Sigma}^{-1} (\mathbf{x} - \boldsymbol{\mu}) \right\}, \quad (\text{F.1})$$

where $\mathbf{x} = (x_1, \dots, x_p)^T$. The $p \times 1$ vector $\boldsymbol{\mu}$ is the expected value of \mathbf{X} , and the $p \times p$ matrix $\boldsymbol{\Sigma}$ is the covariance matrix.

F.2 Error-function

The error function is given by

$$y = \text{erf}(x) = \frac{2}{\sqrt{\pi}} \int_0^x e^{-t^2} dt, \quad (\text{F.2})$$

with the derivative

$$\frac{dy}{dx} = \frac{d}{dx} \text{erf}(x) = \frac{2}{\sqrt{\pi}} e^{-x^2}. \quad (\text{F.3})$$

The inverse error function, denoted

$$x = \text{erf}^{-1}(y), \quad (\text{F.4})$$

satisfies $y = \operatorname{erf}(x)$ for $-1 \leq y \leq 1$ and $-\infty \leq x \leq \infty$. The derivative of the inverse error function is given by

$$\frac{d}{dy} \operatorname{erf}^{-1}(y) = \frac{\sqrt{\pi}}{2} \exp \left\{ \left[\operatorname{erf}^{-1}(y) \right]^2 \right\} . \quad (\text{F.5})$$

APPENDIX G

Properties of the generalized Gamma distribution

The generalized Gamma probability density function of a dimensionless variable X is given by

$$f_X(x) = \frac{c(x - \gamma)^{\lambda c - 1}}{\Gamma(\lambda)\nu^{\lambda c}} \exp \left\{ - \left(\frac{x - \gamma}{\nu} \right)^c \right\}; \quad x > \gamma, \quad (\text{G.1})$$

where λ and c are two shape coefficients, ν is the scale parameter and γ is the location coefficient.

The cumulative probability function is given by

$$F_X(x) = I \left[\lambda, \left(\frac{x - \gamma}{\nu} \right)^c \right], \quad (\text{G.2})$$

where $I[\lambda, u]$ denotes the incomplete Gamma function

$$I[\lambda, u] = \frac{1}{\Gamma(\lambda)} \int_0^u t^{\lambda-1} e^{-t} dt. \quad (\text{G.3})$$

Since all variables of interest (wave amplitude, wave height and wave period) are always non-negative, then $\gamma = 0$.

G.1 Maximum likelihood estimators for the generalized Gamma distribution

The parameters in the generalized Gamma distribution can be found from the maximum likelihood estimators. The maximum likelihood equation is given by

$$L(\lambda, c, \nu) = \prod_{i=1}^N f_X(x_i) = \frac{c^N}{(\Gamma(\lambda)\nu^{\lambda c})^N} \left[\prod_{i=1}^N x_i^{c\lambda-1} \right] \exp \left\{ -\frac{1}{\nu^c} \sum_{i=1}^N x_i^c \right\} \quad (\text{G.4})$$

The parameters that maximize the function $L(\lambda, c, \nu)$ are called the maximum likelihood parameters. These are found by first taking the logarithm of L and then putting the partial derivatives wrt. each parameter equal to zero. The resulting equations are

$$cS_1 - \ln \left(\frac{S_2(c)}{\lambda} \right) - \phi(\lambda) = 0 \quad (\text{G.5})$$

$$\lambda \left[cS_1 - \ln \left(\frac{S_2(c)}{\lambda} \right) \right] + 1 - cS_3(c, \lambda) = 0 \quad (\text{G.6})$$

$$\nu = \left(\frac{S_2(c)}{\lambda} \right)^{1/c} \quad (\text{G.7})$$

where

$$\begin{aligned} S_1 &= \frac{1}{N} \sum_{i=1}^N \ln x_i \\ S_2(c) &= \frac{1}{N} \sum_{i=1}^N x_i^c \\ S_3(c, \lambda) &= \frac{1}{N} \sum_{i=1}^N \left(\frac{x_i}{\left(\frac{S_2(c)}{\lambda} \right)^{1/c}} \right)^c \ln \left(\frac{x_i}{\left(\frac{S_2(c)}{\lambda} \right)^{1/c}} \right) \\ \phi(\lambda) &= \frac{\partial \ln \Gamma(\lambda)}{\partial \lambda} \end{aligned} \quad (\text{G.8})$$

The parameters λ and c must be found through an iterative solution of Eqs. (G.5) and (G.6). Then ν is found from Eq. (G.7).

APPENDIX H

Additional results from data

This chapter presents some additional results from the data.

Appendix H.1 presents the conditional expectation $E[W_{c2}|W_{c1} = w_{c1}]$ for the Japan Sea field data and the laboratory data. Results for the numerical simulations are also included.

Appendix H.2 presents the conditional expectation for the wave heights for the different data sets.

Appendix H.3 presents the conditional expectation for the wave periods for the different data sets. It also presents wave period results for the laboratory data at $d = 78\text{m}$, $d = 41\text{ m}$ and $d = 31\text{ m}$.

H.1 Conditional expectation for wave crest heights and wave trough depths

The expected value of a crest height given the previous crest height is given by Eq. (3.96), and the expected value of a trough depth given the previous trough depth is given by Eq. (3.97). The results of the conditional expectation for the Draupner field data were shown in Fig. 3.15. The results from the corresponding numerical simulations are shown in Fig. H.1. Figure H.2 shows the results from the Japan Sea data, while Figs. H.3 - H.6 show the results from the laboratory data.

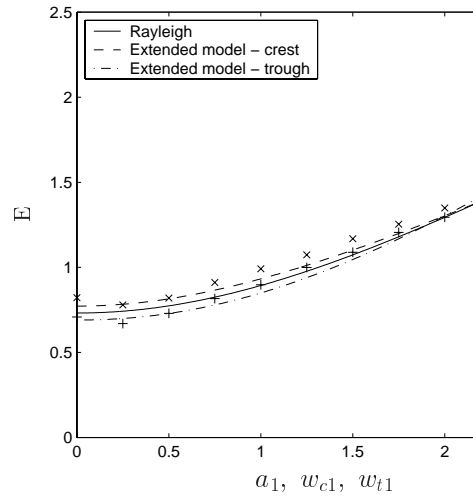
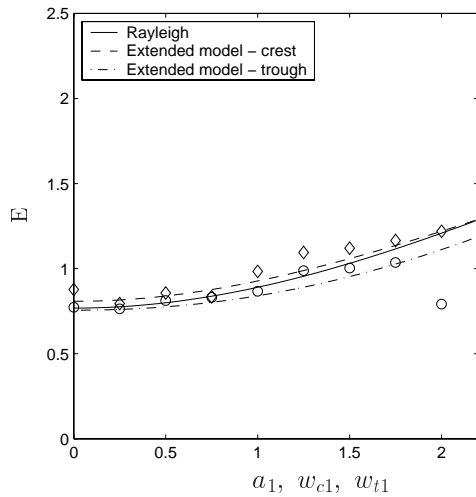
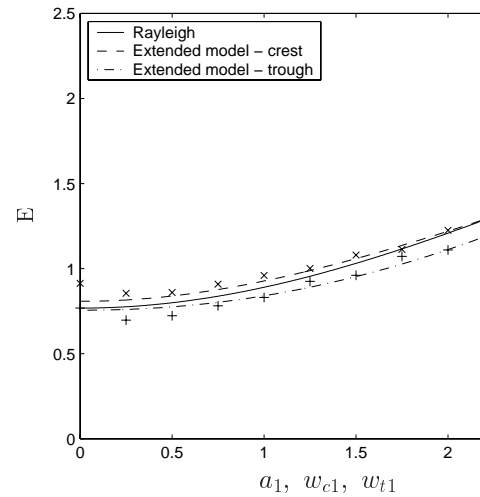


Figure H.1: Conditional expectation of the wave amplitude given the previous wave amplitude. \times crest height data; $+$ trough depth data from numerical simulations corresponding to the Draupner field data.



(a)



(b)

Figure H.2: Conditional expectation of the wave amplitude given the previous wave amplitude. (a) \diamond crest height data; \circ trough depth data from Japan Sea field, (b) \times crest height data; $+$ trough depth data from numerical simulations.

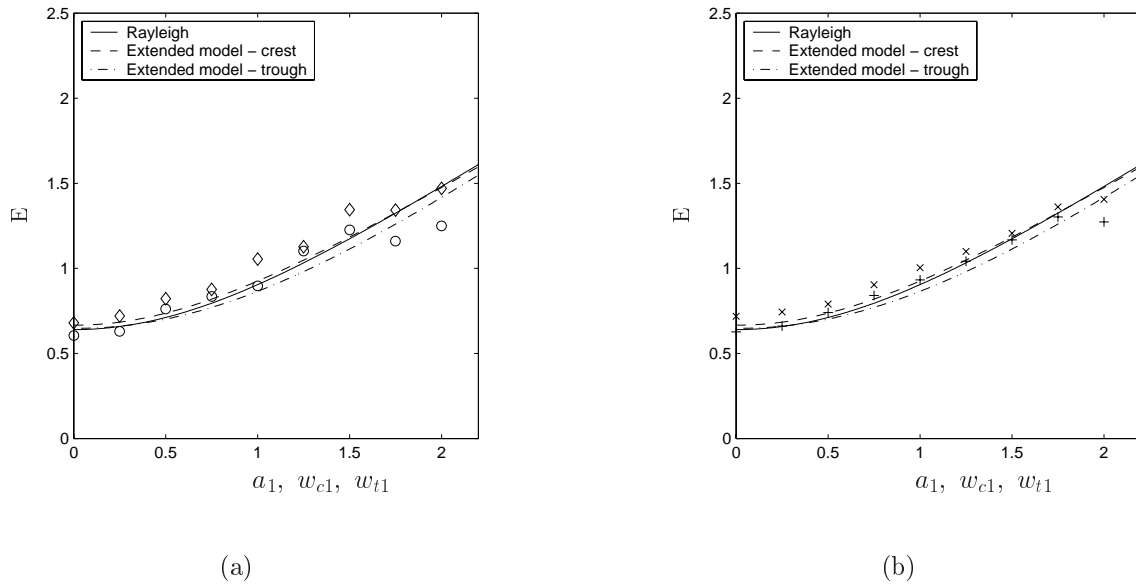


Figure H.3: Conditional expectation of the wave amplitude given the previous wave amplitude. (a) \diamond crest height data; \circ trough depth data from laboratory data, (b) \times crest height data; $+$ trough depth data from numerical simulations. $d = 80$ m.

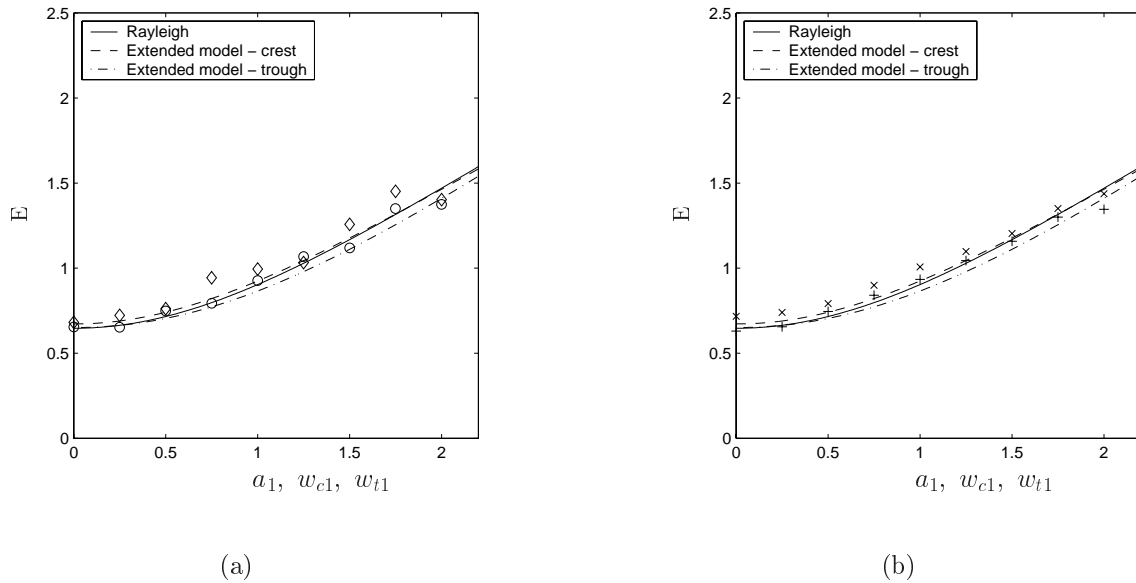
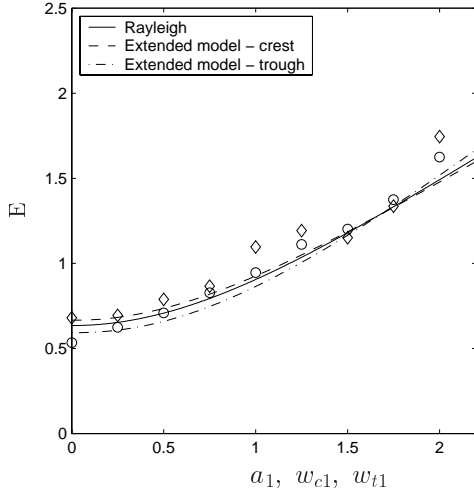
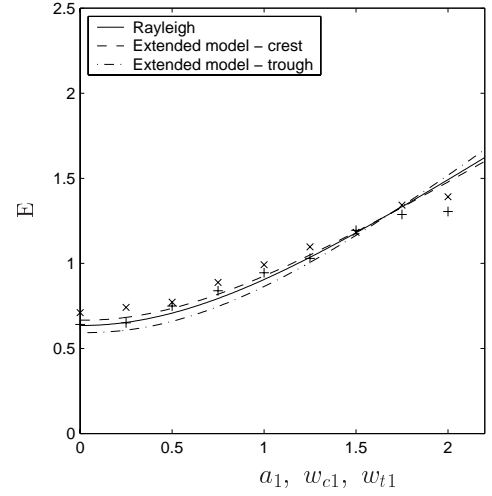


Figure H.4: Conditional expectation of the wave amplitude given the previous wave amplitude. (a) \diamond crest height data; \circ trough depth data from laboratory data, (b) \times crest height data; $+$ trough depth data from numerical simulations. $d = 78$ m.

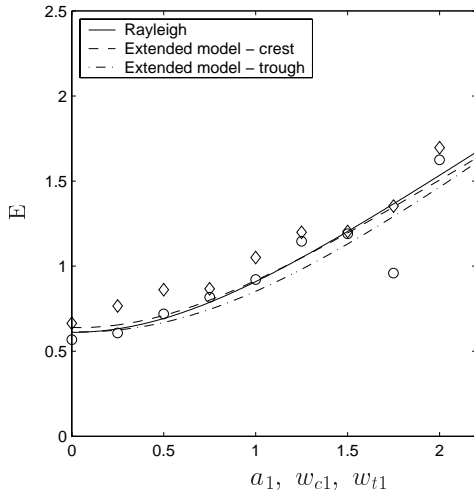


(a)

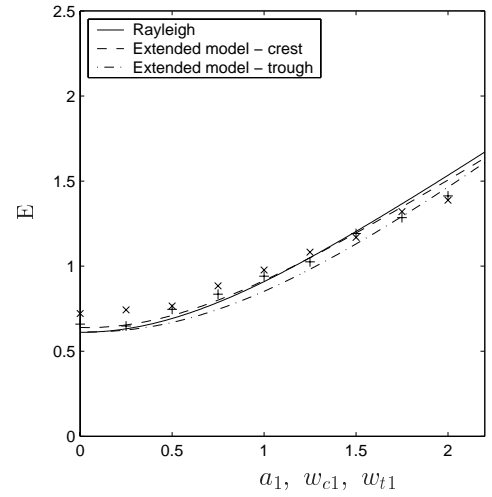


(b)

Figure H.5: Conditional expectation of the wave amplitude given the previous wave amplitude. (a) \diamond crest height data; \circ trough depth data from laboratory data, (b) \times crest height data; $+$ trough depth data from numerical simulations. $d = 41$ m.



(a)



(b)

Figure H.6: Conditional expectation of the wave amplitude given the previous wave amplitude. (a) \diamond crest height data; \circ trough depth data from laboratory data, (b) \times crest height data; $+$ trough depth data from numerical simulations. $d = 31$ m.

H.2 Conditional expectation for wave heights

This section shows the conditional expectation $E[H_2|H_1 = h_1]$ versus h_1 for the Japan Sea field data and the laboratory data. The results are similar to the results for the Draupner field data presented in Chapter 4.2.2, in Fig. 4.9.

Figure H.7 shows the results for the Japan Sea field data. The results for the laboratory data are shown in Figs. H.8 (a), (b) and H.9 (a), (b) for $d = 80$ m, $d = 78$ m, $d = 41$ m and $d = 31$ m, respectively.

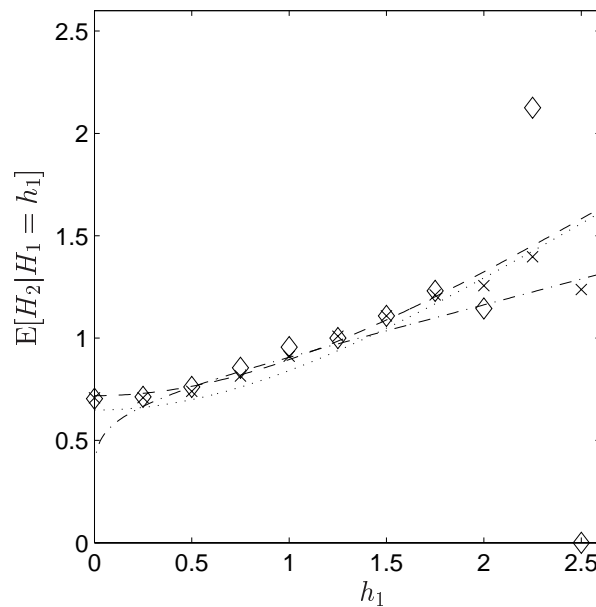
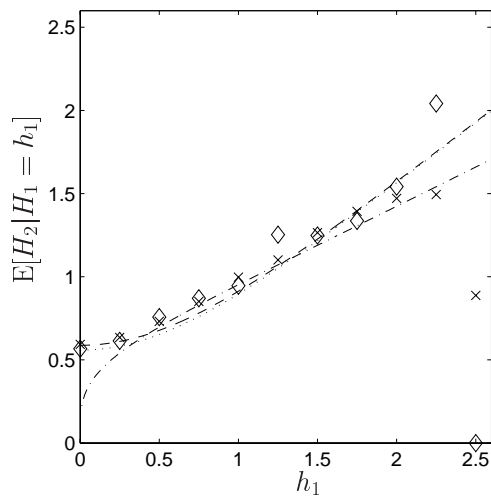
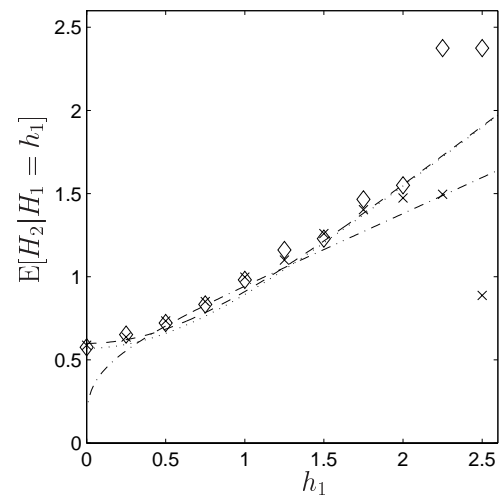


Figure H.7: Conditional expectation of the wave height given the previous wave height. --- Nataf-Weibull model; - - Næss (1985) model; ... Rayleigh distribution; \diamond Japan Sea field data; \times simulations.

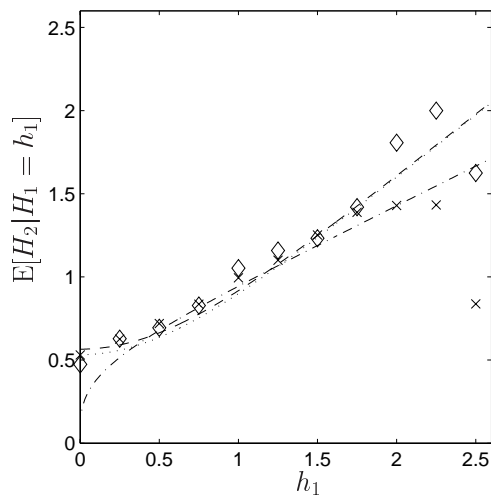


(a)

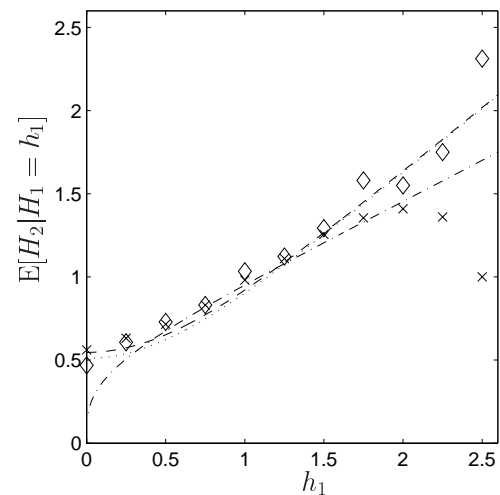


(b)

Figure H.8: Conditional expectation of the wave height given the previous wave height. --- Nataf-Weibull model; — Næss (1985) model; ... Rayleigh distribution; \diamond laboratory data; \times simulations. (a) $d = 80$ m. (b) $d = 78$ m.



(a)



(b)

Figure H.9: Conditional expectation of the wave height given the previous wave height. --- Nataf-Weibull model; — Næss (1985) model; ... Rayleigh distribution; \diamond laboratory data; \times simulations. (a) $d = 41$ m. (b) $d = 31$ m.

H.3 Results for wave periods

H.3.1 Results for Japan Sea field data

Figure H.10 shows a paired plot of the wave period and the corresponding wave height. The conditional expectation $E[T_2|T_1 = t_1]$ versus t_1 is shown in Fig. H.11. The results are similar to the results for the Draupner field data presented in Chapter 5.2.1, in Fig. 5.9.

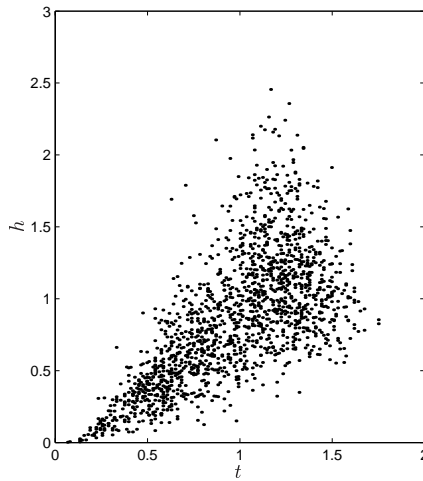


Figure H.10: Paired plot of the normalized wave period and the corresponding normalized wave height from Japan Sea field data.

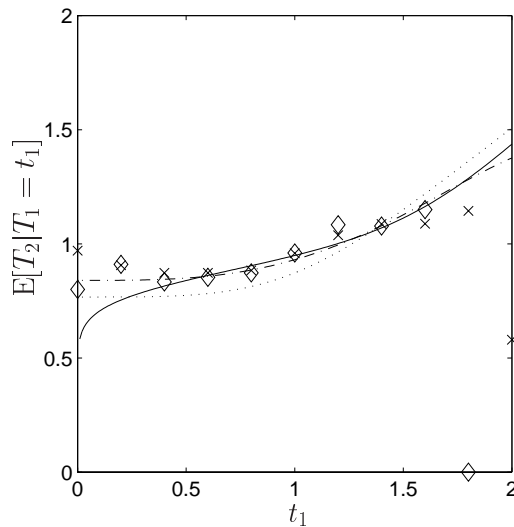


Figure H.11: Conditional expectation of the wave period given the previous wave period. — Nataf-Gamma model; \cdots Myrhaug and Rue (1993) model; $-\cdots$ Myrhaug and Rue (1998) model; \diamond Japan Sea field data; \times simulated data.

H.3.2 Results for laboratory data

This section presents mainly results for wave periods for the laboratory data at $d = 78$ m, $d = 41$ m and $d = 31$ m. The comments given in Chapter 6.1.3 regarding the concerns associated with the data at $d = 41$ m and $d = 31$ m should be kept in mind when considering the results. The comments given earlier in Chapter 6.4.3 for $d = 80$ m are valid for the results presented here.

The conditional expectation $E[T_2|T_1 = t_1]$ versus t_1 is also shown for all water depths.

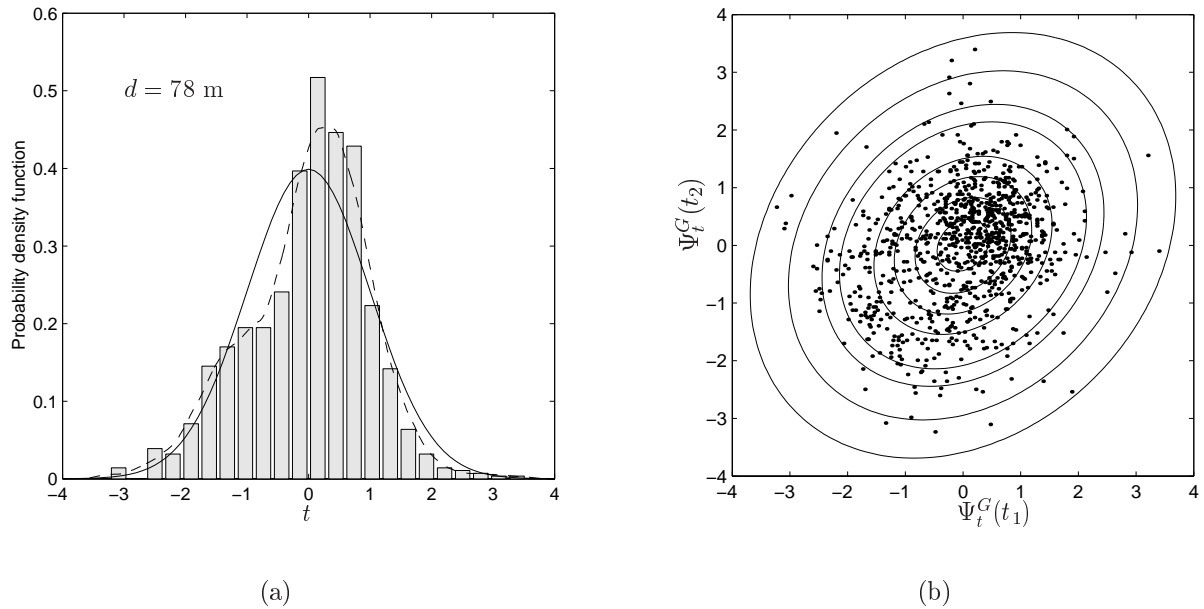
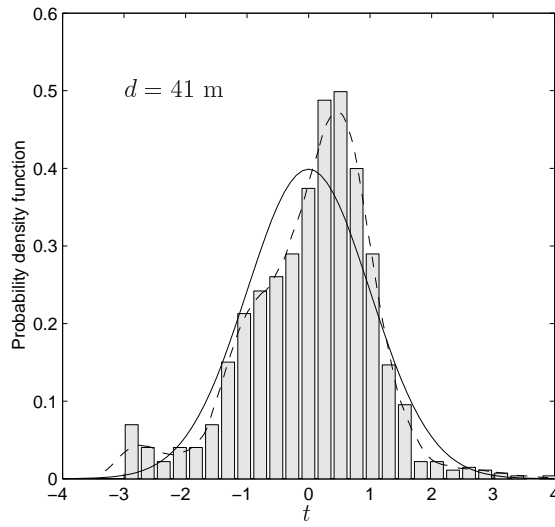
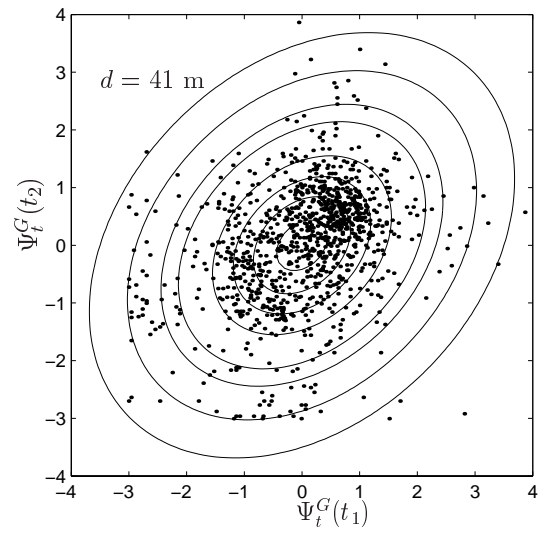


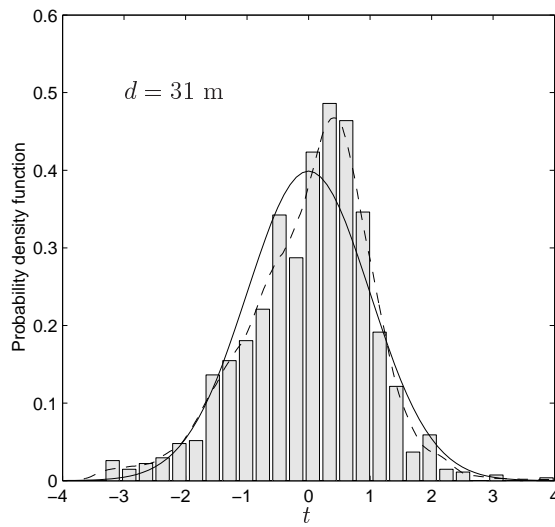
Figure H.12: (a) Histogram of transformed wave period data. — standard Gaussian probability density function; -- KDE of the transformed wave period data. (b) Paired plot of the transformed wave periods between t_1 and t_2 compared with a contour plot of the standard Gaussian distribution. $d = 78$ m.



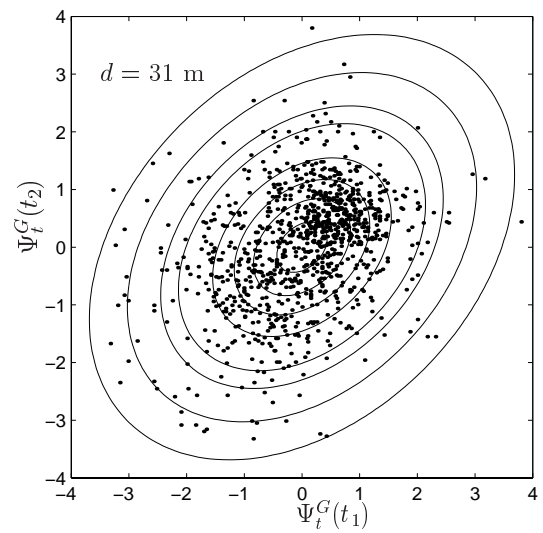
(a)



(b)

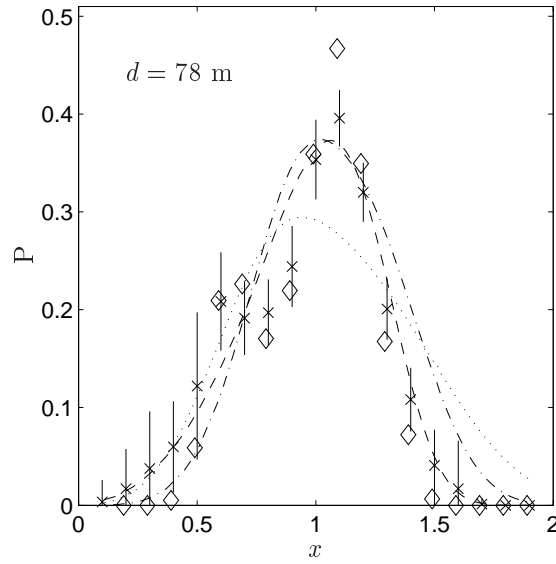


(c)

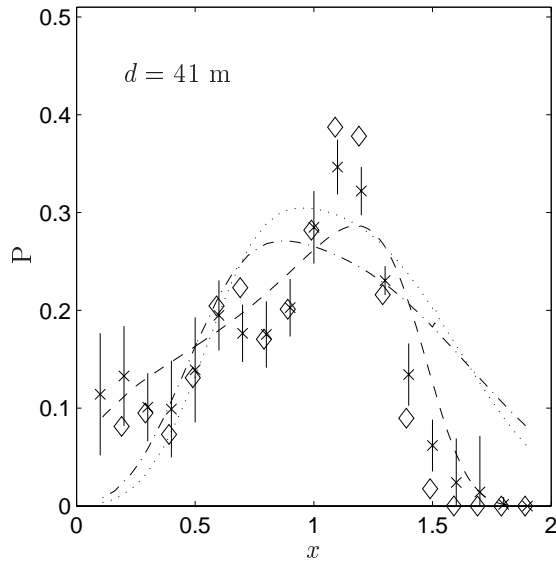


(d)

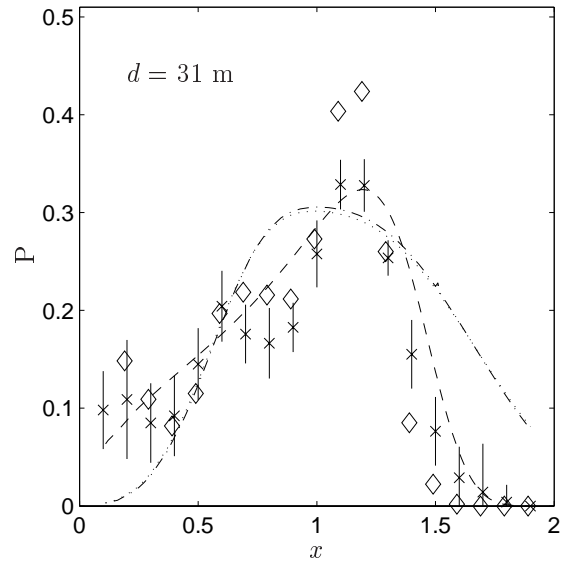
Figure H.13: (a), (c) Histogram of transformed wave period data. — standard Gaussian probability density function; -- KDE of the transformed wave period data. (b), (d) Paired plot of the transformed wave periods between t_1 and t_2 compared with a contour plot of the standard Gaussian distribution.



(a)



(b)



(c)

Figure H.14: The probability that a wave period is in an interval $[\tilde{t}_1, \tilde{t}_2]$ given that the previous wave period was in the same interval, where $\tilde{t}_1 = x - 0.1$ and $\tilde{t}_2 = x + 0.1$. -- Nataf model; \cdots Myrhaug and Rue (1993) model; $-\cdot-$ Myrhaug and Rue (1998) model; \diamond laboratory data; \times simulated data. ($P = P(x - 0.1 < T_2 < x + 0.1 | x - 0.1 < T_1 < x + 0.1)$).

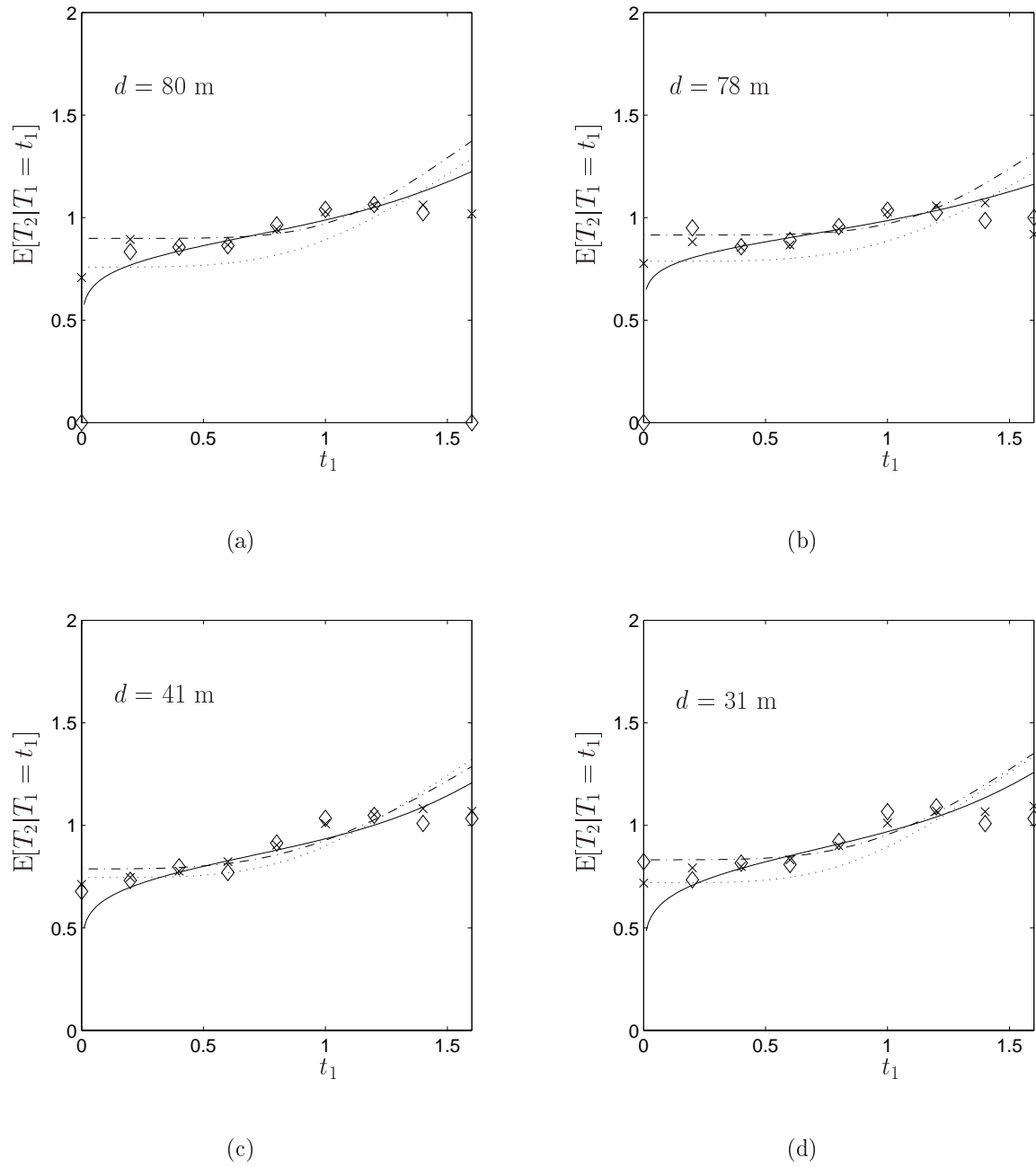


Figure H.15: Conditional expectation of the wave period given the previous wave period. — Nataf-Gamma model; \cdots Myrhaug and Rue (1993) model; --- Myrhaug and Rue (1998) model; \diamond laboratory data; \times simulated data.